Innovative electrode materials for dual band visible – near infrared electrochromic smart windows

Thesis presented by Florian Gillissen
For the grade of Doctor in Sciences
At Department of Chemistry
University of Liège

December 2024

Examination committee

Prof. Gauthier Eppe	President	University of Liège
Prof. Ngoc Duy Nguyen	Secretary	University of Liège
Prof. Rudi Cloots	Supervisor	University of Liège
Prof. Anthony Maho	Co-supervisor	University of Bordeaux
Prof. Luc Henrard	Examiner	University of Namur
Prof. Thierry Gacoin	Examiner	Polytechnic Institute of Paris
Dr. Aline Rougier	Examiner	ICMCB-CNRS
Dr. Abdelfattah Mahmoud	Examiner	University of Liège

Remerciements

J'aimerai tout d'abord remercier Monsieur le Professeur Cloots (le Chef) de m'avoir accueilli au sein du laboratoire GREEnMat depuis mon stage de recherche en Master 1, en passant par mon mémoire de fin d'étude, pour enfin arriver à ces 5 années de thèse, dont il est le promoteur.

Je voudrais également remercier le Professeur ? Docteur ? Anthony Maho (il n'est pas encore sûr de comment il faut l'appeler depuis son nouveau poste), qui a encadré mon travail au GREEnMat depuis mon stage de Master 1, jusqu'à cette thèse, devenant même le co-promoteur de cette dernière après avoir décroché un poste de Professeur Junior à l'Université de Bordeaux. Merci pour ton soutien infaillible durant toutes ses années, pour tes précieux conseils et les nombreuses discussions/réunions qui ont permis de me former à la recherche scientifique, à l'interprétation et la présentation efficaces des résultats, et tant d'autres compétences qui me seront utiles dans la suite de mon parcours (dont le réflexe d'éviter le mauve en présence de mes promoteurs, c'est bien noté). Surtout, merci de m'avoir fait confiance pour ce poste de recherche doctorale, alors que je n'étais pas sur de vouloir continuer sur cette voie, aujourd'hui je présente ce travail de recherche grâce à toi.

Merci également aux membres du (Jury Professeur Eppe, président, Professeur Nguyen, secrétaire, Professeur Henrard, Professeur Gacoin, Docteur Rougier et Docteur Mahmoud) d'avoir accepté l'invitation à en faire partie, pour leur relecture du manuscrit, leur intérêt pour le sujet ainsi que leurs suggestions qui ont permis d'améliorer la qualité de ce travail. Je ne doute pas que leurs questions lors de la défense de cette thèse conduiront à d'intéressantes discussions et de nouvelles idées dans l'optique d'éventuels futurs travaux de recherche sur ce sujet au GREEnMat.

En particulier, je remercie le Professeur Luc Henrard et son équipe, pour leurs nombreux apports et leur aide précieuse dans le cadre la collaboration entre Liège et Namur pour le projet PLASMON_EC (dans lequel s'inscrit cette thèse), et le Docteur Aline Rougier et ses collègues, avec qui j'ai eu l'occasion de travailler dans le cadre d'une collaboration Hubert-Curien, et qui m'ont accueilli à l'ICMCB plusieurs fois au cours de ces 5 années. L'ensemble des discussions et résultats obtenus lors de ces collaborations ont été d'une importance capitale pour la réalisation de cette thèse, notamment les apports en optique et en modélisation du Docteur Michaël Lobet et Nicolas DeMoor, les mesures XPS réalisées par le Docteur Rachel Gouttebaron et les images en microscopie obtenues par le Docteur Jean François Colomer à l'Université de Namur, mais aussi les mesures EPR effectuées par le Docteur Mathieu Duttine et les caractérisations profilométriques accomplies par le Docteur Brandon Faceira à l'ICMCB à Bordeaux.

Merci également à toute l'équipe du GREEnMat, pour votre aide ponctuelle pour des mesures ou caractérisations, pour la formation aux machines, mais surtout pour la bonne ambiance, les temps de midi, les activités de labo, les boulet frite et pain saucisse du cercle, les fêtes du personnel, les repas de fin d'année (toujours suivi d'un passage sur le marché de Noël). Merci en particulier au pôle film, notamment le Docteur Jennifer Dewalque pour son encadrement lors de ces dernières années de thèse, et Gilles Spronck pour son aide au laboratoire, toutes les formations, les mesures réalisées et les services rendus (il aura tenté de trouver comment m'énerver au cours de ces 5 années mais il n'a pas encore trouvé, même s'il parait qu'il a une arme secrète qu'il ne veut pas utiliser), mais aussi les stagiaires et mémorants que j'ai pu encadrer : Illiassou, Ninon et Julien, dont le travail de qualité à pu être intégrer à cette thèse.

Je tiens à remercier le groupe des chimistes, formé il y a presque 10 ans durant nos années d'études et toujours aussi soudé. Merci pour les soirées, les voyages, les sorties cinéma, les après-midis/soirées jeux de société avec certains, les jeudi power avec Thomas Carabin (et ses monologues dans la voiture, il aime bien parler), les temps de midi de la grastronomie. Merci aux autres groupes d'amis formés en dehors de l'université : les zozos, les molqueens, mais aussi ceux rencontrés dans le cadre du sport.

Enfin, merci à ma famille pour leur soutien, mes parents et mes deux sœurs, mes grands parents et surtout Kathy, qui me supporte depuis bientôt 7 ans (elle est courageuse la pauvre).

En gros, merci à tous !

Abstract

The control of the temperature and luminosity represents most of the energy demand in residential and commercial buildings. In response, several technologies have been developed with the aim to better manage their energy expenses. Amongst these, chromogenic materials allow the modulation of incoming visible (VIS) and near infrared (NIR) solar radiations transmitted through windows and contributing to the indoor brightness and heat levels, respectively. In particular, electrochromic materials can be applied as thin films in "smart windows" to actively modulate VIS and NIR on-demand, depending on the weather conditions and/or user's preferences.

Recently, a new generation of electrochromic materials has been developed, working upon dual band functionality: they provide a selective and independent control of daylight and warmth contributions, with the intent to further improve the energy savings brought by the smart windows technology. In the scope of this work, oxygen deficient molybdenum-tungsten mixed oxide "MoWOx" is investigated as novel dual band electrochromic formulation, highlighting enhanced plasmonic behavior when processed in solvothermal conditions; these plasmonic features confer the materials with a strong broadband optical absorption, observed to be electrochromically tunable across the VIS and NIR regions.

The first section of this work focuses on the processing and characterization of MoWOx active materials in the form of powders, studying their morphological, structural, optical and electronic properties using a range of techniques including SEM, TEM, XRD, UV-VIS-NIR spectrophotometry, XPS and EPR. In correlation with literature, MoWOx compounds demonstrate very promising optical and electronic properties, exhibiting intense absorption in both VIS and NIR ranges as a result of the increased combined formation of reduced species and oxygen vacancies. These specifically arise from the Mo/W substitution and from proton insertion taking place during the solvothermal process.

As a second step, electrochromic inks are formulated from the powders and consecutively deposited as thin films using wet deposition approaches, especially spin coating. The layers are characterized in regards to their electrochemical properties and electrochromic performances, notably using a three electrodes setup in a liquid electrolyte. Optical spectra of the films as a function of the applied potential confirm the occurrence of dual band behavior in the studied MoWOx formulations, displaying three optical modes. Remarkably, these are observed to deviate from what is usually found in a typical dual band material, being the VIS/NIR-transparent *bright* state, the VIS/NIR-opacified *dark* state, and the additional intermediate, VIS-transparent and NIR-opacified *cool* state. Indeed, due to the very intense optical absorption being observed, MoWOx exhibits a peculiar mode in its "clear" state, with a high transmittance in the NIR combined with a partial darkening of the VIS region, corresponding *de facto* to a *warm* state. By accessing this new additional state, dual band smart windows integrating MoWOx-based electrochromic layers could therefore further improve their energy efficiency and provide a greater adaptability towards different weather conditions, especially fresh/cold geographies and seasons. The mechanisms and kinetics of the coloration/bleaching of the MoWOx films are further studied by using different electrolytes, Li^+ and TBA^+ based, and electrochemical profiles (cyclic voltammetry, chronoamperometry …); optimal experimental conditions notably show maximized contrasts of 16% and 45% in the VIS and NIR ranges, respectively, in the intermediate NIR-preferential state (+0.0 V), further increasing to 24% and 67% in the fully colored state (-1.0 V).

With the intent to investigate the electrochromic performances of our MoWOx formulations in fully assembled electrochromic devices, efficient counter electrodes have then been developed to be applied in tandem. In this context, CeO_2 has been considered as a well-known optically-neutral counter electrode material, with polyethylene glycol (PEG)-assisted ultrasonic spray pyrolysis (USP) deposition and molybdenum doping proposed as means to enhance both optical and electrochemical properties through the formation of oxygen vacancies and exploiting the numerous oxidation states of molybdenum. Combining those two strategies, the produced films display excellent transmittance levels of 95+%, as well as large capacity of up to 28 mC/cm^2 in the optimum 6%at. Mo sample, surpassing the surveyed literature highlighting average transmittance levels of 70% and at most 25 mC/cm^2 of capacity.

All in all, the great performances of the processed Mo-CeO_2 counter electrodes allow the MoWOx active layers to fully express their electrochromic efficiency. As a final step of this doctoral work, the dual band electrochromic performances of the active materials are assessed from complete devices assembling MoWOx and Mo-CeO_2 electrodes. Liquid setups are first investigated, with the two electrodes parallelly positioned and immersed in an electrolyte solution, followed by the assembly of solid devices involving lamination with gel polymer electrolytes binding the working and counter electrodes as a single solid unit. The spectroelectrochemical characterization of these liquid and solid devices ultimately attest for the viability of proof-of-concept devices assembled from MoWOx and Mo-CeO_2 samples, efficiently displaying the targeted and desired dual band behavior.

In conclusion, the results acquired in the scope of this thesis show the peculiar optical and electrochemical properties of the presently designed and characterized MoWOx-based electrochromic systems, standing as proof-of-concept demonstrators of upgraded dual band smart windows. These will therefore pave the way towards future fundamental and applied developments, leading to an emphasized reduction of heating, air conditioning and artificial lighting related energy consumption and waste in new and renovated buildings.

Résumé

La majorité de la demande énergétique des bâtiments résidentiels et commerciaux est allouée au contrôle de la luminosité et de la chaleur interne. En réponse, de nombreuses technologies ont été développées afin de gérer de manière plus efficace leur consommation énergétique. Parmi celles-ci, les matériaux chromogènes permettent de contrôler les apports de rayonnement solaire visible (VIS) et proche infrarouge (NIR) transmis au travers des vitrages et contribuant respectivement à la luminosité et la chaleur à l'intérieur des bâtiments. En particulier, des composés électrochromes peuvent être exploités en tant que couches minces dans des « fenêtres intelligentes » afin d'y moduler de manière sélective et dynamique les rayonnements VIS et NIR à la demande, et ce en fonction des conditions météorologiques et/ou des préférences de l'utilisateur.

Récemment, une nouvelle génération de matériaux électrochromes a été mise en évidence et étudiée, présentant une filtration optique à double bande permettant le contrôle indépendant des longueurs d'onde VIS et NIR dans le but d'améliorer davantage les économies d'énergie apportées par les fenêtres intelligentes. Dans le cadre de ce travail doctoral, l'oxyde mixte de molybdène-tungstène déficient en oxygène « MoWOx » est étudié en tant que nouvelle formulation électrochrome double bande : obtenue à partir de protocoles en voie solvothermale, celle-ci présente des propriétés plasmoniques résultant en une absorption intense modulable sur une large portion du spectre VIS-NIR.

La première section de la thèse se concentre sur la synthèse et la caractérisation de matériaux actifs MoWOx sous la forme de poudres, étudiant leurs propriétés morphologiques, structurelles, optiques et électroniques via une gamme de méthode d'analyses telles que les microscopies SEM et TEM, la DRX, la spectrophométrie UV-VIS-NIR, l'XPS et la RPE. En corrélation avec la littérature, les composés MoWOx démontrent des propriétés optiques et électroniques très prometteuses, témoignant d'une absorption optique intense tant dans le VIS que dans le NIR provenant de la formation combinée et intensifiée d'espèces métalliques réduites et de lacunes en oxygène. Cette synergie découle directement de la substitution Mo/W et de l'insertion de protons ayant lieu au cours de la synthèse solvothermale.

Dans un second temps, des encres électrochromes sont formulées à partir des poudres et consécutivement déposées sous forme de films minces par le bias de procédés en voie liquide, spécifiquement par spin coating. Les films sont caractérisés du point de vue de leurs propriétés électrochimiques ainsi que pour leurs performances électrochromes, selon une configuration à trois électrodes en milieu électrolyte liquide. Les spectres optiques des films, en fonction du potentiel appliqué, confirment l'occurrence d'un comportement double bande dans les formulations MoWOx, démontrant trois modes optiques. Très remarquablement, ceux-ci dévient des comportements classiquement observés dans les matériaux électrochromes double bande actuels, à savoir l'état *bright*, transparent dans le VIS et le NIR, l'état *dark*, opaque dans le VIS et le NIR, et un état intermédiaire additionnel, transparent dans le VIS et opaque dans le NIR, l'état *cool*. En l'occurrence, vu l'importante absorption optique générée et mise en évidence, le MoWOx présente un état optique particulier dans son état « clair », avec une haute transmittance dans le NIR combinée à une coloration partielle du VIS, correspondant de fait à un état *warm*. En rendant accessible ce mode optique complémentaire, des fenêtres intelligente double bande intégrant des composés MoWOx pourrait présenter une efficacité énergétique améliorée de par une meilleure adaptation à différentes conditions climatiques, en particulier les géographies et saisons froides. Les mécanismes et cinétiques de coloration/décoloration des films sont par ailleurs étudiés plus en profondeur par le biais de l'utilisation de différents électrolytes, à base d'ions Li^+ et TBA^+, et de profils électrochimiques multiples (voltampérométrie cyclique, chronoampérométrie). Sur base de conditions expérimentales progressivement optimalisées, les matériaux MoWOx font notamment état de contrastes optiques de 16% et 45% dans les régions VIS et NIR, respectivement, dans l'état intermédiaire préférentiel des rayonnements NIR (soit pour un potentiel de +0.0 V), avec des valeurs qui augmentent jusqu'à 24% et 67% dans l'état complètement coloré (-1.0 V).

Dans l'optique d'étudier les performances du MoWOx dans des dispositifs électrochromes complètement assemblés, des matériaux de contre électrodes efficaces ont été développés pour une utilisation en tandem. A cet égard, l'oxyde de cérium CeO_2 est un matériau de contre électrode optiquement neutre bien connu de la communauté électrochrome. Dans le cadre de cette thèse, le dépôt de couches minces par spray pyrolyse ultrasonique USP incorporant du polyéthylène glycol PEG comme surfactant / additif, ainsi qu'un dopage au molybdène, sont proposés comme stratégies d'amélioration des performances optiques et électrochimiques des films de CeO_2. En implémentant ces deux approches de manière combinée, d'excellents niveaux de transmittance sont obtenus avec plus de 95%, en plus d'une haute capacité de 28 mC/cm^2, surpassant les performances des formulations rapportées dans la littérature avec une moyenne de 70% de transmittance et une capacité d'au mieux 25 mC/cm^2.

Au final, les performances convaincantes de ces contre électrodes Mo-CeO_2 permettent aux matériaux MoWOx de pleinement exprimer leur efficacité électrochrome. Ainsi, en dernière étape de ce travail, les performances électrochromes double bande des matériaux actifs sont évaluées dans des systèmes complets assemblant des électrodes MoWOx et Mo-CeO_2. Des configurations liquides sont d'abord étudiées, pour lesquelles les deux électrodes sont disposées en parallèle et plongées dans une solution électrolyte ; ensuite des dispositifs solides sont préparés par lamination d'un gel polymère électrolyte pour assembler les deux électrodes sous la forme d'une unique unité solide. La caractérisation spectroélectrochimique de ces configurations liquides et solides démontrent globalement la viabilité des démonstrateurs produits à partir d'échantillons de MoWOx et Mo-CeO_2, présentant tel que ciblé un comportement double bande efficace et robuste.

En conclusion, les résultats obtenus dans le cadre de cette thèse ont permis de mettre en évidence les propriétés optiques et électroniques particulières des composés MoWOx, résultant en leur application convaincantes en tant que matériau actif dans des démonstrateurs « preuves de concept » de nouvelles fenêtres intelligentes électrochromes à modulation double bande. Cette contribution ouvrira sans nul doute la voie à d'autres développements fondamentaux et appliqués, menant au final à une diminution renforcée de la consommation énergétique en chauffage, en conditionnement d'air et en éclairage artificiel dans les bâtiments, et ce tant pour les nouvelles constructions que pour les rénovations.

Table of content

List of figures

List of tables

List of abbreviations

Abbreviations	***Full name***
a. u.	Arbitrary units
ATO	Aluminum-doped tin oxide
AZO	Aluminum-doped zinc oxide
Bmim	1-butyl-3-methylimidazolium
CA	Chronoamperometry
CE	Coloration efficiency
CeMo	Molybdenum-doped cerium oxide
CV	Cyclic voltammetry
EDX	Energy dispersive X-ray spectroscopy
EPR	Electron paramagnetic resonance
FTO	Fluorine-doped tin oxide
HVAC	Heating, ventilation and air conditioning
ICO	Indium-doped cadmium oxide
ITO	Tin-doped indium oxide
IVCT	Intervalence charge transfer
KM	Kubelka-Munk
LSPR	Localized surface plasmon resonance
MoWOx	Molybdenum-tungsten oxide
NIR	Near infrared
PEG	Polyethylene glycol
PET	Polyethylene terephthalate
PTFE	polytetrafluoroethylene
SEC	Spectroelectrochemistry
SEM	Scanning electron microscopy
SERS	Surface-enhanced Raman spectroscopy
SPR	Surface plasmon resonance
TBA	Tetrabutylammonium
TCO	Transparent conductive oxide
TEM	Transmission electron microscopy

TFSI	Trifluoromethanesulfonyl imide
USP	Ultrasonic spray pyrolysis
VIS	Visible
XPS	X-ray photoelectron spectroscopy
XRD	X-ray diffraction

List of articles, oral and poster communications

Scientific papers

- « Hybrid Molybdenum-Tungsten Oxide as VIS-NIR Selective Electrochromic Material for Advanced Dual-Band Smart Windows » F. Gillissen, J. Dewalque, A. Maho, M. Lobet, P. Louette, M. Duttine, A. Rougier, L. Henrard, R. Cloots, resubmitted to Advanced Optical Materials (Wiley) after reviewing, 08/10/24;
- « Optical properties of novel doped metal oxides for electrochromic applications » F. Gillissen, M. Lobet, N. De Moor, A. Maho, R. Cloots, L. Henrard, submitted to ACS Applied Optical Materials (ACS), 10/10/24;
- « Development of Molybdenum Doped CeO_2 Passive Counter Electrodes by PEG-Assisted Ultrasonic Spray Pyrolysis» F. Gillissen, J. Dewalque, P. Colson, A. Maho, R. Cloots, draft currently being written.

Oral presentations

- « Hybrid Molybdenum-Tungsten Oxide as Novel Dual-Band, VIS-NIR Selective Electrochromic Material in Advanced Smart Windows » (F. Gillissen, J. Dewalque, P. Colson, R. Cloots, A. Maho), Materials Research Society Spring Meeting 2023, 11/04/2023;
- « *In-situ* Electrochemistry Applied to Electrochromic Materials » (F. Gillissen, B. Faceira, A. Mahmoud, A. Rougier, R. Cloots, A. Maho), Condensed Matter Division 29, 23/08/2022;
- « Hybrid Molybdenum-Tungsten Oxide as “New Generation” Plasmonic Electrochromic Material for Smart Windows » (F. Gillissen, A. Maho, N. De Moor, B. Faceira, M. Lobet, A. Rougier, L. Henrard, R. Cloots), European Materials Research Society Spring Meeting 2022, 31/05/2022.

Posters

- « Hybrid Molybdenum-Tungsten Oxide as Plasmonic Electrochromic Material for Dual-Band VIS-NIR Smart Windows » (F. Gillissen, J. Dewalque, P. Colson, R. Cloots, A. Maho), Paris Saclay Plasmonic School $(PS)^2$, 23-27/10/2023;
- « Hybrid Molybdenum-Tungsten Oxide Nanoparticles as Novel Plasmonic Materials for Electrochromic Smart Windows » (F. Gillissen, A. Maho, N. De Moor, M. Lobet, L. Henrard, R. Cloots), Belgian Photonics Online Meetup, 23-24/09/2021;
- « Electrochromic Nanomaterials Based on Hybrid Molybdenum-Tungsten Oxide : Synthesis, Wet Coating and Structural / Optoelectronic Chararcterizations » (F. Gillissen, A. Maho, L. M. Manceriu, P. Colson, B. Vertruyen et R. Cloots), Belgium Ceramic Society, 05/05/2021.

Chapter 1 – Introduction, state of the art and objectives of the PhD thesis work

Chapter 1 – Introduction, state of the art and objectives of the PhD research work

1.1. General context

1.1.1. Environmental context

In the current ecological and economical context faced by humanity, it is of the utmost importance to change how much energy and resources is spent on a daily basis, by reducing our carbon footprint but also by modifying our habits to improve and optimize how this energy is spent. Indeed, resources are decreasing, with some becoming scarce, as a greater proportion of earth's population gains access to newer and better technologies as a way to improve their quality of life[1]. However, the overuse of these resources and the corresponding energy expenses come with an ecological cost, leading to anthropogenic-caused climate change[2]. The latter, in turn, impacts the live of billions, with weather conditions becoming more extreme and catastrophic events such as storm, floods, wildfires and heatwaves appearing at higher frequencies[3].

The required paradigm shift to reverse or at least minimize the effects of climate change can arise from numerous sectors, such as choosing different means of transport, consuming local (and seasonal) products, adopting new eating habits such as decreasing meat consumption (especially red meat), and avoiding waste by not falling into the trap of excessive consumerism that can be exacerbated by fast fashion or the latest trends[4].

Besides changing our habits regarding how we eat, move and buy, a lot can be done to improve the energy efficiency of buildings, responsible for most of the energy demand in Europe[5] and US[6]. In this context, the construction sector could greatly improve the global energy demand by promoting the use of more environmentally friendly building materials, but also by incorporating efficient energy saving solutions in new constructions as to enhance their energy demand[7]. Therefore, the construction appears as an obvious sector which can be leveraged to reduced and improve our energetic footprint through efficient building design.

1.1.2. Energy efficiency in residential and commercial buildings

As introduced above, and shown in **Figure 1.1**, residential and commercial buildings are responsible for 40% of the total annual energy demand nowadays, according to recent reports regarding the energetic consumption in Europe[5] and US[6]. The other 60% are allocated to the industry (25-33%) and transport (30-31%). Of the 40% of energy destined for buildings, the demand is evenly split between residential and commercial installations in the USA, while residential buildings represent 60% of the demand in Europe. Three quarter of this energy is used towards the control of the indoor temperature and luminosity through heating, ventilation and air conditioning (HVAC), accounting for 63-64% of the demand, and lighting, representing the remaining 8-10%. The other 25% are allocated to hot water production and appliances/IT equipment.

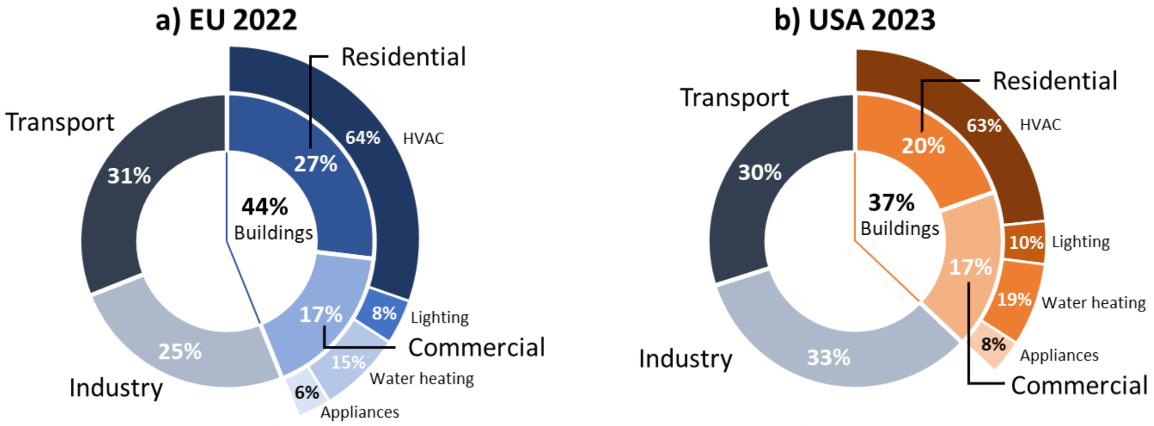

Figure 1.1: Pie charts of the energy demand by sectors in Europe (a, EU-27, 2022)[5] and the United States (b, 2023)[6].

A more precise breakdown of all contributions in residential and commercial buildings indicate a discrepancy between both (**Figure 1.2**). Indeed, in residential buildings, most of the energy is directed towards indoor temperature control, with heating (24%) appearing as the main contribution by far, followed by cooling (11%), with lighting appearing at 6.5% in fourth place. Water heating (13.5%), refrigeration (6%) and electronics (5.5%) also represent significant shares of the total energy demand.

In the case of commercial buildings, the energy demand distribution changes drastically, with heating, cooling and ventilation (HVAC) represent a 12%, 8% and 8.5% contribution, respectively, adding up to a combined 28.5% in comparison to the 36.5% observed in residential buildings. Instead, ventilation and office equipment reach demands of 8.5% and 6%, respectively, while lighting now takes up 8% of the demand.

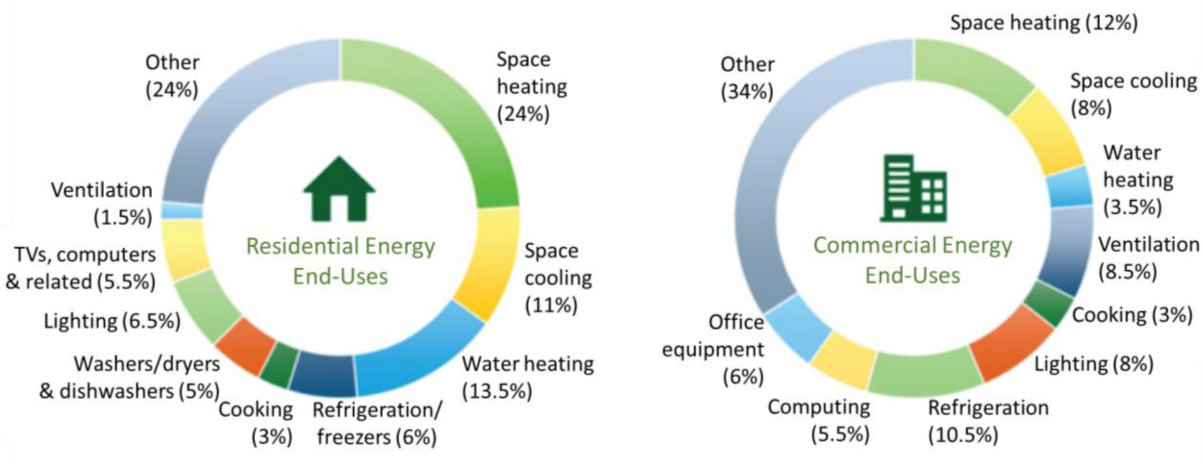

Figure 1.2: Pie chart of the end use of energy demand for residential and commercial buildings in the United States (2018)[8].

In view of the current economic and ecological context faced by our society, the development of novel and innovative energy-saving technologies is of the upmost importance. In developed countries, some of these technologies are already well-established in the domestic and commercial estate. Amongst the most widespread are solar panels[9,10], advanced thermal insulation solutions[9], LED bulbs[11], geothermal heat pumps[9,10] and green roofs[9,12], to cite a few. However, with modern architecture favoring the installation of large bay windows[13,14], sometimes covering the front facade or even the whole building, large quantities of energy can be wasted due to the inefficient fenestration technologies used, as well as the lack of proper adaptability of the windows towards external factors such as the preferences of the user or the weather conditions, being of course influenced by seasons and geographies[15].

1.1.3. Smart glazing in energy-efficient buildings

In order to tackle these limitations, new technologies have been developed in an attempt to reduce the energy demands of the buildings equipped with these new fenestration solutions, as well as to improve their functionality. Amongst this new generation of windows, two categories can be identified: first, the passive technologies, in which the best known are double and triple paned windows[15], as well as low emissivity coatings[15–17] (**Figure 1.3**). These solutions have been developed to lower the amount of heat transmitted into/emitted from the building through the windows, stabilizing the indoor temperature to stay cool in the summer and warm in the winter.

Even though these passive technologies can selectively modulate given regions of the solar spectrum[9,16], for instance blocking the infrared (responsible for the heat contribution from the solar irradiation) while displaying high transmittance in the visible range, they can suffer from their static functioning state, meaning that their functionality cannot be tuned as a function of factors impacting the changing energy demand for heat and luminosity control[15]. This main limitation encountered by these technologies can greatly hinder their energetic efficiency and represents a major drawback for their future implementation, as more and more efficient and selective solutions are being developed.

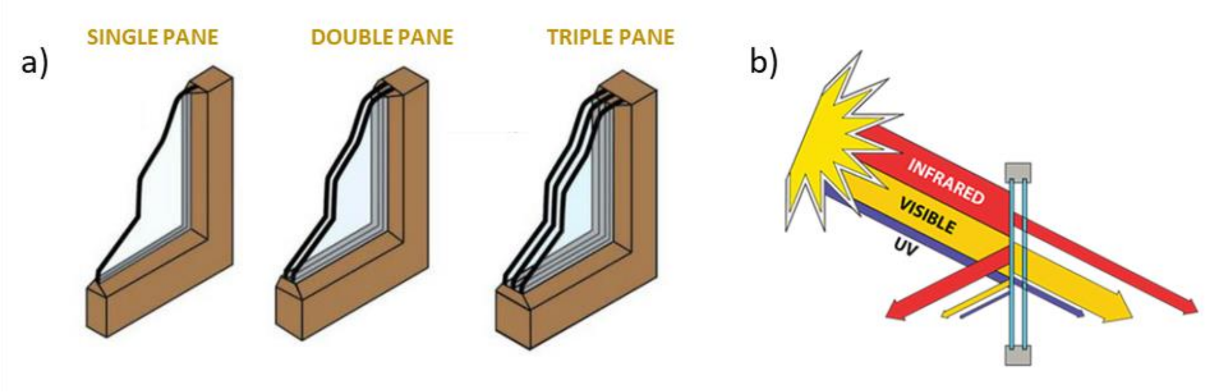

Figure 1.3: Schematic representation of single, double and triple pane windows (a)[18], and low emissivity coatings reflecting infrared light preferentially (b)[19].

However, the problems occurring from those passive materials pose no issues for a second category of fenestration solution: the active, chromogenic glazing technologies[15]. These, also referred to as "smart windows", display changes in their optical properties in response to an external stimulus, by modifying the absorption and/or reflection of the active material in the coating (**Figure 1.4**), resulting in the modulation of solar radiation in a given interval of wavelengths[15]. Three main types of chromogenic windows are generally considered, in function of the nature of the active material used in the "smart" coating[15]:

- *Photo*chromic windows, driven by *light* stimuli *Δhv*: the modulation is activated upon interaction of the active material with an incident electromagnetic radiation possessing enough energy to enable the modification in the optical properties of the device;
- *Thermo*chromic windows, driven by *temperature* variations *ΔT*: they rely on changes in the physico-chemical and structural properties of the active material from a given temperature threshold, leading to modifications in the optical performances of the device;
- *Electro*chromic windows, driven by *voltage* bias *ΔV*: modulation of the incoming solar radiation appears upon the application of a suitable electrical charging.

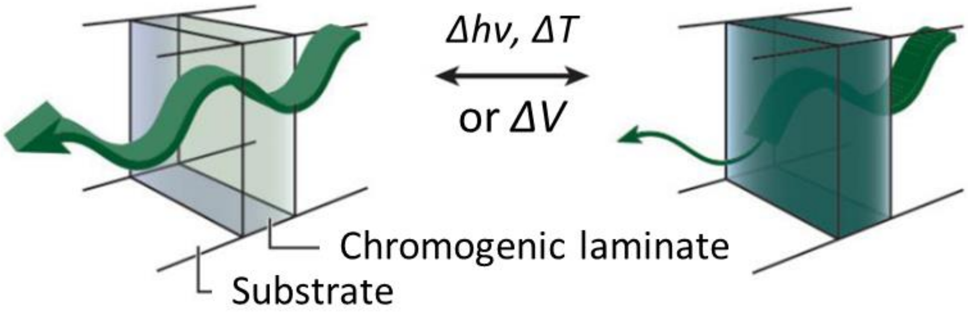

Figure 1.4: Schematic representation of the working principle of chromogenic smart windows[15].

In the first two cases (the photo- and thermochromic materials), even though these technologies exhibit a great benefit, only depending on renewable energy resources (light and heat) that can be harnessed for free, the modulation appears as a result of an external stimulus on which the user has no or only limited control. The remaining category, electrochromic systems, exhibits the possibility of dynamically modulating the solar radiation "on-demand", as the modification of the optical properties relies on the application of an electrical bias, that can be controlled by the user. This high degree of control on the chromogenic activity of the windows comes with a cost, as a difference of potential has to be applied for the window to be operated, and thus impacting the net energy gain of the device in comparison to the two other chromogenic families. However, the bias required to activate the electrochromic effect is usually very low, typically in the range of a few volts; therefore, the small loss in energy necessary for the operation of the window can be largely compensated by the potential energy savings arising from a better adaptability of the technology towards external conditions[20]. **Figure 1.5** below shows how electrochromic devices results in greater energy savings than the other chromogenic solutions, both from temperature and lighting control, and even more compared to passive technologies. Moreover, peak cooling and heating load simulation as a function of the orientation demonstrates the enhanced energy savings brought by smart windows in comparison to passive low-ε coatings and clear glass[21] (**Figure 1.6a**,**b**).

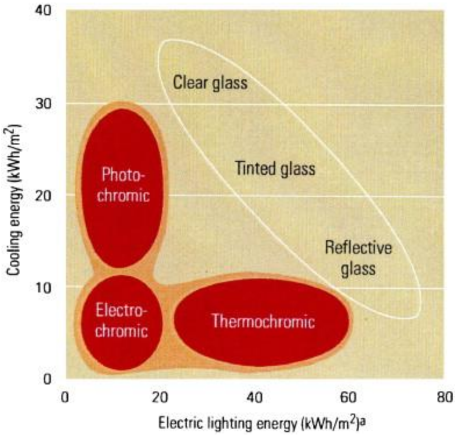

Figure 1.5: Energy expanditure for cooling and lighting for different type of passive and chromogenic window technologies[20].

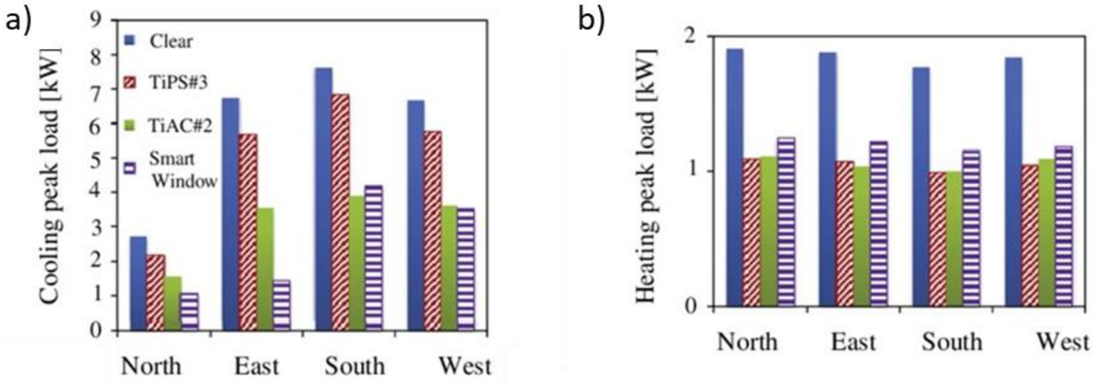

Figure 1.6: Simulations of the cooling peak load (a), and heating peak load (b) for a classic clear glass window, two low-e coatings (TiPS and TiAC), and an electrochromic smart window[21].

Several actors in the glass industry have already developed such "smart windows" with a few of them being able to commercialize such products, notably SageGlass - Saint Gobain[22] and AGC Glass (Halio™)[23]. The smart glazing technologies developed by these companies display the ability to switch on demand between a transparent and a colored state, combinedly modulating the visible and infrared ranges (as illustrated in **Figure 1.7**). Theoretical modelling predicts a decrease in the energy demand of 40 – 170 kWh/m²yr (depending on the initial parameters of the simulation) by using such dynamically activated windows in comparison to clear glass and blinds[24–26]. In practice, the implementation of electrochromic windows in buildings has been able to demonstrate energy saving reaching 10 – 40 kWh/m² per year[27], achieving the lower end efficiency of the simulations in a real life scenario. In comparison, the average household in Europe consumes 1600 kWh/yr per capita[28] and is equipped with around 10 – 20 m² of windows (calculated on the basis of a 100 m² average house surface[29] and the recommendation of at least 20% of glazed surface in comparison to the floor area[30]). This results in yearly savings reaching 100 to 800 kWh, corresponding to a 5-50% decrease in energy consumption in a one-person household, then progressively decreasing for larger households. These projections highlight the energetic efficiency of such devices, and the economic and ecological benefits brought forward by this "smart window" technology. In addition, with more than 37 million m² of glass installed annually all around the world[15], there is a great market opportunity for industrial investment in the technology, which could lead to new advancements in the field, with electrochromic glazing becoming more affordable and promoting their widespread use in commercial as well as residential buildings.

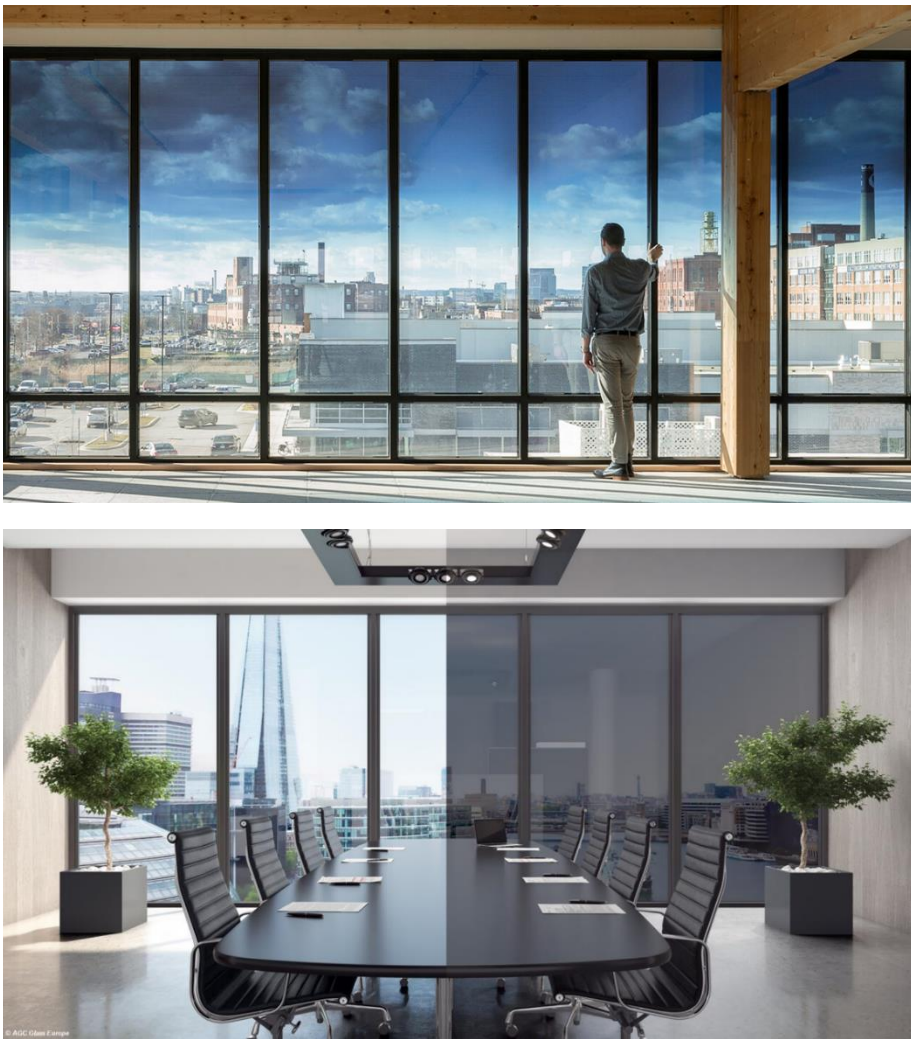

Figure 1.7: Pictures illustrating the electrochromic activity of commercially available smart windows from Saint Gobain[22] *(top) and AGC Glass*[23] *(bottom).*

In view of the elements discussed above, amongst the available chromogenic technologies, electrochromic devices and materials appear to be the best candidate for the development and fabrication of highly efficient, dynamically active “smart windows” enabling the on-demand modulation of the solar radiation, and demonstrating great adaptability towards the user’s preference or changing weather conditions.

1.2. Electrochromic smart windows

1.2.1. Materials overview

The optical activity of an electrochromic smart window arises mainly from the active material used to formulate the glazing. In all generality, electrochromism is characterized by the ability of a given material to reversibly switch between different optical states upon the application of an electrical bias[15,31]. In conventional electrochromic materials, such as those exploited in some of the commercially available glazing presented earlier, the material switches from a high transmittance state (referred to as the “bleached” state) to a low transmittance state (corresponding to the “colored” state), as exhibited in **Figure 1.8**.

Figure 1.8: Pictures of an electrochromic film switching between its bleached (left) and colored states (right)[31].

By tuning the extent of the applied bias and its duration, it is possible to control the intensity of the coloration, giving access to a whole range of intermediate states in between the two extreme ones, depending on the intended application of the device. For example, electrochromic windows have been specially developed by Gentex to equip the Boeing 787 Dreamliner aircraft[32]. **Figure 1.9** below shows the range of coloration expected to be provided by the device, going from transparent, to dimmed (keeping a clear outside view and natural luminosity while cutting sunlight glare), and finally completely opaque, replacing the usual slide-down blinds.

Figure 1.9: Progressive coloration of a Gentex electrochromic glazing used on an Boeing 787 Dreamliner window[32].

Electrochromic properties have been highlighted in a number of materials, that can be organized in four main categories[15,33–38]:

- Organic molecules such as viologens;
- Conjugated conductive polymers such as polypyrroles and polythiophenes;
- Metallic complexes such as Prussian blue;
- Inorganic metal oxides such as WO_3, NiO, V_2O_5.

Depending on the targeted application, each type of material presents benefits and drawbacks. For example, organic formulations are characterized by a wide range of available colors obtained by tuning their properties, notably by changing the length and nature of given side chains and functional groups[39]. In particular, viologens are a wide family of bipyridinium derivatives that can exhibit colored states ranging from purple to red, through blue and green[37,40]. However, many of these small inorganic complexes and organic materials (small molecules and polymers) are usually very sensitive to UV radiation (even though this limitation can somehow be bypassed by the implementation of an anti-UV filter in the device), and are subject to irreversible redox and side reactions, resulting in a loss in efficiency and permanent optical damage, usually translating into an undesirable yellow tinting[15,39]. In addition, these materials often lack the ability to properly modulate the near infrared range[15]. Moreover, the devices should be able to last for a period of 20 to 30 years, at a rate of 3 to 5 complete switches daily, which corresponds to 100k cycles[41]. Given their optical properties and limited durability, these electrochromic compounds present strong limitations for the development of energy efficient electrochromic “smart windows”, aiming at the control of visible (VIS) and neat infrared (NIR) contributions of the solar radiation. However, they clearly appear to be well suited for displays applications[42], even with the possibility of multichromicity by combining different appropriate formulations[15].

Besides, inorganic metal oxides have been shown to exhibit great stability and performances as electrochromic window material[15,43]. While these chemical species only offer a limited range of colors, with colored state usually appearing as blue, brown or grey[44], their high contrast, long term stability and reversibility result in these materials being amongst some of the most studied in the electrochromic field[33]. In particular, transition metal oxides of W, Mo, V, Ir and Ni exhibit great performances, especially WO_3, coloring upon reduction of W(+VI) into W(+V), with contrast up to 98% in the visible range going from transparent to dark blue[43], over 100k bleaching/coloration cycles[43] and high coloration efficiency (CE) up to 150 cm²/C [45]. CE is a figure of merit widely used for quantifying the level of optical and electrochemical functionality of all sorts of electrochromic materials (inorganic, organic …), defined as the intensity of the modulation (contrast) per unit of charge inserted or extracted from the material, according to the following **Equation 1.1**:

$$CE = \frac{\Delta OD}{(Q_{in}/S)} = \frac{\log{(T_b/T_c)}}{(Q_{in}/S)} \tag{1.1}$$

With ΔOD the change in optical density, also defined as the logarithm of the ratio between the T_b and T_c, the transmittance in the bleached and colored state, respectively. Q_{in} is the inserted charge density and is normalized by the area S of the investigated film.

Another broadly studied metal oxide electrochromic material is NiO, often used in combination with WO_3 because of their complementary electrochromic behavior[15,46,47]. Similarly to WO_3, NiO also exhibits great electrochromic performances, coloring upon oxidation of Ni(+II) into Ni(+III), with a visible contrast reaching up to 80%[48], switching between a transparent and a brown colored state, high stability upon cycling (up to 100k cycles)[49] and CE values reaching 100 cm²/C [49]. The high performances displayed by these materials result in their use as electrodes for the development and commercialization of many electrochromic devices from industrial actors, as discussed earlier.

1.2.2. Principle and mechanisms

In conventional electrochromic transition metal oxides, the modification of their optical properties relies on the concomitant insertion/extraction of electrons and ions into/from the crystal lattice of the active species[15,33,49]. As the electrochromic activity can originate from either the insertion or the extraction of ion/electron pairs, electrochromic materials can be divided into two main families, the cathodically charged materials, in which WO_3 and MoO_3 are found, and the anodically charged materials, with NiO and IrO_2 as the main representants[15]. In addition, a small proportion of electrochromic materials, such as V_2O_5, can exhibit both mechanisms due to the large number of different oxidation states that can be found in[50].

In summary, cathodic materials such as WO_3 switch from transparent to colored upon insertion of a cation M^+ (usually H^+ or Li^+, but also other alkali ions such as Na^+, K^+ or multivalent cations such as Al^{3+}), followed by the insertion of electrons to maintain the electroneutrality of the material, and resulting in the reduction of the active species, with W^{6+} typically reduced into their W^{5+} state[15]. The mechanism is represented in the **Equation 1.2** below:

$$Mat\ (bleached) + xM^+ + xe^- \leftrightarrow\ M_xMat\ (colored) \tag{1.2}$$

On the contrary, anodically charged electrochromic materials display a change in their coloration upon oxidation of the material, corresponding to the extraction of cations and electrons from the host lattice in materials such as NiO[15]. The redox switch between Ni^{2+} and Ni^{3+} can be summarized as the following **Equation 1.3**:

$$M_xMat\ (bleached)\ \leftrightarrow\ Mat\ (colored) + xM^+ + xe^- \tag{1.3}$$

From the two equations discussed above, it appears clearly that cathodic and anodic coloration/bleaching mechanisms are complementary, with the electron/ion pairs extracted from one available to be inserted in the other. Taking advantage of this synergistic complementarity between the electrodes, it is possible to obtain the bleached or colored state of both layers simultaneously, allowing a more intense coloration of the dark state while conserving high transmittance levels in the bleached state, resulting in improved contrasts and coloration efficiency[15,33]. Moreover, the superposition of the two colored films (blue WO_3 and brown NiO) can yields a more neutral and aesthetic coloration closer to dark grey or even black[15].

From the point of view of band structures, these two mechanisms were schematized by C. Granqvist in 1994[51]. As reported, most of the well-known electrochromic materials display a structure based on edge-sharing and corner-sharing MeO_6 octahedra (with Me = metal), arranged in a perovskite-like structure (e. g., WO_3, MoO_3), a rutile-like structure (VO_2, IrO_2) or a “layer and block” structure (Nb_2O_5)[51]. Other chemical species, such as NiO, can also adopt a cubic structure in which the atoms can once again be described as an arrangement of MeO_6 octahedra[51]. In these formulations, the electronic *d* shell is split in two levels: e_g and t_{2g}, arising from the arrangement of atoms around the metallic ions, octahedrally surrounded by six oxygen (**Figure 1.10**). The e_g orbitals point directly towards the oxygen atoms while the t_{2g} orbitals are oriented between the oxygen atoms and into empty space, which are therefore of lower energy[51,52].

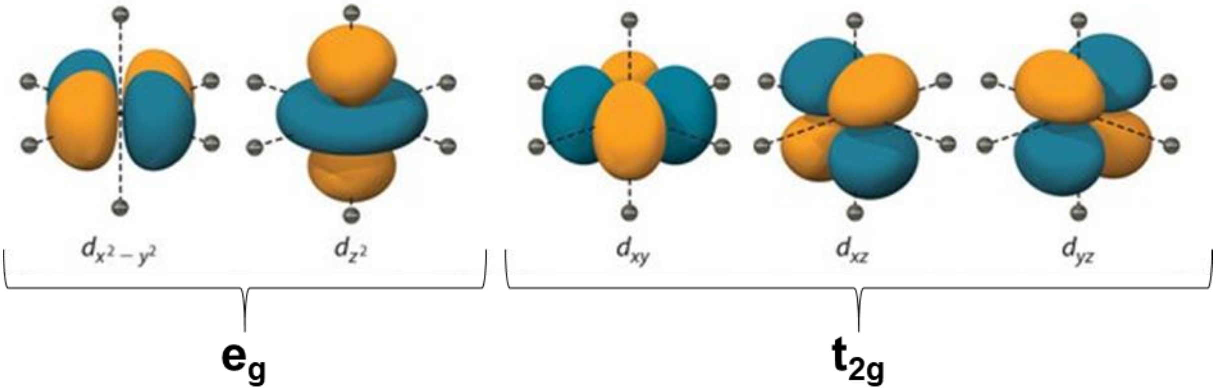

Figure 1.10: Schematic representation of the orientation of the e_g and t_{2g} orbitals around a metallic atom (Me) in a MeO_6 octahedra configuration[52].

The splitting between the two energy levels and the schematized band structure of electrochromic oxides is shown in **Figure 1.11** below. In the case of a cathodic electrochromic material such as WO_3 (**Figure 1.11a**), the Fermi level lies in the bandgap between O_{2p} and t_{2g}. When the t_{2g} level is completely empty and the bandgap large enough, the material appears transparent. When a potential is applied and electron/ion pairs are inserted into the crystal lattice of WO_3, the additional electrons partially fill the t_{2g} band, resulting in absorption in the t_{2g} band and the colored state of the material. On the contrary, anodically active materials such as NiO (**Figure 1.11b**) display a Fermi level in the t_{2g} band, and close to the band gap between the t_{2g} and e_g electronic subshells. In this case, the insertion of electrons upon application of a bias results in the filling of the t_{2g} shell and the Fermi level moving up into the bandgap, the material thus switches from a colored to transparent state.

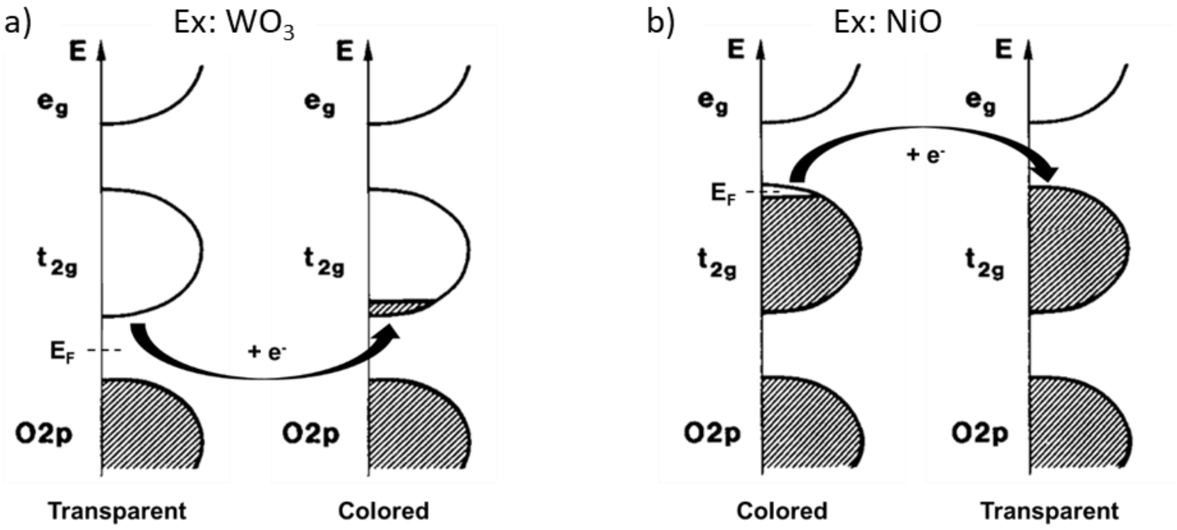

Figure 1.11: Band structures of cathodically (a) and anodically (b) charged electrochromic materials in their respective colored and transparent states[51]*.*

Although the electrochromic activity of the materials arises from the insertion or extraction of charges in the crystal lattice of the investigated materials, more specific models have been proposed to explain the electronic mechanisms at play during the electrochromic switch of selected materials, with the two most widely adopted ones being the intervalence charge transfer and small polaron models.

In the intervalence charge transfer model (IVCT) first proposed by Hush *et al.* in 1961, a significant proportion of the active material can be either reduced or oxidized upon the insertion or extraction of electron/ion pairs[53–56]. This results in the presence of different metallic sites in the crystal lattice of the material, displaying different oxidation states. Electron transfer between two adjacent metallic centers differing by their oxidation level is possible (**Figure 1.12**), inverting the oxidation state of the two metallic ions and resulting in a strong absorption corresponding to the energy required for the electronic transfer to take place[53–56]. Depending on the difference in energy between the two electronic states, the absorption peak will appear in the spectrum of the material at the corresponding wavelength.

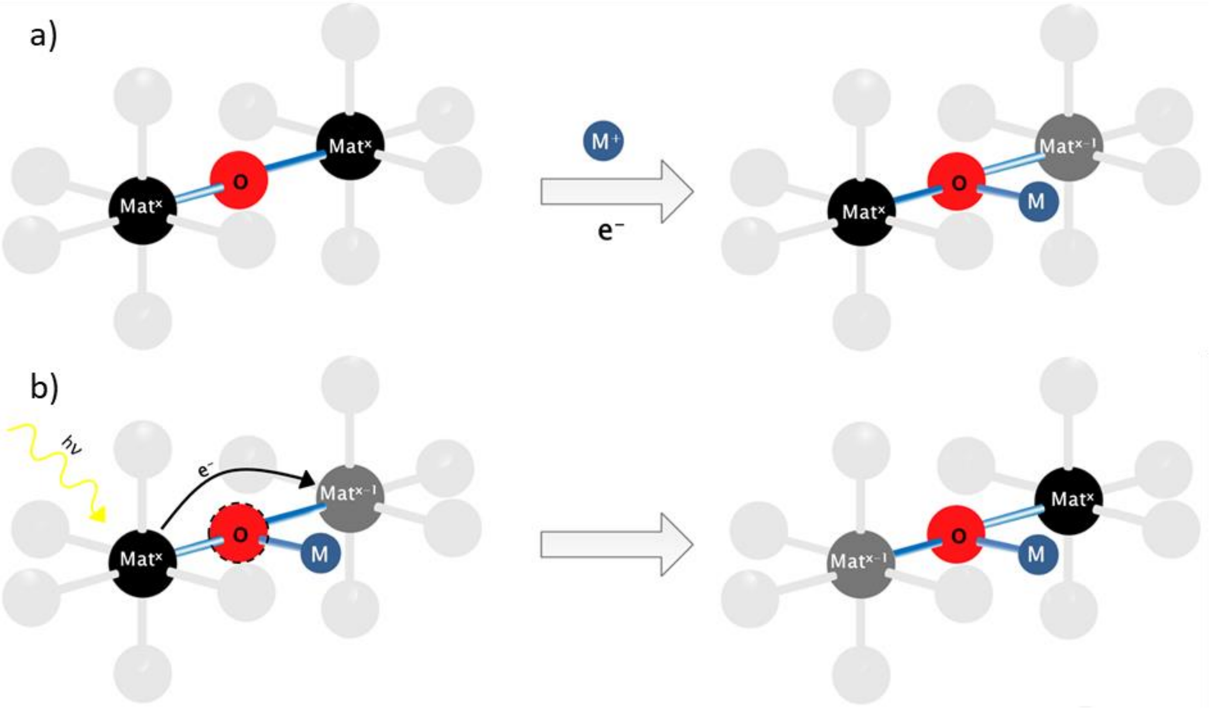

Figure 1.12: Schematic representation of the IVCT absorption mechanism in electrochromic materials: first, the insertion of a cation/electron pair results in the reduction of one of the metallic ion (a). In a second step, the absorption of a photon with the appropriate energy allows the transfer of an electron from the most oxidized metallic center to the most reduced one, inverting the oxidation level of the two atoms (b)[57].

On the other hand, the small polaron model has been developed by Yamashita and Kurosawa[58], Sewell[59] and Holstein[60] in 1958-59 from the initial proposition of the polaron by Landau (1933)[61] and Pekar (1946)[62], and in 1948 in their collective work[63]. This model describes the interaction between an electron and a phonon. The latter corresponds to a local deformation of the crystalline structure, creating a potential well able to localize an electron by phonon-electron coupling, corresponding to the quasiparticle known as a polaron[61]. The coupling between the electron and the surrounding phonon results in the formation of a new electronic (polaronic) state, which energy can lie in the band gap (**Figure 1.13**). This leads to new electronic transitions between the polaronic state and the conduction band, resulting in absorption at greater wavelengths, e.g. shifting from the UV (transparent state) to the VIS range (colored state)[64].

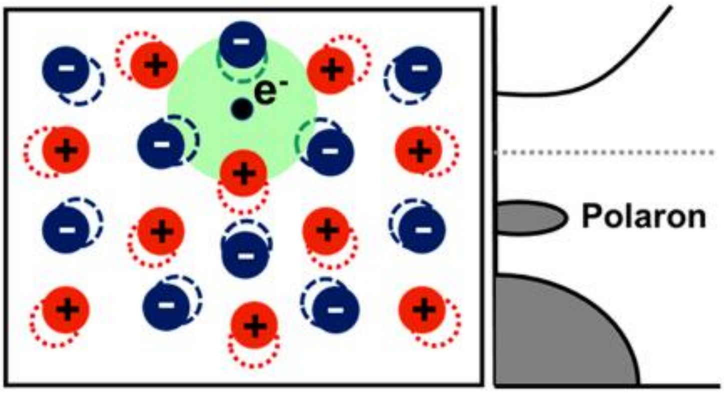

Figure 1.13: Schematic representation of the lattice deformation induced from the insertion of an electron, and the resulting electronic band appearing in the band gap[64].

Usually, polaronic absorption is mostly expected in amorphous materials or those presenting a great concentration in crystal defects, because the lack of local symmetry promotes the formation of phonon in the deformed lattice, able to couple with electrons and create polaronic states[51,65]. In well crystallized materials, intraband absorption and other free electron mechanisms are favored[51]. Moreover, the polaron model is also more often observed in cathodic materials, while the absorption in anodic materials is rather ruled by the intervalence charge transfer, as reported by Granqvist *et al.*[65].

All in all, the combination of complementary cathodic and anodic electrochromic materials, displaying strong absorption originating whether from intervalence charge transfer or the formation of small polarons, results in the production of efficient devices, exhibiting large optical contrasts and coloration efficiencies, as well as the possibility to reach a more neutral tint in the colored state.

1.2.3. Architecture of conventional electrochromic devices

Electrochromic materials can be integrated within devices as a way to modulate incident light through absorption or reflection of the incoming radiation. Such electrochromic devices can be used for a wide range of applications, covering very different fields. Some of the applications targeted for electrochromic materials are: tintable goggles[66], anti-glare rearview mirror[15], electrochromic displays[42], (gas) sensors[67] and of course "smart windows"[15] amongst the most widespread ones, but also more original applications such as stealth coatings for military use[68] and anti-counterfeiting labeling[69,70].

Typically, an electrochromic device is comprised of five layers, assembled as a stack in a battery-like configuration[15,37,49]. In consequence, an electrolyte layer is usually found at the center of the device, between working and counter electrodes. The working electrode consists in an electrochromically active material deposited at the surface of a conducting substrate, while the counter electrode, at the opposite, drives the storage of cations during the electrochemical cycling of the device, and can be made from either active or passive materials[37,49] (both cases are presented in **Figure 1.14** below and are further discussed in **Section 2.3.1**, page 45). Finally, the device is connected to an external circuit allowing for the electronic flow, via the two transparent conductive substrates at each end of the stack.

When a potential is applied through the external circuit, electrons can transit from one electrode to the other. In addition, cations are simultaneously extracted from one electrode into the electrolyte layer and inserted from the electrolyte layer into the other electrode. The coupled insertion/extraction of electrons (through the external circuit) and cations (via the device structure) results in *redox* reactions in both electrodes, leading to the modification of the optical properties of the device[15,37,49].

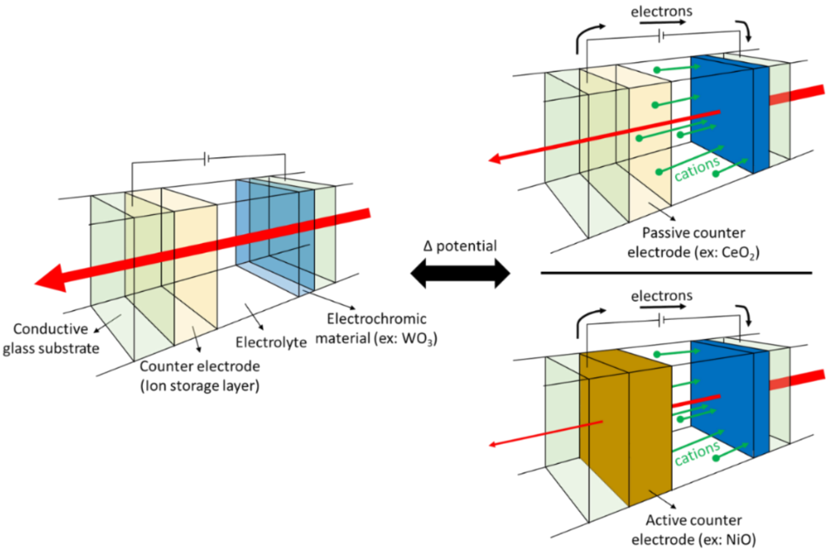

Figure 1.14: Schematic representation of an electrochromic device, in the bleached state (left) and in the colored state in the case of a passive counter electrode (top right) and an active counter electrode (bottom right)[15].

a. Counter electrode

In order to complete the device and access high efficiencies and performances, a suitable counter electrode should be selected so that it matches the properties of the active material in the working electrode. The role of the counter electrode in the device is to store cations as they are extracted from the working electrode (in the transparent state of the device), acting as a reserve of ions required for the expression of the electrochromic properties of the device, but also enhancing the stability of the assembly upon electrochemical cycling[15,33,37,49]. In "smart windows" and electrochromic devices in general, the counter electrode material can be either passive or active[33].

In the case of an active counter electrode, the material used is selected to work accordingly with the electrochromic material on the working electrode side. This means that complementary cathodic and anodic materials should be used together as working and counter electrodes respectively, as their coloration/bleaching mechanisms take place simultaneously (see **Equation 1.2** and **1.3**)[33]. If WO_3 is used as working electrode material and NiO as counter electrode material, this means that applying a negative bias would promote the extraction of charges from the ion storage layer and the concomitant insertion of cation/electron pairs into the working electrode layer. In that context, the oxidation of NiO, as well as the reduction of WO_3, would both yield their colored state simultaneously[15,33,37,49]. The superposition of both colored states would result in a lower transmittance and a more neutral tint for a given potential, leading to a greater efficiency of the device in comparison to the isolated materials[37].

On the other hand, passive electrode materials demonstrate the ability to store cations through redox reactions without any modification in their optical properties. This is the case for CeO_2 and SnO_2, the two most studied materials for such applications[15,49,71,72]. Considering CeO_2 as an example, the material is able to switch from Ce^{4+} to Ce^{3+} while maintaining its transmittance level[73–75]. As these materials do not bring any additional optical modulation in the device due to their lack of optical activity (and thus no net improvement of the contrast and efficiency as discussed for active counter electrodes earlier), they can be used in complete setups with the aim of characterizing the properties of the electrochromically active material only. Besides, active counter electrodes might not always be suitable, especially when working with novel, highly functional materials whose electrochemical behavior is not totally complementary to that of the active ion storage layer. In this case, using a passive counter electrode allows the development of (solid) devices exhibiting the whole range of optical states offered by these novel materials. A more detailed discussion of the role of the counter electrode, and in particular CeO_2, is presented at the beginning of Chapter 4 (page 101).

b. Electrolyte

In such a device architecture, the electrolyte layer should be ion conducting so to ensure the transfer of the cations from one side of the device to the other, but also electron insulating in order to avoid short circuits in the system[15,37]. Moreover, the electrolyte formulation should be highly transparent in the working range of the spectrum, as to not hinder the electrochromic performances of the device[33].

A wide range of electrolytes compounds are available for the development of electrochromic devices implemented in smart windows, divided in three categories: liquid, solid and gel[15,37]. While liquid electrolytes offer a great ionic mobility and maximizes the performances and efficiency of the devices, they present several major drawbacks. Indeed, the liquid state of the electrolyte means that the devices should be suitably encapsulated in order to avoid leakages, which can be dangerous if the solvent and dissolved salts are harmful to health and the environment, in addition to the fire hazard they represent[15,37]. Also, the solvent should be totally anhydrous, as the possible water electrolysis at the electrode would release H_2 and O_2 gases, leading to an increase in pressure inside the device, which could result in the outbreak of the “smart window” if critical conditions are reached.

Solid electrolytes are limited in terms of their ionic mobility, but display great durability towards cycling, being less prone to damages arising from long time exposure to an electrochemical bias, also, their solidity greatly improves the structural integrity of the device[37].

Finally, the gel electrolytes combine the advantages of both solid and liquid formulations, retaining a good ionic mobility while ensuring the sturdiness of the assembly, with no risks of leakage and allowing the development of devices using flexible substrates. Moreover, the formulation of the electrolyte as a gel facilitates the assembling of the device, by simply applying a layer of uncured gel on the individual electrodes and laminating both pieces together, joining them as a single unit[37]. Even though these formulations present numerous advantages, they are still subject to some drawbacks, in particular their poor mechanical strength[76], as well as the risk of the gel to soften or even melt under high temperature conditions[77], either from external factors (*e.g.* solar heat) or internal ones (temperature increase from Joule effect in the circuit). More insights regarding the assembly of electrochromic layers into complete solid devices will be further discussed in Chapter 5 (page 135).

c. Transparent conductive substrates

At both ends of the device are conducting substrates, ensuring the connection of the device to the external circuit and the potential generator. At least one of the substrates should be transparent: for example, in the case of display application, the back substrate could be reflective in order to enhance the coloration of the device[37]. However, in “smart windows”, both substrates are required to be highly transparent in order to not impede the contrast of the active materials[15,37]. Usually substrate is composed of a transparent material, most often being glass or poly(ethylene terephthalate) (PET) plastic if flexibility is desired, covered by a layer of transparent conducting material[37]. The industry standard is based on the use of commercially available transparent conductive oxides, such as fluorine-doped tin oxide (FTO) or tin-doped indium oxide (ITO), exhibiting excellent electronic conductivity and high transmittance levels in the visible range[15,37,49].

1.2.4. Limitations in the conventional electrochromic materials

Despite the numerous benefits exhibited by conventional “smart windows”, they also face major drawbacks hindering their efficiency and widespread commercialization. First of all, the mechanism upon which the coloration/bleaching of the films is based depends on the reversible insertion and extraction of cations (and electrons) in the crystal lattice of the electrode materials. The diffusion of cations through the material can lead to deformations in the crystal lattice and substantial strain upon the structure, which can result in irreversible damage to the material, modifying its properties and hindering its performances[78,79]. The deformation of the lattice also impacts the nature of the active sites present in the material, with some of the inserted ions trapped in sites being turned irreversible[80]. These two effects might greatly hinder the performances of the active material, especially regarding its durability, as the crystal lattice accumulates more damage by experiencing more and more electrochemical cycles, but also its contrast (and the ensuing loss in efficiency), with the proportion in irreversibly inserted cations filling actives sites. This results in a significant amount of the material blocked in a given optical state and thus not available for modulation, effectively decreasing the difference in transmittance between the colored and bleached states.

In addition, the conventional electrochromic materials presented in the previous sections do not allow the selective modulation of specific ranges of the solar spectrum. Taking WO_3 as an example, the modulation upon reduction of the active material takes place simultaneously, combinedly in the VIS and NIR ranges without distinction (**Figure 1.15**)[15,49]. Since some situations require different demand levels in the heat and luminosity contributions, the inability to selectively modulate the VIS and/or NIR regions of the spectrum makes the devices sub-optimal from an energetic point of view. The integration of such advanced functionality in “smart windows” could further push the energy savings they provide, outperforming the 40 – 170 kWh/m^2 per year already reached with conventional electrochromics[24]. For instance, during periods such as the summer, “smart windows” could be used as a mean to lower the heat contribution transmitted into the building. Using conventional WO_3-based windows, the activation of the device would lead to a darkening of the active layer and, consequently, the need to turn on lights in the building to compensate for the loss of natural light from the sun. As a result, the energy savings in HVAC are only partially counterbalanced from the demand directed towards lighting appliances[15]. Therefore, the development of dynamically active, “on demand”, electrochromic devices demonstrating VIS/NIR spectral selectivity could greatly improve the efficiency of “smart windows”, resulting in greater energy savings and, in the long term, making investment in this technology more economically sound for both residential and commercial buildings. Numerical simulations looking into the impact of NIR selective modulation on the energy demand of buildings concluded that this technology could allow savings between 50 and 200 kWh/m^2 per year for materials modulating in the NIR exclusively[81], and up to 60 – 300 kWh/m^2 per year in the case of independent and selective control of both VIS and NIR wavelengths[82].

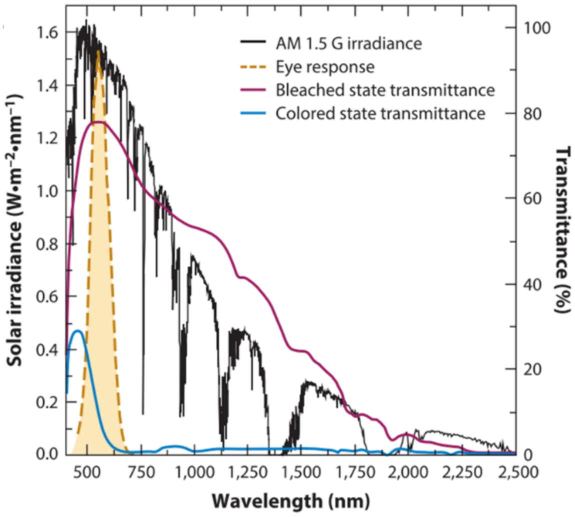

Figure 1.15: Optical spectra of WO_3 in the bleached (purple line) and colored state (blue line), with the solar irradiance at earth's surface and the response of human eye for comparison[15]*.*

1.3. Plasmonic materials

In view of the limitations highlighted in conventional materials, in-depth research for more efficient and more functional materials was carried out in the electrochromic field. The combined efforts of researchers have led to the discovery and development of innovative materials and formulations, focusing on the selective modulation of NIR light, representing over half of the solar spectrum intensity[15,83]. Indeed, plasmonic materials, in particular nanostructured highly doped metal oxide semiconductors, display the ability to selectively modulate the NIR range without interfering with the visible light, resulting in the "on demand" control of the heat contribution of solar radiation, without sacrificing the (free and sustainable) natural light available during the day[15,83]. The implementation of such NIR-selective formulations could lead to energy savings as high as 167 TWh annually in the US, as a result of a lower energy demand in both HVAC and lighting appliances[15].

1.3.1. Principles of localized surface plasmon resonance

In conductive materials such as metals, the Drude model considers valence electrons as a free gas, moving around a space made of stationary cations (due to their mass in comparison to electrons) forming the crystal lattice and resulting in a periodic atomic potential, ignoring the electron-electron and ion-electron interactions apart from collisions between the two latter[83–87]. Each electron can move around in this ion lattice as an isolated particle, as it would in vacuum, explaining the transport of electrons in metals notably, and more precisely describing their properties as conductive materials, with the rate of electrons bouncing off immovable ions representing the resistivity of the material, restricting the flow of electrons in an electric field[84,85]. However, for this approximation to be accurate, a corrective factor has to be applied to the mass of the electron, yielding an effective mass computed from band structures calculations and taking in account the crystal lattice of the material[83]. It should be noted that the effective mass obtained after correction can differ greatly from the real mass of an electron, as to counterbalance the approximations made from the simple Drude model[83]. This model is also applicable to highly doped semiconductor materials, when sufficient free charge carriers are introduced in the material through doping, reaching degeneracy and behaving like a metal[86].

In materials described using the Drude model, the cloud of free electrons described above can experience collective oscillations upon interaction between the material and an incident electromagnetic wave. If the incident light meets the resonance conditions of the material, the electric field is locally enhanced and a strong optical absorption ensues[15,49,64,83,87]. The oscillation, mostly being expressed at the surface of the particles, is known as the surface plasmon resonance (SPR) phenomena, propagating along the surface of the material as an evanescent wave[83]. The plasmon is a quasiparticle resulting from the quantification of the plasma (free electron cloud) oscillations, similarly to the photons being a quantification of optical oscillations, and phonons corresponding to the oscillation of atoms in a crystal lattice. In small-size objects such as nanocrystals and nanoparticles, the plasmon resonance is spatially confined in the nanostructure and gives rise to a non-propagating standing wave, also known as a *localized* surface plasmon resonance (LSPR, **Figure 1.16**)[83].

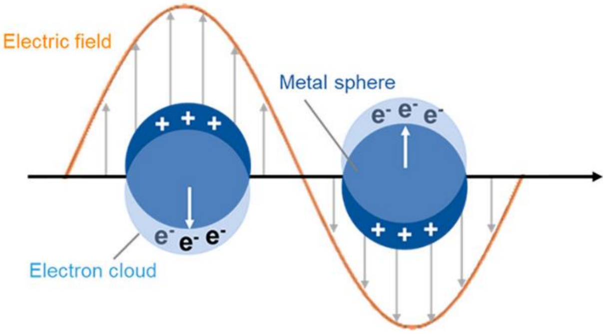

Figure 1.16: Schematic representation of the localized surface plasmon resonance in (metal) nanoparticles in the presence of an electric field[64].

The LSPR phenomena was first observed in noble metal nanoparticles such as gold and silver, displaying the ability to support such optical features because of their large concentration in free charge carriers (10^{22}-10^{23} cm^{-3}), with materializations as old as in the Lycurgus cup, dated from the fourth century and preserved at the British Museum[83]. From the Drude model, it is possible to derive the formula describing the plasma frequency of small spherical particles of a material (in comparison to the wavelength of the incident light. Usually, the dimensions of the particle should be a fifth of the wavelength for those to be considered significantly smaller), with the **Equation 1.4** and **Equation 1.5**:

$$\omega_p = \sqrt{\frac{ne}{\varepsilon_0 {m_e}^*}} \tag{1.4}$$

$$\omega_{LSPR} = \sqrt{\frac{{\omega_p}^2}{1 + 2\varepsilon_m} - \gamma^2} \tag{1.5}$$

Where ω_p and ω_{LSPR} are respectively the plasma and LSPR frequency, n is the concentration in free charge carriers, e is the charge of the electron, ε_0 is the permittivity of free space, $\varepsilon_m$is the permittivity of the surrounding media, ${m_e}^*$ is the effective mass of the electron and γ is the damping constant, representing the scattering of free carriers.

The plasmonic behavior of a (nano)material depends on a number of factors influencing its plasma frequency, such as the size and shape of the particles, but also their composition, the presence of doping agents, as well as their concentration and distribution in the system (homogeneously dispersed or segregated like in a core shell configuration), and finally the dielectric properties of the local environment surrounding the particles[49,64,83].

Given the relationship between the concentration in free charge carriers and the plasma frequency, as expressed in **Equation 1.4** and **1.5**, the plasmonic signature of noble metals nanoparticles lies in the visible range (n = 10^{22}-10^{23} cm^{-3})[83]. In order to modify their optical properties in such a way that they could be used as NIR-selective materials, the size of the particles should increase, or very complex shapes would be required so that the shift in the plasma frequency results in the signal appearing in the NIR region (**Figure 1.17**)[83,88–95]. However, the size of the particles, or at least of the nanostructures found in the particles, should lie in a range in which the electronic band structure is similar to that of bulk material, larger than a few nanometers (as to not cross into quantum dot territory), while being smaller than the resonance wavelength: if $d \ll \lambda$, the interaction between an electromagnetic wave and a particle of size d can be analyzed using the quasi-static approximation (at the scale of the particle, the oscillation of the light is too large to be significantly noticed)[96,97]. In addition, for larger particles, light scattering becomes dominant over the plasmonic absorption phenomena[96].Therefore, the large increase in size needed for the plasma frequency to shift into the NIR would result in the particles not fulfilling the size constraint anymore, and thus preventing them from supporting LSPR features. On the other hand, the development of complex shape would probably prove to be too impractical for the efficient production of these formulations and their affordable application as NIR-selective materials.

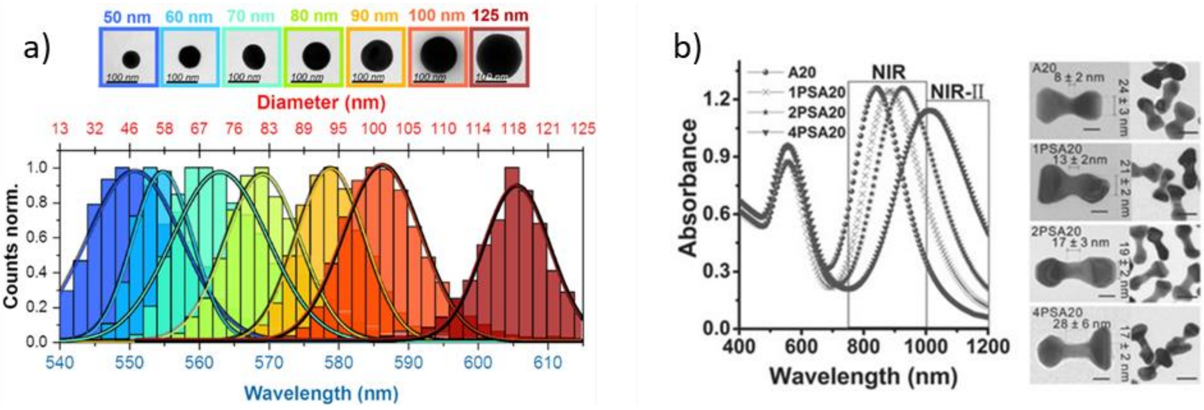

Figure 1.17: Effect of the size[95] and shape[92] on the plasmonic optical properties of gold nanoparticles.

Semiconductors such as metal oxides, are bound to the same rules regarding the size of the particles and/or their nanostructures. However, an additional condition has to be fulfilled for these materials to support LSPR phenomena: their concentration in free charge carriers should be large enough for the material to behave as a metal, *i.e.* the doping rate is large enough for their electronic structure to become degenerated[83,97]. Indeed, if their concentration in free charge carriers is brought over a given threshold, the material can experience a transition from semiconductor to metal-like behavior, allowing the support of LSPR features appearing at a wavelength depending on the parameters discussed previously (size, shape, doping rate, environment)[87,98,99]. With concentrations in free electrons orders of magnitude lower than those of metals, the plasma frequency of these doped semiconductors lies in the near-IR to mid-IR region ($n = 10^{18} - 10^{21}\ cm^{-3}$)[83,87]. In addition, and contrarily to metal nanoparticles, the lower concentration in free charge carriers found in doped semiconductors can be significantly tuned with the injection of additional electrons, whether it is *in-situ* from chemical doping during the synthesis, or *ex-situ* via post-synthetic application of an electrochemical bias[83]. Therefore, the possibility to modify the optical properties of a plasmonic semiconductor upon application of a potential means that these materials could be implemented as electrochromic materials, and especially as NIR-selective formulations. The example of ITO nanoparticles is presented in **Figure 1.18** below, highlighting its ability to modulate in the NIR range while maintaining a transparent VIS state[15,49,83,87].

If both conditions are fulfilled, the semiconductor material is able to support LSPR phenomena at a wavelength depending on the parameters discussed previously (size, shape, doping rate, environment).

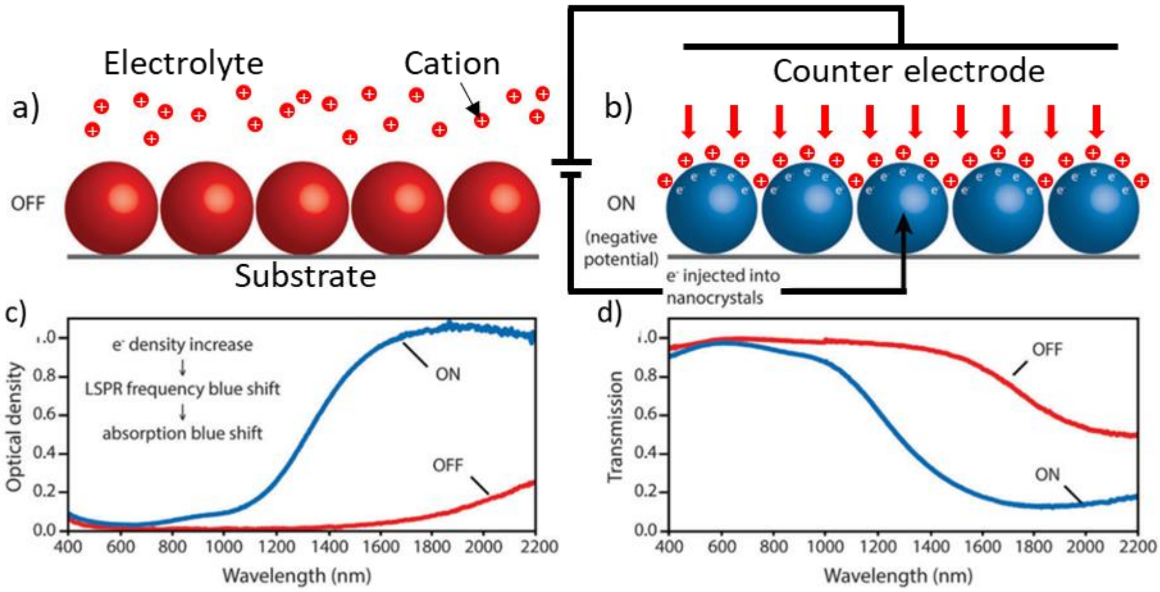

Figure 1.18: Representation of the electrochromic activity of plasmonic materials as a function of their free charge carrier concentration, in the bleached state (a) and the colored state(b), and the corresponding evolution of the optical density (c) and transmission curves (d)[49].

1.3.2. Localized surface plasmon resonance in transparent conductive oxides

Amongst highly doped nanostructured semiconductors (**Figure 1.19**), the first formulations which have been reported to support LSPR features are part of the transparent conductive oxides (TCOs) family. One of the first observation of their NIR-selective electrochromic activity was described in the literature in 1999 by Boschloo and Fitzmaurice, while investigating the optical properties of antimony-doped tin oxide (ATO)[97,100]. Following this, several other materials were shown to support similar plasmonic properties such as aluminum-doped zinc oxide (AZO)[15,49,87], indium-doped cadmium oxide (ICO)[101], as well as tin-doped indium oxide (ITO) [15,49,102], formulated as highly efficient nanocrystals since the 2011 pioneering study by Milliron *et al.*[102], and used for the development of NIR-selective plasmonic electrochromic films and devices.

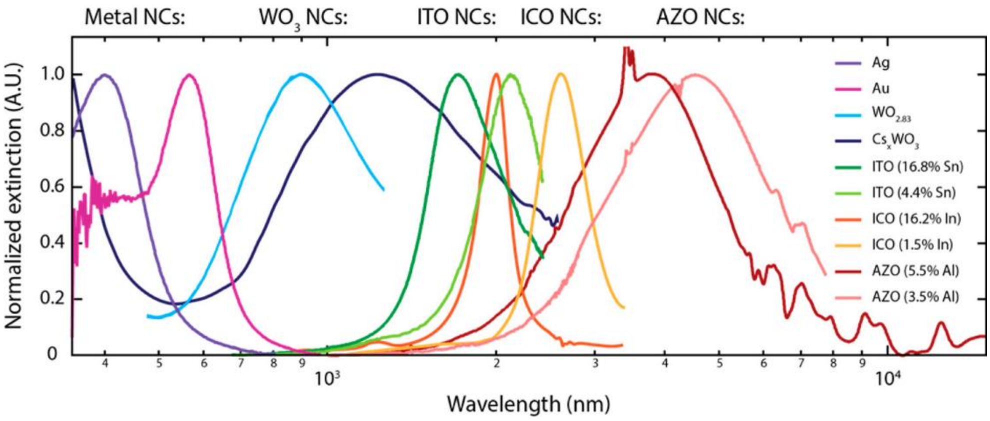

Figure 1.19: Normalized LSPR signature of metal and semiconductor plasmonic nanocrystals[101].

In the optical activity results of ITO, Milliron and her team highlighted the capacitive charging mechanism responsible for the modification of the concentration in charge carrier in ITO, and the resulting electrochromic behavior[102,103]. This electrochemical behavior was proven by cycling the films in a tetrabutylammonium(TBA)-based electrolyte. Given the large radius of the TBA$^+$ cations, insertion into the lattice of electrochromic material is prohibited and only capacitive mechanisms are allowed. The presence of an optical modulation in TBA$^+$ and Li$^+$ without distinction confirmed the peculiar mechanism at play in the ITO[15,102,103]. Worth noting, the same also holds for the other TCO formulations cited above[49]. In addition, this capacitive charging mechanism could also have been anticipated from previous reports of plasmonic materials behaving similarly, with examples such as Au nanorods[104], Ag nanoparticles formulated as colloids[105] and aggregates[106], CdSe quantum dots[107], and more recently in substoichiometric chalcogenide structures like $Cu_{2-x}Se$ exhibiting similar charge/discharge behavior[108].

Since the plasmonic electrochromic behavior of doped metal oxide nanoparticles such as ITO depends on several parameters (cf. **Section 1.3.1** above, page 18), their optical response can be tuned, and with the carrier concentration observed in TCOs, NIR-selectivity can be achieved. Indeed, the application of an appropriate potential will result in the capacitive charging of the material, with creation of a layer of positively charged cation at the outer surface of the particles and the injection of electrons from the external circuit (**Figure 1.18**)[49]. The added free charge carriers will result in an increase in their concentration (n in **Equation 1.4**), leading to the blue shift of the original LSPR signal and enhanced absorption in the NIR range[102,103]. As a result, Milliron *et al.* have highlighted great performances in the investigated NIR-selective ITO, with a large optical modulation (40+ %) limited to the NIR range while VIS light remained unaffected (**Figure 1.20**), fast switching rates (50 ms), large life expectancy (> 20k charge/discharge electrochemical cycles) and a very high coloration efficiency (close to 400 mC/cm²)[102,103].

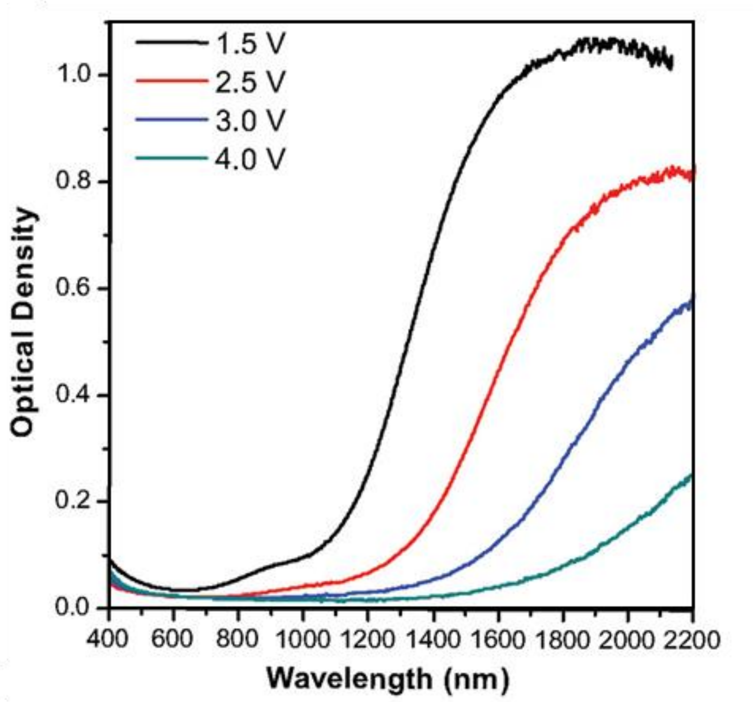

Figure 1.20: Optical spectra of ITO nanoparticles as a function of the applied potential, highlighting the blue shift of the signal upon the increase in free charge carriers (when the bias decreases). It should be noted that the graph is expressed as the optical density, which is inversely proportional to the transmittance[102]*.*

Even though highly doped TCO formulations have shown great promises for the NIR-selective modulation of solar radiation, the position of their LSPR absorptions ultimately limits the efficiency these latter can reach once applied as “smart windows” materials. Indeed, the LSPR response of TCOs lies in the infrared region, stretching from 1600 nm for ITO, up to 4000 nm in the case of AZO and even 5000 nm for ATO[97,101]. When comparing this range of wavelengths with the intensity of the solar spectrum (in the background of **Figure 1.15**), it is clear that the corresponding (N)IR intensity is very low and thus any attempt to modulate this region would result in a relatively limited impact on the transmitted heat contribution from natural sunlight. In order to enhance the effect of electrochromic modulation on the NIR region, new materials have to be investigated and new formulations have to be developed, focusing on the 750 – 1250 nm region, containing half of the IR light emitted from the sun[49,87,97].

1.3.3. Development of more efficient plasmonic formulations

In response to the limitations faced by the TCO formulations discussed in the previous section, new materials were explored in order to develop more efficient plasmonic compounds, which LSPR resonance would lie in the interval of interest, between 750 and 1250 nm. Amongst the studied formulations, WO_3 derivatives were identified as promising. In particular, two strategies stand out: the formation of bronzes by heteroatom-doping with alkali metals such as Li, Na, K, Rb, Cs…,[109–111] or via the creation of oxygen vacancies in the crystal lattice of the oxide, notably by means of synthesis under solvothermal conditions[112–117] or under controlled atmosphere (e.g. Schlenk line thermal degradation)[118–120].

In either case, additional electrons are brought to the material, from the ionization of the alkali metals into their respective cations and one electron, or from the freeing of the two electrons initially allocated to the bonds between oxygen and the two adjacent metal atoms. The addition of electrons leads to the modification of the electronic band structure of the material, and if in a sufficient concentration, the material can reach degeneracy and experiences a transition from a semiconductor to metal-like behavior, with optical properties ruled by free electrons, available for the support of plasmonic features[87,98,99]. For example, in $WO_{3-\delta}$, a set threshold of $\delta = 0.1$ should be exceeded for the material to express LSPR absorption[98]. From **Figure 1.19**, the plasmonic absorption of $WO_{3-\delta}$ and Cs_xWO_3 appear at 900 nm and 1050 nm, respectively, indicating their potential as NIR-selective plasmonic materials with enhanced impact on solar heat transfer into buildings, transmitted through windows. **Figure 1.21** illustrates the difference between WO_3 and its plasmonic formulations, exhibiting a large absorption preferentially situated in the NIR region.

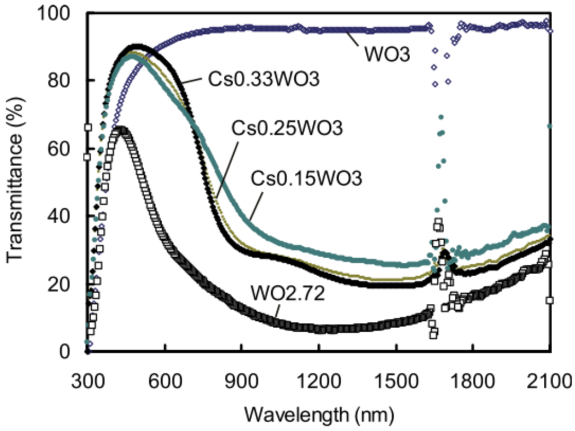

Figure 1.21: Transmittance spectra of various tungsten oxide formulations, in particular: the stoichiometric oxide, several cesium bronzes and the oxygen deficient oxide[110].

With two families of efficient NIR-selective materials clearly identified – TCOs and WO_3 derivatives (further improving the efficiency of the selective formulations), it is now possible to consider the selective and individual modulation of the VIS and NIR region in a so-called "dual band" device. Such an electrochromic system would result in great energy savings by enhancing the adaptability of the device towards external conditions, allowing the independent control of light and heat, leading to further improvements in the functionality and energetic efficiency of "smart windows", exceeding the 25% in energy savings already observed in conventional systems.

1.4. Dual band electrochromism, towards the independent modulation of VIS/NIR contributions

1.4.1. Dual-materials formulations

The development of "dual band smart windows" was initiated by Milliron *et al.*, by coupling niobium oxide (NbO_x, a conventional electrochromic material) and ITO in a single layer mixing two active compounds. This was achieved by embedding ITO nanoparticles in a NbO_x glass matrix[15,49,121]. Since the two electrochromic mechanisms in presence require different electrochemical potentials to be activated, careful application of an appropriate bias should allow the independent activation of spectrally selective mechanisms (**Figure 1.22**)[49,64,121,122]. Indeed, the potential difference required for the plasmonic absorption of the ITO nanocrystals is lower than that of the conventional material, since such plasmonic materials relies on capacitive charging, with the formation of a positive layer at the surface of the particles, and electrons injected from the external circuit. On the other hand, polaron/IVCT mechanisms responsible for NbO_x electrochromic commutation are based on faradaic charging, with the insertion of electrons and cations into the active layer from the substrate and electrolyte side, respectively[15,49,121]. As faradaic charging requires the insertion of cations – being orders of magnitude larger than electrons – into the crystal structure of the material, the applied potential should be large enough to promote the diffusion of the positive ions from the electrolyte into the active layer.

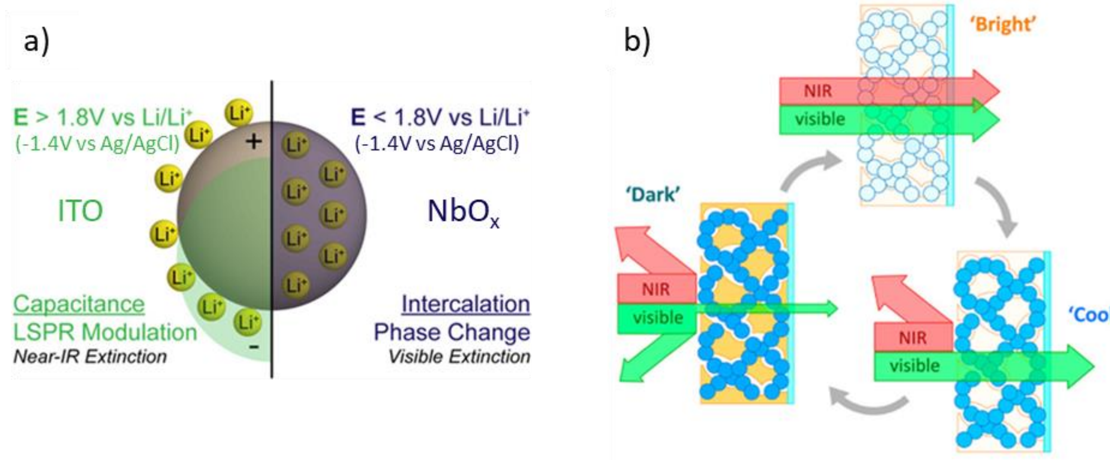

Figure 1.22: Illustration of the two charging mechanisms met in conventional and plasmonic electrochromic materials (faradaic and capacitive) as a function of the applied potential (a)[122], and responsible for the consecutive modulation of the NIR and VIS regions, respectively (b)[123].

Therefore, a device based on such a "nanocrystal-in-glass" structure can switch between three optical states:

- The "*bright*" state, corresponding to the high transmittance mode of the material, in its most oxidized state (*i.e.* 4.0 V vs. Li/Li^+, 0.8 V vs. Ag/AgCl in the following example, **Figure 1.23**);
- An intermediate "*cool*" state, appearing at an intermediary lower potential difference (2.3 V vs. Li/Li^+, -0.9 V vs. Ag/AgCl), leading to the injection of additional electrons in the ITO nanoparticles and activating their NIR-selective modulation;
- Finally, the "*dark*" state, with the conventional modulation of the VIS range when the potential reaches even lower values (1.5 V vs. Li/Li^+, -1.7 V vs. Ag/AgCl), allowing the insertion of cations into the working electrode and the ensuing reduction of the NbO_x active material.

The results presented by Llordés *et al.* highlight the independent modulation of VIS and NIR contributions, depending on the applied potential, with the possibility to reach a novel, third state, in which NIR is selectively modulated[121]. In this new working state, the mixed film was able to reach a contrast of almost 60% at 2000 nm and 15% at 1250 nm, with no impact on the VIS wavelength[121]. Then, as the potential becomes further reducing, the VIS range is also modulated, with up to 40% in optical contrast at 550 nm while maintaining the former NIR opacification[121]. In addition, the film showed great durability, with a 96% capacity retention after 2000 cycles, greater than the performances observed for the individual materials[121]. This could be due to both the open network resulting from filling the ITO mesoporous structure with a NbO_x glass matrix as well as the covalent bond formation between the components of the film, leading to improved ionic diffusion and consequently enhancing the properties of the film[121].

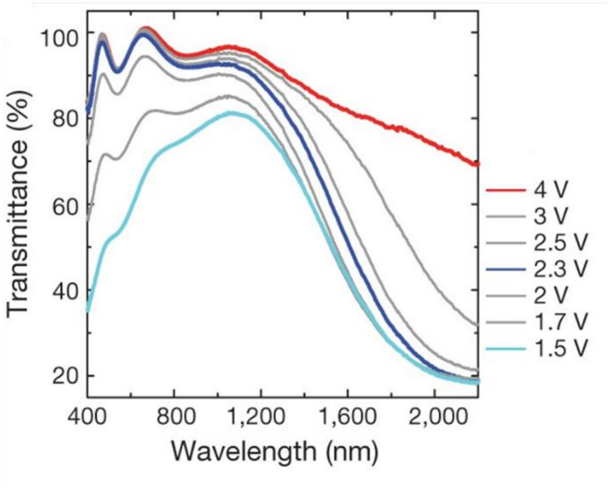

Figure 1.23: Transmittance spectra of ITO-in-Nbo$_x$ exhibiting three working states (bright, cool and dark), as a function of the applied potential (vs. Li/Li$^+$).

Following this breakthrough, the same nanocrystal-in-glass protocol was applied to a $WO_{3-\delta}$/NbO_x system, expecting to further improve the performance of the "dual band" composite, on the basis of the promising plasmonic features of $WO_{3-\delta}$, with the absorption maximum lying in the 750 – 1250 nm region of interest[123,124]. Indeed, the use of $WO_{3-\delta}$ as the NIR-selective material in the composite resulted in enhanced optical properties (**Figure 1.24**), with a small increase in contrast at 2000 nm, reaching 70%, but a tremendous 85% at 1250 nm, corresponding to an additional 70% of contrast in the range of interest in comparison to ITO[123]. In the visible range, the modulation attains 70% at 550 nm when the appropriate potential is applied[123], demonstrating an improvement in both VIS and NIR ranges in comparison to the previous iteration of ITO:NbO_x nanocrystal-in-glass composite. The material also displays great durability and reversibility, with the charge capacity maintained at 94% of the initial value after 2000 cycles[123]. Once again, the solid performances of the composite are enhanced by the porosity and the formation of covalent bonds in the network between NbO_x and $WO_{3-\delta}$, and possible redox cascade (consecutive redox phenomena taking place between the different electrochromic formulations) improving the electrochemical charge/discharge mechanisms[123].

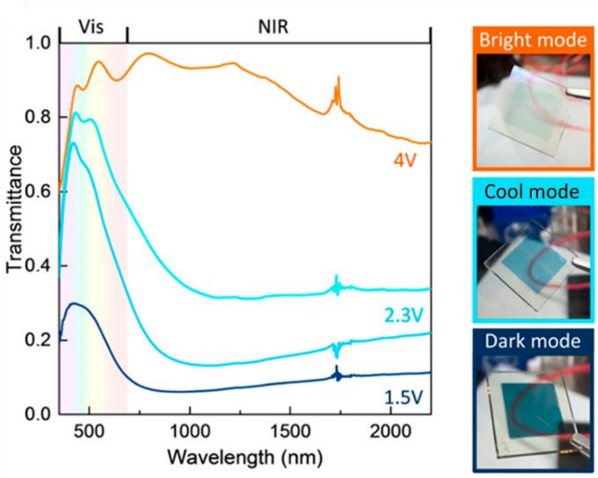

Figure 1.24: Transmittance spectra of the WO3-x:NbOx composite film exhibiting the three working states as a function of the applied potential[123].

1.4.2. Mono-material formulations

a. $WO_{3-\delta}$ and Cs_xWO_3

In addition to their innovative plasmonic properties, formulations such as $WO_{3-\delta}$ and Cs_xWO_3 exhibit another important benefit in comparison to the TCOs developed in the first generation of plasmonic materials: as they are based on WO_3, they could display conventional electrochromic behavior as well. This observation points towards the possibility to host both dual band VIS-NIR electrochromism within one single material, displaying the three working states discussed earlier (bright, cool and dark) and potentially providing access to the fourth, *warm* state – being NIR-transparent and VIS-opaque.

While the electrochromic activity of Cs_xWO_3 has been shown in the VIS region[125] (as well as in other tungsten bronze formulations such as $NaWO_3$[126]), and is also recognized as an efficient NIR-shielding formulation[109,110], no study has been carried out to highlight its ability to modulate those ranges in a dual band fashion, to the best of our knowledge. Nonetheless, Gacoin *et al.* showed the wide tunability of the LSPR response observed in Cs_xWO_3 by varying the shape and size of the oxide nanoparticles[127,128], while Liang *et al.* measured a contrast of over 40% at 633 nm in their Cs_xWO_3 formulation ($x = 0.29$)[125]. These results, although obtained separately, are promising for the application of cesium tungsten bronzes as dual band materials.

Besides, extensive work has been provided on the dual band electrochromism of $WO_{3-\delta}$ formulations since 2018, notably by Lee and co-workers. They showed the ability for this formulation to display NIR-selective modulation in addition to the VIS electrochromism expected in stoichiometric WO_3[118–120]. One possible explanation for this two regimes system relies on the same mechanisms as the composite developed by Milliron *et al.*, with polaronic/IVCT mechanisms responsible for the VIS modulation while the NIR-selective activity arises from the plasmonic properties of the material[49,64,122]. When a slightly reducing potential is applied, the cations in the electrolyte form an adsorbed positive layer at the surface of the particles, and electrons are injected from the external circuit in response, thus increase the concentration in free charge carriers and activating the NIR-selective modulation. When the potential bias is more reductive, cations can be inserted into the crystal lattice of the material and the metal atoms are reduced[49,64,122], as discussed for cathodically charged electrochromic materials (see **Section 1.2.2**, page 10). Therefore, by tuning the applied potential, it is possible to combine both behavior within a single material. Even though the model suggested by Milliron *et al.* is accepted in most of the electrochromic literature, other approaches have been proposed to explain the mechanisms at play in such highly functional materials[99,129–131]. These alternative models will be further discussed with the results presented later in this manuscript (see **Section 3.3.4.d**, page 87).

Optical characterization as a function of the applied potential showed a maximum contrast of 83% in the VIS (633 nm) and 92% in the NIR (1200 nm), depending on the value of the potential (**Figure 1.25a**)[118]. In addition, the films displayed good kinetics, with coloration and bleaching times of 8.0 s and 1.2 s in the cool state, and 21 s and 85 s for the dark state[118]. The coloration efficiency reached values as high as 101.7 cm²/C at 633 nm and 184.3 cm²/C at 1200 nm. Also, 80% of the capacity remained after 1000 cycles[118]. The hypothesis of a plasmonic contribution in the $WO_{3-\delta}$ formulation was also emitted and further analyzed through spectroelectrochemistry characterization in a TBA-TFSI electrolyte, similarly to what was done with ITO. The measurements highlighted an electrochromic activity limited to the NIR-range, as the large radius of TBA^+ only allows capacitive charging mechanisms (**Figure 1.25b**)[118].

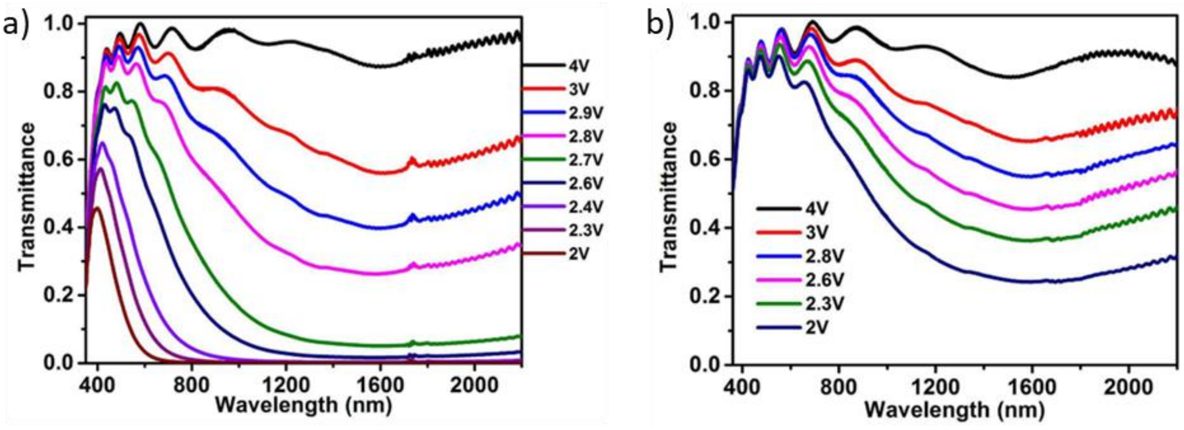

Figure 1.25: Transmittance spectra of dual band $WO_{3-\delta}$ as a function of the applied potential (vs. Li/Li^+) in a lithiated electrolyte (a) and in TBA-TFSI electrolyte (b)[118].

b. Other mono-material dual band formulations

Even before the formulations discussed above, Milliron *et al.* investigated the advanced electrochromic features of TiO_2-based formulations. The dual band behavior of Nb-doped TiO_2 was highlighted in 2015 by her team[122], followed by Manca *et al.* in 2017 (**Figure 1.26a**)[132]. Another paper, published in 2018 by the latter, showed the possibility to selectively modulate the VIS region of the spectrum using a V-doped TiO_2 formulation[133]. More recently, Milliron *et al.* have shown interest in the development of dual band $Nb_{12}O_{29}$ electrochromic formulations. Monoclinic nanoplatelets of this material have been investigated and demonstrated great electrochromic performances (**Figure 1.26b**)[134].

These results highlight the great efforts made over the last decade for the development of highly efficient and functional electrochromic materials displaying novel behaviors improving their energy saving capability. The exploration of novel formulations could further improve the benefits brought by such materials and allow their widespread implementation in buildings.

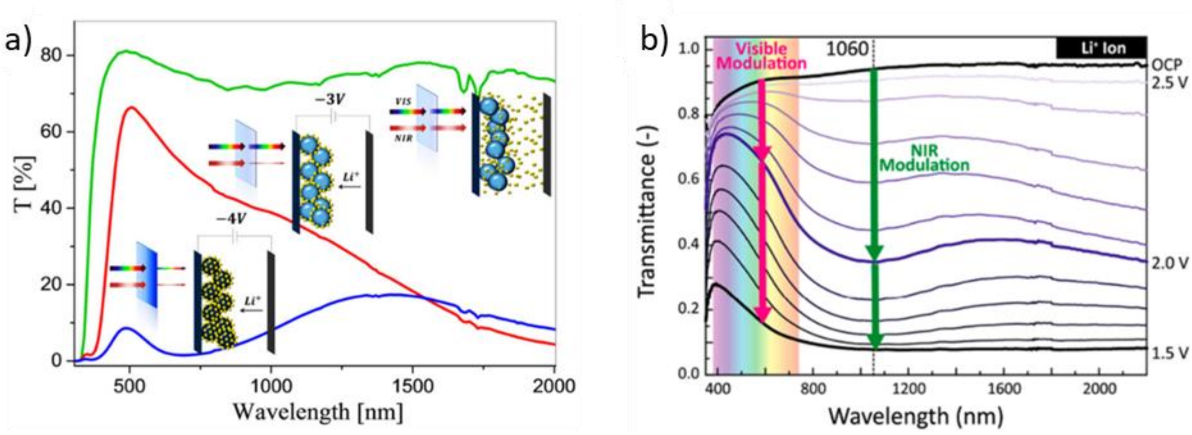

Figure 1.26: Transmittance spectra of Nb-doped TiO_2 (a)[132] *and $Nb_{12}O_{29}$ (b)*[134] *displaying dual band abilities as a function of the applied potential.*

1.4.3. Hybrid molybdenum-tungsten oxides: novel formulations for dual band electrochromism?

a. Plasmonic molybdenum-tungsten oxide formulations in the literature

Although dual-band mono-materials offer innovative functionality in comparison to their conventional counterparts, they still suffer from some limitations preventing them from large scale production and widespread implementation. Solutions as to circumvent these issues have been proposed in previous works of the literature, amongst those: the improvement of their selectivity towards the VIS and NIR ranges[34,135], the development of suitable counter electrodes to improve the selectivity and efficiency of electrochromic devices[64,83], the use of conductive substrates with broadband transparency as not to impair with the electrochromic behavior of the material (particularly in the NIR)[64], and last but not least the straightforward access of the fourth, "warm" filtration mode (VIS-dark and NIR-transparent) so to further improve the functionality and efficiency of the devices[34,122,133,135,136].

Amongst the new generation of plasmonic materials (Cs_xWO_3, $WO_{3-\delta}$…) leading to the development of monomaterial dual band formulations, oxygen deficient molybdenum – tungsten mixed oxide ($Mo_{1-y}W_yO_{3-\delta}$, also referred to as "MoWOx" in the remainder of this work, the contraction of **Mo**-**W** **Ox**ide) looks to be a promising candidate for such highly efficient electrochromic applications. Indeed, previous works from Yamashita *et al.* have highlighted a large increase in the optical signal of this mixed formulation in comparison to the parent oxides ($WO_{3-\delta}$ and $MoO_{3-\delta}$), exhibiting as much as a 20 and 16 fold increase respectively, and appearing near the 750 – 1250 nm interval of interest, presented in **Figure 1.27**[112]. More generally, the typical strategy employed to bestow plasmonic properties to MoWOx formulations relies on the formation of oxygen vacancies, as previously discussed in **Section 1.3.3**, page 23, in the case of $WO_{3-\delta}$.

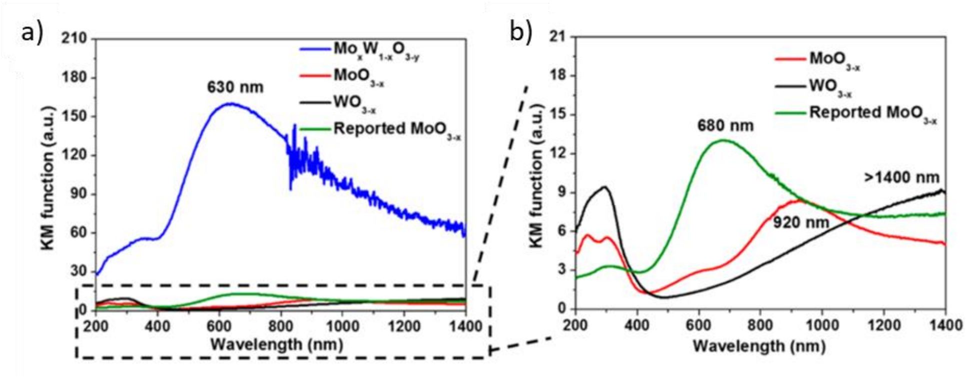

Figure 1.27: Optical spectra obtained from the diffuse reflectance of MoWOx, $WO_{3-\delta}$ and $MoO_{3-\delta}$ powders[112].

While the literature has mainly covered the doping of WO_3 formulations with non-metallic species (F)[137] or by inserted cations (such as K, Na, Li, Cs)[138], it is believed that non-metallic species replace the oxygen in the lattice, whereas the inserted cations locate in the interspace between atoms in the ionic channels of the structure[137,138]. Therefore, the use of dopant with similar properties to those of W was proposed as a way to study the influence of W substitution in the lattice[138]. In particular, Mo fulfills these conditions, being part of the VI subgroup (both Mo and W have similar electronic band structures) and exhibiting a close ionic radius (Mo = 7.3 Å, W = 7.4 Å)[114,138,139]. In addition, molybdenum-tungsten mixed oxides have already been thoroughly investigated for their role as catalytic materials and in optoelectronic applications[112,114–116,138–141]. These oxides are also used for surface-enhanced Raman spectroscopy (SERS) because of the good LSPR properties they can acquire if formulated accordingly[113]. A summary of the recent literature on the subject can be found in **Table 1.1**.

Table 1.1: Literature survey of works addressing Mo-doped $W_{18}O_{49}$ formulations and their applications; note that all considered materials are obtained from solvothermal synthesis protocols.

First author	Year	Doping rate (%)	Application
Zhong[114]	2016	10	Hydrogen evolution reaction
Zhao[115]	2017	1	Hydrogen evolution reaction
Wang[138]	2017	1.5	NIR shielding
Yin[112]	2017	50	Catalysis
Yin[140]	2018	80	Catalysis
Zhang[116]	2018	1	Catalysis
Spetter[139]	2018	50	Water splitting
Yang[141]	2020	3.6	Catalysis
Li[113]	2020	50	SERS
Xiong[142]	2022	2	Catalysis

It is expected that the plasmonic properties of these formulations are enhanced by the coupling of $WO_{3-\delta}$ and $MoO_{3-\delta}$ into the mixed material[112,113,140]. The doping/substitution of WO_3 formulations with Mo therefore allows the formation of solid solutions with tuned electronic and optical properties[138,139]. Apart from Mo, other elements have been investigated for the doping of $W_{18}O_{49}$, namely Mn, Sb, Y, Fe, Sn, Pd, Ni, Te, Co, Ce for catalysis applications[141]. However, the best results were obtained with Mo-$W_{18}O_{49}$, yielding the greater efficiency (**Figure 1.28**)[141]. Therefore, the improved electronic properties displayed by the Mo doped/substituted formulation in the scope of catalysis applications could also prove interesting for electrochromism, as the optoelectronic properties of the material will dictate its electrochromic performances, especially regarding its support of LSPR features in an intense and efficient fashion.

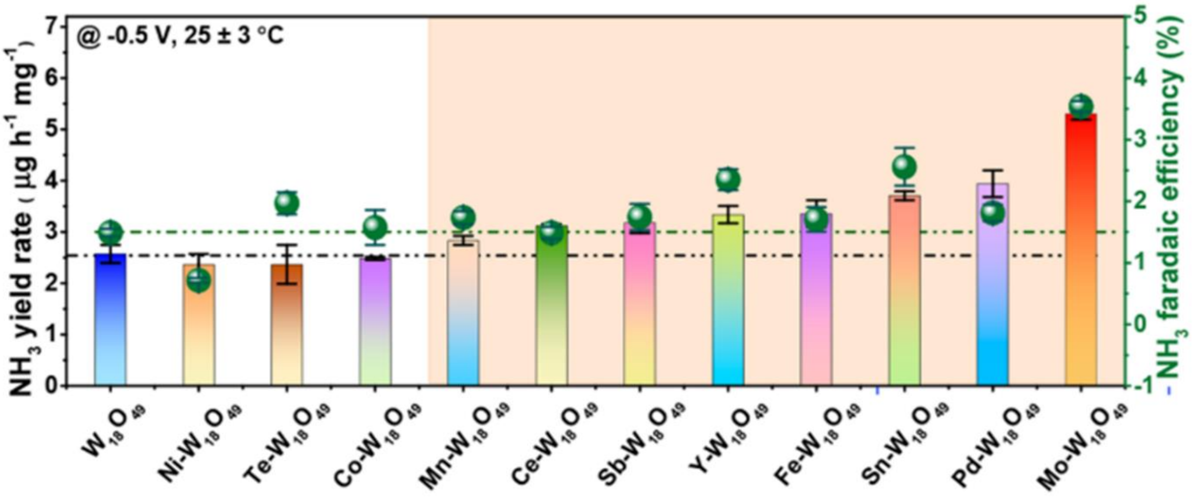

Figure 1.28: Catalytic efficiency of several metal-doped $W_{18}O_{49}$ formulations[141].

According to Yamashita *et al.*, the sudden increase in the spectral properties of the mixed material could arise from the substitution of Mo in the WO_3 octahedra and vice versa of W in MoO_3, promoting deformations in the lattice due to the difference in electronegativity between both elements, resulting in the creation of oxygen vacancies (**Figure 1.29**)[112]. Apart from Yamashita *et al.* other research groups proposed that the deformations of the structure caused by the substitution could ultimately impact the electronic properties of the material[114,115,138]. Therefore, the formulation of a mixed oxide compound in an appropriate Mo/W ratio would lead to enhanced electronic and optical properties. Indeed, several works of the literature demonstrated improved properties of the mixed W oxide in comparison to pure WO_{3-x} in the scope of catalysis applications[112,114–116,139,141,142]. This increased reactivity is reportedly owing to the numerous oxygen vacancies created from the substitution of W by Mo[112,113,140,141], creating more active sites, especially at the surface of the particles[141], but also due to the enhanced covalency of the metal-oxygen bonds favoring a better electron transfer and surface reactivity[116]. In addition, Mo doping/mixing elevates the defect band closer to the Fermi level, resulting in more energetic electrons being available for reactions[116].

In addition, in the synthesis protocol reported by Yamashita *et al.*, the presence of isopropanol in the reactive media, and the proton donor ability of the latter, could result in the insertion of H^+ cations in the already disturbed crystal lattice of the material during synthesis, leading to the occurrence of W^{5+} and Mo^{5+} reduced species[112]. As discussed previously, the creation of oxygen vacancies in a material is a viable way to increase its free charge carrier concentration and allow the support of plasmonic features[87,98,99]. Moreover, the formation of additional reduced species during synthesis leads to the formation of new polaronic absorption centers[80]. Therefore, the combination of plasmonic and polaronic features further increases the optical extinction intensity of the mixed material, especially near the visible range.

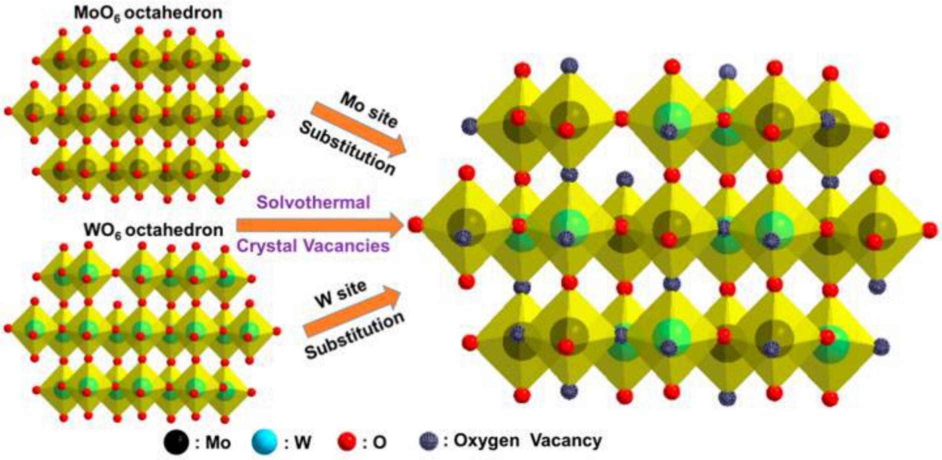

Figure 1.29: Illustration of the W/Mo substitution and formation of oxygen vacancies during the solvothermal synthesis of MoWOx formulations[112].

Such molybdenum – tungsten mixed material has experienced a growing interest lately, especially in the context of heterogenous catalysis. Similarly, other bi-metallic formulations such as Co-Mo-N, Fe-Ni-P and Ni-Mo-S have brought a lot of attention in the field for their exceptional performances for reactions such as oxidation, hydrogenation and hydrogen evolution, as well as light harvesting and photocatalysis[112]. These materials aim to replace noble metals for a fraction of the price, and implementing more abundant and sustainable resources[114]. By using different materials combined in a single formulation, researchers hope to be able to finely tune the morphological, structural and electronic properties of the material, while taking advantage of the synergistic effect of the doping/substitution with another element[112,116,139]. However, while several publications have investigated MoWOx formulations for their potential (photo)catalysis applications, none have discussed the possibility for this material to be applied as the active material in dual band electrochromic devices.

b. Mo doping/mixing as a strategy towards improved electrochromic performances in stoichiometric WO_3

On the other hand, Mo doping is a widespread method used for the improvement of the conventional electrochromic properties of (stoichiometric) WO_3 formulations. Numerous works of the literature have reported superior performances of the materials, namely regarding the contrast between the bright and dark optical states, with the latter exhibiting a more neutral tint, coloration efficiency, and the durability of the produced films upon electrochemical cycling, displaying greater stability and reversibility of the optical and electrochemical processes (summarized in **Table 1.2**)[80,143–150]. Amongst those, several works proved the efficiency of Mo doping, with 2% at. Mo displaying the best results, as shown in the work of Zhou *et al.* in 2016[143] or Wang *et al.* in 2018[148], with the doped formulation exhibiting improved properties in all key performance indicators (contrast, kinetics, coloration efficiency and durability). Besides, Li *et al.* also demonstrated the possibility to obtain good electrochromic performances by substituting a larger amount of W, thus described as hybridization or mixing instead of doping[80,144–146]. Unfortunately, none of the four surveyed articles went into the comparison of the results with the pure WO_3 formulation as reference. Here again, other elements have been investigated for the doping / mixing of stoichiometric tungsten oxide, such as Ti, Pd, Zn, Eu, Fe, Nb, Ni, V, Zn, Ru and Gd[147,149], however, Mo appears as one of the most interesting options, as its properties are similar to those of W (as discussed earlier).

Table 1.2: Literature survey of Mo-doping/mixing towards improvement of the electrochromic performances of non-plasmonic WO_3*. For the contrast, kinetics, efficiency and durability, the performances of the undoped* WO_3 *are presented in the first column while that of the Mo-doped/mixed oxide are in the second column, in italics.*

First author	Year	Synthesis method	Mo doping rate (%at.)	Potential (vs Ag/AgCl)	ΔT (%)		t_b (s)		t_c (s)		CE (cm^2/C)		Max # of cycles*	
Li H.[80]	2015	Hydrothermal	30	+1V/-1V	/	*42.9*	/	*10*	/	*7.5*	/	*36.3*	/	*2000*
Zhou[143]	2016	Hydrothermal	2	+1V/-0.7V	44.4	*56.7*	6.4	*2.6*	7.0	*3.2*	47.8	*123.5*	3500	*5500*
Li H.[144]	2017	Reflux	30	+0.5V/-0.5V	/	*30*	/	*/*	/	*/*	/	*49.3*	/	*400*
Li H.[146]	2018	Reflux	30	+1V/-1V	/	*54.5*	/	*13.9*	/	*22.1*	/	*21.7*	/	*300*
Li H.[145]	2018	Reflux	30	+1V/-1V	/	*30*	/	*/*	/	*/*	/	*/*	/	*100*
Xie[147]	2018	Electroreduction	2	+1V/-1V	66	*83.3*	/	*2*	/	*2.1*	57.3	*86.1*	30	*1500*
Wang[148]	2018	Hydrothermal	2.5	+3V/-3V	55.5	*61.7*	13	*3*	11	*9*	71.4	*73.1*	20	*20*
Kumar[149]	2019	Spray pyrolysis	5	+0.7V/-0.7V	35	*25*	/	*/*	/	*/*	14.1	*43.3*	100	*100*
Li W.[150]	2022	Hydrothermal	2	+0.5V/-0.8V	47.8	*65.9*	/	*7*	/	*10*	/	*81.2*	/	*1500*

**not necessarily the maximum number of cycles before system failure, but the maximum number of cycles attempted and reported in the articles.*

On a different note, some articles even delved into the coupling of electrochromism with energy storage, as electrochromic devices can act as a battery when they spontaneously revert back to their original optical state, highlighting the current tendency in the field to go towards highly functional materials combining several energy related abilities (energy storage, photovoltaic)[143–145,147,150]. Nevertheless, none of these works have highlighted any plasmonic behavior in the studied formulations, neither any dual band electrochromic capability.

In this context, the combination of both approaches could improve the electrochromic performances of the material, as well as its functionality, with an additional intermediate optical state arising from the selective modulation provided by the plasmonic properties. With the plasma resonance of the MoWOx appearing in the 750 – 1250 nm range of interest, and the great absorption it displays in comparison to the parent oxides, this material can be considered as a great candidate for the efficient modulation of NIR wavelengths. Furthermore, the expected large concentration in oxygen vacancies and reduced species in the mixed oxide formulations could lead to large symmetry disruption in the crystal lattice, favoring the coupling of inserted electrons with phonons into polaronic states. Thus, the occurrence of both plasmonic and polaronic features in a single material means that the MoWOx could be used as a dual band plasmonic electrochromic material applied in smart windows, in order to selectively and efficiently modulate the heat (NIR) and luminosity (VIS) contributions of the solar radiation interacting with modern buildings.

1.5. Objectives and methods of the present work

In this research work, various synthesis protocols, deposition methods, physico-chemical and optoelectronic characterization are implemented in an attempt to highlight innovative optical properties in hybrid molybdenum-tungsten oxide formulations and the ensuing plasmonic electrochromic behavior, so to show their applicability as an active material for dual band smart windows applications (**Figure 1.30**).

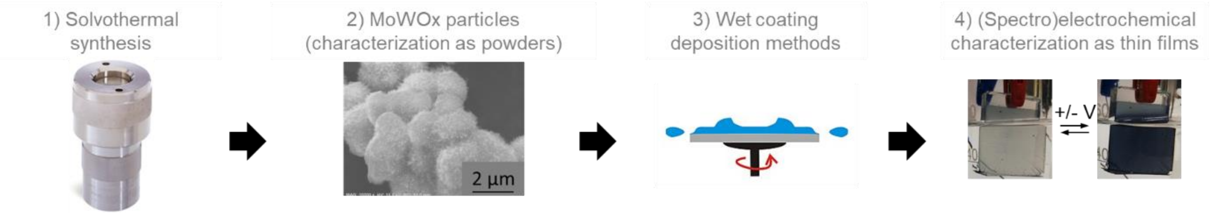

Figure 1.30: Schematic representation of the strategy used in the scope of this work, starting from solvothermally synthesized powders (1)[151]*, which are characterized using various methods (2). Then, thin films are deposited using wet coating techniques (3)*[152]*, and finally, the obtained samples are characterized, in particular for their electrochromic performances (4).*

The results obtained throughout this doctoral research work are organized in four main sections.

In the first section, MoWOx particles and their respective parent oxides are synthesized through a one-step solvothermal process adapted from the work of Yamashita *et al.*, rationalizing the influence of parameters such as the precursors ratio and the duration of the thermal treatment on the composition, morphological, structural, electronic and optical properties of the materials. Samples in the shape of powders are characterized using numerous analysis methods such as scanning and transmission electron microscopy (SEM and TEM), energy dispersive X-ray spectroscopy (EDX), profilometry, X-ray diffraction (XRD), X-ray photoelectron spectroscopy (XPS), electron paramagnetic resonance (EPR) and UV-VIS-NIR spectrophotometry. An optical characterization protocol is developed so to be directly carried out onto the samples as powders, and its implementation as a way to highlight plasmonic features in optically interesting formulations. The powders are characterized using the UV-VIS-NIR spectrophotometer equipped with an integrating sphere in reflectance mode, and using a mathematical model known as the Kubelka-Munk formalism.

In the second section, selected formulations are deposited as thin films onto conductive glass substrates and characterized for their optical and electrochemical properties and their resulting electrochromic performances. The then produced films are investigated using cyclic voltammetry (CV), chronoamperometry (CA) and spectroelectrochemistry (SEC).

Next, the third section addresses the development of CeO_2-based passive counter electrode formulations using an ultrasonic spray pyrolysis deposition method, investigating the effect of Mo doping on the optical and electrochemical performances of the produced materials using the same array of analysis methods as for the MoWOx and parent oxide formulations in the first and second sections. In the scope of this research work, the getting of efficient counter electrode materials is essential for the development of complete devices, as the enhanced functionality expected from MoWOx formulations would be hampered by coupling them with any material displaying a complementary electrochromic behavior. Therefore, highly efficient passive/neutral counter electrode should be used as to not hinder the optoelectonic properties of the active material, maximizing the performances of the complete devices.

Finally, in the fourth and final section, films produced from the wet coating of the MoWOx formulations displaying the best performances are assembled together with the CeO_2-based counter electrodes into complete devices, first in liquid-state, with the films immersed in an electrolyte solution, and then into a solid device, using a polymer gel electrolyte (**Figure 1.31**), as to best approach the intended final application, namely the development of a highly efficient dual band smart window.

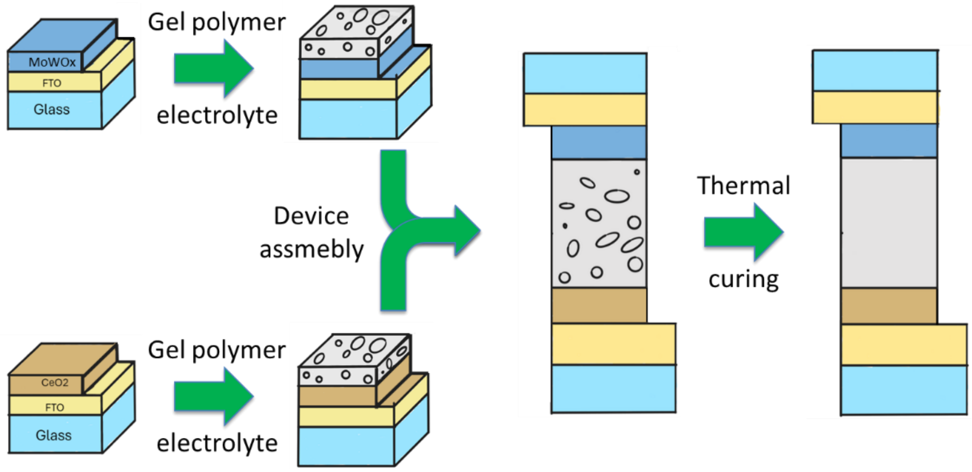

Figure 1.31: Schematic representation of the assembly of a solid device from a MoWOx working electrode and a CeO_2 counter electrode, held as a single unit by a polymer gel electrolyte.

In view of the state-of-the-art, this doctoral research thesis aims at investigating and highlighting the peculiar optical and electrochemical properties of MoWOx formulations. The characterization of the studied materials as powders and films should allow the demonstration of the expected dual band behavior, which has never been shown in MoWOx. With this work, we hope to prove the promising features of mixed molybdenum – tungsten oxide, from samples in the form of powders, to proof-of-concept lab-scale complete devices, as a first step into the development of new – efficient and highly functional – electrochromic materials and their future application as active electrodes in smart windows.

1.6. References

1. https://knowledge4policy.ec.europa.eu/foresight/topic/aggravating-resource-scarcity/more-developments-relevant-aggravating-resource-scarcity_en, accessed on 10/09/2024.
2. Lynas, M. *et al*. *Environ. Res. Lett.* **2021**, 16, 114005, doi.org/10.1088/1748-9326/ac2966
3. https://www.who.int/news-room/fact-sheets/detail/climate-change-and-health, accessed on 19/08/2024.
4. https://youth.europa.eu/get-involved/sustainable-development/how-reduce-my-carbon-footprint_en, accessed on 19/08/2024.
5. https://ec.europa.eu/eurostat/statistics-explained/index.php?title=Final_energy_consumption_in_industry_-_detailed_statistics#Energy_products_used_in_the_industry_sector, accessed on 26/11/2024.
6. https://www.eia.gov/totalenergy/data/monthly/, accessed on 26/11/2024.
7. https://www.energy.gov/eere/energy-efficiency-buildings-and-industry, accessed on 10/09/2024.
8. https://seia.org/research-resources/updating-building-codes-cost-effectively-solar/, accessed on 28/11/2024.
9. Cao, X. *et al*. *Energy Build.* **2016**, 128, 198, doi.org/10.1016/j.enbuild.2016.06.089.
10. Xie, S. *et al*. *Int. Trans. Electr. energy Syst.* **2013**, 20, 1, doi.org/10.1002/etep.418.
11. Taguchi, T. *IEEJ Trans. Electr. Electron. Eng.* **2008**, 3, 21, doi.org/10.1002/tee.20228.
12. Niachou, A. *et al*. *Energy Build.* **2001**, 33, 719, doi.org/10.1016/S0378-7788(01)00062-7.
13. https://www.stainless-structurals.com/blog/a-trend-in-modern-architecture-more-glass/, accessed on 10/09/2024.
14. https://ghi.co.za/industry-trends-the-use-of-glass-in-architecture/, accessed on 10/09/2024.
15. Wang, Y. *et al*. *Annu. Rev. Chem. Biomol. Eng* **2016**, 7, 283, doi.org/10.1146/annurev-chembioeng-080615-034647.
16. Austin, R. R. Solar control properties in low emissivity coatings, patent n°5183700, 02/02/1993.
17. German, J. R. & Pfaff, G. L. Solar control low-emissivity coatings, patent n°2630363, 12/01/2016.
18. https://www.nanawall.com/blog/innovative-materials-found-in-the-anatomy-of-opening-glass-walls, accessed on 20/08/2024.
19. https://oknalux.com.au/importance-of-low-e-glass/, accessed on 12/09/2024.
20. Granqvist, C. G. *et al*. *Sol. Energy Mater. Sol. Cells* **2009**, 93, 2032, doi.org/10.1016/j.solmat.2009.02.026.
21. Dussault, J. M. *et al*. *Sol. Energy* **2012**, 86, 3405, doi.org/10.1016/j.solener.2012.07.016.
22. https://www.sageglass.com/en-gb, accessed on 10/09/2024.
23. https://www.agc-glass.eu/en/news/press-release/discover-halio-agc-glass-europes-new-interactive-windows-and-walls, accessed on 10/09/2024.

24. Tavares, P. F. *et al*. *Energy Policy* **2014**, 67, 68, doi.org/10.1016/j.enpol.2013.07.038.

25. Granqvist, C. G. *Sol. Energy Mater. Sol. Cells* **2007**, 91, 1529, doi.org/10.1016/j.solmat.2007.04.031.

26. Granqvist, C. G. *Sol. Energy Mater. Sol. Cells* **2008**, 92, 203, doi.org/10.1016/j.solmat.2006.10.027.

27. Cannavale, A. *et al*. *Appl. Energy* **2018**, 225, 975, doi.org/10.1016/j.apenergy.2018.05.034.

28. https://ec.europa.eu/eurostat/statistics-explained/index.php?title=Electricity_and_heat_statistics#General_overview, accessed on 10/09/2024.

29. Appolloni, L. *et al*. *Int. J. Environ. Res. Public Health* **2021**, 18, 4278, doi.org/10.3390/ijerph18084278.

30. https://glassforeurope.com/daylight-and-glazing-requirements-in-new-construction/, accessed 10/09/2024.

31. Denayer, J. *et al*. *Sol. Energy Mater. Sol. Cells* **2014**, 130, 623, doi.org/10.1016/j.solmat.2014.07.038.

32. https://www.gentex.com/files/Gentex_Aerospace_Brochure.pdf, accessed on 12/09/2024.

33. Mortimer, R. J. *Annu. Rev. Mater. Res.* **2011**, 41, 241, doi.org/10.1146/annurev-matsci-062910-100344.

34. Zhai, Y. *et al*. *Adv. Funct. Mater.* **2022**, 1, 2109848, doi.org/10.1002/adfm.202109848.

35. Wang, Z. *et al*. *Mater. Sci. Eng. R Reports* **2020**, 140, 100524, doi.org/10.1016/j.mser.2019.100524.

36. Wang, J. *et al*. *Nat. Commun.* **2014**, 5, 1, doi.org/10.1038/ncomms5921.

37. Kraft, A. *ChemTexts* **2019**, 5, 1, doi.org/10.1007/s40828-018-0076-x.

38. Zhai, Y. *et al*. *Nanoscale* **2018**, 10, 3089, doi.org/10.1039/c7nr07803j.

39. Beaujuge, P. M. *et al*. *Chem. Rev.* **2010**, 110, 168, doi.org/10.1021/cr900129a.

40. Kanazawa, K. *et al*. *Phys. Chem. Chem. Phys.* **2017**, 19, 16979, doi.org/10.1039/c6cp08528h.

41. Cannavale, A. *et al*. *Energies* **2020***,* 13, 1449, doi.org/10.3390/en13061449.

42. Mortimer, R. J. *et al*. *Displays* **2006**, 27, 2, doi.org/10.1016/j.displa.2005.03.003.

43. Chatzikyriakou, D. *et al*. *Microporous Mesoporous Mater.* **2017**, 240, 31, doi.org/10.1016/j.micromeso.2016.11.001.

44. Shchegolkov, A. V. *et al*. *Nanomaterials* **2021**, 11, 2376, doi.org/10.3390/nano11092376.

45. Arslan, M. *et al*. *Ceram. Int.* **2021**, 47, 32570, doi.org/10.1016/j.ceramint.2021.08.152.

46. Denayer, J. *et al*. *Appl. Surf. Sci.* **2014**, 321, 61, doi.org/10.1016/j.apsusc.2014.09.128.

47. Moulki, H. *et al*. *Electrochim. Acta* **2012**, 74, 46, doi.org/10.1016/j.electacta.2012.03.123.

48. Wang, F. *et al*. *Mater. Sci. Semicond. Process.* **2022**, 151, 106986, doi.org/10.1016/j.mssp.2022.106986.

49. Runnerstrom, E. L. *et al*. *Chem. Commun.* **2014**, 50, 10555, doi.org/10.1039/c4cc03109a.

50. Prasad, A. K.*et al*. *Electrochim. Acta* **2022**, 422, 140340, doi.org/10.1016/j.electacta.2022.140340.

51. Granqvist, C. G. *Sol. Energy Mater. Sol. Cells* **1994**, 32, 369, doi.org/10.1016/0927-0248(94)90100-7.

52. Zhang, L. Active photonic devices based on spin crossover molecules. (University of Toulouse, **2023**).

53. Hush, N. S. *Trans. Faraday Soc.* **1961**, 57, 557, doi.org/10.1039/tf9615700557.

54. Hush, N. S. Intervalence-Transfer Absorption. Part 2. Theoretical Considerations and Spectroscopic Data in *Progress in Inorganic Chemistry*. 391–444 (published by F. Albert Cotton, **1967**).

55. Hush, N. S. *Electrochim. Acta* **1968**, 13, 1005, doi.org/10.1016/0013-4686(68)80032-5.

56. Crutchley, R. J. *Adv. Inorg. Chem.* **1994**, 41, 273, doi.org/10.1016/S0898-8838(08)60174-9.

57. Dasgupta, B. *et al*. *J. Phys. Chem. C* **2015**, 119, 10592, doi.org/10.1021/acs.jpcc.5b02609.

58. Yamashita, J. & Kurosawa, T. *J. Phys. Chem. Solids* **1958**, 5, 34, doi.org/10.1016/0022-3697(58)90129-X.

59. Sewell, G. L. *Philos. Mag.* **1958**, 3, 1361, doi.org/10.1080/14786435808233324.

60. Holstein, T. *Ann. Phys.* **1959**, 8, 343, doi.org/10.1016/0003-4916(59)90003-X.

61. Landau, L. D. *Phys. Z. Sowjetunion* **1933**, 3, 67, doi.org/10.1016/b978-0-08-010586-4.50015-8.

62. Pekar, S. I. *J. Phys; USSR* **1946**, 10, 341.

63. Landau, L. D. *et al*. *Zh. Eksp. Teor. Fiz* **1948**, 18, 419, http://archive.ujp.bitp.kiev.ua/files/journals/53/si/53SI15p.pdf.

64. Tandon, B. *et al*. *J. Phys. Chem. C* **2022**, 126, 9228, doi.org/10.1021/acs.jpcc.2c02155.

65. Granqvist, C. G. *Appl. Phys. A Solids Surfaces* **1993**, 57, 3, doi.org/10.1007/bf00331209.

66. Ma, C. *et al*. *Polym. Eng. Sci.* **2008**, 48, 2224, doi.org/10.1002/pen.21169.

67. Aller Pellitero, M. *et al*. *Curr. Opin. Electrochem.* **2019**, 15, 66, doi.org/10.1016/j.coelec.2019.03.004.

68. Sauvet, K.*et al*. *Sol. Energy Mater. Sol. Cells* **2009**, 93, 2045, doi.org/10.1016/j.solmat.2009.05.003.

69. Glogic, E. *et al*. *ACS Sustain. Chem. Eng.* **2021**, 9, 11691, doi.org/10.1021/acssuschemeng.1c02348.

70. https://www.peclabel.eu/cms/c_19127792/en/peclabel?id=c_19127792, accessed on 10/09/2024.

71. Krašovec, U. O. *et al*. *ChemInform* **1998**, 29, 3398, doi.org/10.1149/1.1838025.

72. Orel, B. *et al*. *J. Mater. Chem.* **1995**, 5, 617, doi.org/10.1039/jm9950500617.

73. El-Habib, A. *et al*. *Opt. Mater.* **2022**, 127, 112312, doi.org/10.1016/j.optmat.2022.112312.

74. Zimou, J. *et al*. *Mater. Sci. Semicond. Process.* **2021**, 135, 1369, doi.org/10.1016/j.mssp.2021.106049.

75. El-Habib, A. *et al*. *Surfaces and Interfaces* **2021**, 23, 100906, doi.org/10.1016/j.surfin.2020.100906.

76. Xue, X. *et al*. *Gels* **2023***,* 9, 8, doi.org/10.3390/gels9010008.

77. Zhou, X. *et al*. *Chem. Soc. Rev.* **2024**, 53, 5291, doi.org/10.1039/d3cs00551h.

78. Hepel, M., Redmond, H. & Dela, I. *Electrochim. Acta* **2007**, 52, 3541, doi.org/10.1016/j.electacta.2006.10.032.

79. Santos, L. *et al*. *Adv. Electron. Mater.* **2015**, 1, 1400002, doi.org/10.1002/aelm.201400002.

80. Li, H. *et al*. *J. Mater. Chem. C* **2015**, 4, 33, doi.org/10.1039/c5tc02802g.

81. DeForest, N. *et al*. *Build. Environ.* **2015**, 89, 107, doi.org/10.1016/j.buildenv.2015.02.021.

82. DeForest, N. *et al*. *Appl. Energy* **2017**, 192, 95, doi.org/10.1016/j.apenergy.2017.02.007.

83. Agrawal, A. *et al*. *Chem. Rev.* **2018**, 118, 3121, doi.org/10.1021/acs.chemrev.7b00613.

84. Drude, P. *Ann. Phys.* **1900**, 306, 566, doi.org/10.1002/andp.19003060312.

85. Drude, P. *Ann. Phys.* **1900**, 308, 369, doi.org/10.1002/andp.19003081102.

86. Eldlio, M. *et al*. Drude-Lorentz Model of Semiconductor Optical Plasmons in *IAENG Transactions on Engineering Technologies*. 41-49 (published by Springer Science, **2014**).

87. Runnerstrom, E. L. Charge Transport in Metal Oxide Nanocrystal-Based Materials. (University of California, Berkeley, **2016**).

88. Gansel, J. K. *et al*. *Science.* **2009**, 325, 1513, doi.org/10.1126/science.1177031.

89. Mulvihill, M. J. *et al*. *J. Am. Chem. Soc.* **2010**, 132, 268, doi.org/10.1021/ja906954f.

90. Rycenga, M. *et al*. *Chem. Rev.* **2011**, 111, 3669, doi.org/10.1021/cr100275d.

91. Albrektsen, O. *et al*. *JOSA B* **2010**, 27, 1680, doi.org/10.1364/josab.27.001680.

92. Park, J. E. *et al*. *Small Methods* **2017**, 1, 1600032, doi.org/10.1002/smtd.201600032.

93. Kołątaj, K. *et al*. *Environ. Chem. Lett.* **2020**, 18, 529, doi.org/10.1007/s10311-019-00962-1.

94. Kelly, K. L. *et al*. *J. Phys. Chem. B* **2003**, 107, 668, doi.org/10.1021/jp026731y.

95. Calvo, R. *et al*. *Sci. Reports* **2022***,* 12, 1, doi.org/10.1038/s41598-022-21649-8.

96. Maier, S. A. Plasmonics: fundamentals and applications (published by Springer Science, **2007**).

97. Llordes, A. *et al*. Plasmonic Electrochromism of Metal Oxide Nanocrystals. in *Electrochromic Materials and Devices.* 363–398 (published by Wiley-VCH, **2015**).

98. Manthiram, K. *et al*. *J. Am. Chem. Soc* **2012**, 134, 3995, doi.org/10.1021/ja211363w.

99. Salje, E. *et al*. *Philos. Mag. B* **1984**, 50, 607, doi.org/10.1080/13642818408238882.

100. Boschloo, G. *et al*. *J. Phys. Chem. B* **1999**, 103, 3093, doi.org/10.1021/jp9835566.

101. Lounis, S. D. *et al*. *J. Phys. Chem. Lett.* **2014**, 5, 1564, doi.org/10.1021/jz500440e.

102. Garcia, G. *et al*. *Nano Lett* **2011**, 11, 4415, doi.org/10.1021/nl202597n.

103. Garcia, G. *et al*. *Adv. Opt. Mater.* **2013**, 1, 215, doi.org/10.1002/adom.201200051.

104. Novo, C. *et al. J. Am. Chem. Soc.* 2009, **131**, 14664, doi.org/10.1021/ja905216h.

105. Ung, T. *et al*. *Langmuir* **1997**, 13, 1773, doi.org/10.1021/la960863z.

106. Henglein, A. *et al*. *Faraday Discuss.* **1991**, 92, 31, doi.org/10.1039/fd9919200031.

107. Wang, C. *et al*. *New Ser.* **2001**, 291, 2390, doi.org/10.1126/science.291.5512.2390.

108. Coughlan, C. *et al*. *Chem. Rev.* **2017**, 117, 5865, doi.org/10.1021/acs.chemrev.6b00376.

109. Tegg, L. *et al*. *Plasmonics* **2023**, 18, 49, doi.org/10.1007/s11468-022-01749-x.

110. Adachi, K. *et al. J. Mat. Res.* **2012**, 27, 965, doi.org/10.1557/jmr.2012.25.

111. Wang, T. *et al*. *New J. Chem* **2016**, 40, 7476, doi.org/10.1039/c6nj00408c.

112. Yin, H. *et al. J. Phys. Chem. C* **2017**, 121, 23531, doi.org/10.1021/acs.jpcc.7b08403.

113. Li, P. *et al*. *ACS Appl. Mater. Interfaces* **2020**, 12, 19153, doi.org/10.1021/acsami.0c00220.

114. Zhong, X. *et al*. *Adv. Funct. Mater.* **2016**, 26, 5778, doi.org/10.1002/adfm.201601732.

115. Zhao, Y. *et al*. *Int. J. Hydrogen Energy* **2017**, 42, 14534, doi.org/10.1016/j.ijhydene.2017.04.115.

116. Zhang, N. *et al. J. Am. Chem. Soc.* **2018**, 140, 9434, doi.org/10.1021/jacs.8b02076.

117. Xue, N. *et al. RSC Adv.* **2017**, 7, 2351, doi.org/10.1039/c6ra26267h.

118. Zhang, S. *et al*. *Mater. Horizons* **2018**, 5, 291, doi.org/10.1039/c7mh01128h.

119. Zhang, S. *et al*. *Energy Environ. Sci.* **2018**, 11, 2884, doi.org/10.1039/c8ee01718b.

120. Zhang, S. *et al*. *Appl. Mater. Interfaces* **2019**, 11, 48062, doi.org/10.1021/acsami.9b17678.

121. Llordés, A. *et al*. *Nature* **2013**, 500, 323, doi.org/10.1038/nature12398.

122. Dahlman, C. J. *et al. J. Am. Chem. Soc.* **2015**, 137, 9160, doi.org/10.1021/jacs.5b04933.

123. Kim, J. *et al*. *Nano Lett.* **2015**, 15, 5574, doi.org/10.1021/acs.nanolett.5b02197.

124. Heo, S. *et al*. *Nano Lett.* **2017**, 17, 5756, doi.org/10.1021/acs.nanolett.7b02730.

125. Jin, S. *et al*. *Solid State Ionics* **2022**, 385, 116011, doi.org/10.1016/j.ssi.2022.116011.

126. Gao, T. *et al*. *Sol. Energy Mater. Sol. Cells* **2018**, 177, 3, doi.org/10.1016/j.solmat.2017.11.025.

127. Cheref, Y. *et al*. *Chem. Mater.* **2022**, 34, 9795, doi.org/10.1021/acs.chemmater.2c02879.

128. Cleret de Langavant, C. *et al*. *Nano Lett.* **2024**, 24, 3074, doi.org/10.1021/acs.nanolett.3c04849.

129. Hassani, H. *et al*. *Phys. Rev. B* **2022**, 105, 014107, doi.org/10.1103/physrevb.105.014107.

130. Bousquet, E. *et al*. *Phys. Rev. Res*. **2020**, 2, 012052, doi.org/10.1103/PhysRevResearch.2.012052.

131. Salje, E. K. H. *Eur. J. Solid State Inorg. Chem.* **1994**, 31, 805, https://www.researchgate.net/publication/235328412.

132. Barawi, M. *et al*. *ACS Nano* **2017**, 11, 3576, doi.org/10.1021/acsnano.6b06664.

133. Barawi, M. *et al. J. Mater. Chem. A* **2018**, 6, 10201, doi.org/10.1039/c8ta02636j.

134. Lu, H.-C. *et al. ACS Nano* **2020**, 14, 10068, doi.org/10.1021/acsnano.0c03283.

135. Zhao, S. *et al. Carbon Neutralization* **2023**, 2, 4, doi.org/10.1002/cnl2.38.

136. Yilmaz, P. *et al. ACS Appl. Energy Mater* **2020**, 3, 3779, doi.org/10.1021/acsaem.0c00241.

137. Liu, J. *et al. J. Solid State Chem.* **2015**, 221, 255, doi.org/10.1016/j.jssc.2014.10.016.

138. Wang, Q. *et al. Appl. Surf. Sci.* **2017**, 399, 41, doi.org/10.1016/j.apsusc.2016.12.022.

139. Spetter, D. *et al. ACS Sustain. Chem. Eng* **2018**, 6, 12641, doi.org/10.1021/acssuschemeng.8b01370.

140. Yin, H. *et al. J. Mater. Chem. A* **2018**, 6, 10932, doi.org/10.1039/c8ta03125h.

141. Yang, M. *et al. ACS Sustain. Chem. Eng.* **2020**, 8, 2957, doi.org/10.1021/acssuschemeng.9b07526.

142. Xiong, J. *et al. Sep. Purif. Technol.* **2022**, 294, 121167, doi.org/10.1016/j.seppur.2022.121167.

143. Zhou, D. *et al. J. Colloid Interface Sci.* **2016**, 465, 112, doi.org/10.1016/j.jcis.2015.11.068.

144. Li, H. *et al. Adv. Mater. Technol.* **2017**, 2, 1700047, doi.org/10.1002/admt.201700047.

145. Li, H. *et al. Nano Energy* **2018**, 47, 130, doi.org/10.1016/j.nanoen.2018.02.043.

146. Li, H. *et al. Appl. Mater. Interfaces* **2018**, 10, 10520, doi.org/10.1021/acsami.7b18310.

147. Xie, S. *et al. Appl. Surf. Sci.* **2018**, 459, 774, doi.org/10.1016/j.apsusc.2018.08.045.

148. Wang, B. *et al. Materials* **2018**, 11, 1627, doi.org/10.3390/ma11091627.

149. Kumar, A. *et al. J. Sol-Gel Sci. Technol.* **2019**, 90, 281, doi.org/10.3390/ma11091627.

150. Li, W. *et al. Sol. Energy Mater. Sol. Cells* **2022**, 235, 111488, doi.org/10.1016/j.solmat.2021.111488.

151. https://www.parrinst.com/products/sample-preparation/acid-digestion/high-pressure-acid-digestion-vessel-models-4746-4747-23-ml/, accessed on 12/09/2024.

152. https://www.spincoater.com/what-is-spin-coating.php, accessed on 13/09/2024.

Chapter 2 – Synthesis of molybdenum-tungsten oxide active materials as powders, and consecutive structural and optical characterizations

Chapter 2 – Synthesis of molybdenum-tungsten oxide active materials as powders, and consecutive structural and optical characterizations

The main results of this chapter are available as pre-print on (doi.org/10.26434/chemrxiv-2024-vhf83) and, when submitting the present thesis manuscript on 17 Dec 2024, are considered for publication (under review) in the "Advanced Optical Materials" (Wiley) journal.

2.1. Solvothermal synthesis: general principles and state-of-the-art for plasmonic and/or electrochromic metal oxides

In the scope of this work, electrochromically active materials are produced via a single step solvothermal synthesis adapted from a protocol reported in previous works of the literature, in particular those of Prof. H. Yamashita from Osaka University[1,2]. In summary, a mix of precursors and organic solvent (or mix of solvents) are placed in a polytetrafluoroethylene (PTFE, Teflon®) reaction vessel, itself sealed in a stainless-steel autoclave (**Figure 2.1**). The solvothermal reactor is then thermally treated in an oven at a given temperature and for a certain amount of time. This method allows the production of highly crystalline nanoparticles with a high degree of control on their shape, size and composition, as well as good stability and dispersity properties[3–6]. The careful modification of the experimental parameters leads to the fine tuning of the physicochemical properties of the chemical product.

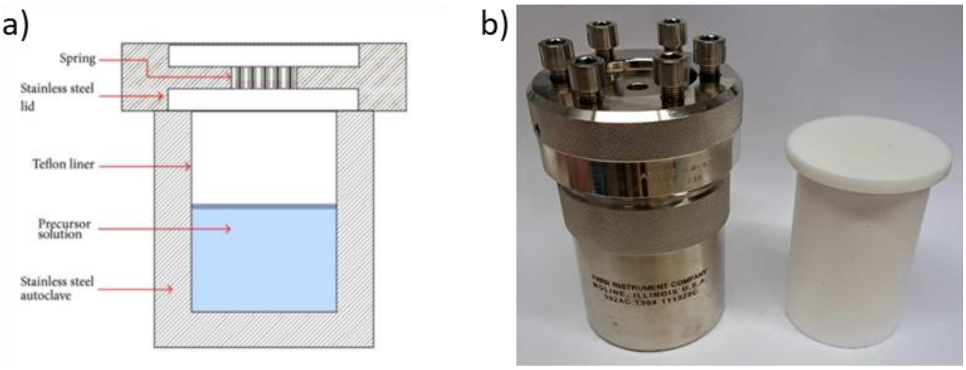

Figure 2.1: Schematic representation of a solvothermal reactor (a)[7] and a picture of the autoclave and Teflon liner used for the synthesis of the materials investigated in this work (b).

The main benefits of the solvothermal method stand in its easiness of use, and more importantly, the increased range of temperature and pressure reactive conditions allowed thanks to the autogenerated pressure in the reactor, leading to the synthesis of materials displaying peculiar properties[3]. Indeed, the evaporation of the solvent inside the airtight autoclave results in an increase in the pressure inside the Teflon liner, giving access to synthetic conditions usually unreachable in a classical glassware in open air setup: for example, pressurized water can be maintained in a liquid state at temperatures largely exceeding its boiling point of 100°C, allowing the production of materials, compositions and morphologies not met under ambient atmosphere. In addition, these particular reactive conditions also enable the "surfactant-free" synthesis of nanostructured particles, usually obtained through surfactant assisted colloidal synthesis under inert atmosphere (using a Schlenk line). However, a big downside of the solvothermal method lies in the fact that it acts as a "black box", in which the reactions taking place during the thermal treatment cannot be monitored and only the properties of the final product can be investigated after retrieving the material[3].

In the context of electrochromic and plasmonic materials, numerous articles have reported the efficient formulation of nanostructured metal oxides using hydro/solvothermal synthesis (**Table 2. 1**). Based on the precursor used and the thermal treatment applied, this technique gives access to a wide range of morphologies such as, notably, nanorods[8,9], nanoplates[8], nanosheets[10,11], nanodots[12–14]. Given the many available nanostructures allowed by the solvothermal method, the properties of the particles can be fine-tuned as to improve their performances for their intended application. Moreover, the peculiar temperature and pressure conditions inside of the reactor can result in the production of oxygen deficient materials, that can in turn support plasmonic properties[15,16]. These unique optical properties can then be exploited for NIR selective electrochromism[4,15] but not only. Indeed, plasmonic materials also find applications in (photo)catalysis[9,10,12,17], sensors[6], spectroscopy (SERS)[18] and health (photothermal therapy[18]). Finally, the solvothermal method has been successively applied for the synthesis of some of the most widespread (plasmonic) electrochromic formulations such as tungsten oxide[5,23], nickel oxide[24], ITO[4] and AZO[25]. These previous results are promising for the use of solvothermal synthesis as an efficient method to produce MoWOx nanostructures for their application as dual band plasmonic electrochromic material.

In comparison to colloidal synthesis protocols under inert atmospheres, the solvothermal processes usually requires lower operating temperatures (160-200°C vs. 180-300°C in a typical Schlenk line setup[19–21]). Also, the solvothermal synthesis can be upscaled by transferring the protocol onto a larger reactor, that can reach over 300 liters[22]. In addition, the possibility offered by the solvothermal method to produce nanostructured particles in solvents of reduced toxicity (mostly alcohols), without the use of additives (in particular surfactants), at ambient pressure and moderate temperature (basic solvothermal reactors are graded for a maximal temperature around 200°C[26]) makes this technique a highly interesting and efficient synthetic approach.

Table 2. 1: Literature survey of solvothermally synthesized materials and morphologies for electrochromic and/or plasmonic applications.

Material	Morphology	Applications
$WO_{3-\delta}$	Nanodots	Photocatalysis[12], fluorescence[13], photoluminescence[14]
	Nanoneedles	NIR plasmonic EC material[15]
	Nanoparticles	Dual band EC material[16]
WO_3	Nanowires/nanotrees	EC material[5]
	Nanobricks	EC material[23]
$WO_3.2H_2O$	Nanorods	Photocatalysis[9]
	Nanosheets	EC material[11]
	Hollow sphere	Photocatalysis[17]
$MoO_{3-\delta}$	Nanoparticles	SERS and photothermal therapy[18]
	Nanosheets	Hydrogen generation[10]
ITO	Nanocrystals	NIR plasmonic EC material[4], tunable LSPR material[27]
	Nanoplates/nanorods	Design of nanostructured morphologies[8]
AZO	Nanocrystals	Plasmonic sensor[6]
	Nanospheres	Plasmonic NIR shielding[25]
NiO	“Yolk-shell”	EC material[24]

2.2. Materials and methods

Chemicals. Metallic tungsten (W, fine powder, 99+%) and molybdenum powders (Mo, 99+%) are purchased from Merck, isopropanol (technical grade) and hydrogen peroxide (H_2O_2, 33%) from VWR, lithium fluoride (LiF, 99.8% anhydrous) is supplied from ROC/RIC and barium sulfate ($BaSO_4$, 99.99%) from Sigma-Aldrich). All chemicals were used as received without further purification.

Synthesis of $Mo_yW_{1-y}O_{3-\delta}$ and $WO_{3-\delta}$ compounds. The active materials are produced following a typical solvothermal synthetic procedure[1], further described in **Section 2.3.1** of this chapter, page 45.

Characterizations. Micrographs of the particles are obtained from transmission electron microscopy (TEM) using a TECNAI G² 20 operated at 200 kV (in collaboration with UNamur – Dr. Jean-François Colomer). The dimensions of the particles (excepted for the $WO_{3-\delta}$ 1h, measured on the TEM micrographs), the molecular ratio of the mixed oxides and top view of the spin coated films are obtained and analyzed using a scanning electron microscope (SEM) TESCAN CLARA, equipped with an energy dispersive X-ray spectroscopy (EDX) detector. X-ray diffraction (XRD) patterns are acquired on a Bruker D8 DISCOVER with Cu Kα (λ = 1.5418Å). The composition and surface properties of the powders are investigated using a Thermofisher K-alpha X-ray photoelectron spectrometer (XPS), equipped with a monochromatic Al Kα source and calibrated with the adventitious carbon (C1s) peak. The bulk electronic properties are characterized by Electron Paramagnetic Resonance (EPR) with a Bruker ESP300E spectrometer operating at 9.54 GHz (X-band), the spectra are acquired at 4K using 20 mW microwave power and normalized in accordance to the mass of the sample, gain and number of accumulated scans. UV-Vis-NIR data are recorded using a Shimadzu UV-3600i Plus spectrophotometer; the absorption of the powders is measured using an integrating sphere (ISR-1503) and exploiting the Kubelka-Munk formalism (see below) to transform diffuse reflectance measurements into data proportional to absorption.

2.3. Solvothermal synthesis and characterization of MoyW1-y$O_{3-\delta}$, $MoO_{3-\delta}$ and $WO_{3-\delta}$ compounds

2.3.1. Adapted synthesis protocol

In a typical synthetic procedure[1,2], 11.5 mL of H_2O_2 are added to 3 mmol of tungsten metallic powder and 6 mmol of molybdenum metallic powder (Mo/W molar ratio = 2/1) and magnetically stirred for 1h, yielding a yellow – clear solution. This solution is mixed with 69.0 mL of isopropanol into a Teflon vessel (125 mL), which is then sealed in a stainless-steel autoclave, heated and maintained at 160°C for a duration varying from 1 to 12h. Following the cooling of the reactor down to room temperature, the obtained suspension is collected, centrifuged and rinsed with ethanol three times, and finally dried under vacuum at 60°C overnight. The protocol is repeated with adapted Mo/W ratio for the synthesis of the 1/1 (4.5 mmol of tungsten and molybdenum) and 1/2 formulations (6 mmol of tungsten and 3 mmol of molybdenum). For the $WO_{3-\delta}$ parent oxide, the same protocol is applied without the addition of molybdenum powder (9 mmol of tungsten).

In a first step, five active formulations are reproduced according to the protocol reported by Yamashita *et al.* in their work[1,2], investigating three MoWOx mixed oxide formulations (Mo/W ratio = 2/1, 1/1 and 1/2), and the two corresponding parent oxides: $WO_{3-\delta}$ and $MoO_{3-\delta}$. These compounds are synthesized from metallic powder precursors solvothermally treated for 12h at 160°C (cf. **Materials and Methods**).

2.3.2. Morphological and structural characterizations

The materials are first characterized from a morphology, composition and structural point of view. SEM micrographs of the as-synthesized powders are presented in **Figure 2.2**. The parent oxides exhibit very different morphologies, with the tungsten oxide particles found in the form of hexagonal platelets with average dimensions of 1.9 x 0.2 µm (± 0.4 x 0.1 µm) (**Figure 2.2a**) while its Mo counterpart takes a feather-like shape, *i.e.* elongated platelets of dimensions 1.9 (± 0.5) x 0.1 (± 0.03) x 0.05 (± 0.01) µm (**Figure 2.2b**). Contrarily, the obtained MoWOx formulations all present similar particle morphologies across three selected Mo/W ratio, with a peculiar "urchin-like" shape consisting in a solid core and a surface covered by nanorods. The urchin aspect is similar in all three samples, but their dimensions varies depending on the precise precursor ratio. In the case of MoWOx 2/1 (**Figure 2.2c**) and MoWOx 1/1 (**Figure 2.2d)**, the particles reach a similar size of 2.6 (± 0.5) and 2.2 (± 0.5) µm, while the MoWOx 1/2 (**Figure 2.2e**) exhibits smaller particles with an average diameter of 1.6 (± 0.4) µm. In addition, the 1/2 mixed oxide further diverges from the other two MoWOx formulations with the combined presence of urchins and of hexagonal platelets closely resembling those found in the $WO_{3-\delta}$ parent oxide. The occurrence of such "impurities" in MoWOx 1/2 could indicate the existence of a limit in the amount of W that can be incorporated in the urchins. In this case, the excess in W precursor in the reactive media would favor the incorporation of the maximal amount of W in the mixed oxide, after which the remaining tungsten precursor would react to form pure $WO_{3-\delta}$, in the shape on hexagonal platelets. Since part of the precursor might be used for the formation of pure $WO_{3-\delta}$ platelets, less material is available for the growth of the urchins, which explains the smaller size of the MoWOx 1/2 particles in this context. In addition to the morphological properties of the investigated materials, their composition is quantified through EDX, in particular the three MoWOx formulations. The results of these analyses (added as inset in the corner of the corresponding micrographs) show the completion of the process, with the measured Mo/W ratios corresponding to the initial mix of precursors in the reactive media. In addition to the SEM micrographs, schematic representations of isolated particles are presented in **Figure 2.3** for a clearer view of the morphologies observed in the powder aggregates.

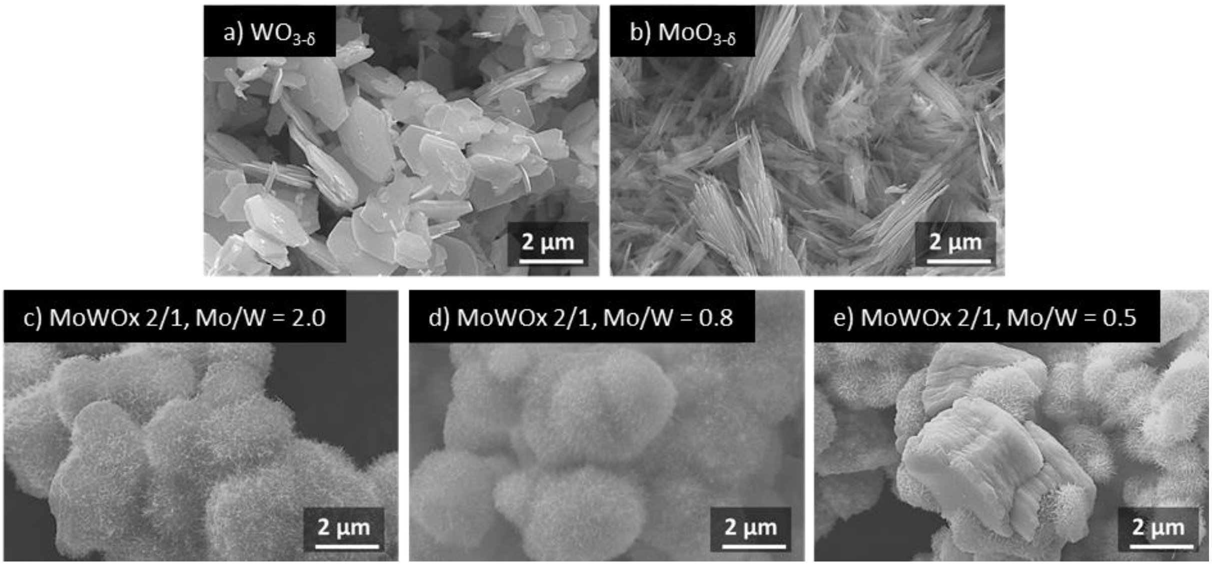

Figure 2.2: SEM micrographs of $WO_{3-\delta}$ (a), $MoO_{3-\delta}$ (b), MoWOx 2/1 (c), MoWOx 1/1 (d) and MoWOx 1/2 (e), with the measured Mo/W ratio as inset in the mixed formulations.

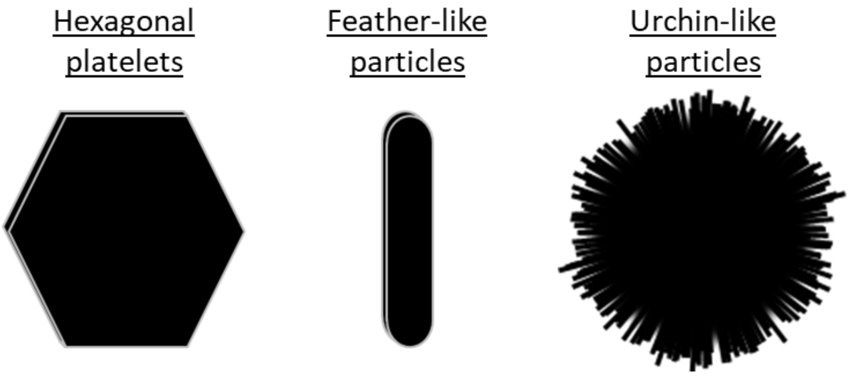

Figure 2.3: Schematic representation of the different morphologies observed in the SEM micrographs as isolated particles.

Then, the structural properties of these five compounds are characterized by XRD analysis (**Figure 2.4**). The $WO_{3-\delta}$ platelets display sharp diffraction peaks that can be indexed to a hexagonal phase (PDF 04-007-2322), consistent with the shape of the particles, and with a crystallite size (D_{hkl}) of 38 nm, measured using the Debye Scherrer **Equation 2.1**:

$$D_{hkl} = \frac{0.9\,\lambda}{\beta cos\theta} \tag{2.1}$$

Where λ is the wavelength (Cu Kα, λ = 1.5418 Å), θ is the diffraction angle, h, k, l are Miller's indices, and β is the full width at half maximum intensity (FWHM). The other parent oxide, $MoO_{3-\delta}$, also presents sharp and intense diffraction peaks corresponding to a monoclinic crystalline structure (PDF 00-047-1320), while the crystallite size comes up to 24 nm. Besides, the three MoWOx formulations exhibit very few diffraction signals, with only two appearing at 22.7° and 46.4°, indexed as the (010) and (020) planes of the monoclinic $W_{18}O_{49}$ nanowires pattern (PDF 04-005-4314; cell constants: a = 18.32 Å, b = 3.79 Å, and c = 14.04 Å). The presence of only two peaks in the same diffraction axis can be correlated to an anisotropic growth of the crystallites alongside the longitudinal axis of the nanowire. Given the preferential growth of nanorods at the surface of the MoWOx particles and diffractograms obtained for these samples, it seems that these outer nanorods are mainly responsible for the crystallinity in the mixed formulations. The computed crystallite size of all three MoWOx 2/1, 1/1 and 1/2 is of 18-19 nm. These values are smaller than that of the parent oxides, owing to the possible deformation of the structure brought by the substitution of Mo and W, and resulting in the disruption of the lattice symmetry, preventing the growth of larger crystallites. Moreover, in the case of MoWOx 1/2, the diffractogram actually consists in a signal including both contributions of MoWOx and $WO_{3-\delta}$ signals, especially the peaks at 28.2°, 36.7°, 50.0° and 55.7°, clearly appearing in both formulations. These results corroborate the hypothesis of the formation of $WO_{3-\delta}$ "impurities" in the MoWOx 1/2 formulation, as suggested from the SEM micrographs (**Figure 2.2**).

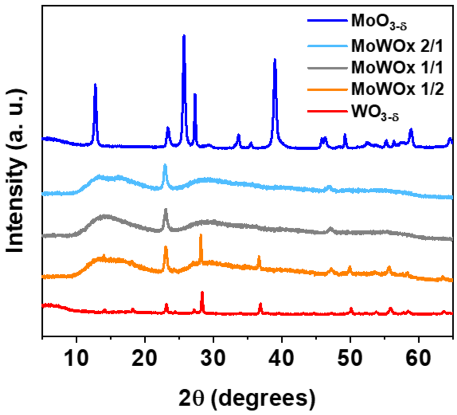

Figure 2.4: XRD diffractograms of the five investigated formulations.

On this basis, we then study how the synthesis duration impacts the evolution of the morphology, composition and structure of the material as the particles grow in the solvothermal reactor. As first representative case, we focus on the MoWOx 2/1 formulation, with syntheses carried out during 1 to 12h. For all durations, urchin-like particles are obtained with a solid core covered by an outer layer of nanorods (**Figure 2.5a**), growing from an average of 1.5 ± 0.5 µm at 1h to 2.8 ± 0.9 µm after 3h and 2.6 ± 0.3 µm for 12h of synthesis (**Figure 2.5b**). Complementary EDX characterization of the MoWOx powders (presented as insets in **Figure 2.5a**) highlights a disparity in the Mo/W ratios, with a molybdenum rich oxide for short-duration synthesis (Mo/W = 5/1 for the 1h case), followed by a decrease in the relative Mo content over longer durations (3h and more) to finally attain the targeted ratio of 2/1 (the initial ratio of the precursors in the reactive medium). These results tend to indicate faster reaction kinetics for the molybdenum species in comparison to the tungsten ones, leading first to the formation of Mo-rich particles, to which the remaining dissolved tungsten incorporates over the next hours of reaction, until the reactive medium is completely depleted from metallic precursors. As the urchin-like morphology and composition of the MoWOx particles do not evolve further after 3h of solvothermal treatment, only the two limit durations of 1h and 12h are considered for the next sections of this thesis. Indeed, the size dispersion of the particles appears to decrease as the duration of the solvothermal process increases, indicating an homogenization of the morphological properties of the urchin-like particles and a more robust protocol. Given the narrower dispersion found after 12h, and with the latter also being the duration studied in previous works of the literature[1,2,28,29], only 1h and 12h durations are selected in the frame of this work.

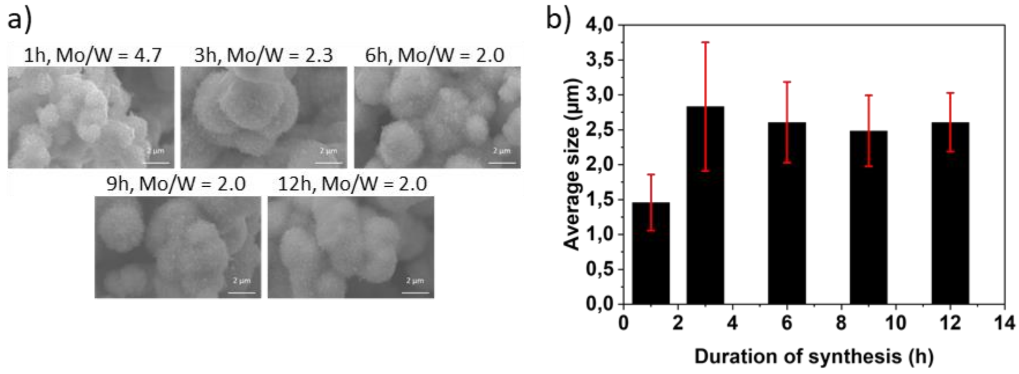

Figure 2.5: SEM micrographs (a, with EDX Mo/W ratios at the top of each) and mean size of the MoWOx 2/1 particles as a function of sythesis duration (b).

In addition to the two MoWOx formulations (2/1, 1h and 12h), two $WO_{3-\delta}$ parent oxides produced following the same synthetic protocols (160°C, 1h and 12h) are also considered as benchmark formulations, and accordingly synthesized and characterized. The samples obtained from the solvothermal process exhibit different colorations, notably: a dark blue tint in the case of both 1h and 12h MoWOx formulations, while the $WO_{3-\delta}$ parent oxides display lighter colors, with the "1h" sample leaning towards a grey/green color and its 12h counterpart being recovered as a light grey powder. Pictures of the powders are available in **Figure 2.6**.

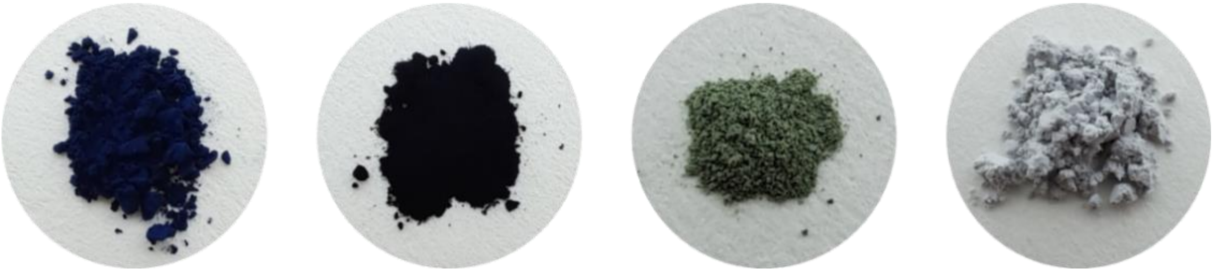

Figure 2.6: Pictures of the four as-synthesized powders, from left to right: MoWOx 1h, MoWOx 12h, $WO_{3-\delta}$ 1h and $WO_{3-\delta}$ 12h.

TEM micrographs of the four formulations of interest are presented in **Figure 2.7**, displaying very different morphologies. In the case of the MoWOx particles, both formulations highlight an urchin-like morphology, with the 1h formulation (**Figure 2.7a**, 1.5 ± 0.5 µm) growing into its larger 12h counterpart (**Figure 2.7b**, 2.6 ± 0.6 µm). However, due to the dense packing of nanorods at the surface of the urchins, the core-to-nanorods ratio could not be monitored nor tuned as a function of the time under solvothermal treatment from these measurements. For the parent $WO_{3-\delta}$ formulations, the morphology varies significantly as a function of the time, evolving from very aggregated nanospheres (6.4 ± 1.6 nm) in the case of $WO_{3-\delta}$ 1h (**Figure 2.7c**), to micrometric hexagonal platelets (1.9 x 0.2 µm (± 0.4 x 0.1 µm)) after 12h of solvothermal treatment (**Figure 2.7d**). Importantly, the nanostructures found in these materials – *i.e.* either the nanospheres (**Figure 2.7c**), the nanometric thickness of the hexagonal platelets (**Figure 2.7d**), or the nanorods at the surface of the urchins (**Figure 2.7a,b**) – could allow the support of plasmonic features in these formulations.

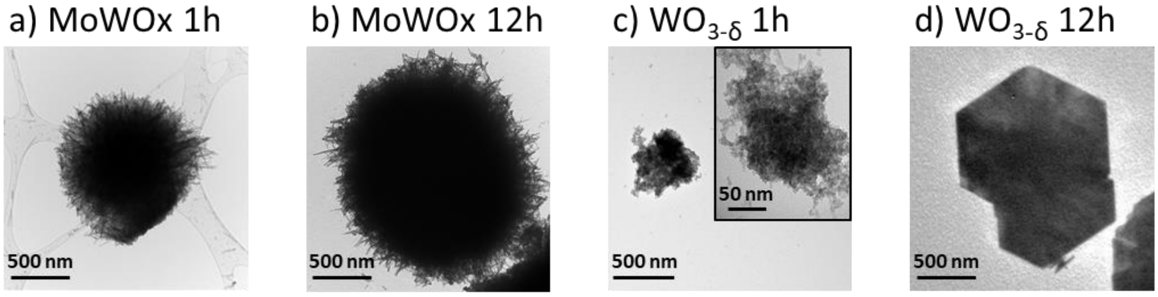

Figure 2.7: TEM micrographs of particles of MoWOx 1h(a), MoWOx 12h (b), $WO_{3-\delta}$ 1h (c, with a greater magnification of an aggregate in inset), and $WO_{3-\delta}$ 12h (d).

In addition, high resolution TEM (HRTEM) imagery is carried out on the four materials to further define their structural properties, presented in **Figure 2.8**. In both MoWOx cases (**Figure 2.8a,b**), the micrographs of the nanorods (at the surface of the urchins) show the presence of crystalline zones exhibiting fringes perpendicular to the orientation of the nanostructure. However, while the crystallites within a given nanorod appear to all be oriented in the same direction, since the surface of the urchins made of numerous nanorods oriented in all directions, the electronic diffraction pattern appears as a ring. The two MoWOx formulations exhibit interplanar distances of 3.7 Å in good accordance with the interplanar distance of previously reported Mo doped monocliniv $W_{18}O_{49}$ [28,29]. Besides, $WO_{3-\delta}$ 1h and 12h (**Figure 2.8c,d**) display clearly defined hexagonal fringes, that could be expected from the hexagonal morphology of the platelets: measurements results in an interplanar distance of 3.5 Å and angles of 60° degrees between the three planar orientations. This observation is further confirmed by the electronic diffraction spot pattern, indicating the presence of well crystallized and large hexagonal grains in the 12h sample. A similar signal is also observed in $WO_{3-\delta}$ 1h (**Figure 2.8c**), although at weaker intensity: given the small dimensions of the particles, the growth of the crystallites is also limited and the diffraction appears as more faint.

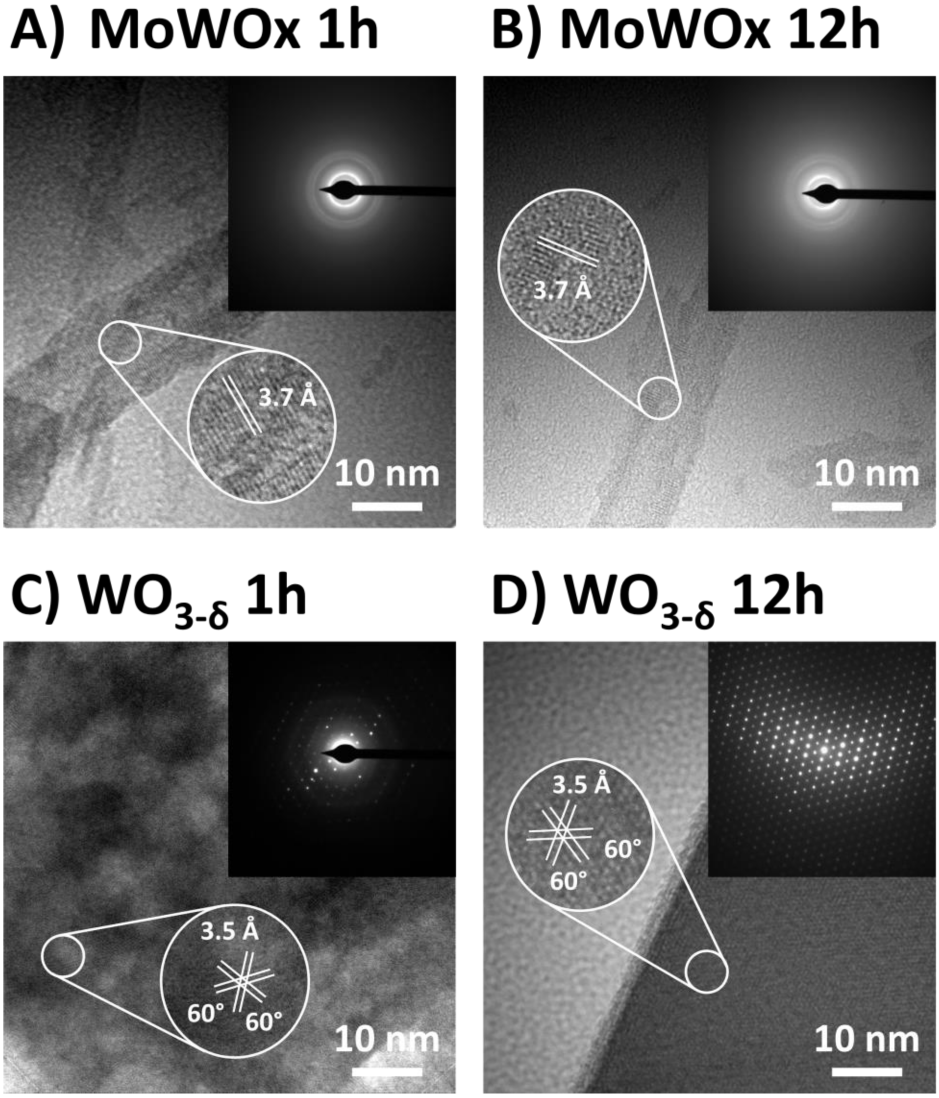

Figure 2.8: High resolution TEM micrographs and electron diffraction patterns as insets of particles of MoWOx 1h (a), MoWOx 12h (b), $WO_{3-\delta}$ 1h (c) and $WO_{3-\delta}$ 12h (d).

XRD characterization of the MoWOx powders (**Figure 2.9**) exhibits only two diffraction peaks at 22.7° and 46.4°, respectively indexed as the (010) and (020) planes of a monoclinic $W_{18}O_{49}$ nanowires pattern (PDF 04-005-4314; cell constants: a = 18.32 Å, b = 3.79 Å, and c = 14.04 Å). The crystallite size of MoWOx 1h and 12h are computed from **Equation 2.1**, exhibiting similar sizes of 16-17 nm. The presence of only two peaks in the same diffraction axis can be correlated to an anisotropic growth of the crystallites alongside the longitudinal axis of the nanowire. Given the preferential growth of nanorods at the surface of the MoWOx particles and diffractograms obtained for these samples, it seems that these outer nanorods are mainly responsible for the crystallinity in the mixed formulations. Since molybdenum rich oxides are obtained for short reaction time, it would seem that the core of the urchins (containing most of the Mo, see EDX discussion above) is mainly amorphous. In addition, the EDX cartography of a MoWOx 1h particle (**Figure 2. 10**) shows an even distribution of the different elements in the core of the urchins, with no formation of large $MoO_{3-\delta}$ segregated grains. This results in only the outermost layer of nanorods appearing as $WO_{3-\delta}$ rich crystallites in the diffractogram while the center of the urchins consists in homogeneous $MoO_{3-\delta}$ rich amorphous material for which no signal is detected in the samples. Besides, the two $WO_{3-\delta}$ compounds can be indexed as a hexagonal diffraction pattern (PDF 04-007-2322), with the difference that $WO_{3-\delta}$ 1h only exhibits part of the diffraction peaks, with weak and broad diffraction signals visible at 23.0°, 28.2°, 36.7°, 50.0° and 55.7° corresponding to the (001), (200), (201), (220) and (202) planes, respectively. The low crystallinity presented by this sample is probably due to the nanometric dimensions of the particles (limiting the crystallite size range that can be reached during the growth of the particles, measured at 30 nm by using Scherrer equation), while the larger $WO_{3-\delta}$ 12h hexagonal platelets can further crystallize during the longer solvothermal treatment they undergo (with an average crystallite size of 49 nm).

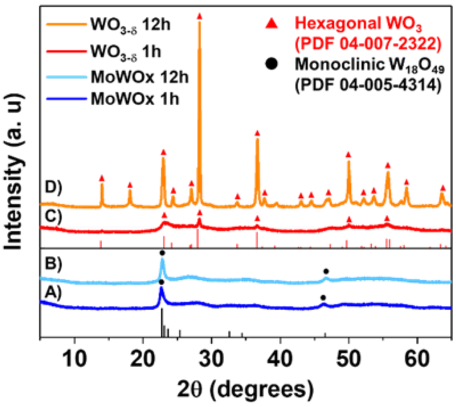

Figure 2.9: XRD diffractograms of MoWOx 1h (a), MoWOx 12h (b), $WO_{3-\delta}$ 1h (c), and $WO_{3-\delta}$ 12h powders (d). The diffraction scans are stacked at regular intervals of 100 counts.

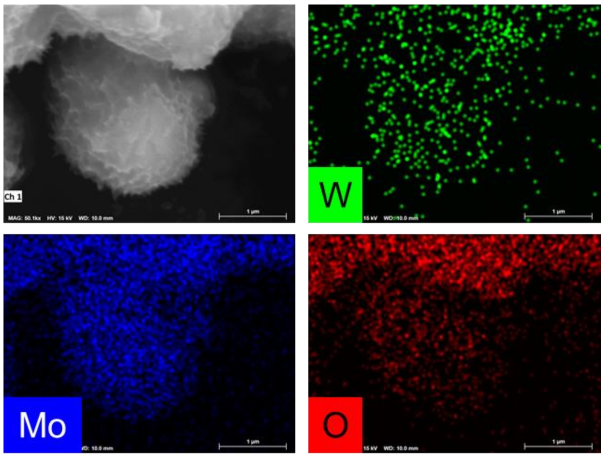

Figure 2. 10: EDX cartography of a MoWOx 1h particle, showing the distribution of W, Mo and O in the synthesized mixed oxide.

2.4. Optical characterizations of MoWOx 2/1 and $WO_{3-\delta}$ powders: application of the Kubelka-Munk theory to plasmonic powder formulations

The main results of this sub-chapter are available as pre-print on (doi.org/10.48550/arXiv.2406.02181) and, by submitting the present thesis manuscript on 17 Dec 2024, are considered for publication (under review in the "ACS Photonics" (ACS) journal.

2.4.1. On the importance of a correct analysis of the optical properties of metal oxides nanostructures

It is obviously essential to evaluate the optical characteristics of the processed metal oxide nanostructures, in particular those anticipated to display plasmonic properties (cf. general introduction). In order for those measurements to be implemented routinely, the characterization of materials as *powders* is a straightforward way of investigating and confirming the expected optical properties without the need of depositing them into *thin films* (or before doing so). Classically, the powders retrieved from the syntheses are dispersed in a solvent and measured by spectrophotometry, using the well-known Beer-Lambert law[30,31] (**Equation 2.1**):

$$\log(I_0/I) = A = \varepsilon l c \tag{2.1}$$

Where I_0 and I are the intensity of the light before and after the sample, respectively, A is the absorbance, ε is the molar attenuation coefficient, l is the length of the optical path and c is the concentration in the attenuating species. In practice, when light passes through a sample of thickness l, part of the electromagnetic intensity is lost and the beam reaches the detection unit with an intensity $I < I_0$ (**Figure 2.11**).

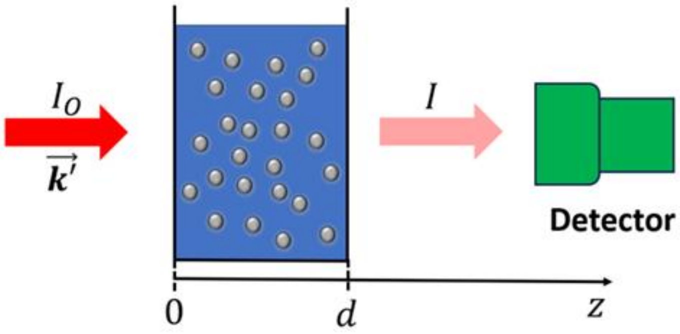

Figure 2.11: Schematic representation of the Beer-Lambert law, describing the absorbance of light by an optically active material in suspension in a solvent[32]*.*

The observed decrease in intensity is due to the extinction cross section of the particles, corresponding to the contribution of both absorption and scattering, responsible for the decrease in the intensity of the emerging light[30,32]. In addition, in the case of plasmonic particles, the diffusive behavior of the material can be neglected if the size of the particles is small in comparison to the wavelength of the plasmonic resonance, leading to the measured response corresponding only to the absorption contribution in the extinction[32]. By plotting the intensity of the resulting beam as a function of the wavelength, the absorption spectra of the material can be obtained. In the case of materials bearing plasmonic features, the maximum absorption corresponds to the plasmon resonance of the material, where the respective frequencies of the incident beam and of the oscillating free charge carriers coincide, resulting in a local enhancement of the electrical field and a large optical absorption[3,33–36].

However, stable suspensions are required for this measurement protocol to yield correct results. If stability conditions are not met in the case of specific materials, owing to their composition, morphology or processing method, the sedimentation of the solids during the characterization fails to provide the optical properties of the studied powders. Additives such as surfactants can be added to the mixture in an attempt to increase the stability of the suspension, or the concentration in solid can be increased in order to promote repulsive interactions between particles. Nevertheless, if tuning the latter parameters does not resolve the stability issues in the suspensions, one way to circumvent these limitations lies in determining the absorption properties of a powder from its diffuse reflectance. Indeed, the direct link between absorption and reflectance is provided by the Kubelka-Munk (KM) formalism[37,38], with the following **Equation 2.2**:

$$KM = \frac{k}{s} = \frac{(1-R_\infty)^2}{2R_\infty} \tag{2.2}$$

With k and s being the absorption and scattering coefficients, respectively, and R_∞ the diffuse reflectance of the sample.

2.4.2. The Kubelka-Munk formalism: state of the art

Historically, the KM model was developed as a non-destructive method for the optical characterization of solid-state samples such as paintings[39]. Due to its ease of use, the KM formalism rapidly spread to other fields of research for the measurement of optical properties in materials such as paper[40,41], pigmented plastics[42] and pigment mixtures such as iron oxide[43], as well as teeth[44,45] and other human tissues[46]. Recently, the method has also been used for the characterization of a range of plasmonic materials, seeking to highlight their plasmon resonance[1,47–50]. However, four main conditions must be met in order to correctly use the KM function[37]:

1) The particles inside the sample should be randomly distributed throughout the layer and should be smaller than the overall thickness of the sample. In practice, these conditions also necessitate that the prepared sample is thick enough so that no light can reach the substrate or sample holder, thus allowing for its reflectance to be negligible;
2) The interactions between particles should be negligible in such way that the system can be considered as a collection of isolated particles;
3) The absorption of the investigated material should not be too strong in order to avoid specular reflections, in particular around the wavelengths corresponding to the plasmon resonance of the sample;
4) For the measured optical signal to be proportional to the absorption coefficient (k) of the material, the diffusion coefficient (s) has to remain constant over the range of measurement.

While the first condition is easily met in practice when preparing the samples, the three others should be considered with care in order to measure the optical properties of the samples correctly.

One way to fulfill those three conditions relies on the dilution of the sample in another powder displaying interesting optical properties. Indeed, by diluting the sample in a low absorption / high diffusion white powder, several conditions are met simultaneously[51]. Mixing the sample with a white diluting agent decreases the intensity of the absorption and thus prevents specular reflectance. In addition, the particles of interest are dispersed in a low absorption media, inhibiting inter-particles interactions and closely resembling the case of isolated particles suspended in a liquid solvent. Finally, as both k and s are wavelength dependent in plasmonic materials, the KM optical characterization of an undiluted plasmonic sample cannot be correlated to its absorption properties, as both coefficients will evolve in the measurement range. Thus, the dilution of the sample allows the fourth condition to be fulfilled, with the diffusion coefficient of the mixture closely equal to that of the diluting agent, which is chosen to be as constant as possible over the whole range of measurement[37]. Therefore, any variation in the optical signal solely results from the absorption coefficient of the sample (given the negligible absorption coefficient of the diluting agent), and the results provided by the KM function can be considered proportional to the absorption properties of the studied material. These effects related to the dilution are described in **Equation 2.3**:

$$KM = \frac{k_{mix}}{s_{mix}} = \frac{k_{sample} + k_{dil}}{s_{sample} + s_{dil}} \cong \frac{k_{sample}}{s_{dil}} \qquad (2.3)$$

With k_{mix}, k_{sample}, k_{dil}, s_{mix}, s_{sample} and s_{dil} corresponding the absorption and diffusion coefficients of the mixture, the active sample and the diluting agent respectively. s_{sample} is considered negligible given the large excess in diluting agent and $k_{dil} \ll k_{sample}$.

Two diluting powders are selected for their non-absorbing properties: $BaSO_4$[52] and LiF[53,54], all demonstrating high and stable diffusion coefficient over a large array of wavelength, as well as low absorption coefficients. These powders can be mixed with the investigated materials in order to satisfy the KM usage conditions cited above. However, when formulating the diluted mixture, it is necessary to reach a compromise in the active sample/diluting agent proportions, with enough active material in order to obtain a measurable signal-to-noise ratio, but not too much in such a way to avoid specular reflections and inter-particles interactions.

As explained earlier in **Chapter 1** (**Section 1.3.1**, page 18), nanoparticles of highly doped – degenerated – semi-conductor can support localized surface plasmon resonance phenomena (LSPR). The plasmon resonance depends on numerous parameters and properties of the particles, namely their shape and aspect ratio, composition, doping rate and how the dopant species are distributed amongst the particle (homogeneous distribution *vs.* segregated as in the case of a core-shell material), inter-particles interaction (coupling) and finally, the dielectric constant κ of the surrounding media[3,34,35]. Indeed, the frequency of the plasmon peak ω_0 is given by **Equation 2.4**:

$$\omega_0 = \frac{\omega_p}{\sqrt{1 + 2\varepsilon_m}} \qquad (2.4)$$

With ω_p, the plasma frequency and ε_m the effective permittivity of the local environment surrounding the particles. There is a direct link between κ and ε_m, as $\kappa = \varepsilon_m/\varepsilon_0$, with ε_0 the permittivity of free space (a constant). Therefore, an increase in the dielectric constant of the direct environment around the particles, and thus an increase in its permittivity, results in a smaller plasmonic frequency ω_0, corresponding to greater wavelengths, described as a red shift as the optical signature is displaced towards the IR range of the spectrum. In the opposite case, if the dielectric constant of the environment decreases, the plasmon frequency increases and the plasmon peak undergoes a blue shift, moving towards smaller values of wavelengths towards the UV region. In addition, the dielectric constant of a material is directly linked to the refractive index through the relation $\kappa = n^2$ (only applicable if both are measured in the same conditions). Therefore, the same conclusions regarding the red/blue shift of the plasmonic frequency can be drawn from an increase/decrease in the refractive index of the material surrounding the investigated particles. By diluting the powders, their environment would change from mainly n_{sample} to n_{dil} corresponding to either diluting agent with $n_{LiF} = 1.39 < n_{BaSO_4} = 1.63$[55,56]. Accordingly, the plasmon resonance of the pure, non-diluted powder and then mixed sample should shift depending on the ratio in diluting agent and its nature.

The measurements are carried out in a spectrophotometer equipped with an integrating sphere. This accessory allows to retrieve the light reflected in any directions from the sample. The setup is schematically represented in **Figure 2.12**, with the sample being placed at the bottom part of the sphere and the incident beam coming from the top aperture, at a 90° angle relative to the surface of the sample. With the detector placed on the side of the integrating sphere, this means that the specular reflectance of the sample exits the sphere from the opening at the top and thus is not considered in the measured signal.

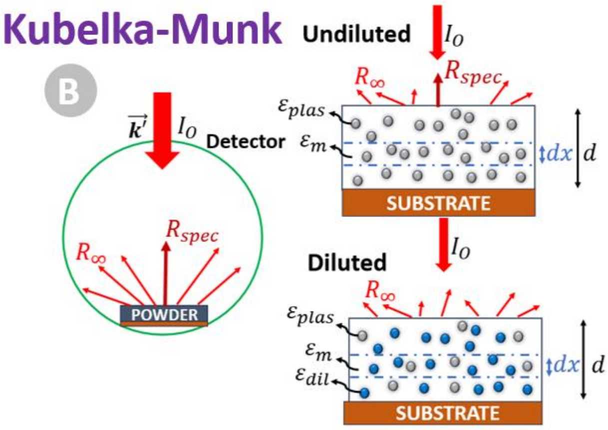

Figure 2.12: Schematic representation of the diffuse reflectance of a sample, in undiluted and diluted conditions[32]*.*

The next sections are therefore discussing the development of a measurement protocol using the KM formalism, for the characterization of solid samples of powders that do not meet the stability requirements for the classical absorption characterization in suspension implementing the Beer-Lambert formula. In this context, the diffuse reflectance of selected plasmonic and non-plasmonic samples is measured and transformed via the KM formula into a response proportional to their absorption coefficient. The samples are measured in diverse dilution conditions in order to rationalize the impact of the diluting agent and of its proportion in the mixture on the optical properties of the active material, in particular plasmonic ones, which depends on the environment surrounding the particles. The application of KM to materials expected to display plasmonic behavior could therefore allow the confirmation of the latter in the investigated formulations, depending on the effect of the dilution on their measured optical response.

2.4.3. Materials and methods

Chemicals. Indium acetate ($In(ac)_3$, 99.99%), tin(II) acetate ($Sn(ac)_2$), oleylamine (technical grade, 70%), oleic acid (technical grade, 90%) and barium sulfate ($BaSO_4$, 99%+) were purchased from Sigma-Aldrich. Reagent alcohol (ethanol 88-91%, methanol 4.0-5.0%, isopropyl alcohol 4.5-5.5%) and toluene (≥ 99.5%) were purchased from Fisher Scientific. Lithium fluoride (LiF, 99.8% anhydrous) is purchased from ROC/RIC. All chemicals were used as received without further purification.

Synthesis of $Mo_yW_{1-y}O_{3-\delta}$, $MoO_{3-\delta}$ and $WO_{3-\delta}$ compounds. The investigated formulations are produced according to the protocol discussed earlier in **Section 2.3.1**, page 45.

Sample preparation. 30 mg of active material ($MoO_{3-\delta}$, $WO_{3-\delta}$ or MoWOx) are used as the pure powder or mixed with one of the prospected diluting agent, preparing enough powder to fill the sample holder used for the measurement. The mixture is placed in the holder and the excess powder is removed with a glass slide in order to leave the powder as an even layer, level with the edge of the holder.

Sample characterization. The diffuse reflectance of the mixed samples is carried out on a Shimadzu UV-3600i spectrophotometer, equipped with an ISR-1503 integrating sphere. The sample holder is placed at the bottom of the sphere and the diffuse reflectance is measured between 350 and 1650 nm. The reflectance value at any given wavelength is replaced in **Equation 2.2** in order to obtain the KM spectra proportional to the absorption of the active material.

2.4.4. Experimental characterizations

a. Characterization of the diluting agent

In order to properly fulfill the conditions of the KM formalism, the analyte should first be diluted in a white powder having a high diffusion coefficient that remains constant over the whole measurement range. In order to evaluate the two selected diluting agents, their diffuse reflectance is measured between 350 and 1650 nm, with a pellet of the reflective coating covering the inside of the sphere used the 100% reflectance reference. The results, shown in **Figure 2.13**, highlight the consistency of $BaSO_4$, with a reflectance close to 100% in most of the studied range. LiF also displays high reflectance, however not as constant as $BaSO_4$, with the LiF signal globally increasing when the wavelength increases. This is expected from the fact that the inside of the integrating sphere is covered in a layer of $BaSO_4$, therefore, this diluting agent will automatically exhibit greater reflectance and stability in comparison to LiF and to any other formulation of white powder. Nonetheless, both powders have shown promising optical properties for their application as diluting agent in the scope of absorption measurement using the KM formula, with diffuse reflectance exceeding 80%R in most of the measurement interval with no significant peaks, testifying for their great diffusion coefficient and very low absorption coefficient. With the diluting agents now identified and validated, the remainder of this section will focus on the characterization of the active materials, either plasmonic or non-plasmonic.

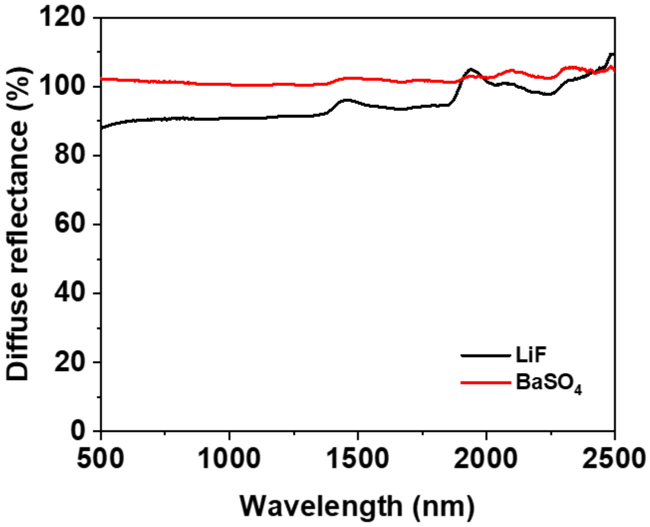

Figure 2.13: Diffuse reflectance signals of the two selected diluting agents, LiF and BaSO$_4$.

b. Reproduction of the literature and rationalization of the dilution

The five formulations initially discussed in the work of Yamashita *et al.* are reproduced for their optical properties to be investigated according to the synthetic protocol reported by the authors[1,2] and presented in **Section 2.3.1**, page 45 of this work. **Figure 2.14a** below shows the optical response of the two parent oxides as well as the best MoWOx formulation identified by Yamashita (MoWOx 1/1) as pure powders, further reproducing the results presented in the literature (**Figure 2.14b**).

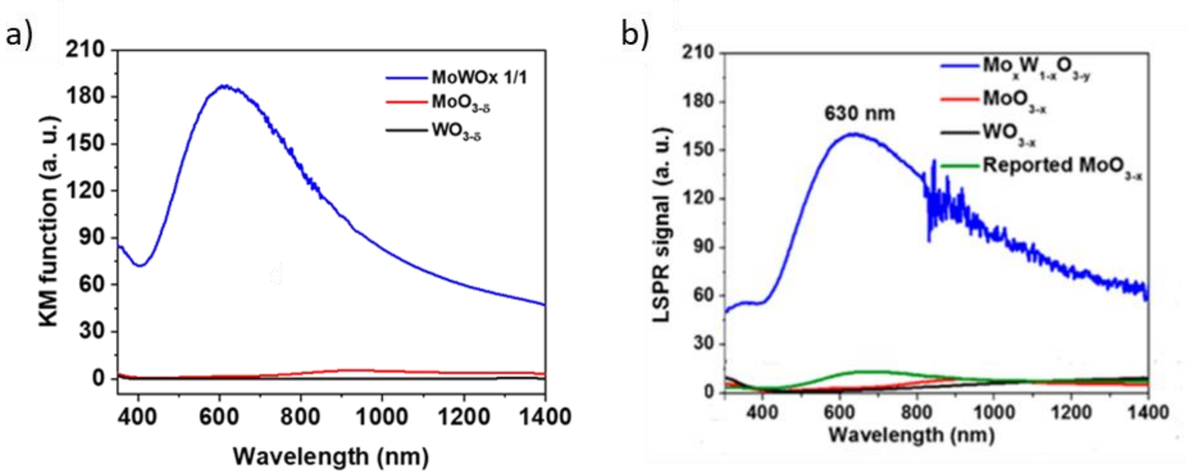

Figure 2.14: KM function obtained from the diffuse reflectance data of MoWOx 1/1 and the two parent oxides (WO$_{3-\delta}$ and MoO$_{3-\delta}$), after 12h of synthesis (a), in comparison to the optical results reported in the work of Yamashita et al (b)[1].

However, as introduced beforehand, the use of the KM formalism should be implemented carefully in order to fulfill the conditions of the model. By measuring the pure powders, inter-particles interactions are promoted and the specular reflectance could arise from the large absorption coefficient of the pure powders, especially for the MoWOx formulations, displaying a dark blue, almost black coloration, indicating great optical absorption properties (cf. **Figure 2.6**). In addition, as the diffusion coefficient of the material might not be constant over the wavelength range being considered here, the KM spectra retrieved from the measurement cannot be considered as proportional to the absorption coefficient of the material. Therefore, so to meet all the conditions required for the accurate use of the KM formalism, diluted samples are prepared by diluting each of the five formulations in LiF, in an initial m_{LiF}/m_{sample} ratio of 100/10. In the context of these preliminary optical results, LiF is selected for its ease of use, demonstrating much less electrostatic charging in comparison to $BaSO_4$, while a 10% dilution rate is selected as a practical “starting compromise” allowing to maximize the signal-to-noise ratio while fully respecting the KM conditions, *i.e.* by avoiding a too high absorption coefficient as well as interactions between the active particles.

The corresponding spectra are presented in **Figure 2.15** and highlight how important it is to take in account the limitations of the KM model, as the intensity, position and shape of the optical signature of the five formulations are significantly impacted by the dilution in a white powder. While the change in intensity clearly arises from the dilution (the amount of optically active particles decreases in the whole probed volume, replaced by the diluting agent), the shift in the optical signature could be due to the modification of the local environment of the particles, shifting from being surrounded in majority by other particles of the same formulation, to being surrounded almost exclusively by LiF, with the change in refractive index resulting in a redshift of the plasmon resonance. While the effect of the dilution is clearly visible on the optical properties of the MoWOx formulations, the parent oxides are not as affected, probably as they better meet the KM conditions because of their intrinsic properties. Indeed, the powders initially present a low absorption coefficient, even as pure powders, exhibiting a light blue tint for $MoO_{3-\delta}$ and a grey, almost white, coloration for $WO_{3-\delta}$. These first results clearly highlight the care that must be taken in order to use and interpret KM optical characterization, which is not done in most of the current literature exploiting KM measurements. The collaboration between the Universities of Liège and Namur in the scope of the FNRS research project “PLASMON_EC”, to which this thesis is connected, thus provides great benefits combining both physical and chemical approaches and visions of a same problem.

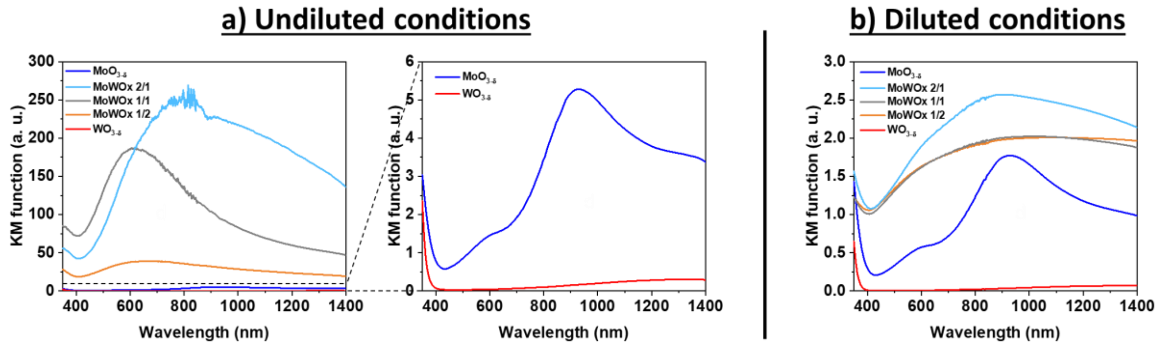

Figure 2.15: KM function obtained from the diffuse reflectance data of the three MoWOx formulations and both parent oxides after 12h of synthesis, (a) in undiluted conditions (with an insert focusing on the parent formulations) and (b) diluted in LiF in a LiF/sample ratio of 100/10.

c. *Application of the progressive dilution method to the selected formulations on interest: MoWOx 1h, 12h*

With the importance of the dilution being established, the KM model is now investigated as a mean of characterizing the presence of plasmonic features in a given material. Further exploration of the effect of the nature and concentration of the diluting agent on the optical properties of the powders is detailly discussed in an article published in collaboration with Prof. Henrard and Dr. Lobet from UNamur[32]. Briefly, in this paper, the influence of the diluting agent on the optical response of plasmonic materials could be highlighted. As expected from the discussion in **Section 2.4.2**, page 53, the plasma frequency of a plasmonic material depends (amongst other parameters) on the refractive index of the environment surrounding the particles. Testing our MoWOx formulations in comparison to plasmonic and non-plasmonic reference materials (ITO and commercial WO_3, respectively – corresponding details are discussed in-depth in the arxiv pre-print[32]), it was possible to demonstrate a similar behavior between our mixed oxide and the plasmonic ITO. Indeed, as the surrounding refractive index evolved from $n_{air} = 1$ to $n_{LiF} = 1.39$, and then $n_{BaSO_4} = 1.63$, the optical signal shifted towards greater wavelength, while nothing was observed in the non-plasmonic reference.

In order to deepen our understanding of the mechanisms at the origin of the shift observed in diluted plasmonic materials, progressive dilution measurements are then carried out on the previously studied ITO as the plasmonic reference. As expected, the ITO spectra exhibit a strong red shift as a function of the dilution in LiF. In addition to the shift of the signal, the peaks become wider and the intensity drops (as the absolute amount of active material decreases when dilution increases). To further validate our experimental observations, the behavior of state-of-the-art ITO has been theoretically modeled by Prof. Luc Henrard's team (UNamur). The resulting spectra demonstrate a very good agreement between experimental and theoretical data, solidifying the importance of dilution to highlight plasmonic behaviors in powder samples.

With the progressive dilution protocol developed and validated for the ITO plasmonic reference, it can now be applied to other formulations to better understand the effect of dilution on their optical properties and prove (or not) the occurrence of plasmonic phenomena in the latter. Two configurations are selected to this end: MoWOx 2/1 synthesized for 1h or 12h (chosen as formulations of interest, see discussions in **Section 2.3.1,** page 45)

In the KM optical spectra of both MoWOx samples (**Figure 2.16**), a clear shift is observed upon dilution in LiF, however, this shift seems to be exclusive to the right shoulder of the peak. The difference in behavior originating from different part of the spectra could indicate the presence of multiple contributions of different natures in the signal of the mixed oxides, as reported in previous works of the literature[57–59]. Upon mathematical fitting of the spectral curves (**Figure 2.17**), two contributions are highlighted, with the first one located around 750 – 850 nm in both case and a second one around 1000 – 1300 nm for MoWOx 2/1 1h and 1000 – 1900 nm in the case of its 12h counterpart. Since the rightmost peak shifts when the sample is diluted, the plasmonic response of the materials is assigned to this contribution. In addition, the plasmonic feature of MoWOx 2/1 12h is obviously located further into the NIR in comparison to MoWOx 2/1 1h, which could be due to the formation of larger particles with increasing synthesis duration, resulting in a red shift of the plasma frequency[3,60–62]. On the other hand, the signal closer to the visible range probably corresponds to a polaronic absorption behavior occurring in the mixed oxides, being caused by the presence of reduced species created during the synthesis, as reported by Yamashita *et al*[1].

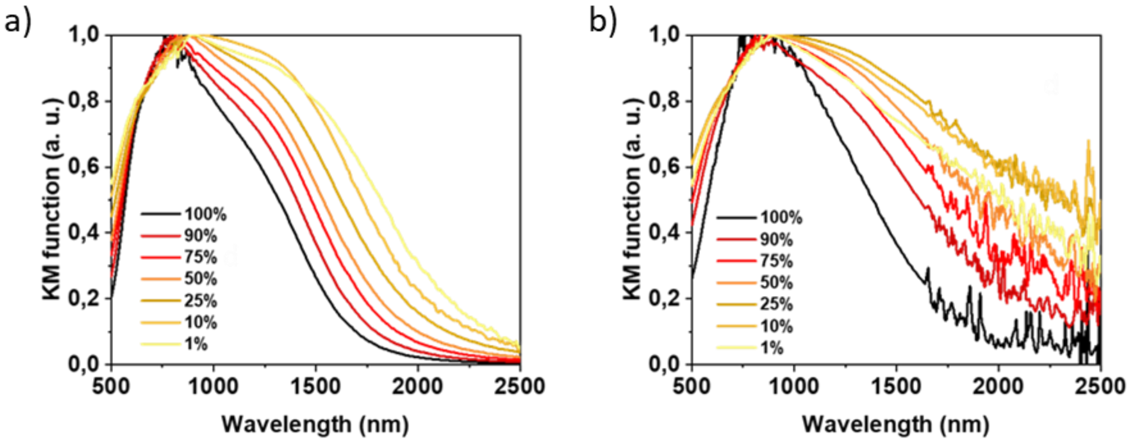

Figure 2.16: KM optical behavior of MoWOx 2/1 1h (a) and MoWOx 2/1 12h powders (b) as a function of their progressive dilution in LiF.

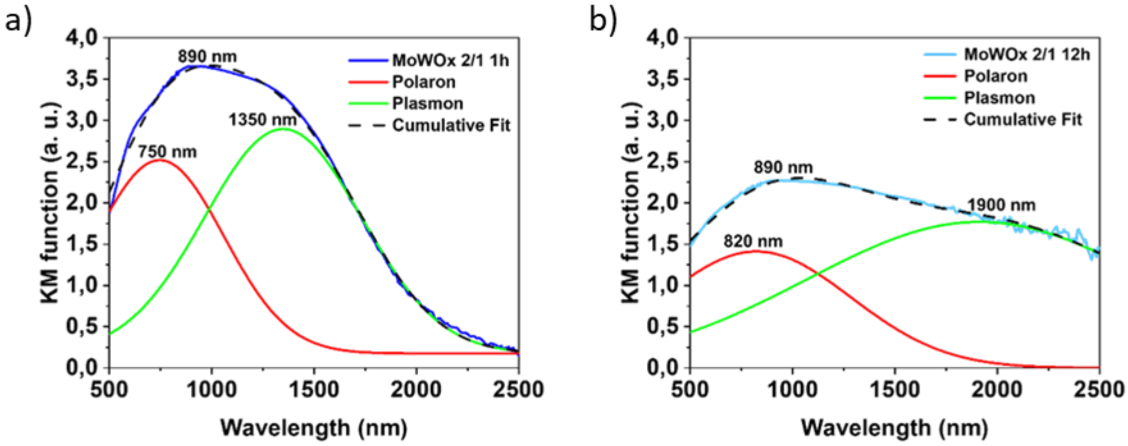

Figure 2.17: Mathematical fitting of the KM optical signals of MoWOx 2/1 1h (a) and MoWOx 2/1 12h (b), diluted in LiF in a 100/10 LiF/sample ratio.

With the plasmonic behavior of the MoWOx powders being now highlighted from the dilution experiments carried out in the previous section above, the mixed samples are compared to their $WO_{3-\delta}$ parent oxides. The KM optical characterization of the four powders, diluted in LiF (10% wt., **Figure 2.18**), show a strong increase in the absorption of the Mo-W mixed oxides formulations in comparison to parent $WO_{3-\delta}$ ones, as expected from previous studies[1,2], but also a more intense absorption signal in both $WO_{3-\delta}$ 1h and MoWOx 1h than for their 12h counterparts. As discussed previously, the absorption signature of MoWOx samples could be interpreted as a superposition of polaronic and plasmonic absorption contributions, as previously reported in the literature[57–59]. For the $WO_{3-\delta}$ parent oxides, the signal can be interpreted as a single contribution at 1470 nm in the 1h case, corresponding to a plasmonic resonance as reported in selected literature[57–59], but also consistent with a polaronic signature of thin films[63], reminiscent of the lack of consensus on the dual band charge/discharge model, as discussed in the introduction. Meanwhile, no apparent peak is observed for $WO_{3-\delta}$ 12h.

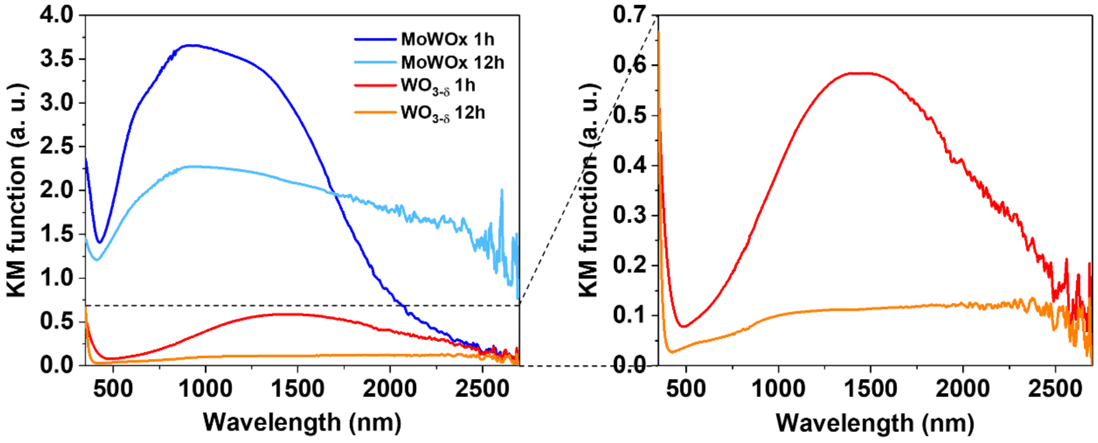

Figure 2.18: KM function obtained from diffuse reflectance data of the MoWOx 1h, MoWOx 12h, $WO_{3-\delta}$ 1h, and $WO_{3-\delta}$ 12h powders (all being diluted in LiF).

2.4.5. Conclusions on the use of the Kubelka-Munk formalism

In this sub-section (and the related article available as pre-print on arxiv and **currently considered for publication** in ACS Photonics), the Kubelka-Munk formalism has been evaluated as a characterization method allowing the detection of plasmonic features in solid samples, focusing on formulations based on molybdenum-tungsten oxides. This method is of great utility when working with materials that do not fulfill the stability conditions required for the classical Beer-Lambert absorption measurement, as a dispersion in a solvent. However, for the measured results to be valid, the KM formalism depends on several conditions, easily fulfilled via dilution of the sample in a highly diffusive white powder[37]. The result presented above highlight the importance of the correct use of the KM theory, with large variations in the optical response of materials in diluted and non-diluted conditions.

Herein, the plasmonic behavior of the investigated MoWOx formulations could be demonstrated by varying the nature and concentration of the surrounding media, resulting in a red shift and loss of intensity of the signal, further confirmed in the case of ITO as plasmonic reference. These results prove the strength of the KM formula in determining the optical properties of solid formulations, and additionally, highlighting the presence of plasmonic features. Theoretical modelling of the investigated particles even allows to predict the position of the LSPR peak as the shape of the particle or the nature of the environment changes.

While this method is very useful for the optical characterization of investigated materials, the latter is only valid if the conditions of the KM model are met. This work demonstrates the possibility to use the KM method for the optical characterization of semiconductor materials bearing plasmonic properties, filling a gap in the literature, as the KM theory has never been investigated as an appropriate method to highlight the presence of plasmonic response in materials. In addition, this aim of this work is to further insist on use of the KM formalism in correct conditions, as to avoid the report of erroneous results which could have been easily avoided.

The results reported in this work are promising for the future use of the KM method in the scope of plasmonic materials investigation, either for NIR-selective or dual-band electrochromic applications, but also for other plasmonic optoelectronic applications such as catalysis or water splitting.

2.5. Electronic properties of “MoWOx” 2/1 and $WO_{3-\delta}$ powders

2.5.1. XPS characterization (achieved in collaboration with UNamur – Dr. Rachel Gouttebaron)

Given the optical results in **Figure 2.18**, more oxygen vacancies and reduced species are likely formed in the mixed formulations, and at the beginning of the thermal treatment (with greater absorption signals in the 1h samples in comparison to the 12h ones). This may owe to the properties of the isopropanol solvent (proton donor and reducing agent[64,65]), that could lead to the possible insertion of H^+ in the crystal lattice, and electrons (either free or localized over W^{5+} and Mo^{5+} species) to retain the charge neutrality. In addition, the substitution of Mo in the WO_3 octahedral sites of the MoWOx (and *vice versa* of W in the MoO_3 sites) could induce strains and the formation of defects, consecutively modifying the electronic and optical properties by creating color center (or polaronic) states and changing the band gap of the material[1,66,67]. As a consequence, the synergistic formation of both reduced species and free electrons originating from the creation of oxygen vacancies can lead to a significant boost in the optical properties of the MoWOx formulations in comparison to the parent oxides. In a second step, the particles could be partially re-oxidized during the remainder of the reaction time, due to their prolonged contact with the H_2O_2 reagent present in the synthetic media, resulting in the 1h samples exhibiting a greater absorption signal than their 12h counterparts.

So to confirm the preliminary assumptions on free electron density made from these optical results, XPS analysis is first performed to evaluate the composition and oxidation states at the surface of the different compounds (**Figure 2.19** and **Table 2.2**). Regarding molybdenum, both oxidized Mo^{6+} and reduced Mo^{5+} species are identified in MoWOx 1h and 12h as doublet contributions on Mo3d signals, respectively at 233.6 / 236.8 eV and 232.4 / 235.5 eV. For tungsten, only W^{6+} (and thus no W^{5+}) appears upon fitting of the W4f signals (doublet at 36.4 / 38.5 eV), highlighting the preferential trapping of the electrons over the molybdenum metallic centers at the surface of the particles[68–70]. The significant presence of reduced species is concomitant with the formation of oxygen defects in the crystal lattice, with some of the excess in electrons left from the missing oxygen trapped by metal atoms[1,28,69,71]. In addition, and even though this interpretation might be subject to much debate in the XPS field[72], the presence of oxygen vacancies (O_{vac}) could be supposed from the O1s signal with a contribution at 532.6 eV, which also appears to be of the same intensity between both formulations. These results show very similar electronic surface properties in the mixed oxides regardless of the time under solvothermal treatment, however, since the XPS only probes the surface of the particles, the differences observed in the optical properties could arise from the bulk of the particles. As for the $WO_{3-\delta}$ parent oxide, a significant proportion of the W metallic centers are found to be in the W^{5+} state. Regarding O1s, the $WO_{3-\delta}$ 1h exhibits similar amounts of O_{vac} to those found in the mixed oxide samples, while the same contribution in the 12h formulation is found to be significantly less intense. In addition, the signal at 533.5 eV corresponds to weakly adsorbed C-O and O-H organic species. The greater contribution of the latter in $WO_{3-\delta}$ 12h could indicate favorable crystalline faces at the surface of the hexagonal platelets, leading to a greater adsorption of organic impurities on the outer layer of the particles. For semiconductor materials such as the $WO_{3-\delta}$ materials investigated in this work to support plasmonic features, it is necessary that their concentration in free charge carriers increases beyond a threshold after which the material undergoes a transition to a degenerated semiconductor displaying a metallic behavior[36,73,74]. All four investigated formulations support a large amount of reduced species and O_{vac}, leading to an oxygen substoichiometry that allows the WO_3-based materials to support LSPR features[54]. That said, the lower concentration in reduced species and O_{vac} obtained for

$WO_{3-\delta}$ 12h in comparison with the other formulations, as well as the large dimensions of the hexagonal particles (~2 µm), could limit their use as efficient plasmonic electrochromic materials. Finally, Mo/W ratios are calculated, showing again that molybdenum-rich compositions are obtained for short-duration syntheses, with 3.7 and 1.6 Mo/W ratios determined for 1h and 12h, respectively, starting from a 2/1 ratio of Mo/W precursors in the reactive media. These results confirm that faster reaction kinetics occur for the Mo species, leading to a gradient going from the center of the urchins to the outer layer of surface nanorods. Noteworthy, Mo/W ratios calculated from XPS are slightly smaller than EDX ones (see **Figure 2.5**), being of 4.7 and 2.0 for 1h and 12h by EDX, respectively. Since the XPS only probes the surface of the material, in comparison to the depth of analysis in the EDX measurements giving access to the bulk of the particles, XPS ratios are logically smaller than EDX ones, further confirming the concentric distribution of the Mo within the mixed oxide particles.

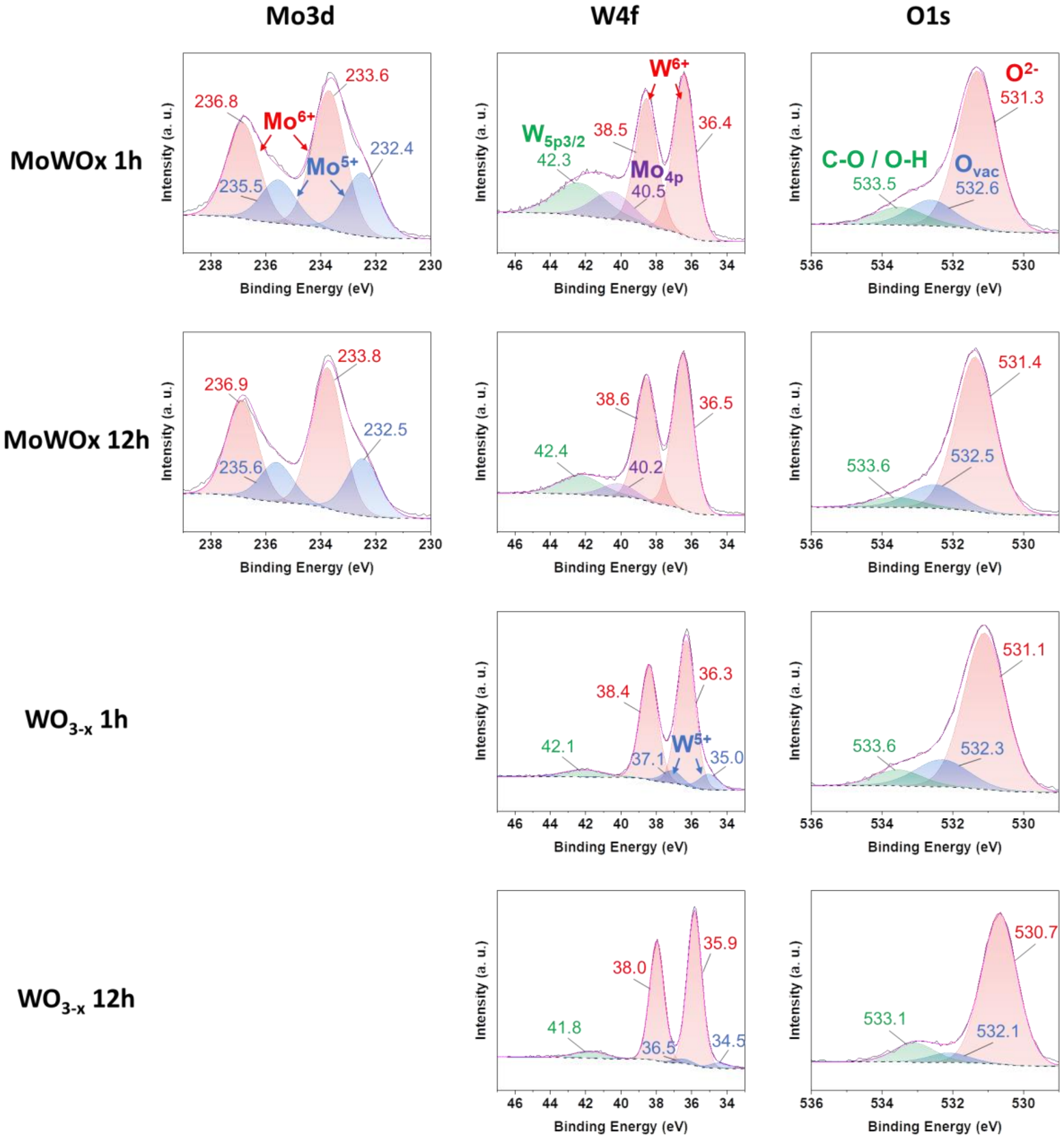

Figure 2.19: Mo3d, W4f and O1s XPS spectra of the MoWOx 1h, MoWOx 12h, $WO_{3-\delta}$ 1h, and $WO_{3-\delta}$ 12h powders.

Table 2.2: Summary of the XPS data of MoWOx 1h, MoWOx 12h, $WO_{3-\delta}$ 1h and $WO_{3-\delta}$ 12h.

	Duration	Mo/W $_{EDX}$	Mo/W $_{XPS}$	Proportion Mo^{sub6+} (%)	Proportion W^{sub6+} (%)
MoWOx	1h	4.7	3.7	0.32	Only W^{6+}
MoWOx	12h	2.0	1.6	0.27	Only W^{6+}
$WO_{3-\delta}$	1h	/	/	/	0.11
$WO_{3-\delta}$	12h	/	/	/	0.05

2.5.2. EPR characterization (achieved in collaboration with ICMCB – Dr. Matthieu Duttine)

EPR characterization is then carried out to assess the presence of free electrons, not only at the surface (as it is the case with XPS) but also in the bulk of the materials. This method allows the detection of unpaired electrons such as those trapped in the oxygen vacancies, those localized over reduced species such as W^{5+} ($5d^1$, $g \leq 1.9$) and Mo^{5+} ($4d^1$, $g \geq 1.9$) or those delocalized into the conduction band ($g < 2$). All four samples show large and well-defined signals below g-values of 2 (**Figure 2.20**), indicating that the electrons freed by the formation of oxygen vacancies during the synthesis are either preferentially localized over metallic ions (yielding Mo^{5+} and W^{5+} reduced species), or delocalized into the conduction band to participate to the free charge carrier concentration. If the electrons were to be trapped inside the vacancies, the measured EPR response would rather appear as a very narrow signal, centered around a g-value close to 2.0023 corresponding to the free electron in vacuum (cf. dashed line in **Figure 2.20a**). The absolute concentration in all paramagnetic species, regardless of the proportion in the different elements (either reduced Mo or W, or free electrons in the conduction band), is proportional to the number of spins in the samples and to the area under the EPR absorption curves (**Figure 2.20b**) calculated by integration. Thus, the double integration of the EPR spectra follows a trend regarding the concentration in reduced species and free electrons in the conduction band: MoWOx 1h > MoWOx 12h > $WO_{3-\delta}$ 1h > $WO_{3-\delta}$ 12h (cf. **Figure 2.20b** and **Table 2.3**), in good agreement with the ranking of optical absorption intensity (see **Figure 2.18**). In the bulk, MoWOx 12h has therefore 45% less reduced species and free conducting electrons than its 1h counterpart, while the signal of $WO_{3-\delta}$ 1h and 12h only represents 11% and 7% of that measured in the MoWOx 1h case.

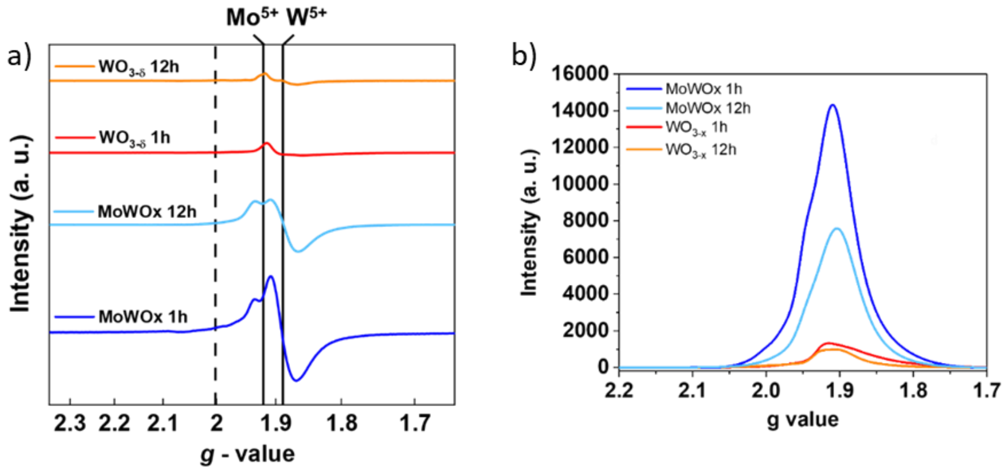

Figure 2.20: Low temperature (4K) X-band EPR spectra of the MoWOx 1h, MoWOx 12h, $WO_{3-\delta}$ 1h and $WO_{3-\delta}$ 12h powders (a) and integration of the area under the curves (b).

Table 2.3: Integrated areas corresponding to the area under the $WO_{3-\delta}$ and MoWOx EPR absorption curves.

		Integrated Area	Normalized Integrated Area (%)
MoWOx	1h	227 900	100.0
MoWOx	12h	122 400	54.9
WO_{3-X}	1h	25 500	11.2
WO_{3-X}	12h	16 200	7.1

All in all, there is a globally good match between XPS and EPR electronic measurements, and also with the UV-VIS-NIR optical results presented above. The presence of a higher quantity in free charge carriers delocalized in the conduction band or localized on reduced species, whether at the surface or in the bulk of the materials, seems to translate into an increased absorption of the particles.

2.6. Conclusions and perspectives

In this chapter, several pure and mixed oxide formulations were characterized as powder samples to evaluate their potential as plasmonic electrochromic materials. Upon preliminary characterization, four formulations of interest are selected: MoWOx 2/1 after 1h and 12h of synthesis, and the $WO_{3-\delta}$ parent oxide, synthesized for the same two durations. The powders are characterized for their morphological, structural, optical and electronic properties.

The morphological assessment of the formulations highlights the presence of nanostructures in all formulations, required for the support of LSPR features. Besides, the optical measurement of the samples shows the expected increase in intensity of the mixed oxide materials in comparison to the pure tungsten parent oxides, already reported in the literature for their plasmonic and dual-band behavior. The Kubelka-Munk characterization of the two MoWOx formulations in environments of varying permittivity proves the plasmonic properties of these nascent materials, never exploited before as electrochromic compounds. The obtained results show a good agreement between the experiment and theory, with general enough results to hopefully be applied to other materials, shape and nanostructures. The model developed by Prof. Henrard's team could allow the prediction of the plasmonic features of a given material with a known morphology. However, this model is only relevant for simple morphologies at the moment, with the properties of ITO nanospheres easily reproduced while those of the peculiar urchin-like MoWOx particles could not be modelled efficiently enough to represent their plasmonic properties (the large number of nanorods at the surface of the urchins would require a large amount of computing power).

The composition, surface state and electronic properties of all four formulations are also investigated to better understand the origin of the boost in optical intensity for the MoWOx compounds. These measurements demonstrate the large presence of oxygen vacancies and reduced species through the whole particles (in the bulk via EPR and at the surface using XPS), respectively responsible for a greater concentration in free charge carriers allowing plasmonic features, and more electronic transitions enhancing the polaronic response of the materials.

Altogether, these results highlight improved optoelectronic properties in the investigated MoWOx formulations, in comparison to the $WO_{3-\delta}$ parent oxide. With the latter widely reported as an efficient dual-band plasmonic electrochromic material, the MoWOx materials (and especially MoWOx 2/1 1h) are expected to display good electrochromic performances across both VIS and NIR regions, while allowing the selective and independent control of both spectral ranges.

However, these assumptions are based on the characterization of the powders only, and are therefore not (yet) correlated to their expected electrochromic properties. The best – and unique – way to determine and compare the electrochromic performances of the four selected formulations will be through their deposition as thin films on top of conductive substrates and their ensuing spectroelectrochemical characterization. Measuring the evolution of their optical properties as a function of an applied potential will enable the demonstration of an electrochromic activity and in particular the occurrence of the sought for three working states (bright, cool and dark).

In future works, the up-scaling of the solvothermal synthesis of MoWOx formulations should be addressed, especially since the necessary equipment is available at the GREEnMat (large liter-scale reactor). However, the current yield of the synthesis – being stopped before all of the precursors have reacted – is too low to consider larger scale production. Moreover, the addition of new elements, such as the presence of a stirring blade, would further require the re-optimization of the synthetic parameters.

2.7. References

1. Yin, H. *et al. J. Phys. Chem. C* **2017**, 121, 23531, doi.org/10.1021/acs.jpcc.7b08403.
2. Yin, H. *et al. J. Mater. Chem. A* **2018**, 6, 10932, doi.org/10.1039/c8ta03125h.
3. Agrawal, A. *et al. Chem. Rev.* **2018**, 118, 3121, doi.org/10.1021/acs.chemrev.7b00613.
4. Maho, A. *et al. Sol. Energy Mater. Sol. Cells* **2019**, 200, 110014, doi.org/10.1016/j.solmat.2019.110014.
5. Li, Y. *et al. ACS Appl. Nano Mater.* **2018**, 1, 2552, doi.org/10.1021/acsanm.8b00190.
6. Šutka, A. *et al. RSC Adv.* **2015**, 5, 63846, doi.org/10.1039/c5ra11910c.
7. Nilofar, A. *et al. Int. J. Photoenergy* **2014**, 2014, 1, doi.org/10.1155/2014/518156.
8. Cheng, Y. *et al. Adv. Mater. Res.* **2011**, 284, 1014, doi.org/10.4028/www.scientific.net/AMR.284-286.1014.
9. Hiroshiba, N. *et al. Trans. Mat. Res. Soc. Japan* **2014**, 39, 423, doi.org/10.14723/tmrsj.39.423.
10. Cheng, H. *et al. Angew. Chemie* **2014**, 126, 2954, doi.org/10.1002/ange.201309759.
11. Chen, Y. *et al. Ceram. Int.* **2023**, 49, 29534, doi.org/10.1016/j.ceramint.2023.06.143.
12. Liang, L. *et al. Chem. Eng. J.* **2022**, 428, 131139, doi.org/10.1016/j.cej.2021.131139.
13. Wang, Y. *et al. Small* **2017**, 13, 1603689, doi.org/10.1002/smll.201603689.
14. Wang, B. B. *et al. J. Alloys Compd.* **2021**, 854, 157249, doi.org/10.1016/j.jallcom.2020.157249.
15. Li, G. *et al. Nanoscale* **2016**, 8, 9861, doi.org/10.1039/c5nr09147k.
16. Park, S. *et al. Sol. Energy Mater. Sol. Cells* **2022**, 242, 111759, doi.org/10.1016/j.solmat.2022.111759.
17. Liu, Y. *et al. CrystEngComm* **2014**, 16, 7493, doi.org/10.1039/c4ce00857j.
18. Zhan, Y. *et al. Nanoscale* **2018**, 10, 5997, doi.org/10.1039/c8nr00413g.
19. Cong, S. *et al. Adv. Mater.* **2014**, 26, 4260, doi.org/10.1002/adma.201400447.
20. Duan, G. *et al. Chem. Res. Toxicol.* 2019, **32**, 1357, doi.org/10.1021/acs.chemrestox.8b00399.
21. Prusty, G. *et al. J. Am. Chem. Soc.* **2020**, 142, 5938, doi.org/10.1021/jacs.9b13909.
22. https://www.deheerbv.com/products/premex-high-pressure-autoclaves/hyper, accessed on 19/09/2024.
23. Kondalkar, V. V. *et al. Superlattices Microstruct.* **2014**, 73, 290, doi.org/10.1016/j.spmi.2014.05.039.
24. Wang, B. *et al. Particuology* **2024**, 84, 72, doi.org/10.1016/j.partic.2023.03.007.
25. Putthithanas, P. *et al. Mater. Sci. Forum* **2020**, 1007, 148, doi.org/10.4028/www.scientific.net/msf.1007.148.
26. https://www.parrinst.com/products/sample-preparation/acid-digestion/high-pressure-acid-digestion-vessel-models-4746-4747-23-ml/, accessed on 12/09/2024.
27. Li, Q. *et al. J. Mater. Sci.* **2019**, 54, 2918, doi.org/10.1007/s10853-018-3050-5.

28. Zhang, N. *et al*. *J. Am. Chem. Soc.* **2018**, 140, 9434, doi.org/10.1021/jacs.8b02076.

29. Li, P. *et al*. *ACS Appl. Mater. Interfaces* **2020**, 12, 19153, doi.org/10.1021/acsami.0c00220.

30. Bohren, C. F. & Huffman, D. R. Absorption and Scattering of Light by Small Particles (published by Wiley-VCH, **1998**).

31. Mayerhöfer, T. G. *et al*. *ChemPhysChem* **2020**, 21, 1218, doi.org/10.1002/cphc.202000301.

32. Lobet, M. *et al. (Preprint) arXiv:*2406.02181, v1, submitted: Jun **2024**. https://arxiv.org/abs/2406.02181.

33. Wang, Y. *et al*. *Annu. Rev. Chem. Biomol. Eng* **2016**, 7, 283, doi.org/10.1146/annurev-chembioeng-080615-034647.

34. Runnerstrom, E. L. *et al*. *Chem. Commun.* **2014**, 50, 10555, doi.org/10.1039/c4cc03109a.

35. Tandon, B. *et al*. *J. Phys. Chem. C* **2022**, 126, 9228, doi.org/10.1021/acs.jpcc.2c02155.

36. Runnerstrom, E. L. Charge Transport in Metal Oxide Nanocrystal-Based Materials. (University of California, Berkeley, **2016**).

37. Kortüm, G. *Reflectance Spectroscopy: Principles, Methods, Applications*. (published by Springer Science, **1970**).

38. Bourdin, M. *et al*. *J. Alloys Compd.* **2020**, 823, 153690, doi.org/10.1016/j.jallcom.2020.153690.

39. Kubelka, P. & Munk, F. *Zeitschrift für Tech. Phys.* **1931**, 12, 593.

40. Džimbeg-Malčić, V., Barbarić-Mikočević, Ž. & Itrić, K. *Tehnički vjesnik* **2011**, 18, 117, https://www.researchgate.net/publication/279555806.

41. Džimbeg-Malčić, V., Barbarić-Mikočević, Ž. & Itrić, K. *Tehnički vjesnik* **2012**, 19, 191, https://hrcak.srce.hr/file/117668.

42. Saunderson, J. L. *JOSA,* **1942**, 32, 727, doi.org/10.1364/josa.32.000727.

43. Barron, V. *et al*. *J. Soil Sci.* **1986**, 37, 499, doi.org/10.1111/j.1365-2389.1986.tb00382.x.

44. Ragain, J. C. *et al*. *J. Dent. Res.* **2001**, 80, 449, doi.org/10.1177/00220345010800020901.

45. Mikhail, S. S. *et al*. *Dent. Mater.* **2012**, 28, 729, doi.org/10.1016/j.dental.2012.03.006.

46. Van Gemert, M. J. C. *et al*. *Lasers Med. Sci.* **1987**, 2, 295, doi.org/10.1007/bf02594174.

47. Pathak, T. K. *et al*. *Phys. B Condens. Matter* **2018**, 535, 114, doi.org/10.1016/j.physb.2017.06.074.

48. Tanaka, A. *et al*. *J. Am. Chem. Soc.* **2012**, 134, 14526, doi.org/10.1021/ja305225s.

49. Kamimura, S. *et al*. *Appl. Catal. B Environ.* **2017**, 211, 11, doi.org/10.1016/j.apcatb.2017.04.028.

50. Wang, Z., Liu, J. & Chen, W. *Dalt. Trans.* **2012**, 41, 4866, doi.org/10.1039/c2dt12089e.

51. Kortüm, G. *et al*. *Zeitschrift fur Naturforsch.* **1964**, 19, 28, doi.org/10.1515/zna-1964-0107.

52. Poh, A. H. *et al*. *J. Near Infrared Spectrosc.* **2019**, 27, 393, doi.org/10.1177/0967033519868241.

53. Lanz, T. *et al*. *Sol. Energy Mater. Sol. Cells* **2012**, 107, 259, doi.org/10.1016/j.solmat.2012.06.044.

54. Griffiths, T. R. *Anal. Chem.* **1963**, 35, 1077, doi.org/10.1021/ac60201a047.

55. H. H. Li. *J. Phys. Chem. Ref. Data* **1976**, 5, 329, doi.org/10.1063/1.555536.

56. Xu, Y. Toward the large-scale continuous synthesis of flaky barium sulfate. (University of Nottingham, **2024**).

57. Adachi, K. *et al*. *J. Mat. Res.* **2012**, 27, 965, doi.org/10.1557/jmr.2012.25.

58. Machida, K. *et al*. *J. Phys. Chem. C* **2016**, 120, 16919, doi.org/10.1021/acs.jpcc.6b02936.

59. Wang, Q. *et al*. *Appl. Surf. Sci.* **2017**, 399, 41, doi.org/10.1016/j.apsusc.2016.12.022.

60. Huang, X. *et al*. *J. Adv. Res.* **2010**, 1, 13, doi.org/10.1016/j.jare.2010.02.002.

61. Mogensen, K. B. *et al*. *J. Phys. Chem. C* **2014**, 118, 28075, doi.org/10.1021/jp505632n.

62. Maier, S. A. Plasmonics: fundamentals and applications (published by Springer Science, **2007**).

63. Triana, C. A. *et al*. *J. Appl. Phys.* **2015**, 118, 024901, doi.org/10.1063/1.4926488/140587.

64. Sarr, M. *et al*. *Appl. Surf. Sci.* **2016**, 379, 523, doi.org/10.1016/j.apsusc.2016.04.096.

65. Chow, W. K. *et al*. *Org. Chem. Front.* **2014**, 1, 464, doi.org/10.1039/c4qo00103f.

66. Dominguez, J. E. *et al*. *J. Appl. Phys.* **2002**, 81, 5168, doi.org/10.1063/1.1530745.

67. Ahmed, N. M. *et al*. *Results Phys.* **2019**, 13, 102159, doi.org/10.1016/j.rinp.2019.102159.

68. Zhang, S. *et al*. *Mater. Horizons* **2018**, 5, 291, doi.org/10.1039/c7mh01128h.

69. Patil, P. *et al*. *Thin Solid Films* **2001**, 382, 13, doi.org/10.1016/S0040-6090(00)01410-3.

70. Zhou, L. *et al*. *J. Phys. Chem. C* **2010**, 114, 20947, doi.org/10.1021/jp104644e.

71. Yin, H. *et al*. *Catal. Sci. Technol.* **2020**, 13, 4141, doi.org/10.1039/c9cy02511a.

72. Idriss, H. *Surf. Sci.* **2021**, 712, 2, doi.org/10.1016/j.susc.2021.121894.

73. Manthiram, K. *et al*. *J. Am. Chem. Soc* **2012**, 134, 3995, doi.org/10.1021/ja211363w.

74. Salje, E. *et al*. *Philos. Mag. B* **1984**, 50, 607, doi.org/10.1080/13642818408238882.

Chapter 3 – Deposition of molybdenum-tungsten oxide active materials as thin films, and consecutive characterization as electrochromic layers

Chapter 3 – Deposition of molybdenum-tungsten oxide active materials as thin films, and consecutive characterization as electrochromic layers

The main results of this chapter are available as pre-print on (doi.org/10.26434/chemrxiv-2024-vhf83) and, by submitting the present thesis manuscript on 17 Dec 2024, are considered for publication (under review) in the "Advanced Optical Materials" (Wiley) journal.

3.1. Energy-efficient film deposition methods

As discussed in the introduction of this work (**Chapter 1**), glazing electrochromic devices are usually comprised of five components, the electrolyte, the working and counter electrodes both deposited at the surface of two glass substrates covered by transparent conducting layers. At University of Liège, the GREEnMat laboratory mainly focuses on deposition methods carried out at ambient pressure conditions and moderate temperatures, in particular wet deposition, in which a solution or suspension is coated / casted onto the substrate. More precisely, the GREEnMat possesses the necessary equipment for spin coating, spray coating, ultrasonic spray pyrolysis (USP), dip coating and blade casting. These methods have several advantages in comparison to the vacuum techniques usually applied in the fenestration research and industry, especially being less energy consumptive, while being easier to set up and use, and also usually requiring simpler and less expensive equipment to be implemented.

Depending on the needs of the project and the level of development of the investigated materials, the different wet coating technologies can be used accordingly. For example, while spray coating or USP can be used to process large-area samples (several 100s of cm²), allowing for the upscaling of the deposition processes for future industrialization, they also require the formulation of stable electrochromic inks as to not sediment into the tubing and nozzle of the apparatus. On the other hand, spin coating presents much less requirements regarding the deposition inks, as the solution / suspension is directly deposited on top of the substrate. However, this method is only applicable to small, lab scale, samples, as the deposition of large homogeneous samples (typically more than 4 x 4 cm) proves to be very challenging.

Therefore, given this works represents the first development steps of the application of MoWOx as electrochromic materials, spin coating is selected as the deposition method of small scale (2.0 x 2.5 cm) samples, further using simple alcohol based suspensions at ambient pressure and temperature conditions.

3.1.1. Description of the spin coating process

As discussed above, spin coating is an easy approach to implement methodology for the deposition of small-scale thin layers. The process consists in four main steps, represented in **Figure 3.1** below: first, the suspension or solution is deposited onto the surface of the substrate, fixed to a rotor. Then, the rotation of the samples and the resulting centripetal force spreads the ink on the whole surface of the substrate, with the excess being expelled at the edges. After that, maintaining the rotation allows the formation of an homogeneous layer over the whole surface of the film, followed by the evaporation of the remaining solvent to obtain the final solid film[1]. The first step of the process can vary slightly in the sense that the deposition of the solution / suspension can be done on the substrate as it sits still (static deposition) or while it is already spinning (dynamic deposition), depending on parameters such as the viscosity of the ink.

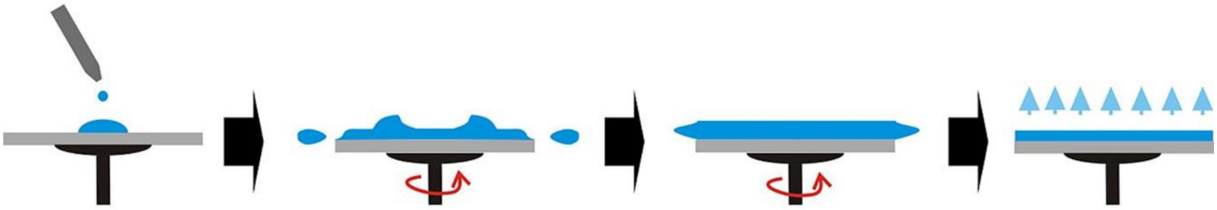

Figure 3.1: Illustration of the spin coating process with, left to right: the deposition of the ink onto the substrate, elimination of the excess liquid by spinning, formation of an homogeneous layer, evaporation of the solvent to obtain the final film[2].

Spin coating is interesting for the easy deposition of thin films in large quantities and in a routinely manner. Indeed, the deposition process only takes a few seconds, up to a few minutes if needed, meaning that the production of samples can be streamlined to reach large numbers of identical films in a short time frame. In addition, spin coating is especially advantageous in the case of materials precipitating rapidly in the solvent, which is the case for our MoWOx powders, as previously reported[3]. For such materials, the rapid sampling of the ink (kept to agitate on a stirring plate during the coating process) and consecutive deposition on the substrate helps avoiding any sedimentation of the materials and ensures the formation of homogeneous films.

Spin coating also faces limitations, such as the size of the produced samples and the lack of upscalability. Other issues can arise from the process in itself, based on the centripetal force spreading the ink as a film: the force is null at the axis of rotation, possibly resulting in a thicker, more concentrated zone in the center of the film. Also, some particles with very high aspect ratios could experience preferential orientation, with the direction of the latter going from the axis of rotation towards the edges of the substrate.

All in all, this wet coating technology, like any other, has advantages and drawbacks; however, the ease of use, low energy demand, the possibility to bypass stability issues from the inks and to produce a large number of equivalent films in a short time makes spin coating a method of choice for the deposition of our MoWOx materials. Moreover, spin coating can be considered as a viable and appropriate technique in the scope of materials with a lower degree of technology readiness level, especially when working at the lab scale.

3.2. Materials and Methods

Chemicals. Lithium perchlorate ($LiClO_4$, 95% anhydrous) is supplied by Alfa Aesar, tetrabutylammonium perchlorate ($TBAClO_4$, 99+%) and propylene carbonate (PC, 99.7% anhydrous) from Sigma-Aldrich. 50 x 50 cm Planibel G fast (15Ω/square) glass panels are graciously supplied by AGC Glass Europe and manually cut into 2.0 x 2.5 x 0.4 cm conducting transparent substrates. All reagents are used as received without further purification.

Film deposition. Suspensions of the four formulations of interest discussed in Chapter 2 are spin coated onto conducting glass substrates, previously cleaned by sonication in acetone and ethanol, further dried under compressed air stream and finally treated by UV-O_3 for 20 minutes. 50 µL of a suspension in ethanol is dynamically deposited onto the substrates, rotating at 2000 rpm for 1 minute. The remaining solvent is subsequently dried on a hot plate at 100°C for 5 minutes. Finally, a "flash" drying treatment of 1 minute on a hot plate at 250°C is applied.

Characterizations. Micrographs of the particles are obtained from transmission electron microscopy (TEM) using a TECNAI G² 20 operated at 200 kV. Top view micrographs of the spin coated films are acquired on a scanning electron microscope (SEM) TESCAN CLARA. Films thickness is measured using a Dektak stylus profilometer (in collaboration with ICMCB – measurements achieved by Dr. Brandon Faceira). The surface properties of the particles are investigated via zeta potential measurements using a DT-1200 electroacoustic spectrometer. Spectroelectrochemical (SEC) characterization of the films is carried out using the same spectrophotometer without the integrating sphere, but rather using an adapted holder for a three-electrode configuration (consisting in the sample, Ag/AgCl reference electrode and Pt foil counter electrode) in an optical glass cell. The electrochemical bias is controlled with a Biologic SP-200 potentiostat/galvanostat.

Interpretation of the electrochromic characterizations. In order to quantify the SEC contrasts of the films in a more precise manner, the latter are computed taking in account the average transmittance over an interval of wavelength representing the VIS (350 – 750 nm) and NIR ranges (750 – 1650 nm), rather than the commonly used single wavelength characterization. The transmittance is integrated over the given intervals and then normalized in comparison to the reference signal, as described in **Equation 3.1** below:

$$T_{int.} = 100 * \frac{\int T\,(\lambda)\,d\lambda}{\int T_{ref.}\,(\lambda)\,d\lambda} \tag{3.1}$$

Where $T_{int.}$ is the integrated transmittance over the VIS or NIR interval, $T\,(\lambda)$ is the transmittance of the sample at any given λ wavelength and $T_{ref.}\,(\lambda)$ is the transmittance of the reference, corresponding to 100% of transmittance at any given λ wavelength.

The average transmittance over a given interval is also used for the calculation of the coloration efficiency (CE) of the electrochromically active layers, determined in both VIS and NIR ranges, from the transmittance spectra and electrochemical data acquired during the SEC characterization, replacing the T_b, T_c (averaged values of transmittance in the bleached and colored states, respectively,) and Q_{in} (inserted charge) terms accordingly in the following **Equation 3.2**[4,5]:

$$CE = (log\,(T_b/T_c))/Q_{in} \tag{3.2}$$

Finally, as a way to quantify the capacitive behavior observed in the SEC characterizations in the $TBAClO_4$ – PC electrolyte, two figures of merits are defined: the first one is the capacitive proportion of the optical contrast ($\Delta T_{capa.}$, **Equation 3.3**), averaged on the VIS and NIR ranges of the sample:

$$\Delta T_{capa.} = 100 * \Delta T_{TBA}/\Delta T_{Li} \tag{3.3}$$

Where ΔT_{TBA} and ΔT_{Li} are the optical contrasts measured in the $TBAClO_4$/propylene carbonate and $LiClO_4$/propylene carbonate electrolyte, respectively. A second one is established to take in account the capacitive behavior in both optical and electrochemical data, and expressed as **Equation 3.4**:

$$Capacitive\ efficiency = \Delta T_{capa.}/\left(100 * Q_{in,TBA}/Q_{in,Li}\right) \tag{3.4}$$

In this equation, the so-called *capacitive efficiency* is calculated by dividing $\Delta T_{capa.}$ by the capacitive proportion of the inserted charge (in $TBAClO_4$/PC or $LiClO_4$/PC, respectively $Q_{in,TBA}$ and $Q_{in,Li}$) in a given optical state (and thus at a given electrochemical bias).

3.3. Spin-coated MoWOx and $WO_{3-\delta}$ films

3.3.1. Optimization of the deposition process

In order to characterize the optical and electrochemical properties of the synthesized formulations and the resulting electrochromic performances, the powders should be dispersed as films at the surface of a transparent conductive substrate. To produce high performing films, MoWOx 1h is investigated as a case study for the development of an optimal deposition protocol, especially regarding the formulation and preparation of the electrochromic inks.

Several parameters are considered for optimization, such as the concentration of the suspensions and the time under stirring. Notably, the nature of the solvent and the addition of surfactants is also tested in a previous work but yielded no significant results[3]. In a first step, films are produced from ethanoic suspensions of different concentrations and characterized by spectroelectrochemistry in $LiClO_4$. Preliminary results, presented in **Figure 3.2**, highlight an optimal concentration of 125 mg/mL, displaying the greater contrast between the bleached and colored states, as 100 mg/mL resulted in a better bleached state but not as dark colored state, due to the presence of less material at the surface of the substrate, while 150 and 175 mg/mL yielded less and less transparent bleached states, especially in the visible range, forming a too thick layer of optically active material. From these first results, a concentration of 125 mg/mL is thus kept for the formulation of the electrochromic inks used for the spin coating of the films discussed in the following sections.

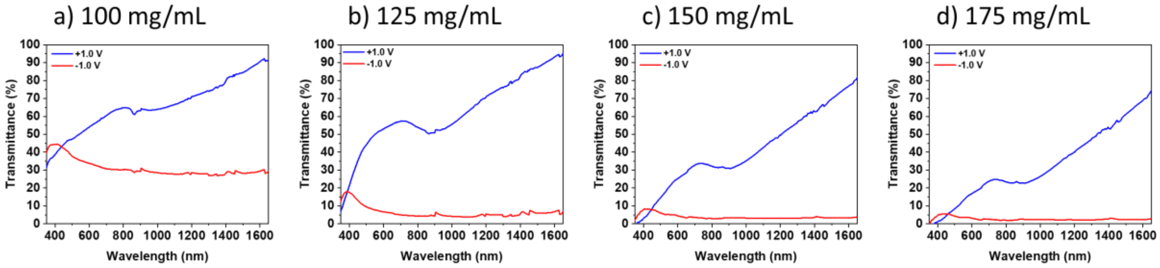

Figure 3.2: Preliminary spectroelectrochemical characterization of MoWOx 2/1 1h in the bleached and colored states, as a function of the applied potential and the concentration of the ink.

In parallel to the optimization of the concentration, it was also observed that the ageing of the suspension as it is kept under magnetic stirring also impacts the properties of the materials, resulting in a modification of the electrochromic performances. A 125mg/mL suspension is monitored throughout a week of stirring, with films produced on day 1, 4 and 7. The resulting samples are once again characterized by SEC in the lithiated electrolyte (**Figure 3.3**) and exhibit an improving contrast as a function of the time under stirring. The recovered spectra show a spectacular increase in the electrochromic properties, with the contrast greatly improving over the week of stirring, maintaining a good transmittance in the bleached state, in particular in the NIR region, while the colored state is darkened to a transmittance of less than 10% in almost all of the measuring interval.

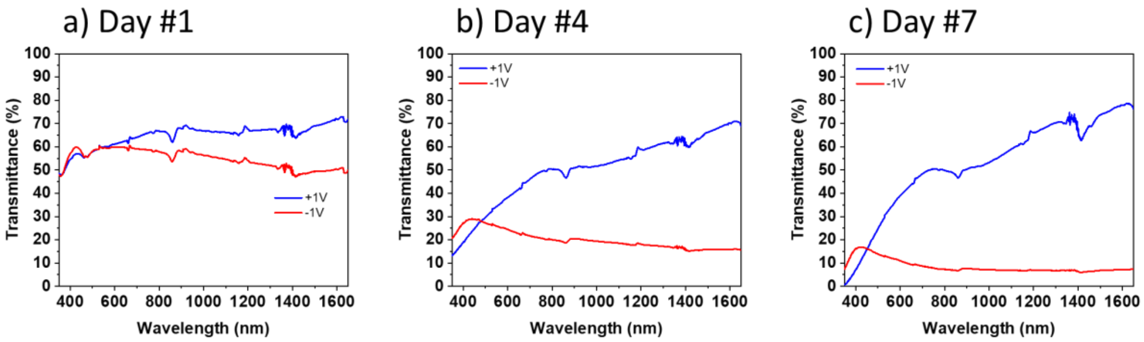

Figure 3.3: Preliminary spectroelectrochemical characterization of MoWOx 2/1 1h in the bleached and colored states, as a function of the time under stirring prior to deposition into thin films.

In the wake of these results, other characterization techniques are considered to monitor the properties of the particles as a function of time. TEM micrographs of the dried suspensions are presented in the **Figure 3.4** below. All samples display the same urchin-like morphology that was described earlier for the MoWOx formulations, however, the nanorods at the surface of the particles are getting eroded as the week progresses. The fragments are then found on the TEM grid next to the core of the particles, with the latter only left with a thin layer of nanorods at their surface. This effect could be due to the collisions between the particles in the rather concentrated suspension, resulting in the fragile surface nanostructures breaking off.

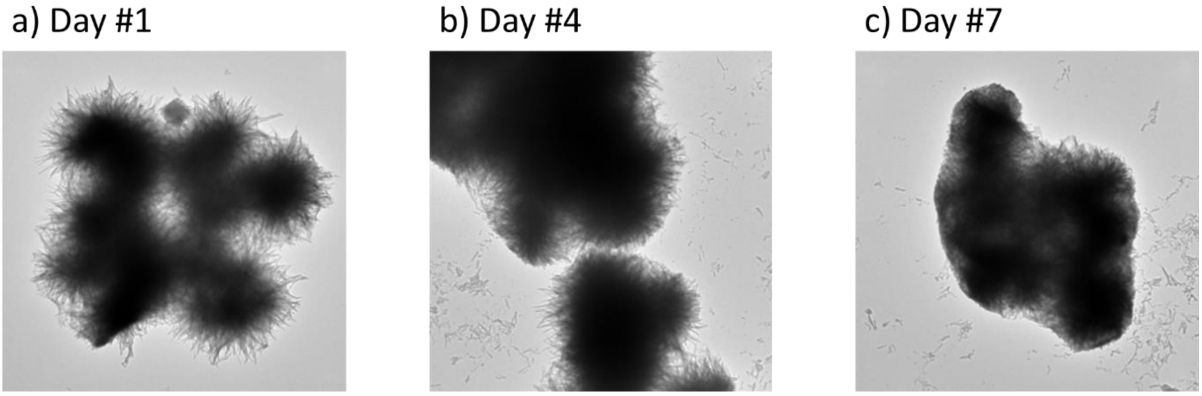

Figure 3.4: TEM micrographs of MoWOx 2/1 1h particles after one (a), four (b), and seven days of stirring (c).

Then, the surface properties of the particles are determined using zeta potential. This technique allows to measure the charge at the surface of the material, depending on several parameters such as the size distribution of the particles and the concentration of the suspension amongst other things. In this case, the obtained values exhibit a large increase in the charge of the particles, with more than a 30% increase over the span of a week (**Figure 3.5**). Besides, since the suspensions are formulated in ethanol (for which the evaporation at room temperature cannot be neglected), their concentration is also measured by drying a mL of the latter and weighing the solid residue: this experiment shows only a 4% increase in the concentration over the same time, proving that the increase in the zeta potential is indeed caused by a modification of the MoWOx properties and not an artifact arising from the solvent evaporation.

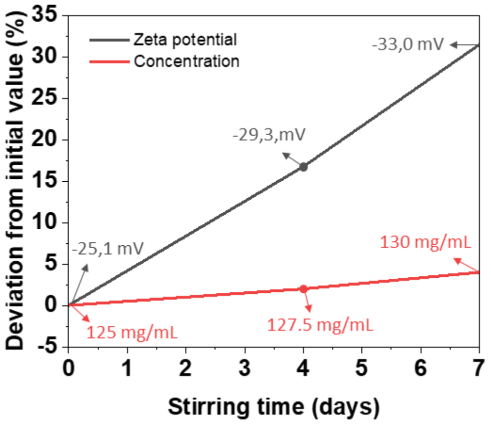

Figure 3.5: Evolution of the zeta potential (black line) and concentration (red line) of the electrochromic ink as a function of the time under stirring.

These experiments highlight the evolution of the properties of the material as a function of time under stirring, providing some paths to explain the sudden increase in performance of the films over a short time period. First of all, the nanorods breaking off the surface of the urchins could enhance the optical properties of the MoWOx, with isolated nanostructures more prone to support strong LSPR features, in addition, the smaller size distribution of the particles allows a better and more homogeneous coverage of the substrates. In addition, the zeta potential results indicate that the modifications are not limited to the morphology of the particles, but also its electronic and surface properties. For example, the erosion of the urchins could give access to new active sites, especially given the concentric distribution of Mo in these formulations. Also, some of the material could be preferentially dissolved in the ethanol during the stirring, fundamentally modifying the nature of the deposited products.

In summary, as the suspensions are stirred over a time span of a week, the properties of the MoWOx particles are modified, from a morphological point of view (as shown in the TEM micrographs in **Figure 3.4**), but also probably in their composition, as well as their distribution of active sites near the surface (deduced and proposed on the basis of the zeta potential measurements). All of these modifications combined could yield enhanced optoelectronic properties in the MoWOx and the films produced from the latter, resulting in the large improvement in the electrochromic performances observed in **Figure 3.3**.

To summarize, with MoWOx 1h as a case study, it has been possible to develop a protocol for the optimized formulation of electrochromic inks spin coated as active films, the selected parameters for the suspensions are: a concentration of 125 mg/mL in ethanol, which is kept under magnetic stirring for a week (7 days) before deposition via spin coating. These conditions are used as routine recipe for the production of the films discussed in the remainder of this work.

3.3.2. Morphology and topography

Films of the four MoWOx and $WO_{3-\delta}$ formulations are deposited on glass substrates by spin coating (see details in **Materials and Methods**), and SEM top view micrographs of the samples are presented in **Figure 3.6.** Using a similar deposition protocol for all four cases, with equivalent quantities of each material being deposited at the surface of the substrate (same concentration and deposited volume across all suspensions), quite homogeneous films are obtained with thickness values of 1.16 ± 0.05 µm for MoWOx 12h, 0.21 ± 0.02 µm for $WO_{3-\delta}$ 12h, 0.84 ± 0.03 µm for MoWOx 1h and 0.87 ± 0.03 µm for

$WO_{3-\delta}$ 1h (**Figure 3.7**). The strong decrease in thickness observed for the $WO_{3-\delta}$ 12h based films probably arises from a preferential orientation of the hexagonal $WO_{3-\delta}$ particles lying parallel to the surface of the substrate, and from a less homogeneous deposition process leading to non-covered regions of the substrate, visible in the micrograph. In the case of the $WO_{3-\delta}$ 1h formulation, the nanoparticles observed in the parent oxide rearrange themselves as microscale aggregates, leading to the deposition of a film with similar morphology and thickness to those of the 1h mixed oxide. Besides, films of MoWOx 12h are thicker in comparison with the other formulations, given the larger radius of the urchins obtained for this synthetic protocol.

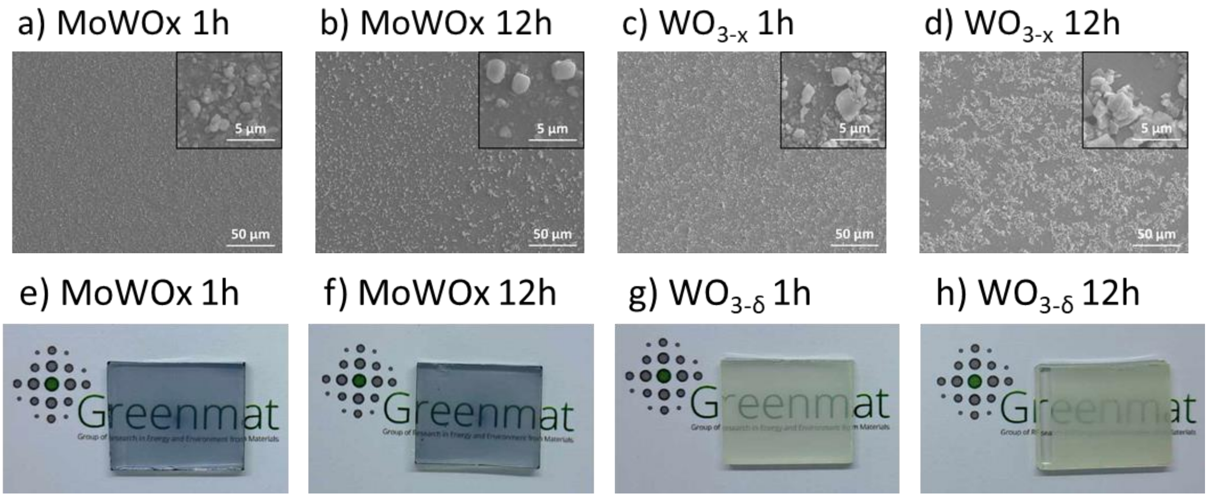

Figure 3.6: Top view SEM micrographs of films produced from MoWOx 1h (a), MoWOx 12h (b), $WO_{3-\delta}$ 1h (c), $WO_{3-\delta}$ 12h(d), with insets at a larger magnification, and pictures of the as-deposited states of MoWOx 1h (e), MoWOx 12h (f), $WO_{3-\delta}$ 1h (g) and $WO_{3-\delta}$ 12h (h).

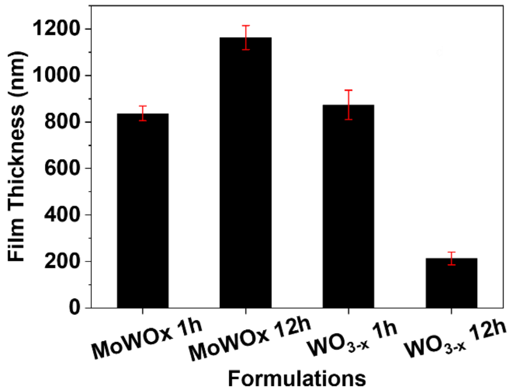

Figure 3.7: Profilometry measurments of the films thickness, produced from the four formulations.

3.3.3. *Ex-situ* electrochemistry

The active layers are then characterized by cyclic voltammetry in a 0.5 M $LiClO_4$ electrolyte solution in propylene carbonate. A characteristic CV curve is obtained for both $WO_{3-\delta}$ formulations (**Figure 3.8**), with a reduction wave starting around 0.02 V (vs. Ag/AgCl) and a return oxidation peak around -0.65 / -0.70 V. In the case of the MoWOx films, the general shape of the CV is retained while the anodic peak appears to comprise two overlapping signals, that could correspond to the oxidation of tungsten (into W^{6+}) around -0.61 / -0.63 V, and molybdenum (into Mo^{6+}) at -0.25 / 0.32 V. The capacity extracted from these electrochemical measurements, presented in **Table 3.1**, highlight at least a threefold increase in capacity in MoWOx layers in comparison with $WO_{3-\delta}$ ones, notably the two 1h samples being of similar thicknesses of 0.8-0.9 µm: 42.8 mC/cm² for MoWOx, 13.5 mC/cm² for $WO_{3-\delta}$. This large improvement in capacity probably arises from the presence in large amounts of molybdenum in the mixed formulations[6], which theoretical capacity (MoO_3, 1117 mAh/g[7]) is superior to that of WO_3 (693 mAh/g[8]). Indeed, Elezzabi *et al.* have reported that while W can mostly be reduced from W^{6+} to W^{5+}, Mo can be reduced from Mo^{6+} to Mo^{5+} and then further reduced to Mo^{4+}, if the structural properties of the material allows it, resulting in the exchange of an additional electron and thus a higher specific capacity[6]. In addition to the redox properties of both oxides, the crystalline structure adopted by the material also comes into play, allowing more or less cationic insertion into the structure. Even though the presence of Mo^{4+} in our mixed oxides has not been highlighted in this work, it is expected that the capacity of the mixed oxides would increase in comparison to the pure tungsten parent oxides, given that our MoWOx formulations consists mostly in molybdenum. Following a similar argument, the capacity of MoWOx 1h is greater than that of MoWOx 12h, 42.8 mC/cm² vs. 28.9 mC/cm², as expected from the Mo-rich 1h compound (5/1 Mo/W ratio vs. 2/1 for the 12h sample). Even though the thickness of both films differs, a globally similar concentration of material per unit area is expected due to the smaller particles of MoWOx 1h being more closely packed at the surface of the substrate. On the other hand, the large urchins obtained after 12h result in more free space in the film due to less compaction of the material, resulting in a well thicker but less dense layer. Therefore, considering comparable materials quantities in both films, the enhanced capacity of MoWOx 1h *vs.* MoWOx 12h is expected to arise from a greater Mo content per unit area in this sample. The presence of a large concentration in oxygen vacancies (responsible for the release of numerous unpaired electrons, leading to the intense EPR response of the mixed oxides, see **Section 2.5.2**, page 64) could also be the reason for the observed increase in capacity.

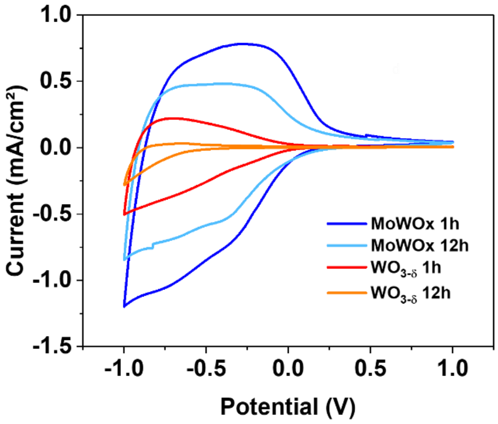

Figure 3.8: CV curves (5th cycle) of MoWOx 1h (blue), MoWOx 12h (cyan), $WO_{3-\delta}$ 1h (red) and $WO_{3-\delta}$ 12h films (orange), acquired in $LiClO_4$/PC, using Pt as counter electrode and at a scanning rate of 20 mV/s.

Table 3.1: Capacity calculated from the CV curves of MoWOx 1h, MoWOx 12h, $WO_{3-\delta}$ 1h and $WO_{3-\delta}$ 12h films.

	Capacity (mC/cm²)	Identified oxidation peaks
MoWOx 1h	42.8	-0.61 V, -0.25 V
MoWOx 12h	28.9	-0.63 V, -0,32V
WO_{3-X} 1h	13.5	-0.70 V
WO_{3-X} 12h	3.3	-0.65 V

3.3.4. *In-situ* spectroelectrochemistry

Spectroelectrochemical (SEC) characterization of the films is carried out to study their electrochromic properties and specifically their functionality as dual-band materials. Similarly to the electrochemical measurements above, 0.5 M $LiClO_4$ in propylene carbonate is used as electrolyte and every potential step is applied for 5 minutes before the acquisition of the transmittance spectra between 350 and 1650 nm, in order to reach a stable optical state. The transmittance values are expressed as the averaged transmittance over a given range of wavelength (350 to 750 nm for the VIS region, and 750 to 1650 nm for the NIR range, see **Materials and Methods**).

FTO, similarly to ITO, absorbs deep into the NIR, resulting in a large drop of transmittance after 1000 nm, reaching down to around 50% of transmittance at 1650 nm. Noteworthy, the two large peaks at 1200 and 1450 nm in **Figure 3.9** are artifacts appearing in all measurements carried out in a liquid electrolyte, probably caused by interferences between the glass and the electrolyte. Given the large difference in the influence of the substrate as a function of the wavelength (almost no transmittance loss in the VIS region, but a large drop in the NIR), it was decided to remove the contribution of the substrate from the SEC measurements. In this purpose, the spectra are simply normalized considering the bare FTO glass as the 100% transmittance baseline, this way, only the influence of the active material is represented in the SEC spectra of the films. Given the shape of the FTO glass spectra, it clearly appears that a greater correction will take place at longer wavelength where the absorption of the FTO occurs. The two large artifact peaks visible in the films submerged in the electrolyte solution should disappear upon normalization of the spectra, however, due to small differences from one substrate to the other, it is possible that the peaks are not perfectly subtracted from the final presented spectra.

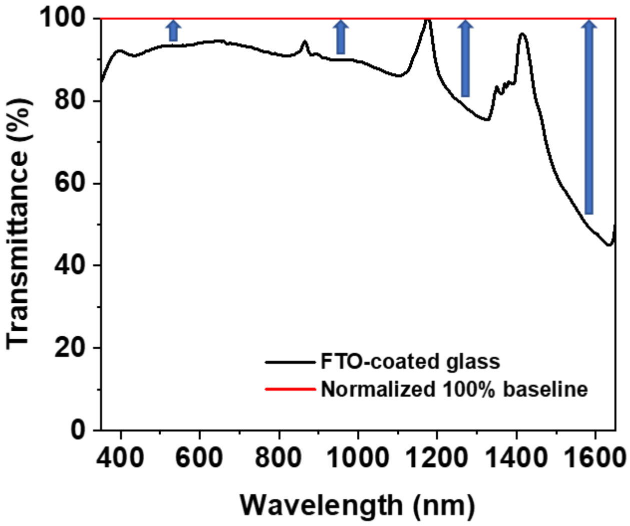

Figure 3.9 : Transmittance spectra of the FTO-coated glass substrate before (black line) and after normalizing the signal (red line), to only take in account the effect of the spin coated layer.

a. Optical behavior of reference conventional and plasmonic materials: WO_3 and ITO

As described in previous sections of this work, the investigated MoWOx formulations are expected to display dual band behavior, corresponding in a two-step electrochromic mechanism, with a NIR-preferential modulation at intermediate potentials, followed by a darkening in both VIS and NIR ranges as the potential becomes more reducing. In order to better understand the optical response expected from the MoWOx, reference materials are selected as to illustrate the typical behavior of conventional materials (represented by WO_3 here) and plasmonic formulations (represented by ITO). According to the model discussed in the introduction (**Chapter 1**), a dual band material should correspond to the combination of conventional and plasmonic electrochromic response. The SEC spectra in **Figure 3.10a,b** below show a different evolution of the transmittance in both materials as the potential changes. In the case of WO_3, W^{6+} are reduced into W^{5+} and the modulation takes place in both VIS and NIR regions. Contrarywise, the spectral modulation of ITO depends on the concentration in free charge carriers (see **Equation 1.4** in **Chapter 1,** page 19): as the plasma frequency of ITO lies in the NIR, the modulation is selective towards this region of the spectra and the VIS wavelengths are left untouched. Finally, **Figure 3.10c** illustrates the behavior of a typical $WO_{3-\delta}$ dual band formulation, consisting in a combination of the conventional and plasmonic mechanisms. When a mildly reducing potential is applied, the NIR-selective plasmonic darkening takes places, followed by the polaronic modulation covering both VIS and NIR ranges. This provides the possibility to reach the three working states previously discussed in **Chapter 1**: the *bright*, *cool* and *dark* states.

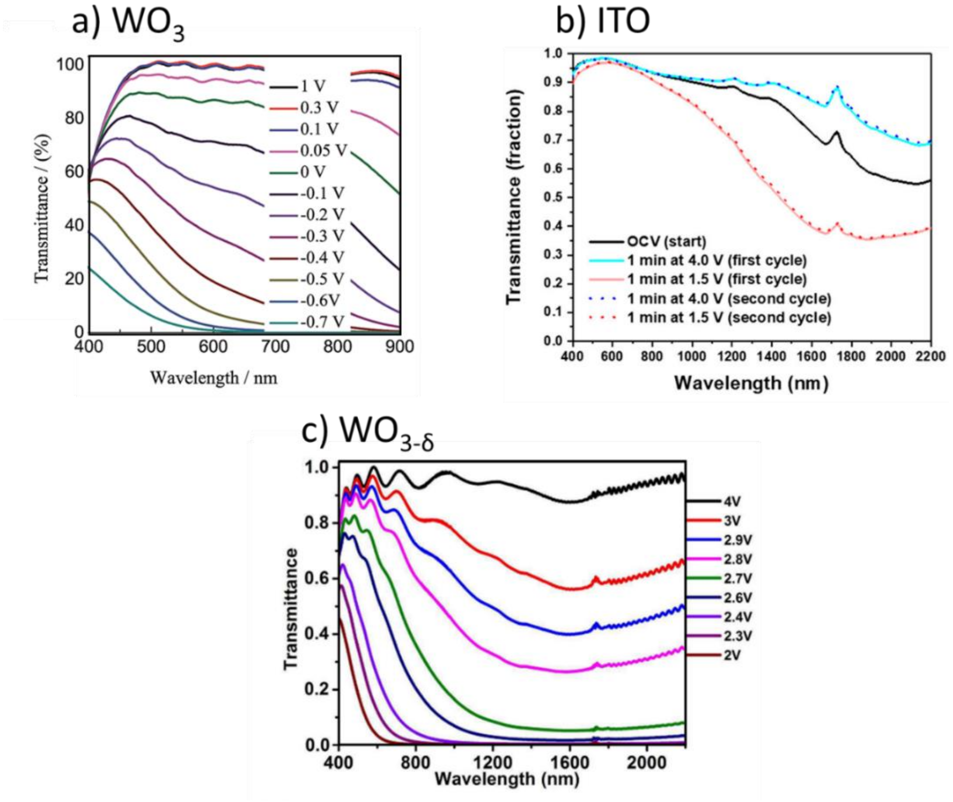

Figure 3.10 : Transmittance spectra of a non plasmonic (WO_3, a), a NIR-selective plasmonic reference (ITO, b) and a dual band formulation ($WO_{3-\delta}$, c) as a function of the applied potential (vs. Ag/AgCl in (a), vs Li/Li$^+$ in (b) and (c)).

Based on the descriptions of the two reference materials above, our MoWOx formulation should exhibit a combination of both behaviors similar to that of $WO_{3-\delta}$, with a continuous NIR-preferential modulation, followed by simultaneous darkening of VIS and NIR once sufficiently reducing conditions are met.

b. Contrasts and coloration efficiencies

According to previous electrochromic literature[9–13], the behavior of dual-band materials, requiring different potential ranges to activate the desired modulation, relies on competitive polaronic *vs.* plasmonic mechanisms, which are based on faradaic *vs.* capacitive charge/discharge processes. Many authors suggest first a plasmonic-based NIR-selective modulation that should be active at slightly reducing potentials given its capacitive behavior, with the faradaic process then occurring once more reducing potentials are reached – which is required to promote the insertion of cations from the electrolyte into the active material[10,12,13]. Even though this approach is considered for the discussion of the results presented later in this work, other interpretations have been proposed (later discussed in **Section 3.3.4.d**, page 87), especially questioning the link between the capacitive/faradaic mechanisms and the plasmonic/polaronic activity they are respectively associated with. In this case, the first model seems possible for the presently studied systems: as shown in **Figure 3.11** and **Table 3.2**, both MoWOx formulations and $WO_{3-\delta}$ 1h display a dual-band behavior, as described above, evolving from a bleached state at +1.0 V to an intermediate state displaying LSPR-based NIR darkening abilities at progressively reduced potentials (+0.5 and +0.0 V). Then, as the voltage reaches more reducing values, the transmittance keeps lowering in the NIR and starts to decrease in the VIS region as well, allowing a third, fully-darkened optical state. Interestingly, no dual-band behavior is observed in the $WO_{3-\delta}$ 12h, certainly as the consequence of their (deduced) low quantity in free charge carriers, reduced species and oxygen vacancies (as shown from the combination EPR and XPS results), as well as the micrometric dimension of the particles limiting their ability to support LSPR features.

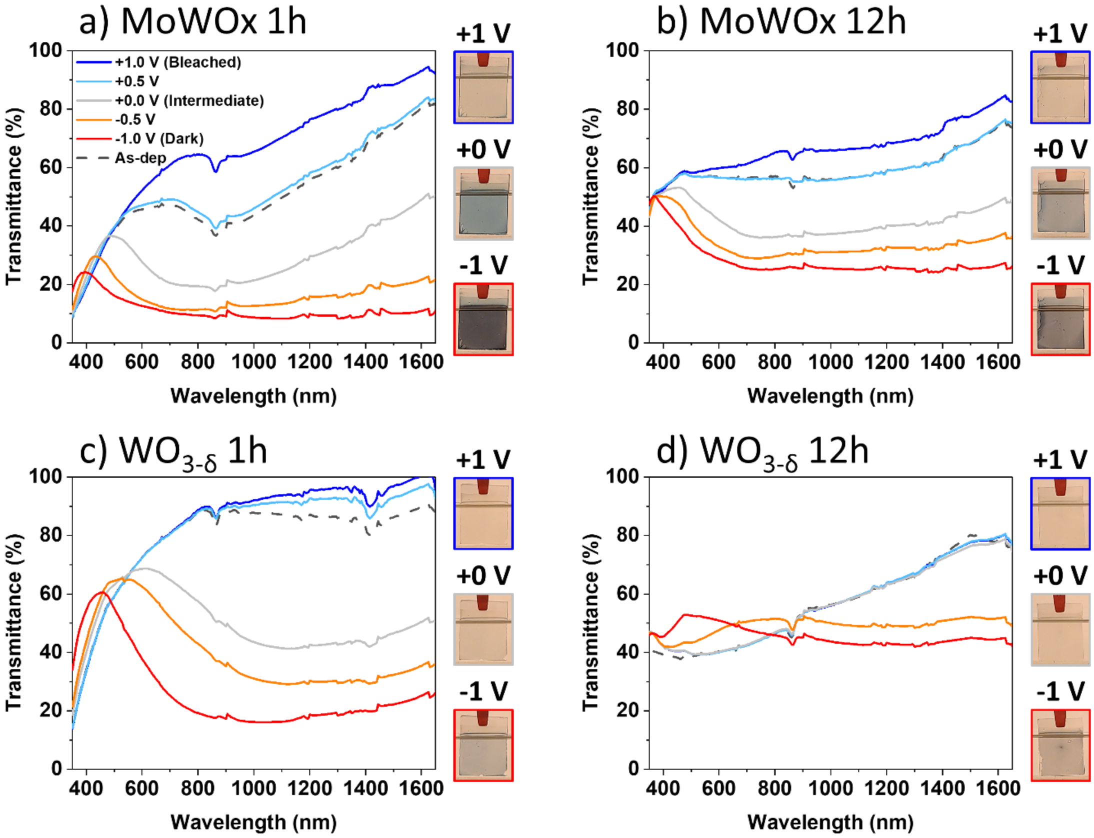

Figure 3.11: SEC transmittance spectra of MoWOx 1h (a), MoWOx 12h (b), $WO_{3-\delta}$ 1h (c) and $WO_{3-\delta}$ 12h (d) films biased in $LiClO_4$-PC, as a function of the applied potential. Pictures of the films in the bleached (+1 V), intermediate (+0 V) and dark state (-1 V) are shown as insets next to the corresponding spectra.

Table 3.2: Summary of the SEC data in $LiClO_4$-PC.

		Bleached (+1V)		Intermediate (+0.0 V)							Dark (-1.0 V)						
		%T		%T		ΔT		Q_{in}	CE		%T		ΔT		Q_{in}	CE	
		VIS	*NIR*	VIS	*NIR*	VIS	*NIR*		VIS	*NIR*	VIS	*NIR*	VIS	*NIR*		VIS	*NIR*
MoWOx	1h	46.8	*76.1*	31.1	*30.8*	15.8	*45.3*	-11.2	15.9	*35.1*	23.3	*9.5*	23.5	*66.6*	-82.1	3.7	*11.0*
MoWOx	12h	58.1	*70.5*	45.0	*40.5*	13.0	*30.0*	-9.6	11.5	*25.1*	34.0	*25.5*	24.0	*45.0*	-59.0	3.9	*7.5*
$WO_{3-\delta}$	1h	61.3	*93.8*	58.7	*46.3*	2.6	*47.5*	-3.0	6.3	*102.2*	42.6	*19.4*	18.7	*74.5*	-32.7	4.8	*21.0*

Photographs illustrating the appearance of films produced from all four formulations as a function of the applied potential are presented in **Figure 3.11** and their L*a*b* parameters are included in **Table 3.3**. As a reminder, these three parameters describe the color of an object, with L* corresponding to the lightness (ranging from white in L+ values, to black in the L- values), while a* and b* corresponds to the four colors of human vision: the a* axis goes from red (a+) to green (a-), and b* starts from yellow (b+) and shifts to blue (b-), with the three axes represented as a sphere (**Figure 3. 12**). Very interestingly, the electrochromic properties exhibited by the MoWOx formulations, especially the 1h case, appears to deviate from the usual dual-band behavior reported in the literature for $WO_{3-\delta}$ based materials[10,11,14–16] and recalled in the previous paragraph. Indeed, in their most oxidized state (at +1.0 V), MoWOx 1h and 12h display some absorption in the VIS range (46.8% and 58.1% of averaged transmittance) together with relatively high transparency in the NIR (averaged transmittance of 76.1% and 70.5%, respectively). This optical absorption response arises from the strong, enhanced absorption signal provoked by the Mo-W mixing (see **Figure 2.18**), that in turn lowers the maximal transmittance values that can be reached in the wavelength range around its maximum optical response (here 850 – 900 nm, corresponding to the superposition of the polaronic and plasmonic signals). Instead of going from a VIS-bright state to first an intermediate cool state (VIS-bleached, NIR-darkened) and then a fully VIS- and NIR-darkened state, the MoWOx samples start from a "warm" transmission mode (NIR-transparent and VIS-darkened), then undergoes NIR darkening before finally achieving the fully VIS- and NIR-darkened state. To the best of our knowledge, such "warm" mode[9,17,18] and consecutive NIR then VIS modulation has not been reported yet for Mo- or W-based electrochromic formulations. The peculiar behavior expressed in the MoWOx formulation probably originates from the large number of reduced species created during the solvothermal synthesis: if the concentration in reduced species is too high, the density of the polaronic states is so large that the application of an external bias is not sufficient to completely oxidize the material back to the bright state, explaining the residual light blue coloration of the film (see inset in **Figure 3.11**). In addition, the large size of the particles leads to an increased thickness of the films, as well as a large contribution of the scattering, resulting in the loss of some proportion of the transmittance in the visible range. Meanwhile, the plasmonic contribution can be fully modulated, as the plasma frequency can be tuned to allow a high transmittance in the NIR by the application of an oxidizing potential, red-shifting the plasmonic signature into greater wavelengths. With both effects combined, and in the most oxidized state, the MoWOx ends up in an optical mode where the plasmon is too far into the NIR to influence the transmittance of the film, while the residual polaronic activity and scattering of the urchin-like particles limit the transparency of the active layer in the visible range. In comparison, MoWOx 12h exhibits a weaker optical activity, but is still subject to an important scattering from the large particles at the surface of the substrate. On the other hand, $WO_{3-\delta}$ possess both a weaker optical signature than MoWOx 1h, and is made of smaller particles less prone to light scattering. This results in a greater VIS transmittance in the parent oxide, followed by MoWOx 12h and finally MoWOx 1h.

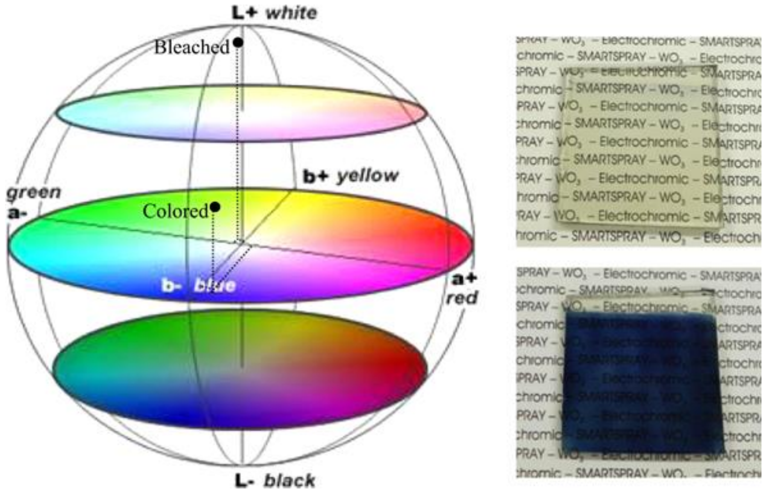

*Figure 3. 12: Schematic representation of the L*a*b* sphere, describing the color of an object, with here, the example of a WO3 film in its bleached and colored state*[19].

*Table 3.3: L*a*b* parameters of MoWOx 1h, MoWOx 12h, $WO_{3-\delta}$ 1h and $WO_{3-\delta}$ 12h films in $LiClO_4$-PC as a function of the applied potential.*

L*/a*/b* parameters in $LiClO_4$-PC

	As-deposited	+1.0 V Bleached	+0.5 V	+0.0 V Intermediate	-0.5 V	-1.0 V Dark
MoWOx 1h	69.5/1.8/17.3	72.4/6.3/21.7	70.4/2.0/17.2	59.7/-10.1/-2.0	46.1/-7.2/-16.1	41.7/-3.7/-10.1
MoWOx 12h	77.0/-0.5/3.0	78.4/0.6/4.7	76.9/-0.5/2.7	69.5/-4.9/-5.6	63.2/-4.6/-10.5	59.4/-3.4/-9.3
WO_{3-x} 1h	73.4/2.1/12.8	73.0/2.0/12.7	73.0/2.0/12.6	76.1/1.7/13.4	77.8/-0.8/12.6	75.0/-6.7/-0.2
WO_{3-x} 12h	66.5/1.1/1.9	66.6/1.1/1.9	66.6/1.1/1.9	66.7/1.2/2.0	70.9/2.9/6.6	73.9/-1.8/3.3

In the case of MoWOx 1h, contrasts of 15.8% and 45.3 % are obtained for the intermediate state, in the VIS and NIR regions respectively, while the colored state exhibits a modulation of 23.5% and 66.6% in those same ranges. The CE of the material reaches values of 15.9 cm²/C (VIS) and 35.1 cm²/C (NIR) in the intermediate state, and 3.7 cm²/C and 11.0 cm²/C in the darkened state. The MoWOx 12h displays a modulation of 13.0% in the VIS and 30.0% in the NIR at +0.0 V, these values then respectively go up to 24.0% and 45.0% once -1.0 V is applied. This formulation displays CE of 11.5 cm²/C and 25.1 cm²/C in the NIR-preferential state, and 3.9 cm²/C and 7.5 cm²/C in the most reduced state, for VIS and NIR regions respectively. For the third dual-band formulation, $WO_{3-\delta}$ 1h, contrasts in the VIS and NIR ranges respectively reach 2.6% and 47.5% in the intermediate state, and 18.7% and 74.5% in the darkened state. In the latter case, the material exhibits CE values of 6.3 cm²/C and 102.2 cm²/C at +0.0 V and 4.8 and 21.0 cm²/C at -1.0 V. For all three active formulations, the additional ability to further oxidize the “as-deposited” state by applying a +1.0 V potential is in good agreement with the assumption that the formation of reduced species, especially with MoWOx configurations, could be due, at least partially, to the insertion of protons provided by the isopropanol in the reactive media into the crystal lattice during the solvothermal process[20], which can in turn be extracted from the material during the electrochemical cycling. The fourth case, $WO_{3-\delta}$ 12h, has not been evaluated in terms of figures of merit in view of its poor intrinsic EC behavior.

Noticeably, in the three considered formulations, the CE of the intermediate state is clearly superior to that of the darkened state: indeed, almost half of the total optical change (especially in the NIR) is already reached at +0.0 V for only 10-16% of the total charge inserted in the darkened mode. As stated earlier, such high efficiency can be linked to a capacitive behavior. These results, in addition to the optical and electronic characterizations of the precursor powders presented earlier, attest the ability of the two MoWOx formulations, as well as the $WO_{3-\delta}$ 1h, to support a dual-band behavior being potentially LSPR-based. From the contrast and CE values presented in **Table 3.2**, MoWOx 1h shows better performances than its 12h counterpart, especially in the NIR region. This improved behavior at shorter solvothermal treatment could result from the differences observed in the powders, with smaller particle size and increased free charge carriers concentration (as shown in the EPR spectra, **Figure 2.18**), leading to a higher surface area and an enhanced optical absorption (see **Figure 2.16**).

c. Kinetics

In addition to its contrasts and CEs, the performance of an electrochromic material also depends on its ability to switch between optical states in an adequate time frame. Presently, the kinetics of the films are measured at three wavelengths: 550, 1000 and 1550 nm, during 10 minutes for each potential step. So-called coloration/bleaching times (t_c and t_b, respectively) correspond to the duration required to reach 90% of the contrast between the bleached and colored state (or reversibly). The coloration and bleaching kinetics of the two MoWOx and the $WO_{3-\delta}$ 1h samples are summarized in **Figure 3.13** and **Table 3.4**.

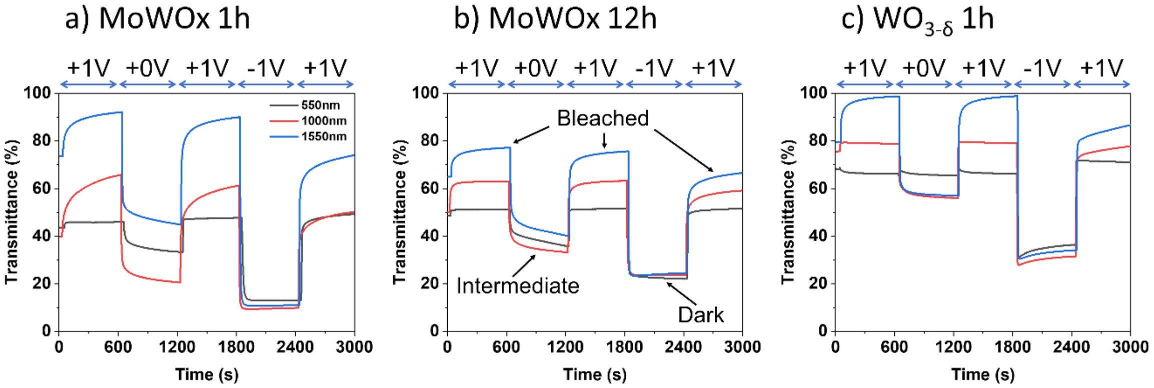

Figure 3.13: SEC transmittance curves of the films obtained from the three dual-band formulations MoWOx 1h (a), MoWOx 12h (b), $WO_{3-\delta}$ 1h (c), as a function of time and applied potential, for three distinct wavelengths.

Table 3.4: Summary of the SEC kinetics data obtained on MoWOx 1h, MoWOx 12h and $WO_{3-\delta}$ 1h films.

	Intermediate (+0.0 V)						Dark (-1.0 V)					
	t_c (s)			t_b (s)			t_c (s)			t_b (s)		
	550 nm	1000 nm	1550 nm	550 nm	1000 nm	1550 nm	550 nm	1000 nm	1550 nm	550 nm	1000 nm	1550 nm
MoWOx 1h	304	74	110	6	252	140	28	8	10	58	160	114
MoWOx 12h	410	138	198	6	52	80	16	16	10	14	106	104
$WO_{3-\delta}$ 1h	484	88	22	2	4	72	6	4	6	4	24	68

To begin with, for all three formulations, the coloration time in the VIS region at the intermediate bias (+0.0 V) appears very long for a very limited modulation (around 10% at best), reaching values ranging from 300 to 500 seconds. Besides, the NIR modulation takes place at faster rates, with a maximum in t_c of 198 s, while displaying greater contrasts (close to 40%). These results highlight the NIR-selective modulation (mainly plasmonic) exhibiting faster kinetics than the VIS modulation (mainly polaronic). During the reverse bleaching step, the discoloration in both VIS and NIR regions is carried out at significantly faster paces, with the exception of MoWOx 1h in the NIR range, exhibiting the longest bleaching times recorded across the three investigated formulations. Regarding the dark state (-1.0 V), the coloration appears very quick since the greater difference in potential allows the easier insertion of the Li^+ cations from the electrolyte into the active layer, resulting in fast kinetics even for large contrasts (30-40% and 60-80% in the VIS and NIR regions, respectively). The discoloration of the darkened state is faster in the VIS region, while the bleaching in the NIR presents slower kinetics, probably due to charge trapping inside the particles, leading to residual darkening after the electrochemical cycling.

Globally, these results highlight the superiority of the capacitive mechanisms at moderate bias, which is then caught up by the faradic behavior once a more reducing potential is applied. However, in comparison with other plasmonic materials of the literature[10,11], quite long switching times are noticed for the NIR modulation, especially for both MoWOx 1h and 12h in comparison to $WO_{3-\delta}$ 1h. . On the basis of the results presented here, these slow kinetics could be due to the complexity of the urchin-like MoWOx particles that somehow hinders the available surface area and increases the mean free path of the positive counter-ions (here Li^+ cations) that have diffused from the bulk electrolyte to the active material surface. In the case of MoWOx 1h, the smaller dimensions of the particles translate into an even more compact packing of the nanorods around the core, further impeding the diffusion of the cations towards the active surface. In comparison, the nanospherical morphology of the $WO_{3-\delta}$ 1h offers larger surface area and shorter diffusion paths, thus globally improving the commutation kinetics for this material.

d. Dual band electrochromism: different mechanisms in literature?

Even though Prof. Delia Milliron and her team have been the first to propose a reaction pathway to explain the observed dual band behavior in their composite and monomaterial formulations, based on the capacitive charging of the material activating the plasmonic absorption, followed by the faradaic insertion of cations resulting in the polaronic modulation of the VIS range[9–11], other models can be proposed on the basis of the existing literature[21–24].

Notably, first-principle simulation of polarons by Salje *et al.*[21,24] and Ghosez *et al.*[22,23] have shown the preferential formation of polarons upon insertion of additional electrons in the lattice. According to the authors, it is energetically favorable for the material to distort in order to localize the electron via electron-phonon interaction (corresponding to the polaron).

In addition, the insertion of Li^+ in the studied system does not result in the modification of the lattice structure and thus leads to the sole insertion of an electron, similarly to capacitive charging mechanisms. Also, the polaronic absorption of WO_3 based formulations has been observed at spectral values ranging from 800 nm up to 1600 nm[23–26]. Since the plasma resonance of Cs_xWO_3 and $WO_{3-\delta}$ formulations lies in a similar range (cf. **Figure 1.19**[27]), it is possible that both absorption signature could be inverted in a given material, with the polaronic response further into the NIR range, while the plasmonic signature is located closer to the VIS region.

On this basis, the dual band mechanisms would not arise from two different mechanisms at play but rather from the filling of the polaronic states in a first step, being 0.6 eV more stable than delocalized electrons[21], followed by the delocalization of additional electrons upon further insertion, leading to the activation of the plasmonic response. In this case, the polaronic mechanisms would be responsible for the NIR modulation of the intermediate state (appearing at lower applied potentials) while the plasmonic resonance would lead to the modification of the VIS optical properties.

However, several works in the electrochromic field have highlighted the effect of Li^+ insertion in the crystal lattice of an active material through *in-situ* and *ex-situ* characterization methods[15,28–30]. The results provided by these publications show the modification of the crystalline structure of the materials, expressed as a shift of the diffraction peaks as a function of electrochemical cycling. In particular, Lee *et al.* (who has developed the dual band $WO_{3-\delta}$ formulation discussed earlier in **Chapter 1**, **Section 1.4.2.a**, page 27) showed an evolution of the crystalline structure of the samples, going from monoclinic, to triclinic and finally cubic phases[15]. At the moderate potentials required for the activation of the NIR-selective modulation, the monoclinic phase of the material is maintained, while the application of more reducing potentials results in the deformation of the lattice and is accompanied by the modulation of the VIS range (**Figure 3.14**).

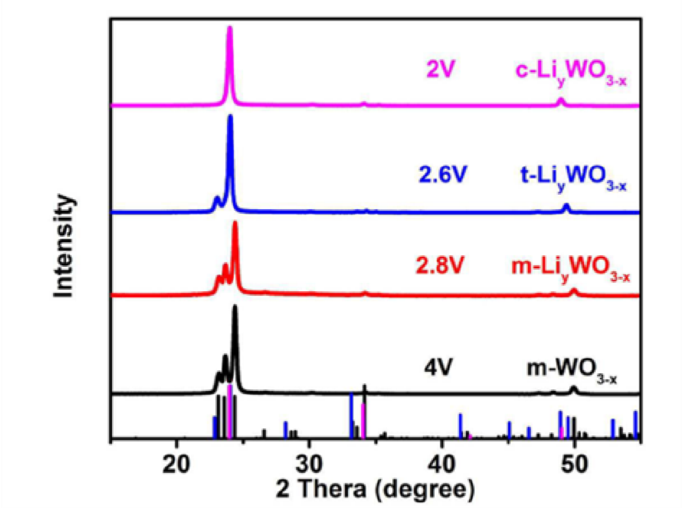

Figure 3.14: XRD diffractogram of a dual band $WO_{3-\delta}$ formulation as a function of the applied potential (vs. Li/Li^+), corresponding to the different working states of the material (bright 4.0 V, cool 2.8 and 2.6 V, dark 2.0 V)[15].

Other authors have highlighted similar effects, although they were not studying the materials for dual band electrochromism purposes, the diffractograms acquired at different biases are presented in **Figure 3.15**. Nonetheless, their results still demonstrate the disruption of the crystalline parameters of the active material upon insertion of cations. Orel *et al.* have studied the *ex-situ* XRD characterization of Li^+ insertion in Nb_2O_5 in 1998[28], followed by Truong *et al.* with the *in-situ* charge/discharge of Li^+ in TiO_2 in 2011[29], and more recently Wang *et al.* have highlighted the same observation for the insertion of Al^{3+} in $WO_{3-\delta}$ in 2021[30]. As discussed in the previous sections, all three of these materials can exhibit electrochromic features and can be modified and formulated as dual band electrochromic materials. Anyway, these publications have shown that in experimental setups, the insertion of a cation results in a local deformation of the surrounding lattice, instead of the non-deforming insertion expected from the theoretical modelling provided by Salje *et al.*[21,24] and Ghosez *et al.*[22,23]. The difference between the theoretical and experimental results could arise from this non-deforming assumption: if the insertion of a cation to counterbalance the charge of an electron indeed causes deformation of the lattice, the delocalization of the electron and capacitive charge of the material could become energetically more favorable than the formation of a polaronic state. Therefore, the first electrons would be injected as delocalized charge carriers, then, the increase in the bias would bring enough energy to the system to force the insertion of cation into the crystal, with the ensuing deformation of the lattice.

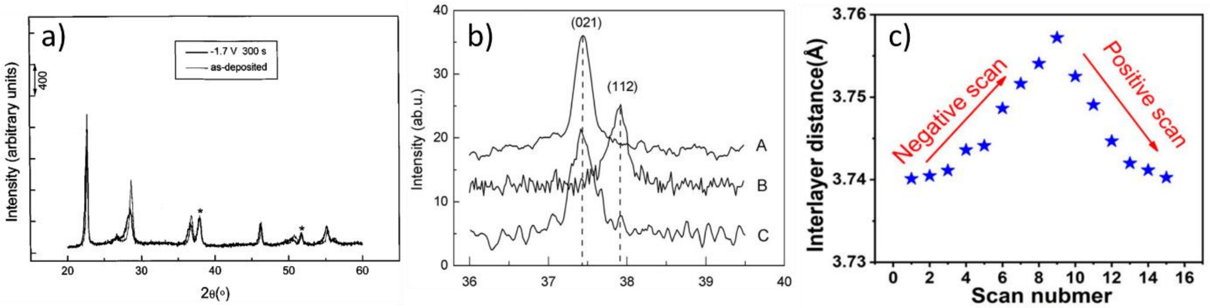

Figure 3.15: XRD diffractograms of Nb_2O_5 (a)[28], TiO_2 (b)[29] and $WO_{3-\delta}$ (c)[30], as a function of the applied potential, highlighting the shift in the signal as cations are inserted into the crystal lattice.

With both hypotheses supported in the state-of-the-art, and on-going debate between the two, it is necessary to determine which model should be used to discuss the results presented in this work. Given the experimental results showing the interdependence between the capacitive/faradaic charge mechanisms, the evolution of the crystalline phase as a function of the applied potential and charging mechanism, and the resulting spectrally selective modulation, the remainder of this work will mainly focus on the approach proposed by Milliron *et al.* [9–11]. Meanwhile the possibility for a different model explaining the reported observation is also acknowledged, with theoretical models supporting the non-deforming Li^+ insertion approach. Moreover, the publications providing this alternative approach mainly focus on the local effect of Li^+ insertion in the lattice, while the optical results expected from the studied materials are more related to a global effect on the material when cations are inserted/extracted.

e. Capacitive vs. faradic mechanisms

In order to further analyze the capacitive behaviors expected from the materials, the spin coated films are electrochemically biased in a 0.5 M $TBAClO_4$ – PC electrolyte. Given the very large radius of the TBA^+ cations, ionic insertion into the crystal lattice of the active layers is prohibited[9,15,31–33]. Therefore, according to the model proposed by Milliron *et al.*[9–11] (and discussed in the previous section), any measured optical change has to originate from a capacitive charge/discharge of the materials. This limitation in the available electrochemical processes is clearly visible in the transmittance spectra and data presented in **Figure 3.16** and **Table 3.5**, with the darkening taking place preferentially in the NIR and reaching optical states similar to the +0.0 V intermediate state obtained with the lithiated electrolyte. Indeed, the MoWOx 1h reaches contrasts of 10.4% (VIS) and 32.9% (NIR) in the intermediate state (+0.0 V), going up to 12.3% (VIS) and 44.3% (NIR) when applying -1.0 V. In the 12h mixed oxide, the VIS contrast ranges from 8.0% at +0.0 V and 8.1% at -1.0 V, while the NIR modulation in the intermediate mode comes up to 23.6% and 24.4% in the colored state. Besides, the 1h parent oxide displays contrasts of 0.5% (VIS) and 22.2% (NIR) in the intermediate +0.0 V state, and -0.4% (VIS) and 26.3% (NIR) in the darkened state. Finally, in the case of $WO_{3-\delta}$ 12h, no modulation appears upon cycling in $TBAClO_4$, indicating the lack of sufficient optoelectronic features in order to display the sought dual-band behavior. Pictures of the films are included as insets in **Figure 3.16** while the L*a*b* parameters of the films are summarized in **Table 3.6**. In all three dual-band active formulations, the modulation in $TBAClO_4$ almost reaches completion at +0.0 V, with a few extra percent of contrast gained when a bias of -1.0 V is achieved, recreating an optical state very similar to the intermediate state (+0.0 V) that was obtained in the lithiated electrolyte. These performances are in good accordance with what was expected from this experiment, limiting the modulation to the capacitive mechanisms, predominantly present in the intermediate state according to the model used for the interpretation of this work.

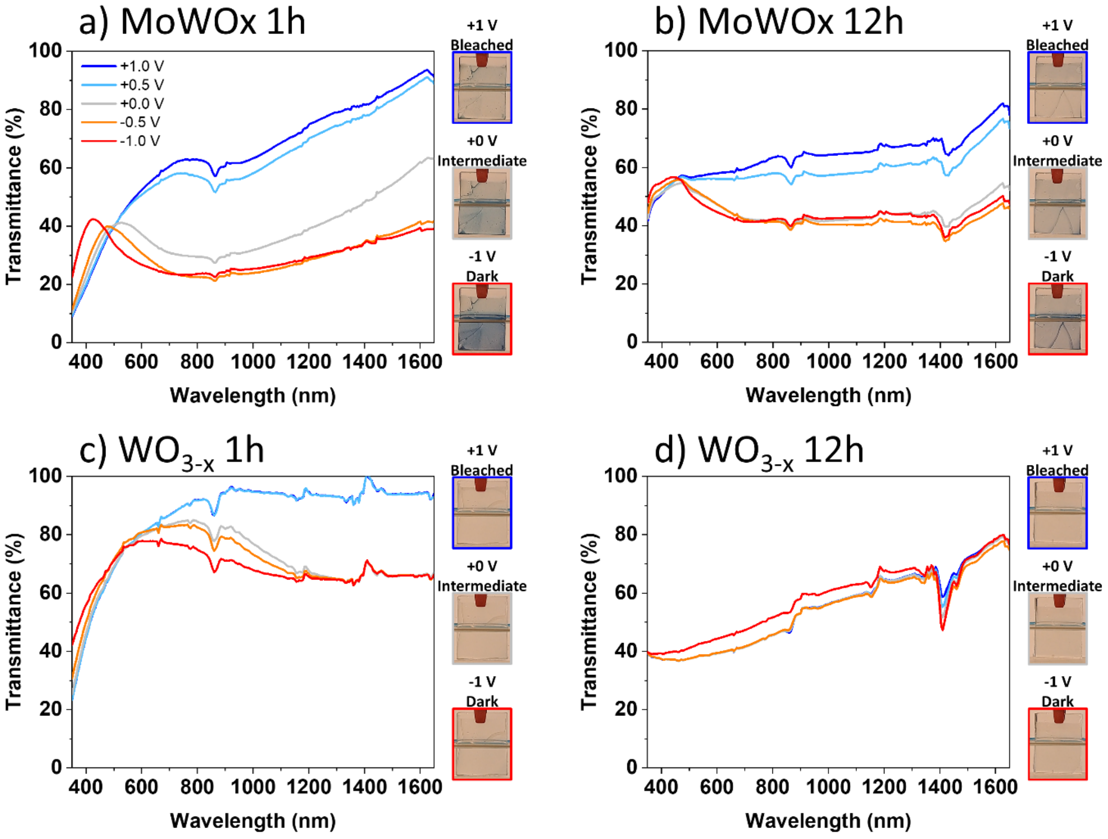

Figure 3.16: SEC transmittance spectra of (a) MoWOx 1h, (b) MoWOx 12h, (c) $WO_{3-\delta}$ 1h and (d) $WO_{3-\delta}$ 12h films biased in $TBAClO_4$-PC, as a function of the applied potential.

Table 3.5: Summary of the SEC data in $TBAClO_4$-PC.

		Bleached (+1V)		Intermediate (+0.0 V)							Dark (-1.0 V)						
		%T		%T		ΔT		Q_{in}	CE		%T		ΔT		Q_{in}	CE	
		VIS	*NIR*	VIS	*NIR*	VIS	*NIR*		VIS	*NIR*	VIS	*NIR*	VIS	*NIR*		VIS	*NIR*
MoWOx	1h	43.0	*74.2*	32.6	*41.3*	10.4	*32.9*	-5.3	22.7	*48.0*	30.6	*29.9*	12.3	*44.3*	-31.7	4.6	*12.5*
MoWOx	12h	56.3	*67.5*	48.3	*44.0*	8.0	*23.6*	-6.0	11.1	*31.1*	48.2	*43.1*	8.1	*24.4*	-31.8	2.1	*6.1*
$WO_{3-\delta}$	1h	69.7	*93.7*	69.1	*71.5*	0.5	*22.2*	-1.2	2.9	*97.7*	70.1	*67.4*	-0.4	*26.3*	-23.8	-0.1	*6.0*

*Table 3.6: L*a*b* parameters of MoWOx 1h, MoWOx 12h, $WO_{3-\delta}$ 1h and $WO_{3-\delta}$ 12h films in $LiClO_4$-PC as a function of the applied potential.*

L*/a*/b* parameters in $TBAClO_4$-PC

	As-deposited	+1.0 V Bleached	+0.5 V	+0.0 V Intermediate	-0.5 V	-1.0 V Dark
MoWOx 1h	73.7/-2.7/18.1	76.8/1.7/21.7	76.4/0.7/20.2	71.7/-7.9/8.3	68.3/-8.6/-1.0	64.4/-1.7/-12.0
MoWOx 12h	75.6/-1.3/3.1	77.1/-0.5/4.6	76.4/-0.9/3.6	72.8/-3.2/-1.1	73.1/-3.2/-1.9	71.5/-1.8/-5.2
WO_{3-x} 1h	95.6/0.4/14.2	95.6/0.4/14.1	95.6/0.4/14.1	95.5/-0.1/12.8	96.4/-0.6/11.6	95.5/-0.9/8.5
WO_{3-x} 12h	65.7/0.6/2.0	65.6/0.6/2.0	65.6/0.6/1.9	65.6/0.6/1.9	65.7/0.6/2.0	68.6/0.9/3.6

From the results respectively obtained in $LiClO_4$ and $TBAClO_4$, it is possible to estimate the proportion of capacitive-related modulation in the materials (cf. **Materials and Methods** for calculation details, and **Table 3.5**). These estimations show a greater percentage of the latter in the MoWOx formulations in comparison to the $WO_{3-\delta}$ 1h: the capacitive mechanisms represent 69.2% and 70.1% of the intermediate state, and 59.4% and 44.0% of the darkened state of the MoWOx 1h and 12h, respectively, while the 1h parent oxide only exhibits 32.9% at +0.0 V and 18.7% at -1.0 V. These values are in good accordance with the optical and EPR characterizations of the powders presented above, that have indicated a larger quantity in unpaired electrons in the MoWOx formulations in comparison to the pure oxides, with a significant proportion being delocalized in the conduction band and leading to a greater contribution of the capacitive behavior in the electrochromic performances of the materials. In addition, the decrease in capacitive contribution at -1.0 V, observed in all formulations, was anticipated since the electrochemical mechanisms in this second working regime are a combination of capacitive behavior and faradaic charge/discharge in the lithiated electrolyte (while the $TBAClO_4$-PC electrolyte is limited to capacitive mechanisms). The same calculation can then be carried out for the inserted charges: since both the optical change and the quantity of inserted charges are important for the electrochromic performances of a material, the capacitive proportion of optical modulation can be divided by that of inserted charges in order to obtain a figure of merit equivalent to the CE, but for the contribution of the capacitive behavior in the different formulations (cf. **Materials and Methods**). Higher values are consecutively determined for the mixed oxides in comparison to the parent oxide, with MoWOx 1h displaying the greatest capacitive efficiency out of the three dual-band formulations (1.46 and 1.79 in intermediate and darkened modes, respectively, vs. 1.12 and 1.30 for MoWOx 12h, and 0.82 and 0.45 for $WO_{3-\delta}$ 1h), once again highlighting the potential of this material for future developments.

f. Reversibility

Finally, the evaluation of the reversibility of the optical changes undergone by the different materials is performed. Transmittance modulation spectra of MoWOx 1h and 12h, and of $WO_{3-\delta}$ 1h and 12h samples are presented in **Figure 3.17**, being biased between +1.0 and -1.0 V for 5 cycles. In addition, the evolution of the L*a*b* parameters of the films during the electrochemical cycling is shown in **Table 3.7**. In MoWOx 1h, a significant drop of transmittance in the bleached state already appears after the second cycle (minus 20 % in the NIR, stable in VIS), followed by a stabilization of the transmittance values in both bleached (+1.0 V; 43.6% and 51.6% in VIS and NIR, respectively) and darkened states (-1.0 V; 15.5% in VIS and 27.5% in NIR). The loss of transmittance appearing after the first coloration seems to indicate some propensity to irreversible Li^+ insertion in some of the active sites. On the other hand, MoWOx 12h and $WO_{3-\delta}$ 1h display a similar stability of the colored state (maximum of 5-6% change in MoWOx 12h and 10-11% in $WO_{3-\delta}$ 1h, versus 4-6% in MoWOx 1h) but a more gradual decay of the bleached state (minus 7.1% and 4.4% after the first coloration in MoWOx 12h and $WO_{3-\delta}$ 1h, respectively). Nevertheless, in all 3 cases, an optical state similar to the "as-deposited" state is obtained within the first two cycles. One possible explanation of this process could be that the H^+ potentially present in the "as-deposited" samples (originating from the reducing effect / proton-donor effect of the isopropanol in the reactive medium) can be electrochemically extracted from the materials, with the transmittance of the film increasing to reach the +1.0 V state. However, after the first coloration, due to their size difference, Li^+ could be irreversibly inserted in the sites previously occupied by the protons, irreversibly modifying the crystalline properties, as previously reported for other metal oxides (such as $Li_{1.12}(Ni_{0.425}Mn_{0.425}Co_{0.15})_{0.88}O_2$[34], $Li_xH_{1-x}NbO_3$[35], $H_2Ti_6O_{13}$[36], MnO_2[37]) and thus limiting the transmittance of the films to their previous "as-deposited" state.

Looking into the dual-band functionality of the investigated formulations, the SEC spectra highlight the loss of their intermediate NIR-selective state after the first complete coloration of the films (-1.0 V). Indeed, the previously well-defined +0.0 V state merges with the bleached mode into a single state showing no modulation when the potential is switched from +1.0 V to 0.0 V and vice versa. The disappearing of the intermediate state (expected to arise from plasmonic processes), indicates a probable modification of the surface properties of the materials, supporting the plasmonic features. This could be due to a number of factors, for example: dissolved species in the electrolyte such as oxygen and water, that could react with the active layer and modify its surface properties, irreversibly inhibiting their plasmonic capabilities. Finally, in the case of the $WO_{3-\delta}$ 12h, the bright, cool and dark states almost completely merge after the first coloration cycle, thus not fulfilling the requirements to be considered as an electrochromic material, which should exhibit a reversible modulation of its optical properties upon the application of a potential.

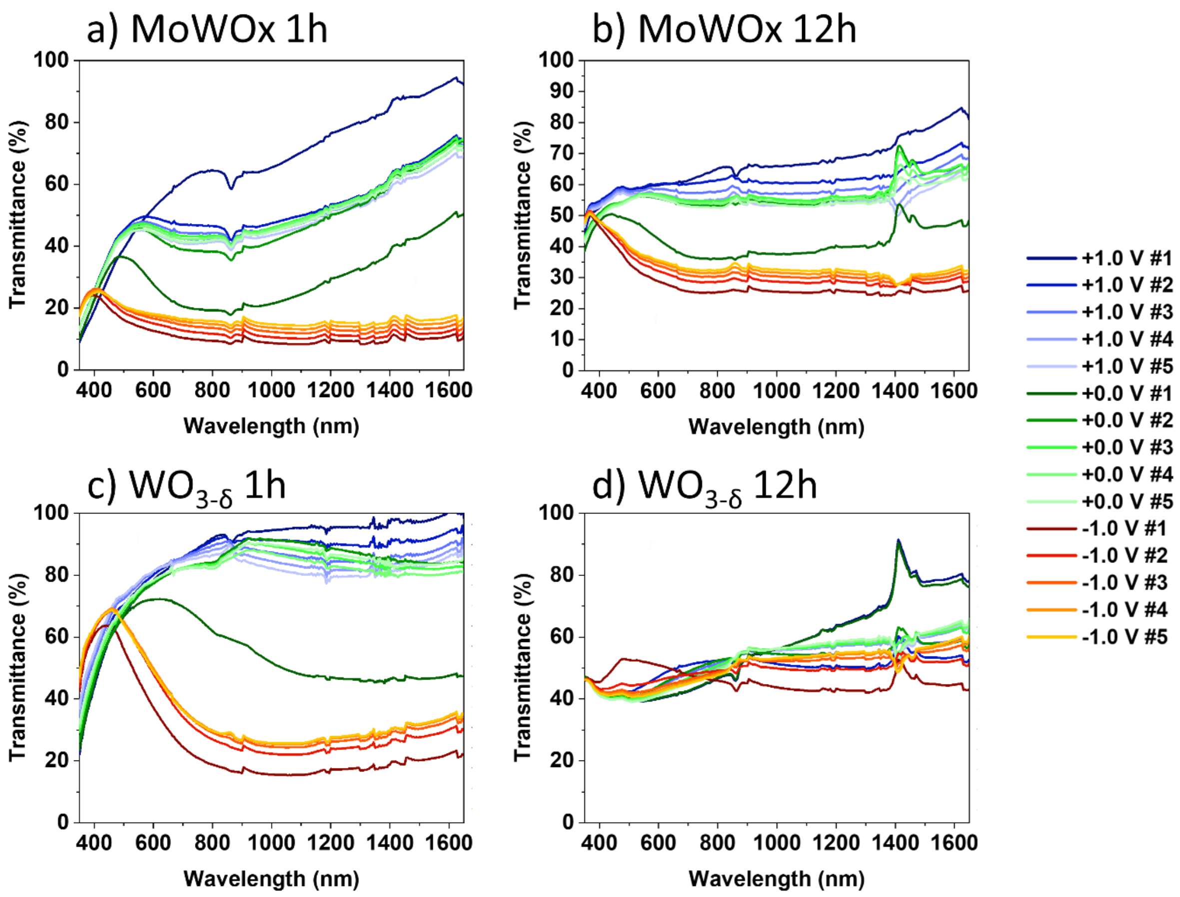

Figure 3.17: SEC transmittance spectra of (a) MoWOx 1h, (b) MoWOx 12h, (c) $WO_{3-\delta}$ 1h and (d) $WO_{3-\delta}$ 12h films biased in $LiClO_4$-PC, as a function of the electrochemical cycling.

*Table 3.7: L*a*b* parameters of MoWOx 1h, MoWOx 12h, $WO_{3-\delta}$ 1h and $WO_{3-\delta}$ 12h films as a function of the number of electrochemical cycles (+1 V/-1 V).*

L*/a*/b* parameters in $LiClO_4$-PC							
	Cycle #	**+1.0 V Bleached**	**-1.0 V Dark**		**Cycle #**	**+1.0 V Bleached**	**-1.0 V Dark**
MoWOx 1h	**1**	72.4/6.3/21.7	41.7/-3.7/-10.1	**$WO_{3-\delta}$ 1h**	**1**	73.0/2.0/12.7	75.0/-6.7/-0.2
	2	71.6/-3.3/14.1	45.8/-0.6/-8.6		**2**	74.3/2.2/12.6	76.7/-5.1/5.0
	3	70.7/-3.9/13.2	47.5/-0.5/-7.5		**3**	74.6/2.2/12.6	76.3/-2.9/-7.8
	4	69.9/-4.2/12.5	48.2/-0.4/-6.3		**4**	74.7/2.2/12.6	76.6/-3.3/7.4
	5	69.1/-4.4/12.0	48.7/-0.4/-5.3		**5**	74.8/2.2/12.7	76.9/-3.9/6.8
MoWOx 12h	**1**	78.4/0.6/4.7	59.4/-3.4/-9.3	**$WO_{3-\delta}$ 12h**	**1**	66.6/1.1/1.9	73.9/-1.8/3.3
	2	78./0.5/4.2	61.9/-3.0/-7.8		**2**	70.5/3.4/7.1	70.3/1.3/4.1
	3	77.8/-0.1/3.7	63.2/-2.7/-6.9		**3**	68.5/2.9/4.9	68.8/1.6/3.4
	4	77.1/-0.6/3.2	63.9/-2.5/-6.2		**4**	67.7/2.5/4.0	68.2/1.6/3.2
	5	76.6/-1.0/2.8	64.4/-2.3/-5.7		**5**	67.3/2.3/3.6	67.9/1.6/3.1

All in all, the results obtained from the characterizations of the films highlight the remarkable properties of $WO_{3-\delta}$ 1h and both MoWOx, especially MoWOx 1h, as dual-band plasmonic electrochromic materials. In all active formulations, it was possible to demonstrate the preferential modulation of NIR wavelengths at slightly reducing potentials; the origin of this NIR-selective activity seems to arise from a capacitive / plasmonic behavior as proposed from the SEC measurements in $TBAClO_4$-PC. Amongst the mixed oxides, MoWOx 1h exhibited the most promising performances, owing to a greater quantity of free charge carriers leading to a greater optical absorption. Even though $WO_{3-\delta}$ 1h displayed faster kinetics and a more selective modulation towards NIR in the intermediate state (+0.0 V), a greater proportion in capacitive behavior was shown in both MoWOx formulations. In addition, the MoWOx, especially in the 1h case, displays a very peculiar and novel optical behavior in the as-deposited state and after +1.0 V polarization ("bleached"), involving a large transmittance in NIR coupled with relatively strong absorption in VIS corresponding to a so-called "warm" optical mode (VIS/light-blocking and NIR/heat-transparent). In comparison to the existing literature regarding dual band formulations, summarized in **Table 3. 8**, MoWOx 1h performs well in terms of NIR contrast, in both intermediate and dark states, and VIS contrast in the intermediate state. However, our mixed oxide material lacks some modulation in the VIS region, and its CE values are far lower than those reported in the surveyed works of the literature. This could be due to the colloidal synthesis route used in these latter, carried out under inert atmosphere and usually granting a more refined level of control over the size, morphology, composition and stoichiometry of the produced particles. Given these results, such synthesis approach should be considered for future research work about the MoWOx formulations. Nonetheless, the "warm" mode offered by our MoWOx represents a technological opportunity that should be maintained through future trials and developments. Besides, the loss of the dual-band functionality of the active formulations should be further investigated: from the proposed paths of deterioration, the samples could be assembled with a counter electrode in a glove box, using dry reactants and encapsulating the complete device to avoid any water or oxygen in the system, as to rationalize their impact on the functionality of the materials.

Table 3. 8: Comparison of key performance indicators of dual band electrochromic materials from the literature and the MoWOx 1h formulation

Formulations	**ΔT_{VIS} (%) (intermediate)**	**ΔT_{VIS} (%) (dark)**	**ΔT_{NIR} (%) (intermediate)**	**ΔT_{NIR} (%) (dark)**	**CE (cm^2 C^{-1}) (Intermediate)**	**CE (cm^2 C^{-1}) (Dark)**
$WO_{3-\delta}$ [43]	15	83	59	93	102	184
Nb-TiO_2 [44]	10	70	45	60	Not mentioned	Not mentioned
$Nb_{12}O_{29}$ [45]	20	70	60	80	77 (VIS) 186 (NIR)	136 (VIS) 70 (NIR)
MoWOx 1h (this work)	16	24	45	67	16 (VIS) 35 (NIR)	4 (VIS) 11 (NIR)

3.4. Conclusions and perspectives

This chapter shows that novel electrochromic materials based on mixed molybdenum – tungsten oxide formulations ($Mo_yW_{1-y}O_{3-\delta}$, "MoWOx") can be obtained from single-step solvothermal synthesis procedures, with various Mo/W stoichiometries and reaction times being investigated; these compounds are then spin-coated into thin films that attest dual-band optical modulation. Specifically, a VIS/NIR-selective electrochromic behavior is observed in MoWOx 2/1 formulations obtained after 1h and 12h of synthetic duration, as well as in the parent $WO_{3-\delta}$ formulation obtained after 1h; a preferential NIR-darkening is obtained when a slightly reducing potential of +0.0 V (vs. Ag/AgCl) is applied, followed by an opacification over both VIS and NIR regions when using a more reducing potential of -1.0 V. The dual-band properties exhibited by these materials are correlated to the presence of a large amount of unpaired electrons, obtained through the promoted formation of oxygen vacancies and reduced species during the synthesis, and to the presence of nanostructures (nanospheres of $WO_{3-\delta}$ 1h, and nanorods at the surface of the MoWOx urchins) allowing them to support LSPR features. Amongst the mixed oxides formulations, MoWOx 1h displays the most remarkable optical performances, with large transmittance contrasts in both VIS (23.5 %) and NIR (66.6 %) regions, as well as a greater proportion in the capacitive contribution to the electrochromic processes. Nevertheless, the parent $WO_{3-\delta}$ 1h formulation exhibits higher coloration efficiencies than both MoWOx oxides, mostly because of the nanospherical morphology of the particles probably providing more surface area for the plasmonic features to be expressed. In addition, while the presently processed $WO_{3-\delta}$ nanostructures display a behavior similar to what was expected from previous work of the literature[10,11,14–16], MoWOx compounds present a “warm” mode (VIS-darkened, NIR-transparent) in the as-deposited state and after +1.0 V polarization (“bleached”), which, to the best our knowledge, has not been reported so far with tungsten or molybdenum oxide based electrochromic materials. This uncommon optical state is therefore uniquely obtained thanks to the large quantity of free charge carriers originating from the Mo/W mixing process, leading to a strong optical absorption signal centered around 850-900 nm. Such a remarkable solar filtration behavior could ultimately be of great interest to improve the functionality of fenestration solutions in buildings by broadening the modes of solar tunability, and therefore the adaptability range of the devices towards different weathers, seasons, geographies and/or user’s needs.

Within the scope of this research work, we attribute the dual-band electrochromism of MoWOx to the presence of both plasmonic excitation (in the IR) and polaronic-like resonance (in the visible), in line with the proposed interpretation of the electrochemical response of reported $WO_{3-\delta}$ nanoparticles[10,12,13] and with the detailed analysis of the Kubelka-Munk experiment on the compounds studied herein[38]. The debate of the link between the doping mechanism (capacitive/faradaic) and the type of excitation (plasmonic/polaronic) is however still open. The clear modification of the optical response when the redox potential reaches negative enough value to allow the cation insertion supports the hypothesis of a causal relation between the cationic insertion and the polaronic optical response. However, simulations performed in literature show that inserted cations are totally ionized and occupy existing cavities in WO_3 with no local deformation of the atomic structure[39,40]. In that case, both capacitive and faradaic doping would have the exact same effect on the optical response. The modification of the structural parameter following the cation insertion could then be associated with the charge doping of the crystal[41]. Further experimental and numerical investigations are required to settle the debate, but this goes beyond the scope of the present work.

Future developments of MoWOx materials processing should be directed towards the consolidation of their electrochromic performances, notably the switching speed and reversibility. Moreover, additional electrochemical characterization will be required to better understand the limitations faced by the MoWOx materials. For example, by modifying the shape and size of the counter electrode to avoid high current densities that could damage the sample, or by monitoring the ageing of the samples during cycling at given temperature and humidity levels. If necessary, the synthetic and deposition processes could be adapted in order to obtain more favorable morphologies, optical and electronic properties, leading to improved performances of the films. The addition of surfactant or different solvents (or mix of aqueous/organic solvents) to the solvothermal process could be investigated in an attempt to favor the production of nanometric particles, more inclined to display highly efficient plasmonic optical properties. In addition, several other synthetic paths could be explored, such as colloidal synthesis or supercritical processes, but also different deposition methods like spray coating[42], allowing for the scale-up of the film processing. Finally, the next step after reaching convincing electrochromic properties will be to fabricate full devices comprising the active layer, a suitable counter electrode material (either electrochromically active such as NiO, or optically neutral/passive such as CeO_2), and an electrolyte layer, all incorporated between two conducting glass substrates.

With this work as a first proof of concept of the original, advanced optical functionality of the MoWOx formulations, the results presented herein are very promising for the future development of highly efficient, dual-band electrochromic systems based on these mixed oxides formulations. Relying on the enhanced efficiency and selectivity of these materials towards VIS and NIR wavelength ranges, looking into their ability to access multiple working modes, the MoWOx formulations are promising candidates for the development of “new generation” dual – band smart windows.

3.5. References

1. Scriven, L. E. *MRS Proc.* **1988**, 121, 717, doi.org/10.1557/proc-121-717.
2. https://www.spincoater.com/what-is-spin-coating.php, accessed on 13/09/2024.
3. Gillissen, F. Hybrid molybdenum-tungsten oxide as novel plasmonic electrochromic nanomaterial. (Université de Liège, Liège, Belgique, 2019).
4. Granqvist, C. G. *Electrochim. Acta* **1999**, 44, 3005, doi.org/10.1016/s0013-4686(99)00016-x.
5. Li, H. *et al*. *J. Mater. Chem. C* **2015**, 4, 33, doi.org/10.1039/c5tc02802g.
6. Li, H. *et al*. *Nano Energy* **2018**, 47, 130, doi.org/10.1016/j.nanoen.2018.02.043.
7. Zhou, H. *et al*. *Appl. Mater. Interfaces* **2017**, 9, 18669, doi.org/10.1021/acsami.7b01871.
8. Inamdar, A. I. *et al*. *Mater. Lett.* **2018**, 215, 233, doi.org/10.1016/j.matlet.2017.12.109.
9. Dahlman, C. J. *et al*. *J. Am. Chem. Soc.* **2015**, 137, 9160, doi.org/10.1021/jacs.5b04933.
10. Runnerstrom, E. L. *et al*. *Chem. Commun.* **2014**, 50, 10555, doi.org/10.1039/c4cc03109a.
11. Tandon, B. *et al*. *J. Phys. Chem. C* **2022**, 126, 9228, doi.org/10.1021/acs.jpcc.2c02155.
12. Agrawal, A. *et al*. *Chem. Rev.* **2018**, 118, 3121, doi.org/10.1021/acs.chemrev.7b00613.
13. Wang, Y. *et al*. *Annu. Rev. Chem. Biomol. Eng* **2016**, 7, 283, doi.org/10.1146/annurev-chembioeng-080615-034647.
14. Zhang, S. *et al*. *Appl. Mater. Interfaces* **2019**, 11, 48062, doi.org/10.1021/acsami.9b17678.
15. Zhang, S. *et al*. *Mater. Horizons* 2018, **2018**, 5, 291, doi.org/10.1039/c7mh01128h.
16. Zhang, S. *et al*. *Energy Environ. Sci.* **2018**, 11, 2884, doi.org/10.1039/c8ee01718b.
17. Barawi, M. *et al*. *J. Mater. Chem. A* **2018**, 6, 10201, doi.org/10.1039/c8ta02636j.
18. Yilmaz, P. *et al*. *ACS Appl. Energy Mater* **2020**, 3, 3779, doi.org/10.1021/acsaem.0c00241.
19. Denayer, J. *et al*. *Sol. Energy Mater. Sol. Cells* **2014**, 130, 623, doi.org/10.1016/j.solmat.2014.07.038.
20. Yin, H. *et al*. *J. Phys. Chem. C* **2017**, 121, 23531, doi.org/10.1021/acs.jpcc.7b08403.
21. Salje, E. *et al*. *Philos. Mag. B* **1984**, 50, 607, doi.org/10.1080/13642818408238882.
22. Hassani, H. *et al*. *Phys. Rev. B* **2022**, 105, 014107, doi.org/10.1103/physrevb.105.014107.
23. Bousquet, E. *et al*. *Phys. Rev. Res*. **2020**, 2, 012052, doi.org/10.1103/PhysRevResearch.2.012052.
24. Salje, E. K. H. *Eur. J. Solid State Inorg. Chem.* **1994**, 31, 805, https://www.researchgate.net/publication/235328412.
25. Triana, C. A. *et al*. *J. Appl. Phys.* **2015**, 118, 024901, doi.org/10.1063/1.4926488/140587.
26. Hassani, H. First-principles study of polarons in WO_3 (University of Liège, **2023**).
27. Lounis, S. D. *et al*. *J. Phys. Chem. Lett.* **2014**, 5, 1564, doi.org/10.1021/jz500440e.
28. Orel, B. *et al*. *J. Solid State Electrochem.* **1998**, 2, 221, doi.org/10.1007/s100080050092.

29. Nang Dinh, N. *et al*. *Sol. Energy Mater. Sol. Cells* **2011**, 95, 618, doi.org/10.1016/j.solmat.2010.09.028.

30. Wang, S. *et al*. *NPG Asia Mater.* **2021***,* 13, 1, doi.org/10.1038/s41427-021-00319-7.

31. Garcia, G. *et al*. *Adv. Opt. Mater.* **2013**, 1, 215, doi.org/10.1002/adom.201200051.

32. Garcia, G. *et al*. *Nano Lett* **2011**, 11, 4415, doi.org/10.1021/nl202597n.

33. Liang, Y. *et al. ACS Appl. Electron. Mater.* **2022**, 4, 5118, doi.org/10.1021/acsaelm.2c01225.

34. Tran, N. *et al*. *Chem. Mater.* **2008**, 20, 4815, doi.org/10.1021/cm070435m.

35. Ohsaka, T. *et al*. *Mater. Res. Bull.* **2001**, 36, 2141, doi.org/10.1016/S0025-5408(01)00690-0.

36. Pérez-Flores, J. C. *et al*. *RSC Adv.* **2012**, 2, 3530, doi.org/10.1039/c2ra01134d.

37. Jouanneau, S. *et al*. *Solid State Ionics* **2001**, 140, 223, doi.org/10.1016/S0167-2738(01)00811-6.

38. Lobet, M. *et al. (Preprint) arXiv:*2406.02181, v1, submitted: Jun **2024**. https://arxiv.org/abs/2406.02181*.*

39. Okada, M. *et al*. *J. Am. Ceram. Soc.* **2019**, 102, 5386, doi.org/10.1111/jace.16414.

40. Bondarenko, N. *et al*. *Phys. Rev. B - Condens. Matter Mater. Phys.* **2015**, 92, 165119, doi.org/10.1103/physrevb.92.165119.

41. Walkingshaw, A. D. *et al*. *Phys. Rev. B - Condens. Matter Mater. Phys.* **2004**, 70, 1, doi.org/10.1103/physrevb.70.165110.

42. Maho, A. *et al*. *Coatings* **2023**, 13, 1, doi.org/10.3390/coatings13111879.

43. Zhang, S. *et al*. *Mater. Horizons* **2018**, 5, 291, doi.org/10.1039/c7mh01128h.

44. Lu, H.-C. *et al*. *ACS Nano* **2020**, 14, 10068, doi.org/10.1021/acsnano.0c03283.

45. Barawi, M. *et al*. *ACS Nano* **2017**, 11, 3576, doi.org/10.1021/acsnano.6b06664.

Chapter 4 – Development of efficient passive counter electrode materials for electrochromic devices

Chapter 4 – Development of efficient passive counter electrode materials for electrochromic devices

4.1. Introduction

While the previous chapters of this thesis mainly focused on novel working electrode materials, electrochromic devices also require an electrolyte layer, and more importantly, a counter electrode material, which can be either optically active or passive (**Figure 4.1**)[1,2]. An active counter electrode is an electrochromic material that colors / bleaches in complementarity with the working electrode electrochromic material (for example, NiO as counter electrode for WO_3: NiO colors upon oxidation while WO_3 colors upon reduction, and reversibly)[1–4]. In the other case, a passive counter electrode is able to store cations during the electrochemical cycling without modification of its optical properties[1,2,5–9].

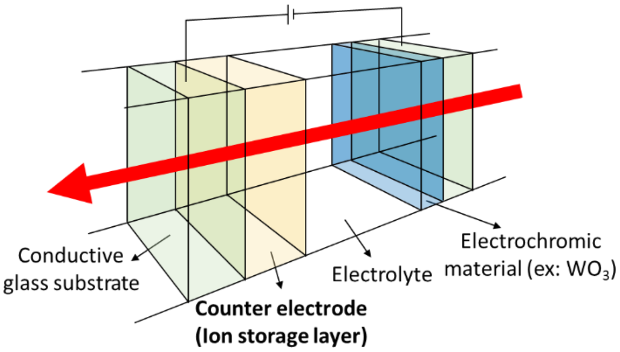

Figure 4.1: Schematic representation of an electrochromic device with the counter electrode indicated in bold in the system[1]*.*

Amongst the passive counter electrode materials reported in the electrochromic literature, cerium oxide is probably sparking the strongest interest in the research community. Indeed, this material displays a high transparency over a large interval of wavelength – especially in the visible range given its large band gap (3.2 eV) – as well as the ability to easily switch between Ce^{4+} and Ce^{3+} states when cations (H^+, Li^+, K^+…) are inserted/extracted into/from the crystal lattice during the electrochemical cycling[8–11]. However, while displaying a good reversibility towards lithium insertion[12], the slow reaction kinetics and lower capacity of cerium oxide, in comparison to usual electrochromically active materials (such as WO_3), can be a limiting factor for the performance of the final device[7,13–15]. Usually, it is accepted that the slow kinetics of the insertion reaction arise from the diffusion of the lithium into the lattice of the CeO_2, being the limiting step. Moreover, there is a large difference between the size of the insertion site (1.02 Å) and the Li^+ cation (0.60 Å), which is not favorable for the effective insertion of cations[12]. In order to overcome these issues, numerous attempts were reported in the literature, working towards the improvement of the opto-electronic properties of cerium oxide. In particular, the introduction of other transition metals (V[7,13,14], W[16], Ni[7,8], Co[7–9], Cu[8], Mn[17], Ti[10,13–16], Zr[8,10,13,14], Y[9]) and non-transition metals (In[7], Sn[9,10,13,14], Sm[7–9], Sr[8], Gd[7,9], Er[8,9], Si[10]) as doping elements has allowed improvements in the capacity, kinetics and electrochemical cycling stability of cerium oxide. Amongst the various doping agents identified in previous works of the literature, molybdenum has been proposed as an interesting candidate by Verma *et al.*[15]. In addition, Daubry *et al.* suggested using smaller dopant species in order to obtain a better complementarity between the size of the active sites and the Li^+ cations[12]: molybdenum indeed follows this condition, with its ionic radius of 0.75 Å being smaller than that of cerium (1.03 Å)[8]. However, the optical and electrochemical performances of such Mo doped CeO_2 passive counter electrodes have never been investigated yet. In addition, the choice of molybdenum as a doping candidate for transparent electrodes for electrochromic applications is further consolidated by the good results obtained by Orel *et al.*[6] and Krašovec *et al.*[5], highlighting an improvement in the performances of SnO_2, another material used as passive counter electrode in the electrochromic field and displaying the same valency than CeO_2. The expected increase in capacity arising from Mo doping of CeO_2 could be due to the presence of new redox centers in the doped material, arising from the multiple oxidation states available in Mo [6] and the creation of oxygen vacancies upon doping due to the different size and valence of the Mo ion in comparison to Ce [18], allowing greater insertion of cations into the counter electrode layer. When Mo(+VI) replaces Ce(+IV) in the face-centered cubic structure of CeO_2, the Mo atom is bound to 8 oxygens, each of them shared between 4 Ce/Mo atoms. In the case of Ce(+IV), this results in the electrons of the oxygen compensating for the positive charge, leading to the electroneutrality of the material. Meanwhile, in the same environment, Mo would still bear a 2+ charge: to restore the electroneutrality, oxygen atoms can be stripped from the structure, resulting in the freeing of electrons able to localize on the Mo to compensate for the remaining positive charge.In the scope of this work, Mo doping/substitution has been shown to improve the electrochemical capacity and to increase the concentration in oxygen vacancies in the investigated MoWOx formulations discussed earlier, which is also a good indicator of the viability of this approach to improve the optoelectronic properties of a material through the tuning of its composition.

While multiple deposition methods have been used to produce CeO_2 based passive counter electrodes, most of the work done on doped CeO_2 implemented sputtering and wet deposition routes such as spin coating and spray pyrolysis. Ultrasonic Spray Pyrolysis (USP) is a remarkable wet coating methodology that has to be further explored for such materials. This technology relies on the pulverization of a liquid precursor (solution or suspension) onto a heated substrate, reaching temperatures sufficient to dry the solvent and decompose the reactants into a solid (an oxide in the present case), deposited as a film at the surface of the substrate (**Figure 4.2a**)[19,20]. With the use of an ultrasonic generator within the spraying nozzle, the USP approach offers greater control over the homogeneity of the produced droplets, by breaking potential aggregates in suspension, and generating a narrower distribution of droplet of smaller sizes. In comparison to the aforementioned deposition techniques, USP presents multiple advantages, being less energy intensive than vacuum methods such as sputtering[21], inducing lower levels of overspray than classical spray deposition[22,23], and unlike spin coating, it allows the up-scaling of the process for future developments into larger scale production[23,24]. When using USP as a deposition method, the properties of the precursor solution (viscosity, surface tension, solvent) can be tuned in order to produce high quality films. For example, surfactants such as polyethylene glycol (PEG) can be added to the precursor solution in an attempt to obtain smoother films: this approach has already been demonstrated in previous work carried out at the GREEnMat laboratory, especially in the field of electrochromic materials (WO_3, NiO, LiNiO)[19,25]. The addition of PEG in appropriate amounts can lower the surface tension of the solution, leading to a smaller size distribution in the droplets and a better spreading of the latter over the surface of the substrate, avoiding “coffee ring” effect due to the material concentrating at the edges of the droplet during the evaporation of the solvent (**Figure 4.2b**). This also leads to improved optical properties because of the decreased diffusion of light in the homogeneous films, yielding more transparent films. In this context, the selection of PEG 400 as surfactant is motivated by the compromise it offers: its viscosity is not too high, as to not obstruct the tubing of the USP equipment, but still enough to positively impacts the properties of the deposition solution.

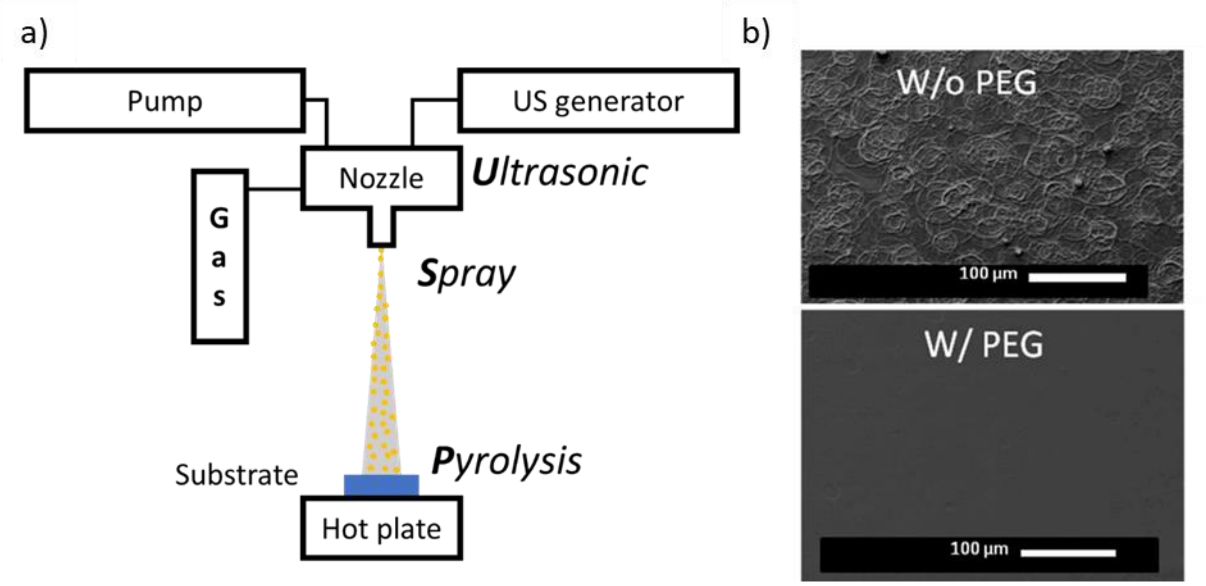

Figure 4.2: Schematic representation of the ultrasonic spray pyrolysis (USP) deposition process (a)[26], and SEM micrographs of PEG-assisted USP deposited WO_3 (b)[27].

In this section, films of Mo doped CeO_2 are produced in a single step protocol through PEG assisted aqueous USP coating method. The films are then characterized in terms of their morphology, crystallinity, optical and electrochemical properties in order to rationalize the impact of the incorporation of molybdenum in various concentrations on the physicochemical and optoelectronic properties of the material and assess their potential as passive counter electrode material for electrochromic applications.

4.2. Materials and Methods

Materials. Cerium (III) chloride heptahydrate ($CeCl_3.7H_2O$) and molybdenum chloride ($MoCl_5$, 95%) were purchased from Merck, polyethylene glycol (PEG, average Mn 400) and lithium perchlorate ($LiClO_4$, 95% anhydrous) from Alfa Aesar, and propylene carbonate (PC, 99.7% anhydrous) from Sigma-Aldrich. The films are deposited onto fluorine doped tin oxide (FTO) covered glass from Greatcell Solar (TEC15, 15 Ω sq^{-1}, 2.2 mm thick). All chemicals are used as received without further purification.

Sample preparation. The samples are prepared adapting a USP protocol used in previous works of GREEnMat[19,25], with the parameters tuned to reproduce the conditions met in the surveyed literature[7–10,13–16]. The main parameters are presented in **Table 4.1** below. First, the FTO glass substrates are cut into 2.5 x 2.5 cm^2 pieces and their edges are beveled in order to avoid the formation of cracks during deposition. The pieces are then washed with soap, acetone and ethanol under ultrasonication, and finally blow dried with air. The reactive solution is prepared by dissolving 0.05 M of metal chloride (Ce + Mo) and an appropriate amount of PEG (the optimum will be discussed in the results) in milli-Q water for the synthesis of pure and Mo-doped CeO_2 (Mo %at. = 2, 4, 6, 8, 10%), referred to as CeMo0, CeMo2, CeMo4, CeMo6, CeMo8 and CeMo10. The doping rate is limited to 10% based on the available CeO_2 spray coating literature, but also because MoO_3 is electrochromic: too large of a concentration would result in the loss of the passive behavior of the electrode. The deposition of the films is carried out on a Sono-Tek ExactaCoat automated spray system equipped with an AccuMist nozzle. In this configuration, 20 mL of the solution is used for the deposition of films onto pre-heated FTO glass substrates (T_{sub} = 300 - 450°C). The spraying nozzle is located 5.5 cm above the surface of the substrate, following a S-shape deposition pattern at a speed of 40 mm/s, with a solution flow rate of 0.25 mL/min. The pressure of the carrier gas (clean air) is set to 0.5 psi and the ultrasound generator is operated at 3W[19,25]. The substrates are kept on the heating plate for 5 minutes before and after the spraying process to allow the surface of the substrate to reach the desired set temperature and to complete the decomposition of the precursors into oxides after the deposition.

Table 4.1: Summary of the synthesis parameters used in this work and where they were adapted from.

Parameters	Value	Adapted from
Concentration	0.05 M	CeO_2 literature
Doping rate	1 – 10 %	
T_{sub}	300 – 450 °C	
Nozzle distance	5.5 cm	GREEnMat protocol
Nozzle speed	40 mm/s	
Flow rate	0.25 mL/min	
Pressure	0.5 psi	
Power	3 W	

Sample characterization. The morphology and thickness of the samples are characterized on samples in top view and cross section by scanning electronic microscopy (SEM), on a TESCAN CLARA. X-ray diffraction (XRD) patterns are acquired on a Bruker D8 DISCOVER with Cu Kα (λ = 1.5418Å), operated in grazing incidence mode, with the incident X-ray beam fixed at a Theta angle of 1°. Raman spectra of the samples are acquired using a Horiba LabRAM 300 interfaced with a 785 nm laser and an Olympus BX40 microscope. The composition and surface properties of the films are investigated using a Thermofisher K-alpha X-ray photoelectron spectrometer (XPS), equipped with a monochromatic Al Kα source and calibrated with the adventitious carbon (C1s) peak. Total and diffuse transmittance spectra are acquired using a Shimadzu UV-3600i Plus spectrophotometer equipped with an ISR-1503 integrating sphere. The electrochemical properties of the films are assessed using a Biologic SP-200 potentiostat/galvanostat for cyclic voltammetry (CV) and chronoamperometry (CA) measurements. Spectroelectrochemical (SEC) measurements are carried out in a three-electrode configuration, consisting in a reference electrode (Ag/AgCl), a counter electrode (Pt foil) and the working electrode (sample) in an optical glass cell, connected to the potentiostat and placed inside the measurement chamber of the spectrophotometer in direct mode.

4.3. USP deposition of CeO_2 films: optimization of the deposition parameters

4.3.1. Temperature

In a first step, the deposition parameters used for the production of pure CeO_2 films are optimized. As a starting point, the conditions are kept identical to those reported in previous projects carried out at the GREEnMat laboratory, in particular for the deposition of electrochromic WO_3 thin layers[19]. The initial parameters are detailed in the **Materials and Methods** section, with the impact of the temperature on the properties of the pure CeO_2 films being investigated by varying the latter from

300°C to 450°C, corresponding to the range of temperatures used in the previous works studying CeO_2 spray coating[7–10,13–16]. The temperature should be high enough that the pyrolysis takes place in an efficient fashion, but should not be too high as the precursors would not reach the substrate before all of the solvent evaporates. Samples produced for four temperatures (300°C, 350°C, 400°C and 450°C) are methodically characterized from a morphological, structural, optical and electrochemical point of view.

The SEM top view and cross sections of the four films are presented in **Figure 4.3**, highlighting the poor coverage of the FTO glass substrates, with disperse particles spread over the surface of the film and the presence of "coffee ring" patterns, arising from the concentration of the material at the edge of the droplets as they dry on the pre-heated glass. The thickness of the deposited layers is measured from the cross sections of the films (**Figure 4.3b, d, f, h**), starting as low as 90 ± 30 nm and up to 220 ± 80 nm, with the general tendency indicating an increasing thickness as an inverted function of the temperature.

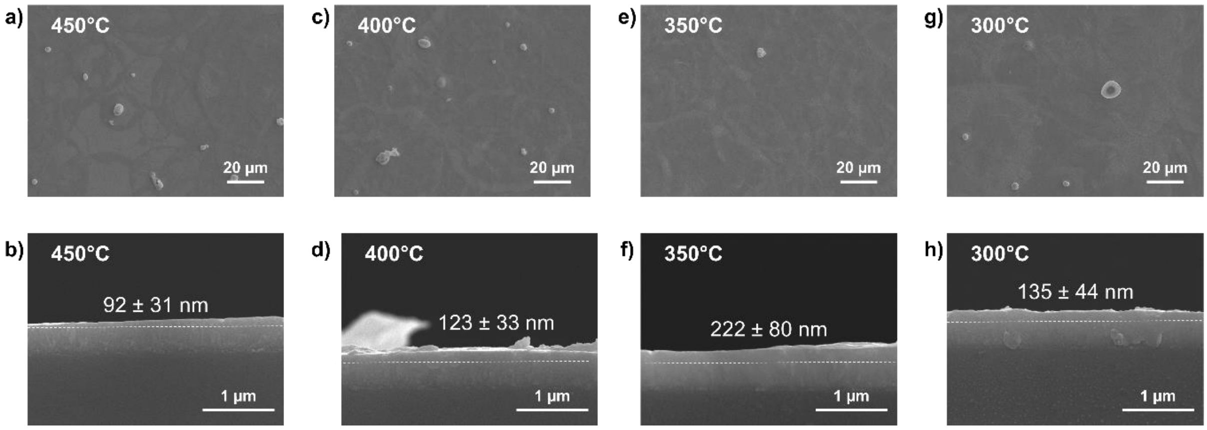

Figure 4.3: SEM top view and cross section micrographs of CeO_2 films deposited at 450°C (a, b), 400°C (c, d), 350°C (e, f) and 300°C (g, h). The dotted line in the cross sections indicate the interface between the FTO coating and the CeO_2 film.

Indeed, if the temperature increases, the solvent droplets dry faster during their flight-time, and the precursor can reach the substrate either as a gas, a liquid or a solid, resulting in a different film quality and homogeneity depending on each case. This effect is well represented in

Figure 4.4 below, schematically representing the evolution of the droplets as a function of temperature and time of flight[20]. In case A, the droplet is not completely dried before reaching the surface, the remaining solvent dries off onto the substrate and the contained precursors are decomposed into solid materials (cerium oxide in the present case). In the B case, no solvent is left as the precursors reach the substrate as salt precipitates (here, $CeCl_3$), that finally decompose into their corresponding oxides. If the temperature is further increased (case C), the precipitates are sublimated in-flight, the thus-formed vapor can be oxidized and deposited onto the substrate to form a film similarly to what is observed in chemical vapor deposition (CVD). Finally, if the temperature of the substrate exceeds a given limit (case D), the material is formed on its way to the substrate, and cannot be deposited as a thin layer but rather as isolated particles on top of the conductive substrate. As a result, decreasing the temperature allows more material to reach the surface of the glass and, in turn, the production of thicker films.

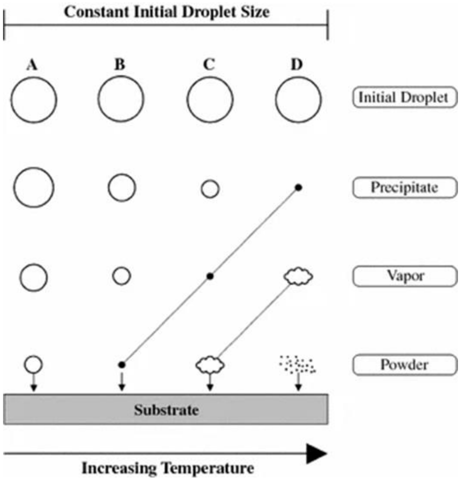

Figure 4.4: Schematic representation of the evolution of the droplets as a function of time of flight and temperature[20].

Regarding their structural properties, all four CeO_2 films display similar diffractograms (**Figure 4.5**) regardless of the deposition temperature, with several peaks appearing at 28°, 33°, 47° and 56° indexed as the (111), (200), (220) and (311) lattice planes, corresponding to the face centered cubic fluorite structure (PDF 01-086-4481), as expected from previous works of the literature[7–10,13–16] and the phase diagram of CeO_2[28]. The intense and sharp signals observed at 26°, 34°, 38°, 52° arise from the conducting FTO layer underneath the CeO_2 films, increasing in intensity in thinner films. Qualitatively, this result corroborates the observations made from the SEM cross section micrographs. In addition, the presence of the same phase throughout the different temperatures investigated shows that the crystallization of the material already takes place at temperature as low as 300°C[29], with a slight improvement in the sharpness of the signals with increasing temperatures. The average size of the crystallites is measured to be of 18, 12, 14 and 8 nm at 450°C, 400°C, 350°C and 300°C, respectively. These results confirm the viability of the temperature range (300 – 450°C) investigated in this study, with all samples exhibiting the desired crystalline phase.

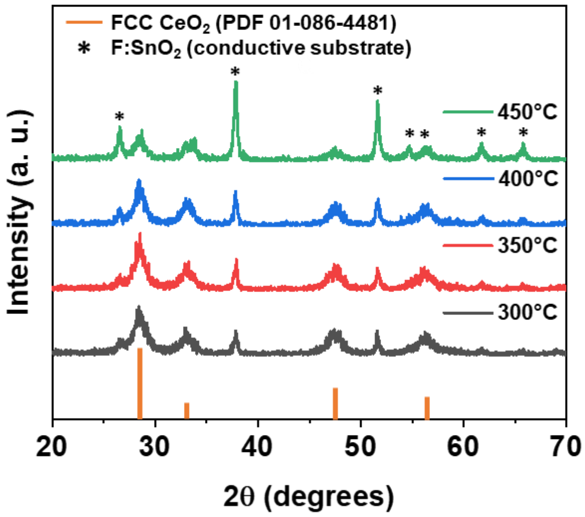

Figure 4.5: XRD diffractogram of the CeO_2 films spray coated at various temperatures.

Knowing that the films are successfully formed at the surface of the substrates with the desired crystalline phase, the electrochemical and optical properties of the films are characterized through several methods. First, cyclic voltammetry curves of the films are recorded between +1.0 and -1.0 V vs. Ag/AgCl at a scanning rate of 20 mV/s in 0.5 M $LiClO_4$/propylene carbonate. The electrochemical curves, presented in **Figure 4.6a**, display a reduction wave starting around -0.1 V when the potential is swept towards negative values, followed by an oxidation peak around 0.0 V on the way back, corresponding to the transition between Ce^{4+} and Ce^{3+} as a function of the potential, in good accordance with the values reported in the literature[7–9]. As the area under the CV curves can be used to evaluate the capacity of the material, it is clear that the lower temperature deposition conditions yield films displaying a greater capacity.

In order to further probe the capacity of the spray coated layers, additional measurements are carried out in a chronoamperometry regime (**Figure 4.6b**), leading to more cations being inserted/extracted during the electrochemical cycling, as the extreme potential values are applied constantly for longer duration in comparison to the CV. The samples are cycled in 0.5 M $LiClO_4$/propylene carbonate electrolyte, first by applying -1.0 V for a minute and then +1.0 V for another minute, following the same electrochemical profile as the convention of the literature, to be able to compare our results (**Table 4.2b**). The capacity is measured as the value reached after one minute of negative potential (corresponding to the insertion of the Li^+ cations). In addition, the reversibility of the redox processes is evaluated by comparing the inserted and extracted charges, respectively referred to as Q_{in} and Q_{out}. Q_{in} is defined as the difference in capacity after one minute at -1.0 V, while Q_{out} corresponds to that after +1.0 V is applied for the same duration. The electrochromic reversibility can be defined as the ratio between those two values, defined as **Equation 4.1**:

$$R = 100 * Q_{out}/Q_{in} \tag{4.1}$$

These results, presented in **Table 4.2**, highlight the increase in capacity already identified in the CV curves with the 300°C film displaying 9.1 mC/cm², corresponding to almost a two-fold increase in comparison to the film deposited at 450°C, indicating a greater amount of material deposited at the surface of the films when the temperature decreases. Moreover, the reversibility of the insertion / extraction process appears to be more efficient as the temperature decreases, indicating a better morphology and crystalline structure of the 350°C and 300°C films, less prone to irreversible insertion of cations into the lattice of the material.

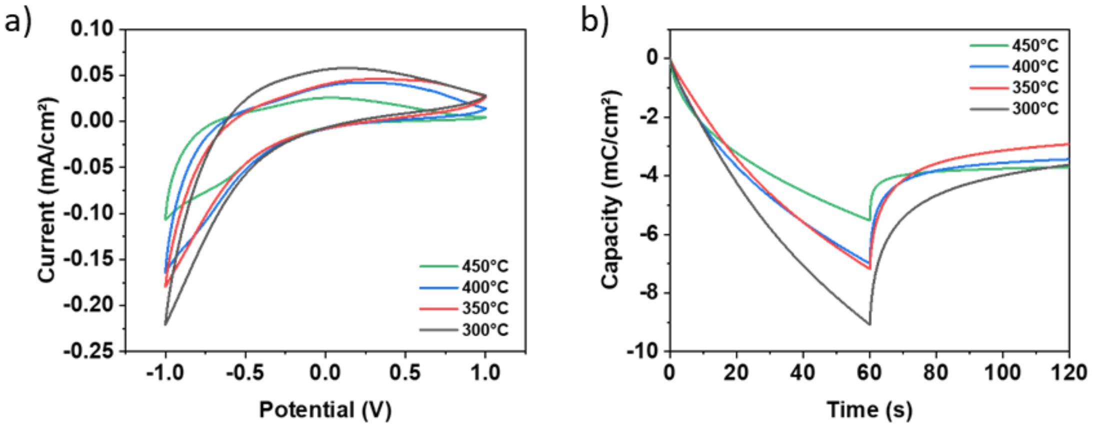

Figure 4.6: Cyclic voltammetry acquired in $LiClO_4$/PC, using Pt as counter electrode and at a scanning rate of 20 mV/s (a) and chronoamperometry (b) characterization of the CeO_2 samples spray coated at different temperatures.

Table 4.2: Quantification of the capacity and reversibility of the CeO_2 samples, calculated from the CA curves.

	Capacity / Q_{in} (mC/cm²)	Capacity / Q_{out} (mC/cm²)	Reversibility (%)
450°C	5.5	1.8	33
400°C	7.0	3.5	50
350°C	7.2	4.3	60
300°C	9.1	5.5	60

As passive counter electrode material, (Mo-doped) CeO_2 should display a high transparency in the visible range as to not infer with the active electrochromic electrode. On the basis of previous literature studying doped CeO_2 as a transparent electrode for electrochromic applications, a lower limit in transmittance was set to 70% (measured at 550 nm) as a performance indicator for the films produced herein, in order to not hinder the performances of a fully assembled device. In this context, the transmittance of the films is measured using an integrating sphere: measuring both the total transmittance and diffuse transmittance allow the calculation of the haze, quantifying to the cloudy appearance that can be found in transparent objects. For transparent applications, a haze of no more than only a few percent is usually required. It can be calculated using the following **Equation 4.2**:

$$Haze = 100 * \frac{T_d}{T_t} \tag{4.2}$$

With the T_t and T_d the total and diffuse transmittance, respectively. The results, presented in **Figure 4.7**, show a high transmittance of over 90% in all samples, especially at 450°C, expected from the thinner films produced at this temperature. On the other hand, the diffuse transmittance of the samples increases for lower temperatures. Even though the total transmittance of these formulations is very high, their diffusive behavior results in very large haze values, between 5 and 15% (**Table 4.3**). In these conditions, these samples must be further optimized before being considered as fully viable options for the long term development of efficient counter electrodes.

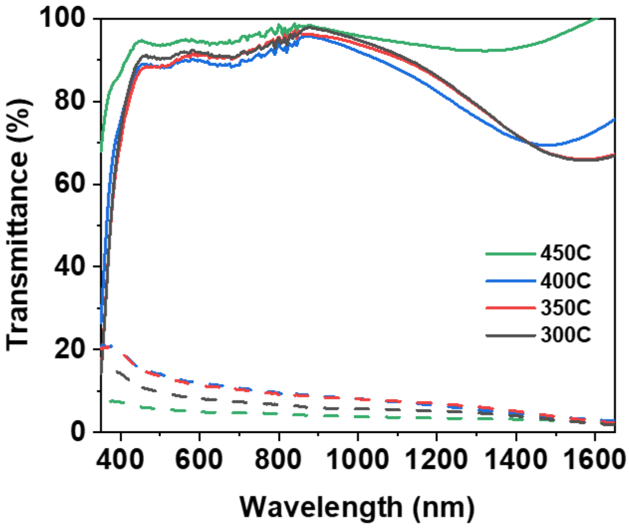

Figure 4.7: Total transmittance (solid lines) and diffuse transmittance spectra (dashed lines) of the CeO_2 layers deposited at different temperatures.

Table 4.3: Total and diffuse transmittance obtained from the optical characterization of the CeO_2 samples deposited at different temperatures, and haze values calculated from T_t and T_d.

	T_t at 550 nm (%)	T_d at 550 nm (%)	Haze (%)
450°C	94.6	5.3	5.6
400°C	89.6	12.9	14.4
350°C	90.1	12.3	13,7
300°C	91.7	8.7	9.5

To further check the optical properties of the produced films in similar conditions as their intended use, the samples are cycled in the $LiClO_4$ / PC electrolyte, with the potential applied for one minute before performing the optical measurement (under electrochemical bias conditions this time). Similarly to what has been presented in the previous chapter, the optical spectra are normalized as to subtract the FTO coated glass contribution from the signal, and only keep the influence of the working electrode. The transmittance spectra of the four samples are presented in **Figure 4.8**, all displaying transmittance well over 75% at 550 nm, and following the same trend as the other characterization methods, with the layers deposited at higher temperature being more transparent than those deposited at lower temperatures, with 80-85% of transmittance at 300-400°C and 95% at 450°C. Once again, these results point towards the effect of this parameter on the properties of the produced films, with temperature and thickness linked by an inversely proportional relationship. In addition, the investigated formulations display no electrochromic activity, i.e. no change of coloration/transparency, as expected from a passive counter electrode material. The CeO_2 processed here is thus considered as a promising starting material for the development and optimization of efficient counter electrodes. The 300°C sample, displaying the greater capacity amongst the considered formulations, while keeping a high level of transmittance, is selected for the next optimization steps investigated in this work.

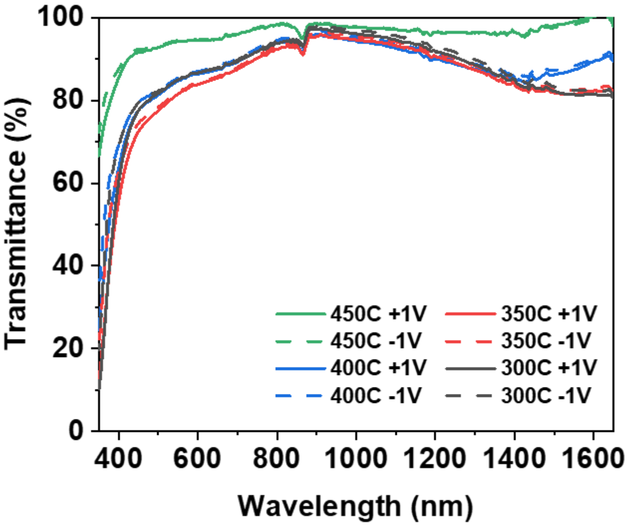

Figure 4.8: Spectroelectrochemical characterization of the CeO_2 films as a function of the applied potential, at +1.0 V (solid lines) and -1.0 V (dashed lines).

4.3.2. Addition of PEG

One approach for the improvement of the morphology of USP produced films lies in the use of additives in the precursor solution in order to fine tune its properties. In view of GREEnMat expertise, the addition of PEG in appropriate amounts to the deposited solution has been shown to greatly improve the quality of the films obtained by USP deposition. In particular, similar PEG assisted USP protocols have been implemented for the production of electrochromically active layers such as WO_3[19] and LiNiO[25], displaying improved performances. According to these works, the presence of PEG brings several ways of improvements, notably, the modification of the surface tension of the solution through the surfactant properties of the PEG, leading to a greater wettability between the droplets and the surface of the substrates, resulting in an improved morphology of the layers with a greater homogeneity and reducing the occurrence of "coffee ring" effect.

Based on the knowledge previously acquired by the GREEnMat team, and with the expected advantages and drawbacks arising from the addition of PEG into the precursor solution in mind, four formulations are investigated, with m_{PEG}/m_{Ce} ratio = 1/1, 2/1, 5/1 and 10/1[19], deposited at 300°C (strategically kept constant with the optimum temperature being determined in the previous section). The effect of the polymer is immediately visible on the micrographs of the samples, especially on the cross sections (**Figure 4.9**), showing a large increase in the thickness of the layers, with 250 ± 20 nm, 540 ± 140 nm, 750 ± 80 nm and 440 ± 50 nm for the 1/1, 2/1, 5/1 and 10/1 formulations respectively (the globular particle layer at the surface of the cross sections is a byproduct of the conductive gold sputtering deposited on the films before SEM imaging, the sputtering might have been too long for these particular samples). It appears that the thickness increases as a function of the amount of added PEG up until the 10/1 case, with the film appearing thinner than the previous samples. From the cross-section micrographs, it is visible that the morphology of the layers is impacted by the addition of the polymer, with the structure appearing as porous and less dense, especially in the case of PEG 2/1 and PEG 5/1. This could indicate that the thermal degradation of PEG into gaseous byproducts can result in an enhanced porosity of the films, corresponding to a large increase in the surface area of the samples, that could lead to improved electrochemical properties in comparison to bulk films. Moreover, as the PEG is thermally degraded during the deposition, more than 90% of the solid sprayed material is burned away from the film in the case of PEG 10/1, which would result in the deposition of thinner films, even when taking in account the gain in thickness arising from the then created porosity. Besides, the top view micrographs in **Figure 4.9** clearly show in improvement in the homogeneity of the deposited films, with the "coffee ring" effect disappearing as the PEG concentration increases, due to the enhanced properties of the solution in presence of this surfactant, resulting in the droplets spreading in a more even fashion on the substrate. In the case of a 10/1 PEG ratio, a continuous and very smooth film is visible at the surface of the substrate, but is covered with smaller particles, looking like cube edges. The formation of larger cubic particles on top of the continuous face-centerd cubic (fcc) CeO_2 film is probably due to the large modification of the solution properties brought with such an amount of polymer, modifying the viscosity of the solution and changing the deposition process at a smaller scale.

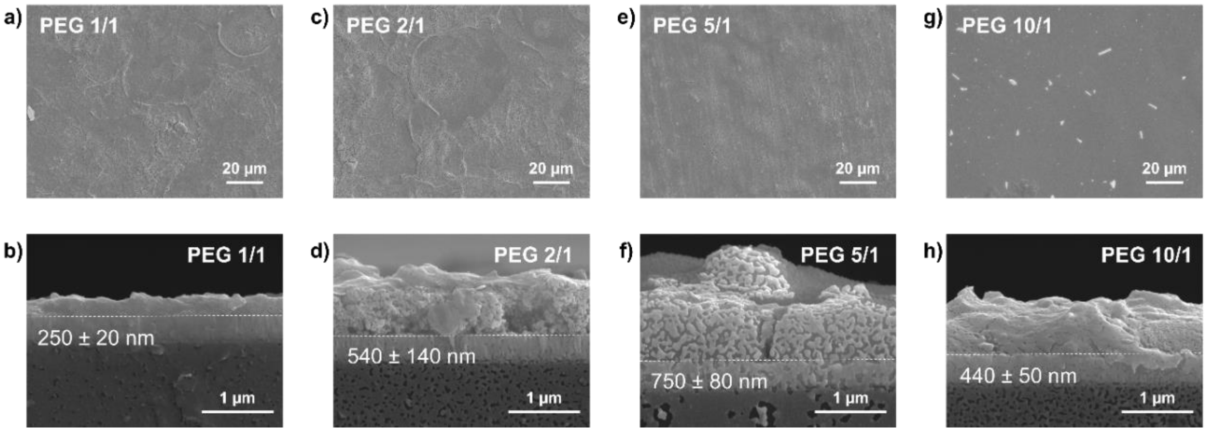

Figure 4.9: SEM top view and cross section micrographs of CeO_2 films deposited in the presence of PEG in a 1/1 ratio (a, b), 2/1 ratio (c, d), 5/1 ratio (e, f) and 10/1 ratio (g, h). The dotted line in the cross sections indicate the interface between the FTO coating and the CeO_2 film.

The structural analysis of the samples by XRD (**Figure 4.10**) shows similar diffraction signals as the non-PEG-assisted deposition process, with the intensity of the peaks corresponding to the FTO decreasing as the thickness of the layers increases. The crystalline phase of the materials can still be indexed as the fcc CeO_2 lattice, indicating that the PEG does not impede the good crystallization of the oxide during the deposition process and simultaneous thermal treatment.

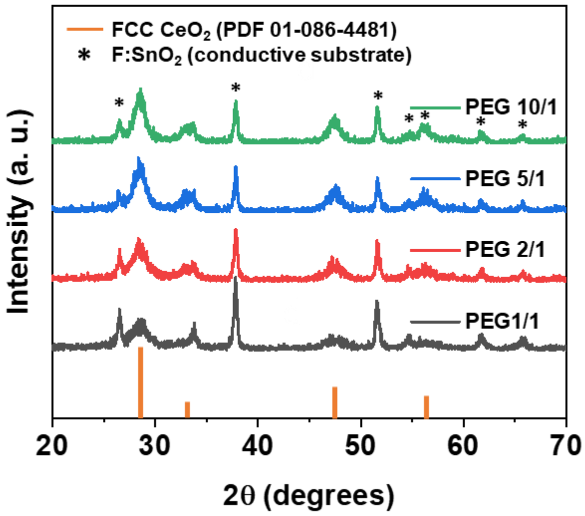

Figure 4.10: XRD diffractogram of the CeO_2 films spray coated in the presence of various PEG/Ce ratios.

With the confirmation of the crystalline phase, the impact of the improved morphology and increased thickness of the thin films on the electrochemical and optical properties is investigated. The CV curves displayed in **Figure 4.11a** kept a similar shape to those presented in the previous section, except that the oxidation peak is shifted towards more negative potential values. This observation could arise from the observed increase in thickness of the films when PEG is used. Indeed, as a film grows thicker, its polarizability decreases (ease of the material to change as a response to an electric field) and the CV peaks measured for this sample are shifted towards more extreme values of the potential because of the slower electron transfer kinetics in the electrode[30,31]. The capacity of the film is measured in CA conditions (**Figure 4.11b**), and highlights a large improvement in capacity for the 5/1 sample reaching a capacity of 15.0 mC/cm², followed by a large decrease in the 10/1 formulation, with a capacity of 8.4 mC/cm² (the measured capacities are summarized in **Table 4.4** below). The superiority of the 5/1 formulation could be due to the greater surface area of the material brought by the PEG degradation induced porosity, as shown in the SEM cross section measurements, while the sudden drop in the 10/1 sample could arise from the films becoming denser, giving access to less active sites and hindering its capacity. However, even though the 5/1 sample exhibits the largest capacity, its reversibility decreases in comparison to the other formulations. This could be due to the porosity of the film, that could trap some of the cations inside of the channels created in the structure.

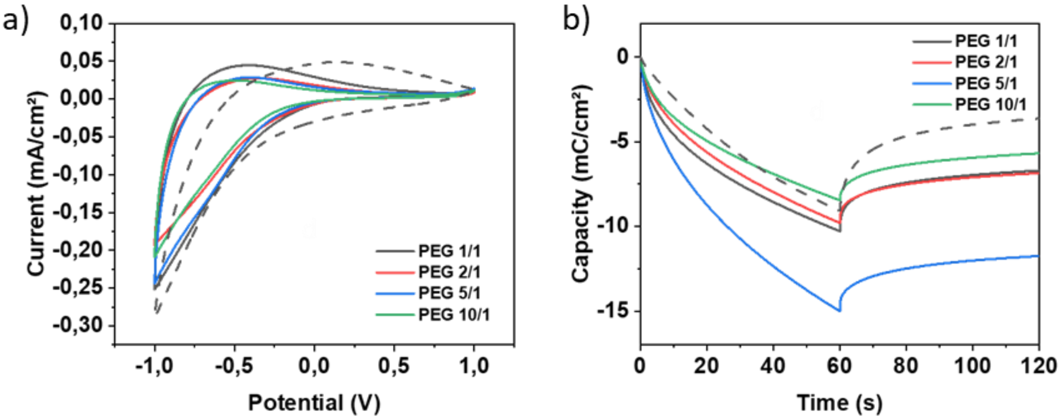

*Figure 4.11: Cyclic voltammetry acquired in $LiClO_4$/PC, using Pt as counter electrode and at a scanning rate of 20 mV/s (a) and chronoamperometry (b) characterization of the CeO_2 films spray coated in the presence of various PEG/Ce ratios. The dashed lines correspond to the results obtained without PEG in **Figure 4.6**.*

Table 4.4: Quantification of the capacity and reversibility of the CeO_2 samples, calculated from the CA curves.

	Capacity / Q_{in} (mC/cm²)	**Capacity / Q_{out} (mC/cm²)**	**Reversibility (%)**
No PEG	9.1	3.1	33
PEG 1/1	10.3	3.6	35
PEG 2/1	9.8	2.9	30
PEG 5/1	15.0	3.2	21
PEG 10/1	8.4	2.7	32

Besides, the optical characterization of total and diffuse transmittance demonstrates the effect of PEG addition on the morphology and homogeneity of the ion storage layers (**Figure 4.12**). Once again, the total transmittance of all four films is good, becoming more transparent as the PEG content increases. In the case of the diffuse transmittance, it appears to be worse than with no added PEG. T_d increases sharply for the 2/1 ratio, and then decreases as the surfactant behavior of the polymer takes effect, with the best results in the case of the 10/1 ratio, as already observed from the smooth surface of this formulation in the SEM micrographs. The calculated haze follows the same tendency as the diffuse reflectance, as observed in **Table 4.5**, increasing from the 1/1 to the 2/1 ratio before dropping in the case of PEG 10/1. As the PEG 5/1 ratio exhibits the largest capacity of the batch, while PEG 10/1 displays excellent optical properties, it would be interesting to find the best compromise between the two for future works and optimizations.

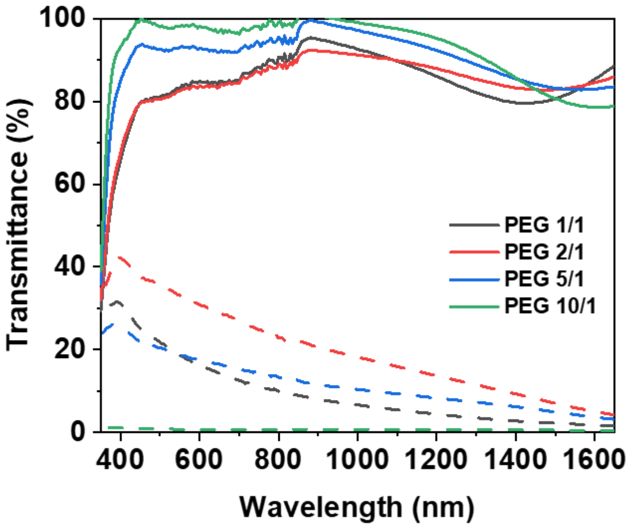

Figure 4.12: Total transmittance (solid lines) and diffuse transmittance spectra (dashed lines) of the CeO_2 films spray coated in the presence of various PEG/Ce ratios.

Table 4.5: Total and diffuse transmittance obtained from the optical characterization of the CeO_2 samples spray coated in the presence of various PEG/Ce ratios, and haze values calculated from T_t and T_d.

	T_t at 550 nm (%)	T_d at 550 nm (%)	Haze (%)
PEG 1/1	83.2	18.7	22.5
PEG 2/1	82.5	33.1	40.1
PEG 5/1	92.9	18.8	20.2
PEG 10/1	98.0	0.8	0.8

In addition, SEC characterization of the samples allows the dynamic investigation of their optical properties. In all formulations investigated in **Figure 4.13**:, no electrochromic modulation is detected upon cycling in the $LiClO_4$/PC electrolyte. Besides, the transmittance of the films evolves as a function of two parameters: the thickness of the layer and its homogeneity. Increasing the first one will cause a loss of transmittance due to a greater absorption cross section of the material, while an improvement in the second will result in a decreased diffusion of the incident light, translating into an improved direct transmittance and a more transparent appearance of the sample. In the 1/1 sample, the low thickness of the film results in a transmittance of 80.5%, close to that of the non-PEG-assisted sample. In the case of the 2/1 PEG ratio, the thickness increases but the amount of PEG is not yet sufficient to really improve the homogeneity and quality of the film, resulting in a decreased transmittance of 66.9%. Then, the addition of larger quantities of PEG starts to overcome the effect of the thickness, with the 5/1 formulation displaying a boost in transmittance back up to 74.9%, followed by the 10/1 ratio and its 99.2% in transmittance, arising from the highly homogeneous and smooth film produced in the latter case, in addition to being thinner.

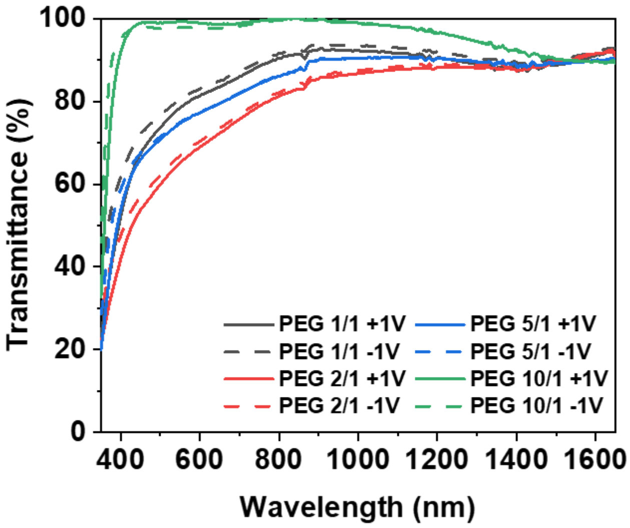

Figure 4.13: Spectroelectrochemical characterization of the CeO_2 films as a function of the applied potential, at +1.0 V (solid lines) and -1.0 V (dashed lines).

While the 10/1 PEG ratio provides the best optical results, with a transmittance close to that of a bare FTO glass, its lower capacity could be detrimental for its application as a passive counter electrode. Indeed, if the capacity of the counter electrode is too small in comparison to the working electrode, the performance of the latter could be hindered, especially its contrast and coloration efficiency. Therefore, the 5/1 ratio was chosen instead for the remainder of this work as the best formulation for the next step towards the improvement of the counter electrode electrochemical and optical performances, given its satisfying transmittance (75%) and capacity (15 mC/cm²).

Given the viscosity of the PEG surfactant used in the protocol, an additional test was conducted on the PEG 5/1 formulation, investigating the effect of a longer stirring time before deposition. Instead of one hour, the solution was left to agitate overnight in an attempt to obtain a highly homogeneous mixture. Preliminary SEM characterization of the films demonstrate a great improvement of the morphology (**Figure 4.14**), with a smooth surface appearing for the longer stirring time, resulting in a highly transparent film exhibiting very low haze (these results will be further detailed in the following section discussing the impact of molybdenum doping).

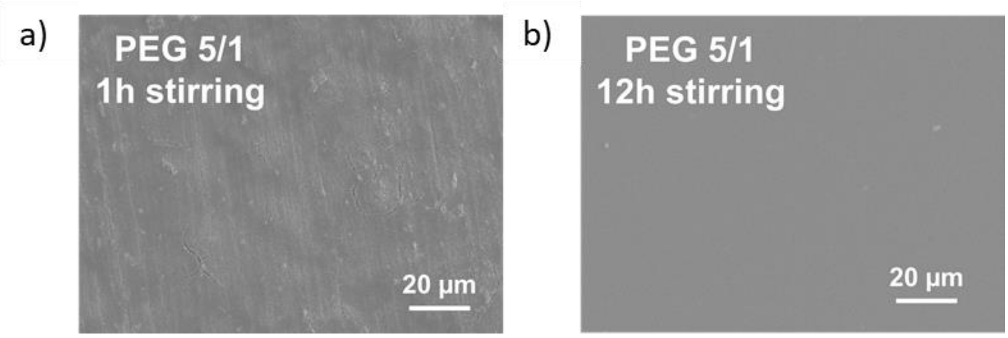

Figure 4.14: Comparison of the SEM micrographs of CeO_2 PEG 5/1 films after 1h and overnight stirring.

Table 4.6 below has been completed by surveying the literature discussing the influence of doping of cerium oxide for applications as a passive counter electrode for electrochromism. For now, the results presented in this table are limited to the undoped formulations produced by the authors as reference material to investigate the effect of doping (**Table 4.11**, presented later in this section, will discuss the performance of the doped formulations investigated in each of these studies of the literature). These previous works date back from 1998, up to 2022, and show a tendency in the choice for the deposition method, shifting from under-vacuum and expensive sputtering, to wet coating methods being more affordable and that can be carried out at ambient pressure and moderate temperature, first using spin coating, and then spray coating, with the latter allowing more homogeneous deposition and to scale up the process if required. In most cases, the selected formulations displayed little to no contrast at 550 nm, with a transmittance superior to 65%, while presenting various capacities ranging from 1 up to 21 mC/cm². Based on this literature survey, the pure CeO_2 produced herein through PEG-assisted USP deposition already surpasses all but one of the previous works in regards of the undoped capacity (15 mC/cm²), while its transmittance (74.9%) lies in the average of the literature standard. The quality of the results acquired for the undoped CeO_2 formulation produced in this work thus appears very promising for the development of a highly efficient counter electrode material based on the Mo doping of CeO_2 using PEG as a surfactant and USP for its deposition into thin films.

Table 4.6: Literature survey of the doped CeO_2 literature, temporarily focusing on the undoped results obtained in these works.

Author	Year	Deposition method	Thickness (nm)	Capacity (mC/cm²)	Transmittance at 550 nm (%)	Contrast at 550 nm (%)
Azens[16]	1998	Sputtering	450	/	85	5
Varsano[13]	1999	Sputtering	100	13.0	/	/
Verma[15]	2005	Spin coating	800	12.5	70	/
Bhosale[10]	2015	Spin coating	/	20.6	/	/
Dalavi[14]	2020	Spray pyrolysis @ 400°C	/	N/A	/	/
Zimou[8]	2021	Spray pyrolysis @ 450°C	/	0.9	65	/
El-Habib[9]	2021	Spray pyrolysis @ 450°C	/	/	65	≈0
El-Habib[7]	2022	Spray pyrolysis @ 450°C	/	5.4	80	≈0
This work	2024	USP @ 300°C		9.1	85	≈0
		USP + PEG 5/1 @ 300°C		15.0	75	≈0

4.4. Rationalization of the effect of Mo doping on the properties and performances of CeO_2 films

4.4.1. Morphological and structural characterization of the Mo doped films

With the optimized deposition conditions identified, this section of the chapter will focus on the investigation of the doping concentration and its effect on the properties of the films produced. As explained earlier, the addition of dopant species into CeO_2 can result in improvement of the material properties, with numerous tested elements highlighting improved performances in the corresponding doped CeO_2 formulations.

In the scope of this work, doped CeO_2 films containing from 2 up to 10% of Mo were produced following the same protocol as the optimal pure CeO_2 sample discussed in the previous section: the deposition took place at 300°C, with 5 passes of a solution containing 0.05 M of precursor ($M_{Ce} + M_{Mo} = 0.05$ M) and PEG in a 5/1 ratio. The only difference lies in the fact that in this case the deposition solution was kept under magnetic stirring overnight to make sure the molybdenum precursor is completely solubilized and the mixture is homogeneous. As a reminder, the doped formulations are referred to as CeMo2, CeMo4, CeMo6, CeMo8 and CeMo10 (cf. **Materials and Methods**), while the undoped optimized sample corresponds to CeMo0. From the top view micrographs (**Figure 4.15**) and cross sections (**Figure 4.16**), it is possible to investigate the impact of the concentration in the doping agent on the morphology of the films and their thickness. From a morphology standpoint, highly smooth and homogeneous films are produced in the case of the undoped formulation, highlighting the benefits brought by the overnight stirring of the deposition solution, resulting in a more homogeneous mixture and deposited films. The addition of the doping agent leads to the formation of small isolated particles/islands dispersed in the continuous film, with more of the latter appearing as the doping rate increases. These particles act as originating points for the formation of cracks: in the case of CeMo8 and CeMo10, the large amount of particles at the surface of the films results in the cracks merging and propagating across the whole surface of the substrate, leading to highly disordered and inhomogeneous layers. This could arise from a modification of the structural properties of the material, resulting in distortions and the ensuing cracks over the surface of the films, or the formation of a solid solution of CeO_2 and MoO_3, that might exhibit incompatible crystalline structure and thus resulting in fractures between the different regions of the films. While these large cracks could be detrimental to the good adherence and light diffusion of the films, the resulting granular and porous morphology could also lead to an advantageous increase in surface area, beneficial for the sought-after improvement in the capacity of these materials. Regarding the thickness of the films, the cross section micrographs of the samples are presented in **Figure 4.16**. Keeping the solution under stirring overnight visibly decreases the thickness of the layer, going from 750 nm down to 120 ± 30 nm. Once the molybdenum is added, the thickness of the films increases to 290 ± 90 nm, 250 ± 70 nm and 250 ± 40 nm for CeMo2, CeMo4 and CeMo6, respectively, probably due to a less efficient stacking of the grains due to deformations of the crystals brought by the doping or the limitation of crystal growth by the latter. When the doping increases further, up to 8 and 10 %at., the films become highly disordered and exhibit a large rugosity, increasing the thickness to 340 ± 100 nm for CeMo8 and 520 ± 120 nm for CeMo10. This change in the properties of the films arises from the large cracks observed in the top view micrographs of the samples (**Figure 4.15**), caused by the deformations of the lattice brought by the substitution of Ce^{4+} by Mo^{6+}. Moreover, even though the layers are not as clearly porous as the ones observed in the previous section (especially PEG 2/1 and 5/1, **Figure 4.9**), the doped films are composed of numerous small particles, efficiently packed as a dense film, which might allow the diffusion of cations through the structure between the grains and offering a high surface area that should result in a large capacity of the layers.

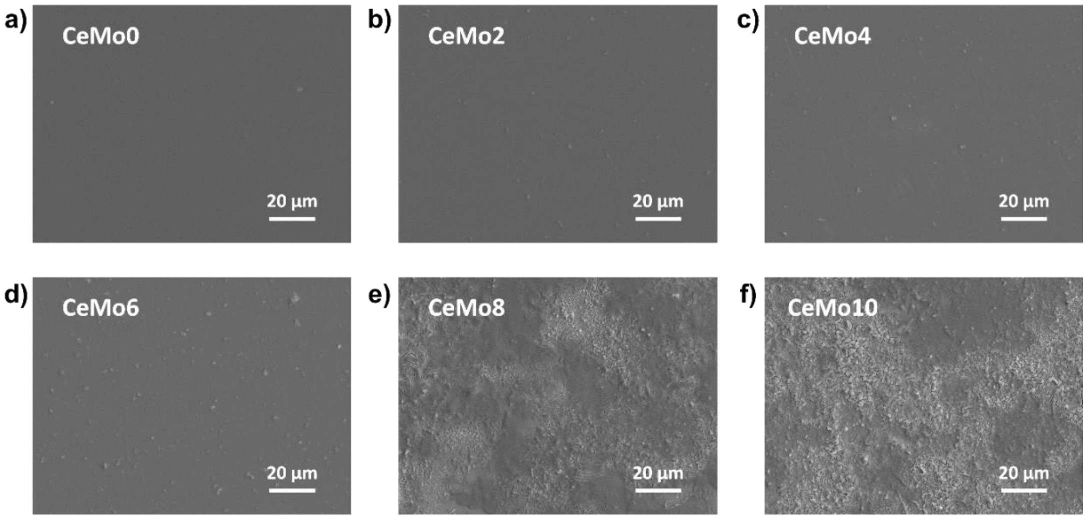

Figure 4.15: SEM top view micrographs of CeO_2 films doped with 0%at. Mo (a), 2%at. (b), 4%at. (c), 6%at. (d), 8%at. (e) and 10%at. (f).

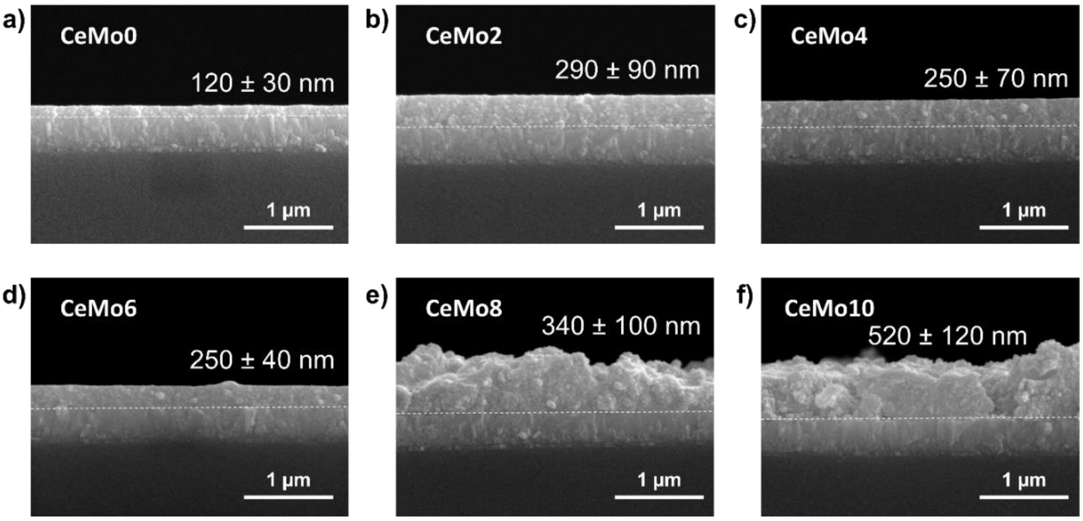

Figure 4.16: SEM cross section micrographs of CeO_2 films doped with 0%at. Mo (a), 2%at. (b), 4%at. (c), 6%at. (d), 8%at. (e) and 10%at. (f). The dotted line in the cross sections indicate the interface between the FTO coating and the CeO_2 film.

In addition to those observations, EDX characterization is carried out on the doped samples in order to confirm the presence and quantify the amount of molybdenum in the thin films. Well-defined signals corresponding to both Ce and Mo are clearly visible in the measured spectra presented in **Figure 4.17**, with the main contribution of the Ce appearing at 0.9 and 4.8 keV, while that of the Mo lies at 2.3 keV. As expected, no Mo signal is detected in the pure CeMo0 sample, in the doped samples, the molybdenum content is measured to be 1.6 (± 0.3) %, 2.0 (± 0.4) %, 4.0 (± 0.4) %, 5.8 (± 0.1) % and 8.6 (± 0.3) % in CeMo2, CeMo4, CeMo6, CeMo8 and CeMo10 respectively. From these results, it looks like a lesser amount of molybdenum is substituted into the cerium oxide lattice during the USP deposition in comparison to the initial concentration. Moreover, the effective concentration in Mo in the doped CeO2 films still follows a linear tendency, with a $R^2 = 0.95$ (**Figure 4.18**), indicating that the decrease in the concentration of the dopant species does not depend on the doping rate. This effect could arise from the high reactivity with water reported for the $MoCl_5$ precursor, that could result in the formation of less soluble species and thus decrease the effective amount of Mo being sprayed during the USP process, or a different behavior during the droplets time-of-flight, leading to some portion of the Mo precursor not reaching the substrate.

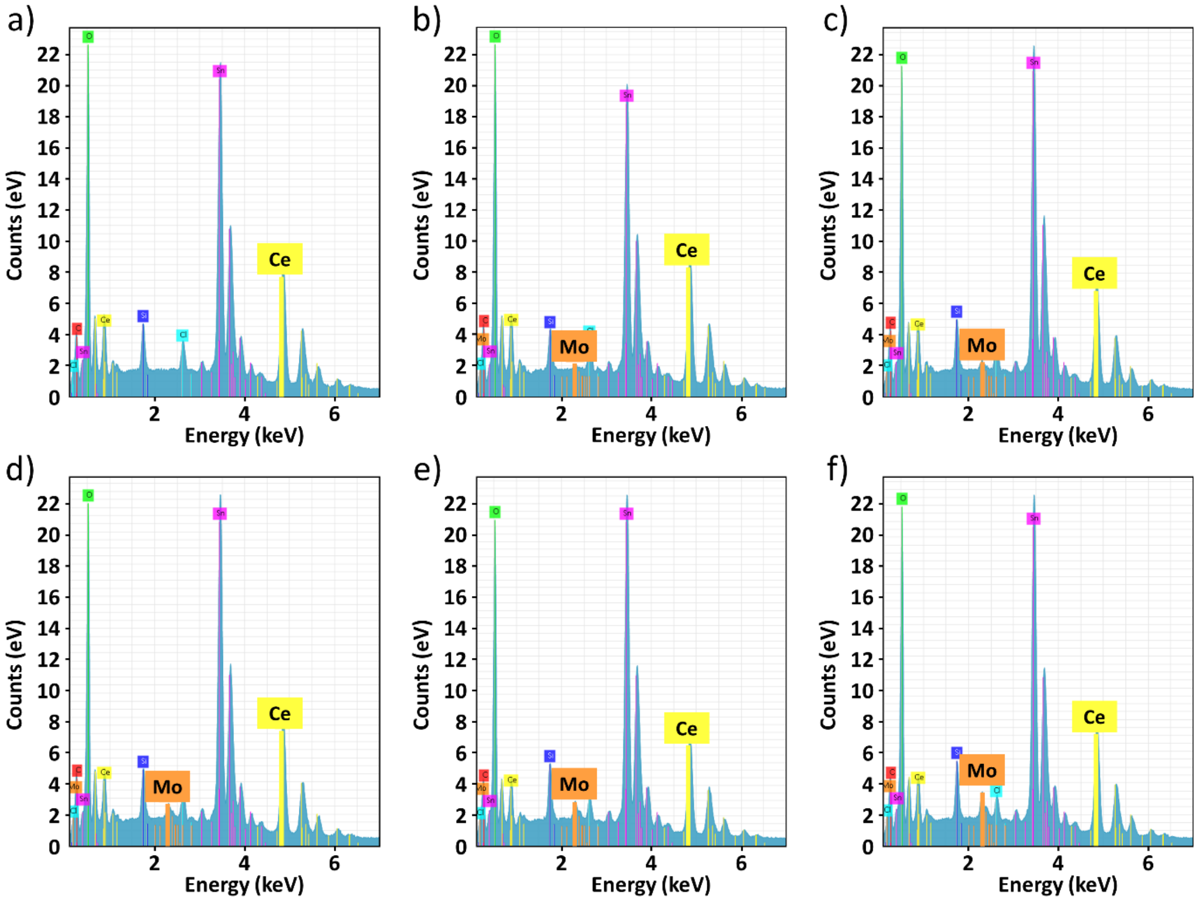

Figure 4.17: EDX spectra of CeO_2 films doped with 0 %at. Mo (a), 2 %at. (b), 4 %at. (c), 6 %at. (d), 8 %at. (e) and 10 %at. (f). The main rays of the species of interest are highlighted in yellow (cerium) and orange (molybdenum).

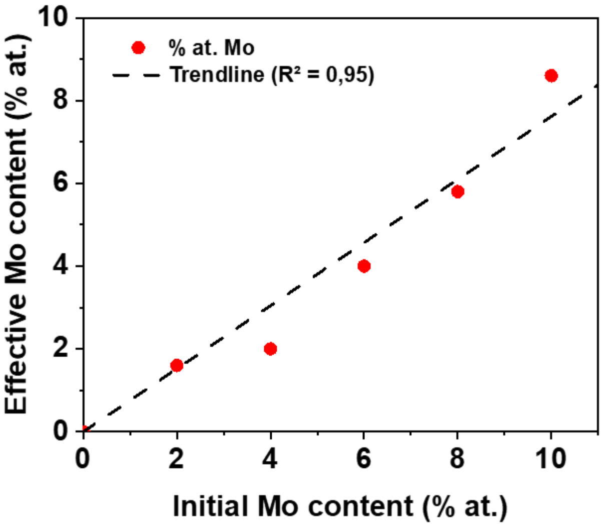

Figure 4.18: Comparison of the ratio in Mo in the initial reaction media and the final content measured from the EDX characterization.

As for previous undoped samples, the crystallinity of the films is investigated through grazing incidence XRD, with the diffractograms of the films presented in **Figure 4.19**. All samples display similar signals, with diffraction peaks at 27°, 34°, 47° and 56° as observed in the undoped formulation and indexed as the (111), (200), (220) and (311) lattice planes of the face centered cubic fluorite structure of CeO_2 (PDF 01-086-4481), and indicating that the fcc structure is maintained as Mo atoms are incorporated/substituted to form a solid solution. In addition, the shift of the (111) diffraction peak towards larger 2θ values (**Table 4.7**) indicates a shrinking of the crystal lattice, which could arise from the substitution of Ce^{4+} ions (ionic radius = 1.03 Å) by Mo^{6+} metallic centers (0.73 Å). Thus, smaller metallic ions replacing the original ones could lead to the lattice decreasing in size. Furthermore, the crystallite size (D_{hkl}) and cell parameters (lattice constant a) are determined using the Debye Scherrer **Equation 2.1** (**Section 2.3.2**, page 46) and **4.3**, respectively:

$$a = \frac{\lambda}{2sin\theta}\sqrt{h^2 + k^2 + l^2} \tag{4.3}$$

Where λ is the wavelength (Cu Kα, λ = 1.5418 Å), θ is the diffraction angle, h, k, l are Miller's indices, and β is the full width at half maximum intensity (FWHM). The results obtained from these calculations are also summarized in **Table 4.7**. In all samples (doped or not), it is worth noting that the lattice parameter is in good accordance with that of standard CeO_2 single crystals (a = 5.41 nm)[7–9], suggesting a good crystallinity of the films. When doping with Mo, the size of the crystallites decreases with increasing doping rates, highlighting the impact of the doping agent on the crystallization of the material, inhibiting the growth of the grains upon the introduction of impurities, and favoring the amorphization of the deposited layers, probably resulting in the formation of the cracks observed in the SEM micrographs. This effect is also visible on the diffractograms, displaying larger FWHM as the doping rate increases.

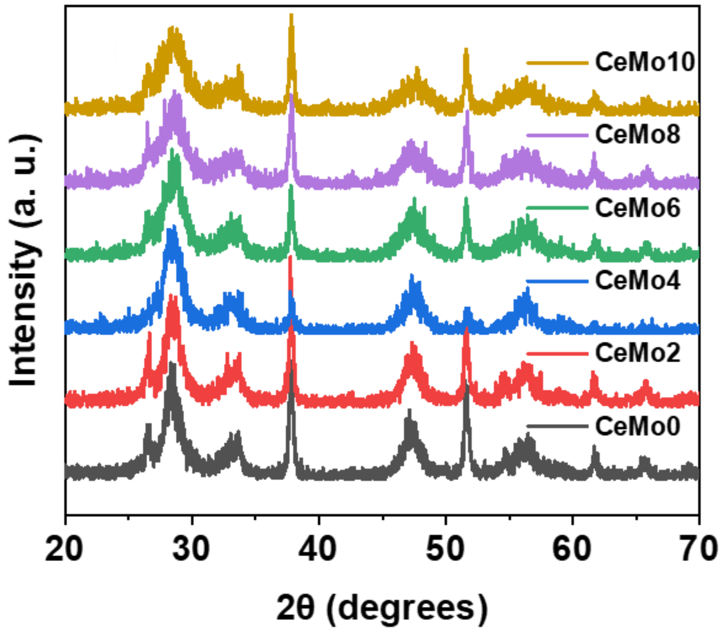

Figure 4.19: XRD diffractogram of the CeO_2 films doped with a 0-10%at. Mo content.

Table 4.7: Summary of the main structural properties of the doped CeO_2 films, calculated from the diffractograms using the Debye Scherrer equations.

CeO_2 (111)	2θ (°)	FWHM (°)	d_{hkl} (Å)	a (nm)	D (nm)
CMo10	28.42	2.40	3.14	5.44	3.38
CMo8	28.63	1.78	3.12	5.40	4.56
CMo6	28.40	1.48	3.14	5.44	5.49
CMo4	28.55	1.45	3.13	5.41	5.58
CMo2	28.31	1.55	3.15	5.46	5.24
CMo0	28.35	0.94	3.15	5.45	8.64

4.4.2. Raman spectroscopy (achieved in collaboration with ULiège – Dr. Cédric Malherbe)

To further analyze the effect of molybdenum on the structural properties of CeO_2, Raman spectroscopy is used to characterize the investigated formulations, with the corresponding spectra displayed in **Figure 4.20**. The spectra are normalized as a function of their maximum intensity in order to better highlight the modifications in the signal of the different samples. As expected from the surveyed literature, the main CeO_2 contribution appears at 460 cm^{-1}, corresponding to the F_{2g} mode of the fcc structure (symmetrical bend of the octahedral O around the Ce^{4+} atom)[8]. As the doping ratio increases, the signals shift towards smaller frequencies and becomes wider, indicating a broader distribution of bonds in the sample arising from the incorporation of Mo. Indeed, the signal is probably composed of a superposition of contributions, with a main one appearing at 460 cm^{-1} while additional populations appear at both higher and lower frequencies as the structure of the material is further modified by the addition of more molybdenum in the compound.

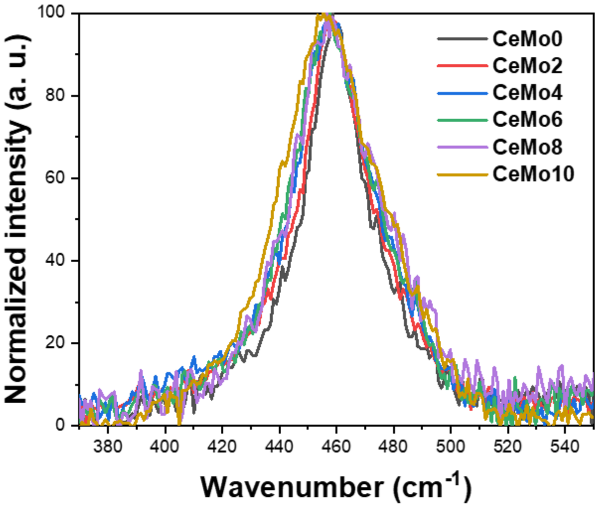

Figure 4.20: Raman spectra of the CeO_2 films doped with a 0-10%at. Mo content.

4.4.3. XPS characterizations (achieved in collaboration with UNamur – Dr. Rachel Gouttebaron)

Since the performances of CeO_2 as a passive counter electrode material strongly depends on its optical and electrochemical properties, themselves depending on the valence state of the cerium and molybdenum in the material, as well as the presence of oxygen vacancies in the sample, XPS characterization of the samples is carried out. The XPS survey indicates the presence of cerium and oxygen as well as molybdenum in the doped species, and carbon, coming from almost unavoidable atmospheric contamination and used as an internal reference for the calibration of the peak position. The deconvolution of the high resolution Ce3d spectra (**Figure 4.21**) shows the presence of Ce^{4+} and Ce^{3+} in all samples, appearing in the form of doublets at 882.1-882.6 eV and 888.7-889.3 eV, and an additional doublet contribution appears at 880.1-880.8 eV and 885.2-885.4 eV, respectively. The concentration in reduced species increases as a function of the doping rate, increasing from 26% in CeMo0 to 28-32% in the Mo doped samples (**Table 4.8**), indicating the possible formation of oxygen vacancies in the material, as well as new redox centers. In turn, this should result in an increase of the capacity of the material, as observed in the previous reports of Orel *et al.*[6] and Krašovec *et al.*[5]. The occurrence of Ce^{3+} in a large concentration even in the undoped sample could be due to the presence of PEG in the deposition solution, which has been reported as a reducing agent for the production of silver nanoparticles[32,33]. On the other hand, the presence of Ce^{3+} could also arise from the use of $CeCl_3$ as the precursor, leading to the presence of a significant proportion of reduced species if not completely oxidized during the deposition process. Besides, the Mo3d spectra (**Figure 4.21**) highlight the presence of only Mo^{6+} as a doublet at 232.5-232.8 and 235.7-236.0 eV. If the precursors are not completely oxidized during the deposition, the presence of only Mo^{6+} could indicate a preferential electron transfer between Mo^{5+} and Ce^{4+} to obtain Mo^{6+} and Ce^{3+}, further increasing the concentration in the cerium reduced species. Moreover, the O1s spectra in **Figure 4.21** shows 3 contributions, corresponding to O^{2-}, O_{vac} and C-O/O-H species, respectively at 529.3-529.7 eV, 530.9-531.3 eV and 532.0-532.5 eV. The spectra indicate the presence of oxygen vacancies in significant amounts, even though this interpretation is subject to debate in the XPS field (see **Chapter 2**, **Section 2.5.1**, page 62)[34]. In addition, the Mo content of the films is quantified and presented in **Table 4.8**, in comparison to the EDX quantification results. The XPS ratio show a slightly larger concentration at the surface (XPS) than in the bulk of the films (EDX), indicating the migration of Mo towards the surface of the films. All in all, these results demonstrate the efficient formation of reduced species (Ce^{3+}) and oxygen vacancies upon incorporation of Mo as a doping agent, which are expected to improve the electrochemical properties of the studied materials.

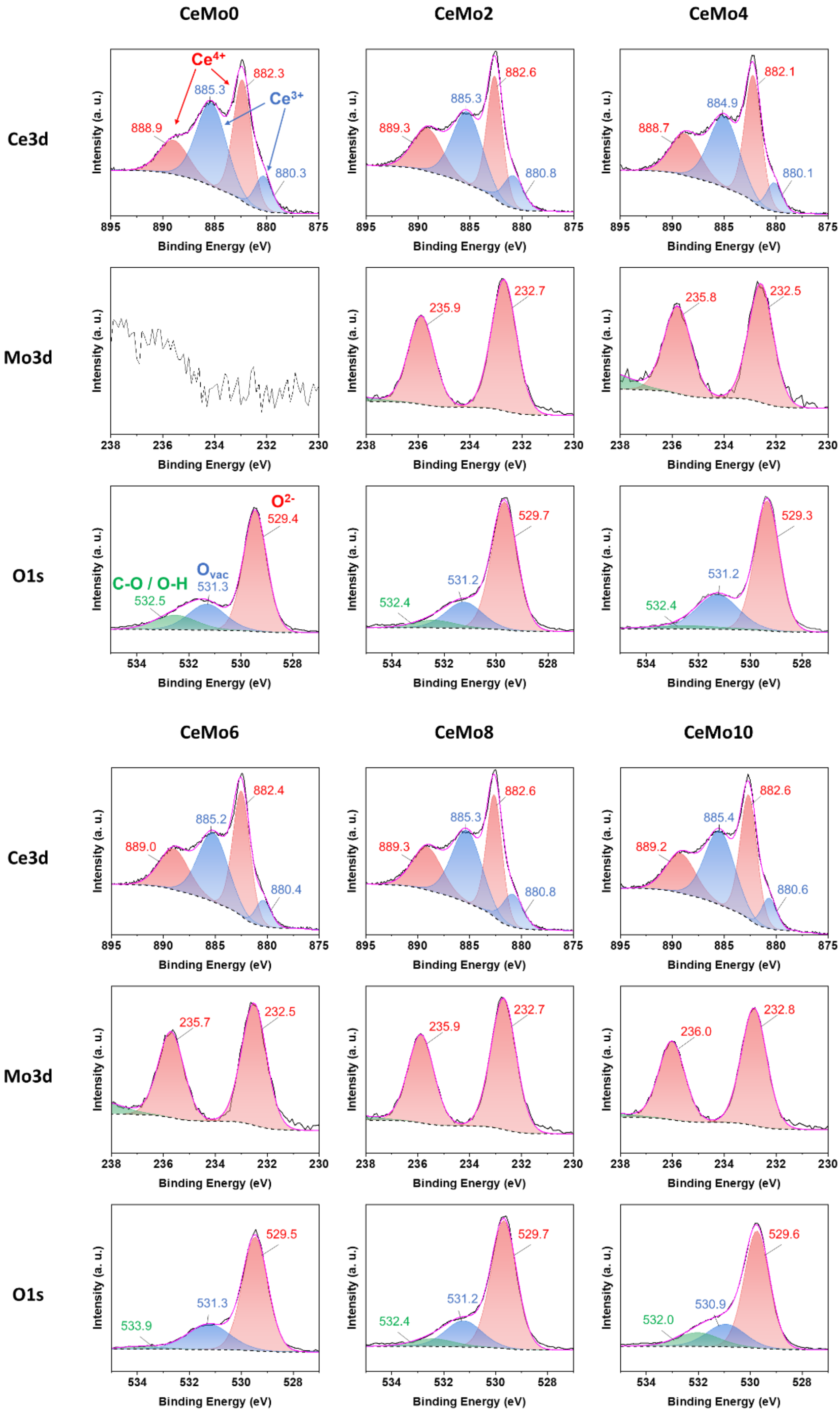

Figure 4.21: Ce3d, Mo3d and O1s XPS spectra of the CeO$_2$ films doped with a 0-10%at. Mo content.

Table 4.8: Summary of the data measured from the XPS characterization of the CeMo0-10 samples.

	Effective %at. Mo_{EDX}	Effective %at. Mo_{XPS}	Proportion Ce^{3+} (%)
CeMo0	/	/	26.4 (± 0.1)
CeMo2	1.6 (± 0.1)	1.4 (± 0.1)	28.6 (± 0.3)
CeMo4	2.0 (± 0.4)	4.3 (± 0.4)	28.7 (± 0.5)
CeMo6	4.0 (± 0.4)	6.7 (± 0.1)	27.9 (± 0.1)
CeMo8	5.8 (± 0.1)	10.1 (± 0.6)	31.6 (± 0.6)
CeMo10	8.6 (± 0.3)	11.4 (± 0.3)	27.8 (± 0.4)

4.4.4. Optical characterization of the thin films

UV-Vis-NIR spectra of total transmittance of the “as-deposited” films (using an integrating sphere) are shown in **Figure 4.22**. The films exhibit very high transmittance across VIS and NIR regions, reaching values as high as the bare FTO glass substrate, with only CeMo10 exhibiting a slightly lower transmittance in the VIS, but still significantly exceeding the 70% limit set from the literature survey, with all samples exhibiting a 90%+ transmittance at 550 nm. It should be noted that the overnight stirring protocol required for the solubilization of the mixed precursors solution, applied to the undoped CeO_2 formulation, results in an improvement of the transmittance, probably due to a more homogeneous mixing of the halide precursor and the surfactant leading to a thinner and smoother deposition and less light diffusion from the layer.

In addition, the measurement of the diffuse transmittance and haze of the films (**Equation 4.2**) show very good values for CeMo0, CeMo2 and CeMo4, around 1%. This improvement could be due to the highly homogeneous deposition of the layer, owing to the PEG-assisted USP deposition method, limiting the diffusion of light and thus improving the transparency of the samples. The longer time under stirring before the deposition (overnight vs. 1h), results in great improvements of the optical properties, as observed in the case of CeMo0, corresponding to the PEG 5/1 case in the previous section. This small change in the protocol led to an increase in total transmittance and large decrease in diffuse transmittance, yielding an excellent haze value of < 1%. In the case of CeMo6, CeMo8 and CeMo10, the small particles/islands and cracks appearing at the surface of the films from the doping-induced amorphization of the material results in an increase of the diffuse transmittance and larger haze values (summarized in **Table 4.9**).

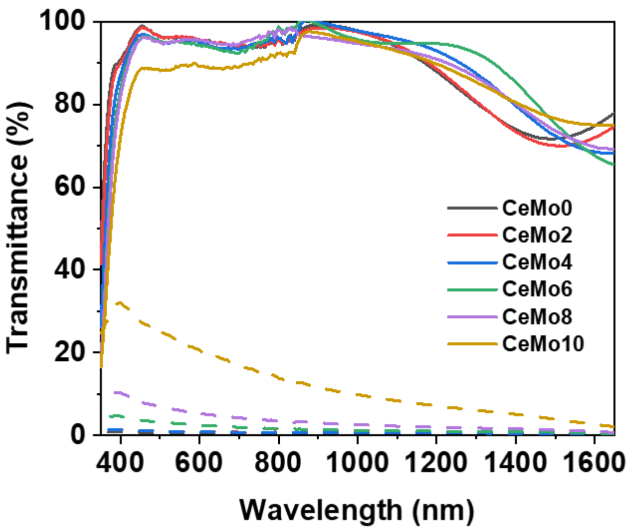

Figure 4.22: Total transmittance (solid lines) and diffuse transmittance spectra (dashed lines) of the CeO_2 films doped with a 0-10%at. Mo content.

Table 4.9: Total and diffuse transmittance obtained from the optical characterization of the CeO_2 samples doped with a 0-10%at. Mo content, and haze values calculated from T_t and T_d.

	T_t at 550 nm (%)	T_d at 550 nm (%)	Haze (%)
CeMo0	96.1	0.7	0.7
CeMo2	96.1	1.0	1.0
CeMo4	95.2	1.0	1.1
CeMo6	95.0	2.9	3.1
CeMo8	95.2	6.1	6.4
CeMo10	89.3	22.7	25.4

In addition to the optical spectra, the direct band gap (E_g) of the materials is determined using a Tauc plot shown in **Figure 4.23**. The data is obtained from the Tauc relation, explicated in **Equation 4.4**:

$$(\alpha h\nu)^2 = A\left(h\nu - E_g\right) \tag{4.4}$$

Where α is the absorption coefficient, $h\nu$ is the photon energy, A is a constant and E_g is the optical band gap, by extrapolating the linear portion of the curve to find its intersection with the $h\nu$ axis (α = 0; $h\nu$ = E_g). The E_g values were found to be 3.62, 3.58, 3.52, 3.47, 3.46 and 3.43 eV for CeMo0, CeMo2, CeMo4, CeMo6, CeMo8 and CeMo10, respectively. These results highlight a decrease of the band gap as a function of the doping rate, arising from the formation of oxygen vacancies or Ce^{3+} reduced species, both potentially responsible for the emergence of new electronic states in the band gap, effectively lowering it[7–9] upon doping with Mo.

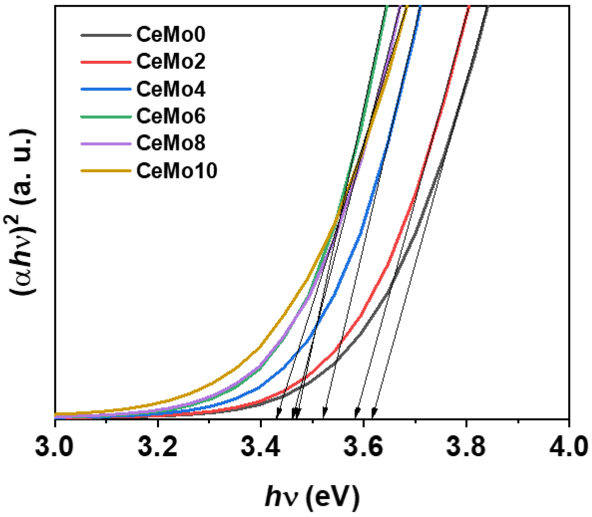

Figure 4.23: Tauc plot of the doped CeO_2 formulations, extrapolated to determine the band gap of the samples.

4.4.5. Electrochemical characterizations

With the impact of the doping on the morphology, structural and optical properties of the films rationalized, the doped formulations are tested in regard of their electrochemical performances, in order to quantify how the incorporation of molybdenum affects those latter and evaluate which formulations are most promising for applications as passive counter electrode. First of all, cyclic voltammetry measurement between +1.0 and -1.0 V are performed at 20 mV/s : the electrochemical curves, shown in **Figure 4.24a**, display a reduction wave corresponding to the transition between Ce^{4+} and Ce^{3+} states, starting around -0.1 V when the potential is swept towards negative values. On the way back, an oxidation peak is highlighted around -0.5 V, which is more negative than in other reported works of the literature compiled in **Table 4.10**. As explained earlier, this difference in oxidation potential could arise from the thickness of the films and their polarization, with the oxidation peak drifting towards more reducing potentials when the thickness increases, but also from the addition of PEG as a surfactant, decreasing the conductivity of the coating (even though a majority of the polymer should be degraded the deposition at 300°C). In addition to the CV, the capacity of the layers is monitored by chronoamperometry, successively applying -1.0 and +1.0 V for 60 seconds each. The measurements, presented in **Figure 4.24b**, show an increase in capacity with the doping rate. This improvement in the electrochemical properties of the films could be due to the formation of new available redox centers in the material thanks to the reduction of cerium into its Ce^{3+} state, as well as the formation of oxygen vacancies, favored by the difference in valence between the host Ce^{4+} cations and the substituted by Mo^{6+} dopant species. These new redox centers and oxygen vacancies can give rise to the insertion of additional cation/electron pairs and therefore increase the capacity of the counter electrodes. In this context, an optimal capacity is reached for CeMo10 (**Table 4.7**), exhibiting an excellent value of 29.2 mC/cm², significantly greater than those of previously reported dope CeO_2 formulations. Looking into the reversibility properties of these samples, it appears that overall they perform better than the other 300°C formulations discussed earlier, indicating that Mo doping might also improve the electrochromic behavior of the material. Here again, it is noteworthy that the overnight stirring of the undoped solution improves its electrochemical performances, owing to the more homogeneous deposition of the materials.

Additionally, the capacity of the samples is normalized as a function of their thickness. In the previous section, the highly porous structures obtained from the addition of PEG to the deposition solution made this normalization pointless given the non-proportional relationship between thickness and the amount of material in the film with such morphologies. In this new batch of (un)doped samples, the similar density from one sample to the other allows the calculation of a normalized capacity.

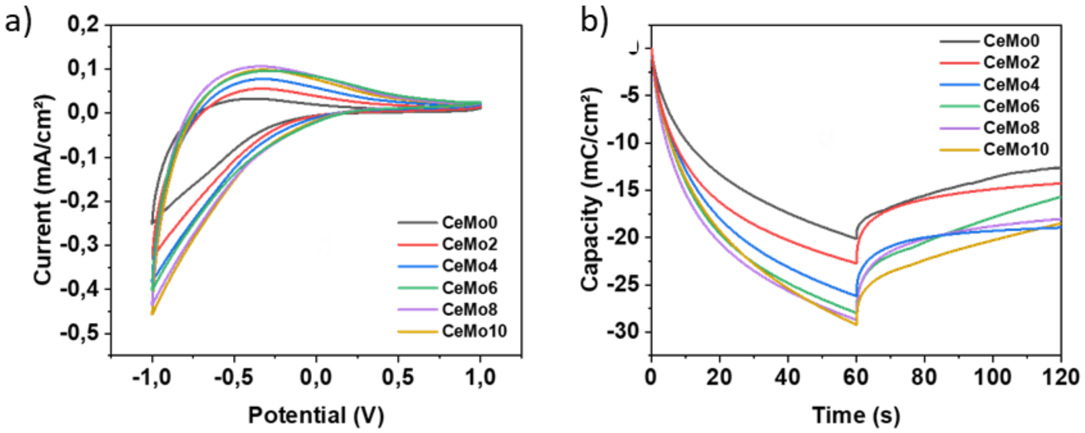

Figure 4.24: Cyclic voltammetry acquired in $LiClO_4$/PC, using Pt as counter electrode and at a scanning rate of 20 mV/s (a) and chronoamperometry (b) characterization of the CeO_2 films doped with a 0-10%at. Mo content.

Table 4.10: Quantification of the capacity and reversibility of the doped CeO_2 samples, calculated from the CA curves

	Capacity / Q_{in} (mC/cm²)	Capacity / Q_{out} (mC/cm²)	Reversibility (%)
CeMo0	20.1	7.4	37
CeMo2	22.7	8.4	37
CeMo4	26.2	7.3	28
CeMo6	27.9	12.3	44
CeMo8	28.7	10.6	37
CeMo10	29.2	10.5	36

4.4.6. Spectroelectrochemical characterizations

In addition to their optical and electrochemical properties, the spectroelectrochemical performances of the studied formulations should also be assessed. The SEC spectra of all samples are presented in the **Figure 4.25**, for an applied potential of +1.0 V (solid lines) and -1.0 V (dashed lines), both maintained for 5 minutes before the optical data is acquired. The bias is applied for a longer duration than for the CA characterization (1 minutes), in order to reproduce the protocol applied to active materials such as the four MoWOx and $WO_{3-\delta}$ formulations in the previous chapter (**Chapter 3**, **Section 3.3.4.b**, page 83). The transmittance of the CeMo0, CeMo2, CeMo4 and CeMo6 samples rises past 90%, a significant improvement in comparison to the total transmittance (T_t) measurement discussed previously: this could be due to the optical interaction at the interface between the film and the environment. Indeed, for the T_t characterization, the films are measurement in air, while the SEC data is acquired in a liquid $LiClO_4$/PC electrolyte, depending on the refractive index of the different materials, the optical interaction between the latter can favor more or less transmittance. However, in the case of CeMo8 and CeMo10, an abrupt loss in visible transmittance is observed in comparison to the T_t values, explained by the large diffuse transmittance (T_d) displayed by these samples (and probably originating from the cracks appearing at their surface). In the SEC spectra, only the parallel transmittance (T_p) is detected, and since $T_t = T_p + T_d$, the rise in T_d observed in the highly doped samples limit the maximum value of T_p exhibited by the films. Moreover, in all cases, the contrast exhibited by the films is almost negligible, reaching at most 4.5% for CeMo6 and CeMo8. The SEC characterization of these samples solidifies their potential for passive counter electrode applications, with most presenting satisfying transmittance levels, and no significant contrast upon Li$^+$ insertion/extraction, thus not impeding the optoelectronic performance of the electrochromically active material in a fully assembled device.

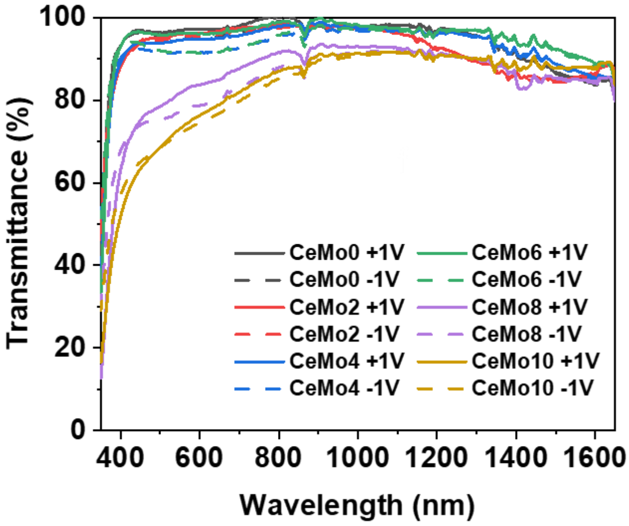

Figure 4.25: Spectroelectrochemical characterization of the doped CeO_2 films as a function of the applied potential, at +1.0 V (solid lines) and -1.0 V (dashed lines).

Based on the transmittance and capacity of the investigated samples, it would seem that two optima can be highlighted: the first one, based on the maximum capacity measured in the films, corresponds to CeMo10 (29.2 mC/cm^2). However, its transmittance (73.1%) is only a few percents over the set limit determined from the literature (70%): its non-optimal optical properties could thus slightly hinder the proper functioning of an assembled device. However, another optimum can be determined from an optical point of view: in this case, the best sample would be CeMo6 given its very high transparency (96.1%) while still displaying a high capacity of 27.7 mC/cm^2. Going back to the surveyed literature, but now focusing on the doped formulations (see **Table 4.11** below), both identified formulations (CeMo6 and CeMo10) display excellent performances, exceeding the capacity of all previously investigated formulations, while presenting transmittance levels higher than the average, especially in CeMo6, surpassing this value by more than 20%. From these results, all doped formulated materials studied in this work appears to be promising for applications as passive counter electrodes in electrochromic devices, not hindering the optical activity of the working electrode while ensuring a good match between the capacity of both electrodes, as to avoid limiting the electrochemical performances of the electrochromically active material. CeMo8, standing halfway between the optical and electrochemical optima discussed above, could also be considered as the overall optimum, combining both high transmittance (81.7 %) and capacity (28.7 mC/cm^2).

While the characterization discussed in this chapter seems to indicate an optimum at higher doping rates, somewhere amongst CeMo4, CeMo6, CeMo8 and CeMo10, the combination of the different counter electrode formulations into complete devices and the measurement of their electrochromic performances (especially their coloration efficiency) will allow to determine which key parameter (transmittance or capacity) mostly dictates the efficient electrochemical behavior of the assembled devices.

Table 4.11: Literature survey of the doped CeO_2 literature, in comparison to the best performances obtained in the scope of the present doctoral research work.

Author	Year	Doping agent	Deposition method	Thickness (nm)	Capacity (mC/cm²)	Transmittance @ 550 nm (%)	Contrast @ 550 nm (%)
Azens	1998	Ti (50%)	Sputtering	450	20.0	75	≈0
Varsano	1999	V (20%)	Sputtering	100	22.0	90	10
Verma	2005	Ti (50%)	Spin coating	800	12.5	70	≈0
Bhosale	2015	Ti (3%)	Spin coating	/	25.4	75	≈0
Dalavi	2020	V (4%)	Spray pyrolysis @ 400°C	/	14.0	65	5
Zimou	2021	Co (6%)	Spray pyrolysis @ 450°C	/	2.1	60	N/A
El-Habib	2021	V (4%)	Spray pyrolysis @ 450°C	/	N/A	60	≈0
El-Habib	2022	In (8%)	Spray pyrolysis @ 450°C	/	11.2	80	≈0
This work	2024	Mo (0%)	USP + PEG @ 300°C	120	20.1	97	2
		Mo (2%)		290	22.7	96	1
		Mo (4%)		250	26.2	95	3
		Mo (6%)		250	27.7	96	5
		Mo (8%)		340	28.7	82	5
		Mo (10%)		520	29.2	73	1

4.5. Conclusions and perspectives

In the scope of this research work, Mo doped CeO_2 films were successfully produced through a one-step, PEG-assisted aqueous USP process. The influence of several parameters on the morphological, structural, optical and electrochemical properties of the films is methodically evaluated. Several characterization methods are employed for this purpose, namely SEM, XRD, UV-VIS-NIR spectrophotometry, Raman, XPS and (spectro)electrochemistry.

Herein, PEG-assisted USP is used for the first time to produce CeO_2 passive counter electrodes. This method allows the formation of homogeneous films displaying very good optical and electrochemical properties, outperforming most of the doped and undoped surveyed literature. The great performances exhibited by this film could be attributed to a double effect of the PEG surfactant: first, the addition of PEG to the precursor solution modifies the surface tension of the droplets and allows a more homogeneous deposition, leading to a high transmittance across the measured interval. Moreover, using a large excess of PEG results in the formation of channels and porosity in the structure of the film as the polymer is thermally degraded into gases byproducts escaping the layer. The synergistic effect of homogeneity and porosity in the processed film results in a large transmittance, due to the very little diffusion of light, and a great capacity, due to the large surface area of the porous structure and the numerous available active sites.

From these already well performing undoped films, it was possible to further improve their properties upon doping with a small amount of molybdenum (2 – 10%). Adding the dopant species results in small modifications of the crystalline structure and results in the partial amorphization of the layers, resulting in cracks at the surface of the films and hindering the optical performances in the case of large doping rates (8 – 10%). However, the addition of molybdenum leads to an increase in the capacity of the films, as the substitution of Ce^{4+} by Mo^{6+} results in the formation of oxygen vacancies and new available redox centers in the material due to the multiple oxidation states of Mo and Ce. Therefore, the optimum formulation consists in a tradeoff between the increase in capacity while maintaining a high transparency and low haze. On this basis, the best results are obtained for **CeMo6** with **PEG in a 5/1 ratio**, exhibiting an excellent transmittance and capacity, and an adequate haze value. Lower doping rates lead to improved optical performances but a smaller capacity, while greater dopant concentrations demonstrate larger concentration but a loss in transmittance due to an increase in haze arising from the cracks at the surface of the films.

All in all, the results presented in this chapter show the very good performances that can be reached by Mo doped CeO_2, deposited via PEG assisted USP, with both the doping species and the deposition method being investigated here for the first time, to the best of our knowledge. The combination of these two strategies proves to be very promising, as this first proof-of-concept of the CeMo formulations already outperforms all of the previous articles found during the survey of the existing literature. Therefore, CeMo is an excellent candidate to be used as passive counter electrode in complete electrochromic devices involving highly functional working electrodes, such as dual band plasmonic materials. Since there is currently no known compatible material to act as an active counter electrode for plasmonic materials, and in particular dual band materials, the passive counter electrode should be highly efficient for the final device to express all of its electrochromic properties in an efficient way. The development of promising formulations such as the discussed CeMo are of the greatest importance for the future commercialization of highly energy efficient smart windows, switchable across multiple states and acting upon several regions of the solar spectrum.

While the performance of the films produced in this work are already good, it might be possible to improve those further in future works. Doped formulations without the addition of PEG could be investigated, as well as different PEG ratios. For example, this study could be further completed by evaluating the performances of the doped materials using the other PEG ratios (1/1, 2/1, 10/1), that were ruled out here due to time constraints. Further fine tuning of the composition of the deposition solutions could also allow the production of an optimum formulation exhibiting both great optical and electrochemical properties. Finally, the nature of the PEG surfactant could impact the properties of the films, with the length of the polymer chain modifying its viscosity, surface tension, degradation temperature, notably. Therefore, it could be interesting to test different PEG formulations, and even other surfactants, to rationalize their impact on the morphology and structure of the films, and the resulting optoelectronic performances exhibited by the samples.

4.6. References

1. Wang, Y. *et al. Annu. Rev. Chem. Biomol. Eng* **2016**, 7, 283, doi.org/10.1146/annurev-chembioeng-080615-034647.
2. Runnerstrom, E. L. *et al. Chem. Commun.* **2014**, 50, 10555, doi.org/10.1039/c4cc03109a.
3. Mortimer, R. J. *Annu. Rev. Mater. Res.* **2011**, 41, 241, doi.org/10.1146/annurev-matsci-062910-100344.
4. Kraft, A. *ChemTexts* **2019**, 5, 1, doi.org/10.1007/s40828-018-0076-x.
5. Krašovec, U. O. *et al. ChemInform* **1998**, 29, 3398, doi.org/10.1149/1.1838025.
6. Orel, B. *et al. J. Mater. Chem.* **1995**, 5, 617, doi.org/10.1039/jm9950500617.
7. El-Habib, A. *et al. Opt. Mater.* **2022**, 127, 112312, doi.org/10.1016/j.optmat.2022.112312.
8. Zimou, J. *et al. Mater. Sci. Semicond. Process.* **2021**, 135, 1369, doi.org/10.1016/j.mssp.2021.106049.
9. El-Habib, A. *et al. Surfaces and Interfaces* **2021**, 23, 100906, doi.org/10.1016/j.surfin.2020.100906.
10. Bhosale, A. K. *et al. Bull. Mater. Sci.* **2015**, 38, 483, doi.org/10.1007/s12034-015-0861-8.
11. Özer, N. *Sol. Energy Mater. Sol. Cells* **2001**, 68, 391, doi.org/10.1016/S0927-0248(00)00371-8.
12. Baudry, P. *et al. J. Non. Cryst. Solids* **1990**, 121, 319, doi.org/10.1016/0022-3093(90)90151-b.
13. Varsano, F. *et al. Ionics* **1999**, 5, 80, doi.org/10.1007/bf02375908.
14. Dalavi, D. S. *et al. Mater. Today Proc.* **2020**, 43, 2702, doi.org/10.1016/j.matpr.2020.06.146.
15. Verma, A. *et al. Indian J. Chem. - Sect. A Inorganic, Phys. Theor. Anal. Chem.* **2005**, 44, 1756, https://nopr.niscpr.res.in/handle/123456789/20191.
16. Azens, A. *et al. Sol. Energy Mater. Sol. Cells* **1998**, 54, 85, doi.org/10.1016/s0927-0248(97)00267-5.
17. Pavan Kumar, C. S. S. *et al. J. Alloys Compd.* **2014**, 602, 180, doi.org/10.1016/j.jallcom.2014.02.143.
18. Nan, C. *et al. ChemPlusChem* **2023**, 88, 202300023, doi.org/10.1002/cplu.202300023.
19. Denayer, J. *et al. Sol. Energy Mater. Sol. Cells* **2014**, 130, 623, doi.org/10.1016/j.solmat.2014.07.038.
20. Nakaruk, A. *et al. J. Coatings Technol. Res.* **2010**, 7, 665, doi.org/10.1007/s11998-010-9245-6.
21. Maho, A. *et al. ECS Meet. Abstr.* **2015**, doi.org/10.1149/ma2015-01/34/1927.
22. Chatzikyriakou, D. *et al. Microporous Mesoporous Mater.* **2017**, 240, 31, doi.org/10.1016/j.micromeso.2016.11.001.
23. Maho, A. *et al. Sol. Energy Mater. Sol. Cells* **2019**, 200, 110014, doi.org/10.1016/j.solmat.2019.110014.
24. Maho, A. *et al. Coatings* **2023**, 13, 1, doi.org/10.3390/coatings13111879.
25. Denayer, J. *et al. Appl. Surf. Sci.* **2014**, 321, 61, doi.org/10.1016/j.apsusc.2014.09.128.

26. Maho, A. *et al*. *J. Electrochem. Soc.* **2017**, 164, 25, doi.org/10.1149/2.0071702jes/xml.

27. Maho, A. *et al. 15th International Conference on Organic Electronics - ICOE2019* **2019**, https://orbi.uliege.be/handle/2268/238465.

28. Ivas, T. *et al*. *Calphad* **2012**, 36, 57, doi.org/10.1016/j.calphad.2011.10.005.

29. Lopez, H. F. *et al*. *Int. Sch. Res. Not.* **2013**, 2013, 208614, doi.org/10.1155/2013/208614.

30. Chang, B. Y. *J. Electrochem. Sci. Technol.* **2015**, 6, 146, doi.org/10.5229/jecst.2015.6.4.146.

31. Mahmudul Hasan, M. *et al*. *J. Saudi Chem. Soc.* **2012**, 16, 145, doi.org/10.1016/j.jscs.2011.06.006.

32. Luo, C. *et al*. *J. Colloid Interface Sci.* **2005**, 288, 444, doi.org/10.1016/j.jcis.2005.03.005.

33. Díaz-Cruz, C. *et al*. *Eur. Polym. J.* **2016**, 83, 265, doi.org/10.1016/j.eurpolymj.2016.08.025.

34. Idriss, H. *Surf. Sci.* **2021**, 712, 2, doi.org/10.1016/j.susc.2021.121894.

Chapter 5 – Assembly of dual band electrochromic films and counter electrode layers into prototype devices

Chapter 5 – Assembly of dual band electrochromic films and counter electrode layers into prototype devices

5.1. Comparison of liquid setups and solid devices

In the final stage of this doctoral research, the performances of the active materials are investigated in full devices, as to more accurately represent the final application intended for these compounds, namely smart windows, besides the SEC characterization of the films in a classical 3-electrode cell configuration. Using the materials previously developed in the context, it is possible to assemble electrochromically active electrodes with CeO_2-based counter electrodes. In addition, the successful production of proof-of-concept devices based on the investigated formulations from this research work would represent a great first step towards the future optimization and upscaling of the processes discussed in the scope of this doctoral thesis.

In a first step, so-called liquid setups are investigated, by immerging the two electrodes, working and counter, facing each other into an electrolyte solution (see **Figure 5.1a,c**). In this situation, the presence of a liquid electrolyte allows efficient ion mobility and high concentrations of cations, as to not hinder the kinetics and functionality of the active material. In a second step, a solid electrolyte layer can be casted between the two electrodes to form a solid device (**Figure 5.1b,d**)[1]. In the present case, a commercial formulation (Solvionic®) of polymer gel electrolyte is used to produce the solid devices: a layer of gel is deposited on both electrodes, which are then assembled, and kept together using clamps while a specific thermal treatment, detailed below, insures the curing of the gel, securing the assembly as one solid unit. While this step enables the assembly into prototype devices as a step towards the upgrading from individual thin films to assembled smart windows, the use of a non-liquid electrolyte brings several additional limitations to the performances of the materials. First, the incorporation of an additional layer can lower the transmittance of the complete stack, therefore the gel should be highly transparent. Moreover, the gel-then-solid nature of the electrolyte will limit the diffusion of the cationic species in comparison to the liquid case, while the total amount of these latter is now fixed as the amount initially present in the electrolyte and not in large excess anymore. These two parameters may strongly hinder the performances of the solid device in comparison to its liquid counterpart, and even more compared to the active film considered separately in a 3-electrodes cell configuration.

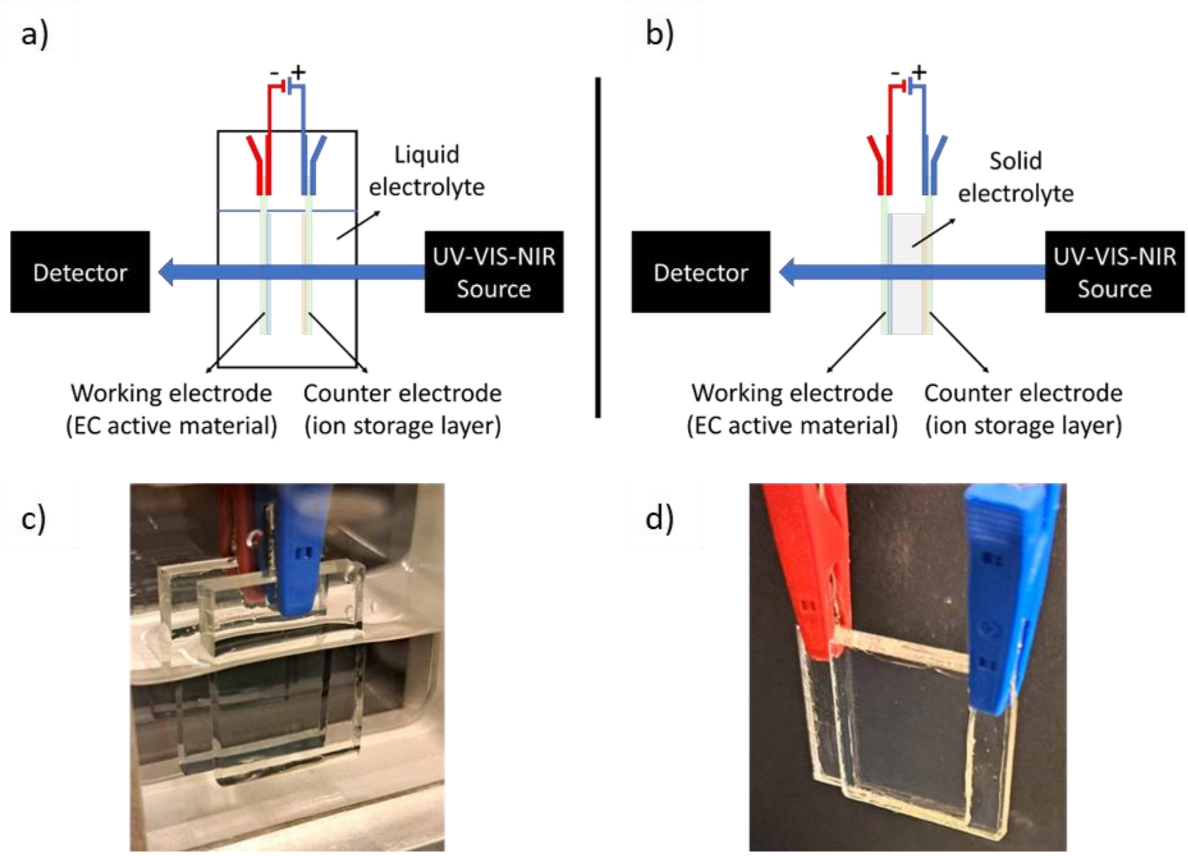

Figure 5.1: Schematic representation of the two assembly configurations: a liquid setup (a), and a solid device (b). Pictures of the actual setups are also presented at the bottom of the the figure (c, d).

In the scope of this doctoral research work, the investigated (Mo)CeO_2 formulations discussed in **Chapter 4** are characterized as liquid and then solid devices, first using reference WO_3 working electrodes processed by ultrasonic spray pyrolysis (USP). These particular WO_3 formulations have been developed at the GREEnMat since 2012, notably in the framework of the Région Wallonne funded “SMARTSPRAY” project, and displays excellent properties, namely a great contrast (83%), a large coloration efficiency ($28cm^2/C$), fast kinetics (< 1 minute), as well as a very good reversibility and durability upon electrochemical cycling (94%)[2]. These first characterizations using an optimal working electrode will allow to determine the best counter electrode formulation and assembly protocol, which will in turn be used to produce proof-of-concept devices using the MoWOx materials as processed and studied earlier (see **Chapter 3**).

5.2. Materials and Methods

Chemicals. Lithium perchlorate ($LiClO_4$, 95% anhydrous) is provided by Alfa Aesar, and propylene carbonate (PC, 99.7% anhydrous) from Sigma-Aldrich. 0.3 M lithium bis(trifluoromethanesulfonyl) imide (LiTFSI) in 1-butyl-3-methylimidazolium bis(trifluoromethanesulfonyl)imide (BmimTFSI) + 8 wt. % poly(methyl methacrylate (PMMA), in butanone was purchased from Solvionic. All chemicals are used as received without further purification.

Assembly of the solid devices. The solid devices are prepared according to a protocol developed by the GREEnMat team, using the LiTFSI in BmimTFSI gel electrolyte. In summary, 100 µL of the gel are casted on top of each electrode, and placed on a hot plate at 80°C for 5 minutes to initiate the evaporation of the butanone solvent. Then, the electrodes are assembled into a stack and thermally treated for 1h at 80°C, followed by the same thermal treatment, but this time in a JiuTu bubble remover, consisting in a pressurized chamber (6 bar) to prevent the formation of bubbles in the electrolyte during the evaporation of the solvent, as they collapse under the pressure conditions.

Spectroelectrochemical characterization. The electrochromic performances of the devices (either liquid or solid) are measured using a Shimadzu UV-3600i Plus spectrophotometer in direct transmittance mode. For the liquid setups, an optical glass cell is placed inside the spectrophotometer analysis chamber and the two electrodes are plunged into a 0.5M $LiClO_4$/PC electrolyte solution. In the case of the solid devices, the sample is maintained using an appropriate film holder (Shimadzu) installed in the apparatus (**Figure 5.1**). In both cases, each electrode is connected to a Biologic SP-200 potentiostat/galvanostat, and the spectral properties of the devices are monitored as a function of time and the applied potential. The transmittance levels of the devices, in the VIS and NIR regions, is computed as an average of the transmittance between 350 and 750 nm and 750 and 1650 nm, respectively, as previously done in **Chapter 3**.

5.3. Reference assembly made from WO_3 and (Mo)CeO_2 working and counter electrodes

5.3.1. Characterization of liquid setups

As specified in the introduction of this section, liquid setups are first investigated as to limit the parameters hindering the good functioning of the devices. The potential window is adapted from +1.0/-1.0 V in the 3-electrode configuration to +3.0/-3.0 V in the devices, with each bias step applied for 3 minutes before the acquisition of the full optical spectra to reach a stable optical state. This new potential window is determined empirically by investigating the spectroelectrochemical properties of a preliminary CeO_2/WO_3 device, increasing the potential by steps of 1.0 V to reach an optimal contrast while maintaining a good reversibility of the coloration (**Figure 5.2**). The experiment is carried out up to maximum +3.0/-3.0 V to avoid too intense bias that could damage the electrolyte after a few cycles only. The difference in the boundaries of the applied bias could arises from the counter electrode also becoming the reference in a 2-electrode configuration, with the potential being measured as “vs. (Mo)CeO_2” instead of “vs. Ag/AgCl”, which can cause a shift of the potential range. In addition, changing the counter electrode from a Pt foil to our (Mo)CeO_2 films can require higher potentials to reach similar optical states given the lower conductivity usually observed in (semiconducting) oxides in comparison to metals, lowering the transfer of charges between the electrodes.

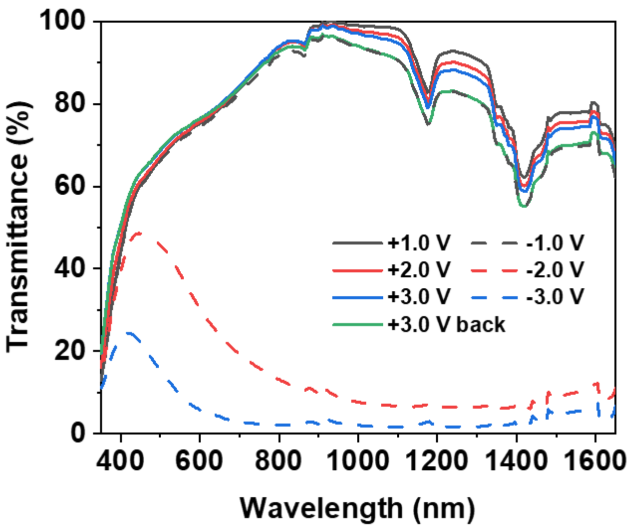

Figure 5.2: Spectroelectrochemical spectra of a WO_3/CeO_2 device as a function of the applied potential, in the bleached state (solid lines) and dark state (dashed lines).

Films of WO_3 “SMARTSPRAY” are studied as working electrodes in tandem with the $(Mo)CeO_2$ counter electrodes developed in the previous chapter (Mo = 0, 2, 4, 6, 8, 10 % at.). In addition to these samples, a reference device is produced by coupling a WO_3 film with a bare FTO-glass substrate as basic counter electrode. The optical spectra of the devices as a function of the applied potential are presented in **Figure 5.3** and their measured performances are included in **Table 5.1**.

The general shape of the bleached spectra is similar in all setups, maintaining a high transmittance in the VIS range with a slight decrease in the NIR. Moreover, the samples follow the same trend as the transmittance measurement of the standalone counter electrode films, with the transmittance (mainly in the VIS range) decreasing as a function of the doping rate. Once a voltage is applied, all devices are able to switch to the dark state, with a large drop in transmittance in the whole NIR range and most of the VIS region. From the values summarized in **Table 5.1**, it appears that most devices display similar performances, with 65 – 70% contrast between optical states, with a bleached state in the 80 – 90% range and a dark state around 15 – 20%, highlighting the good optoelectronic properties of both electrodes. Only CeMo10 diverges from this tendency, with a slightly lower contrast of 54%, starting at 63% at +3.0 V going down to 9% at -3.0 V. Nevertheless, all samples exhibit coloration efficiencies in a narrow range between 12 and 15 cm^2/C, therefore, it is not possible to clearly highlight a significant optimum formulation from these measurements without carrying out further investigation, notably from a statistical point-of-view. As the liquid setups are immerged in the electrolyte solution, there is a large excess in the Li^+ cations required for the coloration of the WO_3 working electrode and thus not limiting the electrochromic behavior of the material. It should be noted that even though the contrast in the $CeMo10/WO_3$ device is the lowest amongst all samples, the CE formula mathematically tends to favor a deeper coloration rather than a highly transparent bleached mode, and since all formulations display a relatively similar level of inserted charges, the low transmittance in the reduced state of the CeMo10 device results in a coloration efficiency value comparable with that of the other devices. Moreover, the reverse bleaching of the materials (after the initial coloration) shows very good results, with a reversibility of more than 95% in all samples, owing to the intrinsic performances of the USP-processed WO_3 active electrode reported in previous works of the GREEnMat team[2].

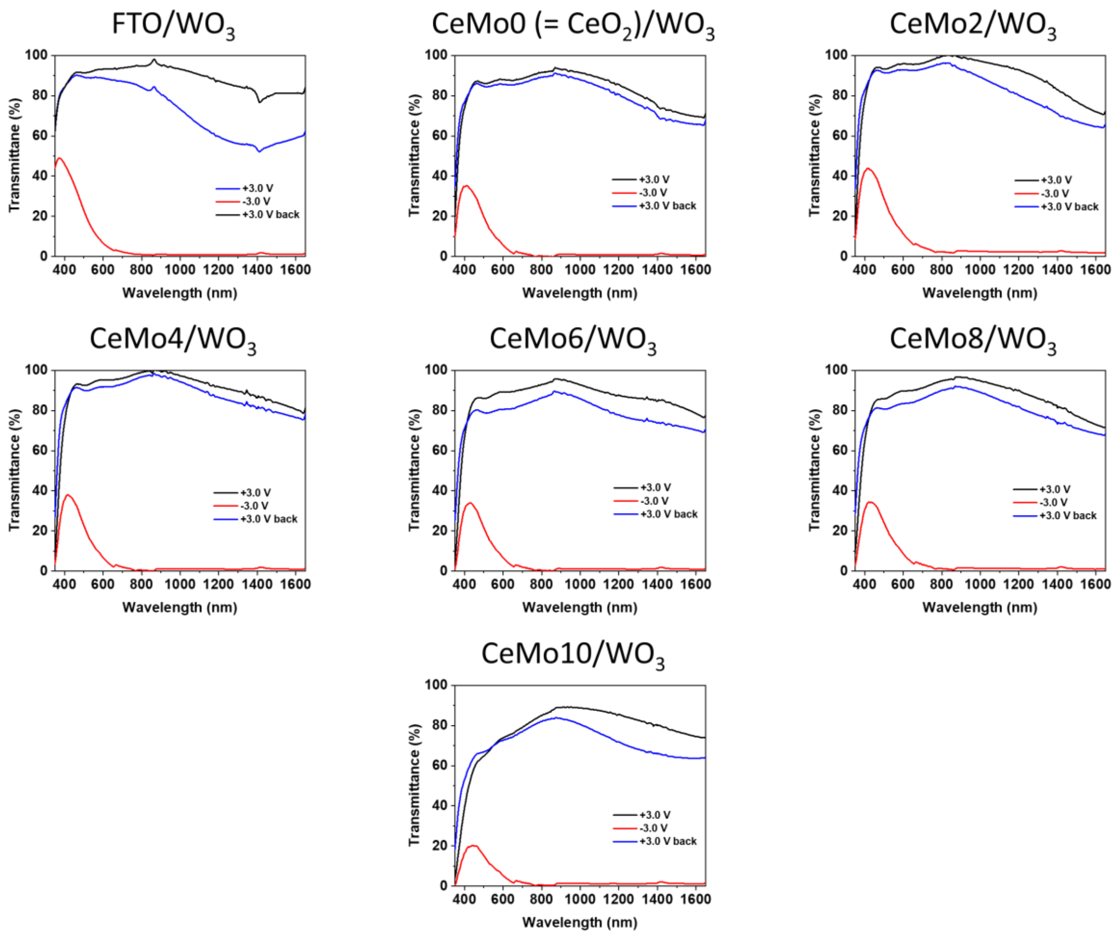
FTO/WO_3 CeMo0 (= CeO_2)/WO_3 CeMo2/WO_3 CeMo4/WO_3 CeMo6/WO_3 CeMo8/WO_3 CeMo10/WO_3

Figure 5.3: Spectroelectrochemical characterization of liquid setup made from WO_3 working electrodes and FTO or CeMo counter electrodes. The samples are cycles between the bleached state (black line), dark state (red line) and back to the bleached state (blue line) to check the reversibility of the coloration in the setup.

Table 5.1: Summary of the electrochromic performances of the FTO/WO_3 and CeMo/WO_3 liquid setups.

Counter electrode	Working electrode	T_b (%)	T_c (%)	ΔT (%)	Reversibility (%)	t_c (s)	t_b (s)	$Q_{in.}$ (mC/cm²)	CE (cm²/C)
FTO	**WO_3**	86.9	19.3	67.6	96.1	58.4	4.8	43.4	15.1
CeMo0	**WO_3**	82.6	14.5	68.1	99.5	39.2	3.8	52.2	14.5
CeMo2	**WO_3**	88.8	20.5	68.3	94.6	27.2	7.2	55.0	11.6
CeMo4	**WO_3**	87.4	15.5	71.9	99.1	22.4	6.4	53.4	14.1
CeMo6	**WO_3**	81.0	14.0	67.0	96.7	20.8	6.4	49.5	15.4
CeMo8	**WO_3**	81.1	15.6	65.5	97.3	14.4	7.2	63.1	11.9
CeMo10	**WO_3**	63.3	9.1	54.2	95.6	17.6	11.2	58.2	14.5

5.3.2. Characterization of solid devices

Even though the characterization of the liquid setups has highlighted the convincing properties of the produced (Mo)CeO_2 layers, and especially in the case of CeMo6, further measurements are required as to further determine the level of performances in a solid device configuration. Indeed, switching from a liquid to a solid electrolyte brings critical limitations to the system, such as a limited amount of available cations or a decrease in ionic diffusion in the electrolyte layer, and can lead to other formulations taking over as the optimum for the intended application.

Solid devices are produced using reference WO_3 "SMARTSPRAY" as the working electrode, and binding the electrodes together with the help of a gel polymer electrolyte layer. The experimental details are available in the **Materials and Methods** section above. Briefly, a layer of gel is casted on both films, which are then assembled into a single unit, staggered as to keep a portion of each electrode uncovered for the connection with the potentiostat. The devices are characterized for their spectroelectrochemical properties using a film holder (**Figure 5.1**), applying +3.0 and -3.0V potential steps for 5 minutes each before starting the optical measurement. The time under tension is increased in comparison to the liquid devices to allow the device to reach a stable optical state, given the lower ionic diffusion of the solid gel in comparison to the liquid electrolyte in the previous experiments.

In comparison to the liquid setups, the solid devices maintain a similar optical behavior, with a high transmittance in the VIS range and a slight drop in the NIR. The overall transmittance of the samples is slightly lower than in their liquid counterparts, indicating the excellent optical properties of the gel, not impeding with the electrochromic activity of the electrodes. Here again, the transmittance of the different formulations follows the trend observed in the previous chapter, with the bleached state consistent from CeMo0 to CeMo6, while CeMo8 and CeMo10 exhibit lower optical performances – probably because of the numerous cracks observed at their surface. Looking at the data summarized in **Table 5.2**, all devices display contrasts approximately between 60% and 70%, with the exception of CeMo10, similarly to the previous section, in which case the contrast only reaches a value of 50%. Moreover, all (Mo)CeO_2 based samples show high CEs ranging from 17 to 22 cm^2/C, improving in comparison to the liquid configuration even though the contrasts decreased, because of the limited amount charge flowing between the electrodes, resulting in a favorable CE calculation. However, for the device produced with a simple FTO-glass counter electrode, a very large number of cations is inserted in the active layer to reach a contrast similar to that of the other counter electrode formulations, leading to a low CE value. In addition, the device does not bleach back at +3.0 V, and up to +5.0 V is required to initiate the bleaching process, highlighting the poor counter electrode abilities of the bare FTO substrate.

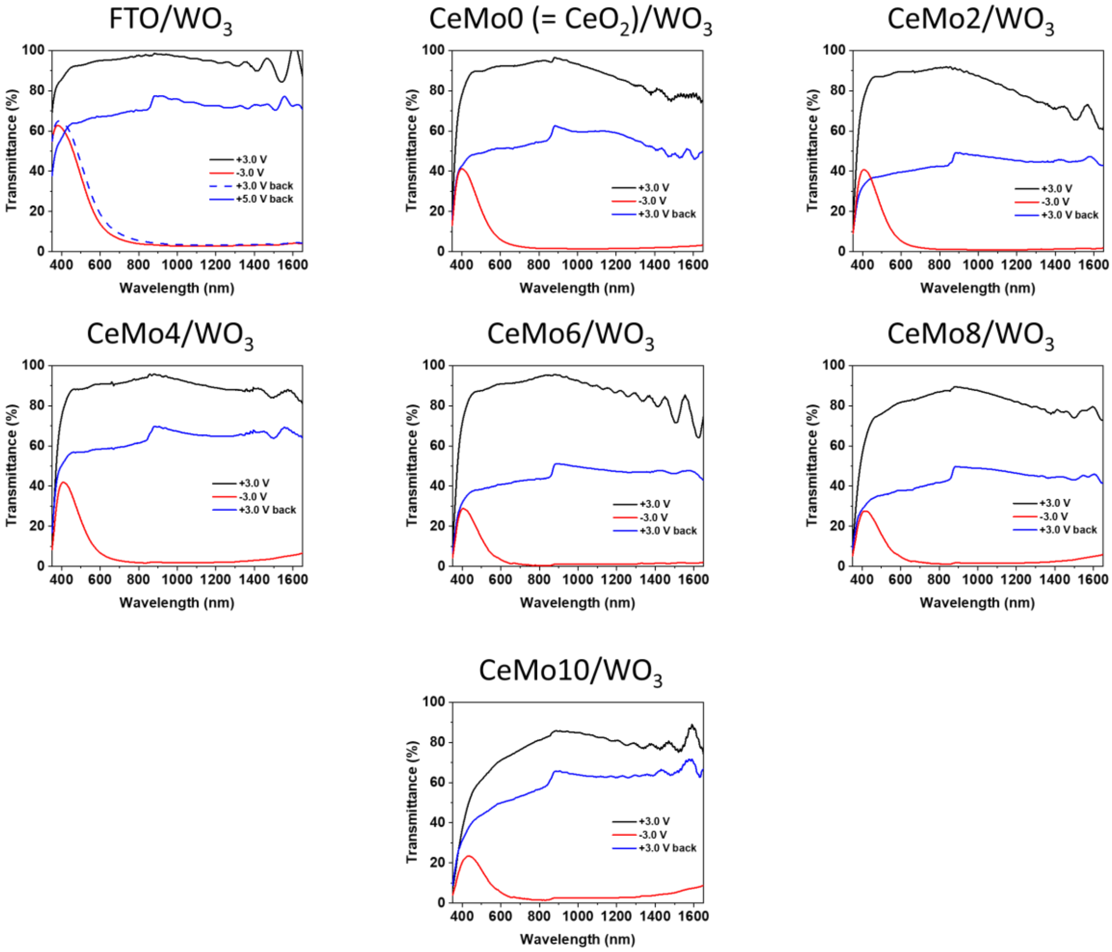

Figure 5.4: Spectroelectrochemical characterization of solid devices made from WO_3 working electrodes and FTO or CeMo counter electrodes. The samples are cycles between the bleached state (black line), dark state (red line) and back to the bleached state (blue line) to check the reversibility of the coloration in the setup.

Table 5.2: Summary of the electrochromic performances of the FTO/WO_3 and CeMo/WO_3 solid devices.

Counter electrode	Working electrode	T_b (%)	T_c (%)	ΔT (%)	Reversibility (%)	t_c (s)	t_b (s)	$Q_{in.}$ (mC/cm^2)	CE (cm^2/C)
FTO	**WO_3**	92.0	29.6	62.4	55.1	258.0	64.8	133.5	3.7 ± 1.6
CeMo0	**WO_3**	86.3	16.6	69.7	44.7	246.0	4.4	38.0	18.8 ± 0.7
CeMo2	**WO_3**	83.1	15.9	67.2	68.7	272.4	6.4	41.4	17.3 ± 3.5
CeMo4	**WO_3**	84.2	17.1	67.1	65.7	255.9	5.2	37.3	18.6 ± 0.6
CeMo6	**WO_3**	83.3	10.7	72.6	40.0	311.6	9.2	47.2	18.8 ± 0.9
CeMo8	**WO_3**	73.0	11.4	61.6	59.5	334.4	5.6	35.9	22.5 ± 2.2
CeMo10	**WO_3**	60.7	10.6	50.1	68.8	272.4	3.6	40.2	18.9 ±1.8

The reversibility of the coloration/bleaching process is also investigated. However, the results indicate a limited recovery of the bleached state. This is due to the electrolyte layer degrading during the electrochemical bias of the devices, exhibiting some form of crystallization all over the surface of the film and appearing less transparent than initially. Another explanation could lie in the electrically-induced thermal degradation of the polymer, being locally "burned" and resulting in the opacification of the electrolyte layer, also known as Lichtenberg figures[3]. Pictures of a device taken before and after the electrochemical cycling illustrate this phenomenon in **Figure 5.5** below. Nonetheless, the lack of a residual blue coloration in the sample highlights the good performances of the electrodes even in these conditions, indicating the need to improve the deposition conditions of the gel or its composition as to maintain a fully transparent layer regardless of the applied potential.

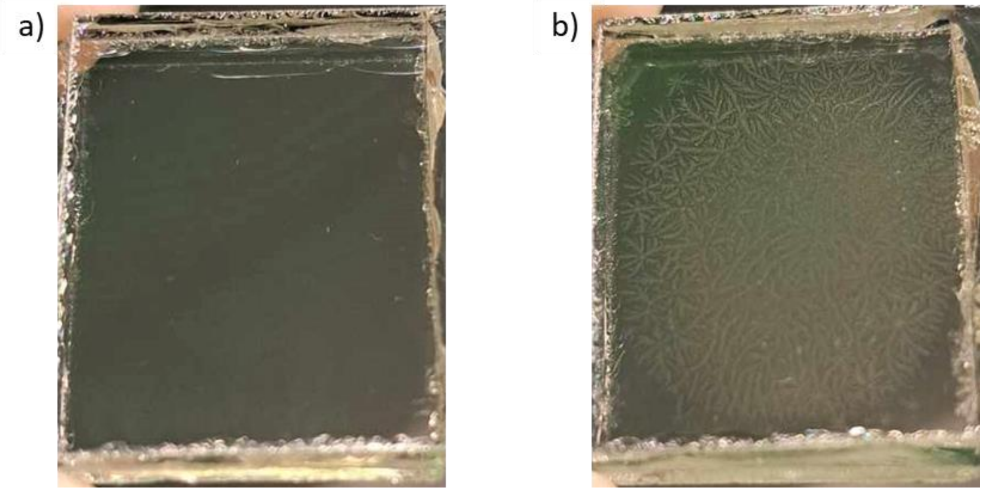

Figure 5.5: Example of the polymer gel in a solid device damaged by the electrochemical cycling, going from a clear appearance (a) to opacified (b).

The kinetics of the devices are also quantified by measuring the evolution of the transmittance as previously state (Table 5.2). The computed values for t_c and t_b show similar coloration behavior in all samples, with FTO or any (Mo)CeO_2 formulations as the counter electrode, with durations of a few minutes, from 250 to 350 s. Meanwhile, the bleaching time improves when our (Mo)CeO_2 counter electrode materials are implemented, with no significant difference highlighted between all Mo doping rates.

Once more, the (Mo)CeO_2 produced samples prove to be a viable solution of counter electrode, and are definitely better than using a standard bare FTO glass substrate. Greater CEs can be obtained due to the limited insertion of charges while keeping a large contrast between the bleached and dark states. While no optimum formulation could be highlighted from the present results, all CeO_2 based counter electrodes display good performances, getting closer to applied requirements targeted in the scope of the SMARTSPRAY project: a transmittance of 60% (or higher) in the bleached state, and of 10% (or lower) in the dark state, while switching from one mode to the other in a timeframe of 10 minutes maximum[2]. Nevertheless, future developments will have to look into ways to improve the coloration kinetics and the reversibility of the electrochromic process, adapting the electrolyte layer to support the electrochemical charge/discharge protocol.

5.4. Application of plasmonic electrochromic materials in liquid systems

Following the developments made using the reference “WO_3 SMARTSPRAY” active electrode in the previous section, the main formulations of interest investigated in this work, MoWOx 2/1 1h and $WO_{3-\delta}$ 1h, can be coupled to selected counter electrode formulations chosen on the basis of the performances observed in **Sections 5.3.1**, page 139 and **5.3.2**, page 141. While all (Mo)CeO_2 showed great potential for their implementation as counter electrode in a complete electrochromic system, CeMo4 and CeMo6 could be highlighted to be amongst the optimal formulations, as standalone films as well as in liquid setups and solid devices. These two formulations are tested for the development of devices using the highly functional – dual-band – $WO_{3-\delta}$ and MoWOx produced in the scope of this thesis. However, preliminary results showed similar results for either counter electrode formulations. Therefore, in the interest of efficiency, the following section will only cover the characterization of liquid and solid systems involving CeMo6, selected as the mainly investigated formulation as a compromise between its high transmittance and improved capacity in comparison to CeMo4 (as discussed in **Chapter 4**).

5.4.1. $WO_{3-\delta}$ 1h

In a first step, a liquid setup is investigated by coupling a $WO_{3-\delta}$ 1h sample as working electrode with CeMo6 as “passive” counter electrode. The use of passive CeO_2 based formulations as counter electrode allow the investigated plasmonic electrochromic materials to express all three of their working states (bright, cool or warm, and dark) without any risks of a complementary electrode hindering their ability to do so. Given the earlier state of development of $WO_{3-\delta}$ and MoWOx compounds in comparison to WO_3 SMARTSPRAY, each bias step is applied for 5 minutes to ensure a stable optical and electrochemical state of the active layer. The spectra obtained using either counter electrode formulations are presented in **Figure 5.6**. In comparison to the previously acquired spectra of the standalone film (**Figure 3.11c**), the setups maintain the same optical properties as the $WO_{3-\delta}$ layer, namely a large transmittance in across the whole measurement interval. Thanks to the great transmittance exhibited by the CeMo formulations across VIS and NIR ranges, no significant loss of signal is observed in comparison to the $WO_{3-\delta}$ layer on its own. The device also exhibit the ability to switch between three optical states, with properties almost identical to those of the films in the 3-electrode configuration. The performances of both devices are summarized in **Table 5.4**, highlighting no significant difference between the two counter electrode formulations. Indeed, the sample exhibits a very efficient NIR selective state, with almost no contrast in the VIS (1.4%) and 51% in the NIR at -1.0 V, resulting in CE values of around 1 and 43 $cm^2 C^{-1}$ in the VIS and NIR ranges, respectively. Once -3.0 V is applied, the device reaches its most reduced state, darkening in both VIS and NIR regions, displaying contrasts of 24% (VIS) and 75% (NIR), and efficiencies of 6 $cm^2 C^{-1}$ in VIS and 23 $cm^2 C^{-1}$ in NIR. The optical activity at -1.0 V demonstrates the peculiar behavior of $WO_{3-\delta}$ in comparison to the conventional WO_3 SMARTSPRAY formulation, which showed no electrochromic effect at -1.0 V (**Figure 5.2**), with the transmittance only dropping when at least -2.0 V is applied.

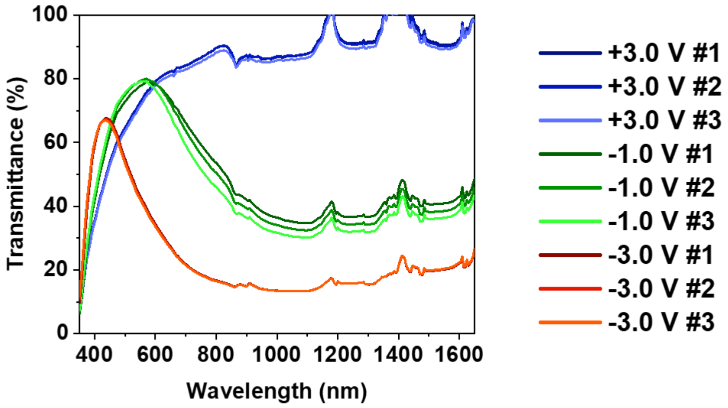

Figure 5.6: Transmittance spectra of the $WO_{3-\delta}$/CeMo6 liquid setups as a function of the applied potential, and repeated over three electrochemical cycles.

Table 5.3: Summary of the electrochromic performances of the $WO_{3-\delta}$/CeMo6 liquid setups.

+3.0 V		**-1.0 V**							**-3.0 V**						
T (%)		T (%)		ΔT (%)		$Q_{in.}$ (mC cm^{-2})	CE (cm^2 C^{-1})		T (%)		ΔT (%)		$Q_{in.}$ (mC cm^{-2})	CE (cm^2 C^{-1})	
VIS	*NIR*	VIS	*NIR*	VIS	*NIR*		VIS	*NIR*	VIS	*NIR*	VIS	*NIR*		VIS	*NIR*
65.1	*92.0*	63.7	*41.1*	1.4	*50.9*	-8.2	1.2	*42.7*	40.8	*17.0*	24.3	*75*	-32.1	6.3	*22.9*

Moreover, in the liquid setups, the $WO_{3-\delta}$ film displays great kinetics: the films are cycled back and forth between +3.0 V and -1.0 V / -3.0 V, with each bias step applied for 10 minutes (**Figure 5.7**). The measured coloration and bleaching times are summarized in **Table 5.4**. In the intermediate state (-1.0 V), bleaching and coloration times are measured to be under 10 seconds, in good agreement with the expected capacitive charge/discharge at this potential. When the potential reaches -3.0 V, the sample exhibits a fast coloration, also around 10 seconds, while the bleaching is slightly slower, especially in the NIR range (22 seconds). These results appear to confirm the faster kinetics of the intermediate state, expected to be ruled by capacitive / plasmonic mechanisms according to the model proposed by Milliron[4–6]. Furthermore, in comparison to the standalone films studied in **Chapter 3**, the kinetics appear to be faster when the active film is coupled with an appropriate counter electrode of comparable size.

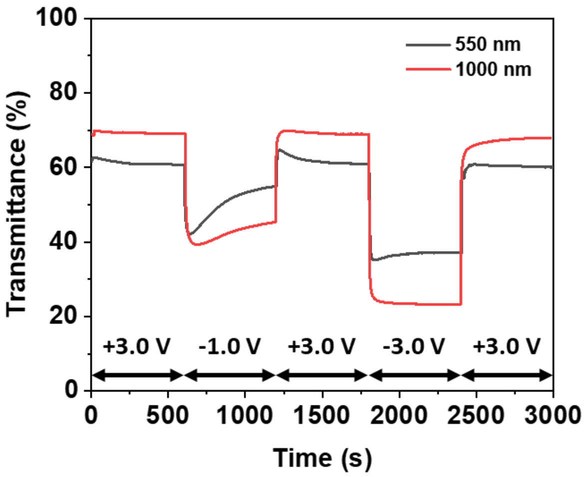

Figure 5.7: Transmittance spectra of the $WO_{3-\delta}$/CeMo6 liquid setups as a function of the applied potential and time under tension, measured at two wavelength representing the VIS range (550 nm) and NIR region (1000 nm).

Table 5.4: Summary of the results calculated from the kinetics measurements of the $WO_{3-\delta}$/CeMo6 liquid setups .

Intermediate (-1.0 V)				Dark (-3.0 V)			
t_c (s)		t_b (s)		t_c (s)		t_b (s)	
550 nm	1000 nm	550 nm	1000 nm	550 nm	1000 nm	550 nm	1000 nm
2	6	2	6	10	12	4	22

In addition, it was possible to apply a few complete coloration/bleaching cycles while conserving the intermediate state – that was previously lost right after the first complete coloration of the film (see **Figure 3.16** page 90). The improved reversibility of the different optical states displayed by the liquid device (Table 5.5) could be due to the counter electrode changing from a small Pt foil (1-2 cm²) in the 3-electrode configuration, to the CeMo4 and CeMo6 film (5 cm²). Moreover, the position of the counter electrode relative to the working electrode changes from one setup to the other: with three electrodes, the Pt foil is placed on the side of the sample to not cross the incident light beam (see **Figure 5.8**), while the CeMo films are placed directly in front of the MoWOx film at a close distance of 2-3 mm (**Figure 5.1c**). The combination of the position and size of the Pt counter electrode could result in high current densities in the active layer, leading to irreversible damages to the material, especially at the surface of the material, impacting its plasmonic properties. Therefore, using a more appropriate counter electrode exhibiting sufficient area for the efficient transfer of charges in the system avoids damaging the active layer and allows the intermediate state to occur even after a complete electrochemical cycle.

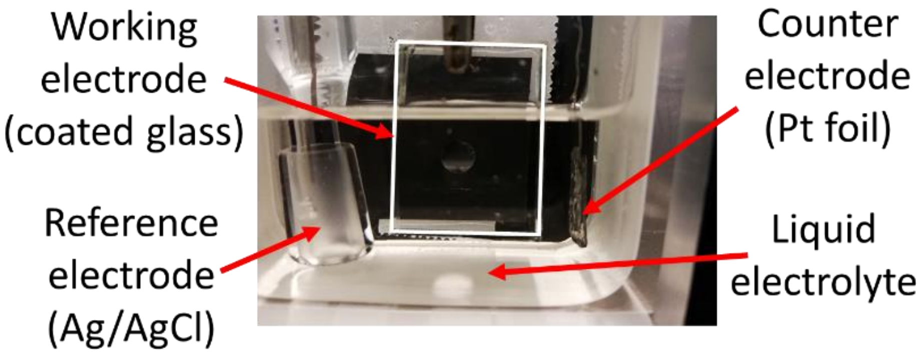

Figure 5.8: Picture of the three electrode setup, comprised of the working, counter and reference electrodes.

Table 5.5: SEC characterization of the $WO_{3-\delta}$/CeMo6 liquid devices across multiple electrochemical cycles.

Cycle #	**+3.0 V**		**-1.0 V**				**-3.0 V**			
	T (%)		T (%)		ΔT (%)		T (%)		ΔT (%)	
	VIS	*NIR*	VIS	*NIR*	VIS	*NIR*	VIS	*NIR*	VIS	*NIR*
1	65.1	*92.0*	63.7	*41.1*	1.4	*50.9*	40.8	*17.0*	24.3	*75.0*
2	65.3	*91.8*	64.0	*38.6*	1.3	*53.2*	40.7	*17.0*	24.6	*74.8*
3	64.3	*90.6*	62.7	*36.0*	1.6	*54.6*	40.5	*17.0*	23.8	*73.6*

From the quantification of their respective performances, no clear liquid device optimum can be highlighted, reminiscent of the close performances displayed by the CeMo4 and CeMo6 formulations when studied as films or in devices with WO_3 SMARTSPRAY. Nonetheless, both setups exhibit very good properties, displaying a very efficient NIR-selective intermediate state, as well as good contrasts in both VIS and NIR ranges at appropriate potentials, while switching between the three working states in an excellent time frame for their expected application as smart windows (< 10 seconds at -1.0 V and < 30 seconds / 1 minute at -3.0 V). Moreover, the assembly of the electrodes allows more reversible redox phenomena, especially at the surface of the films, resulting in highly reversible optical states and more importantly the conservation of the intermediate state previously lost in the standalone film characterizations.

5.4.2. MoWOx 2/1 1h

From there, additional experiments are carried out using the same liquid assembly protocol, but applied to MoWOx 2/1 1h this time, and coupled with the selected counter electrode formulations: CeMo4 and CeMo6 (**Figure 5.9**). Once again, both setups display very similar results, with no significant difference arising from the difference in the counter electrode formulation used to assemble the setup. The general shape of the optical spectra is retained in comparison to the films in the three electrodes configuration (**Figure 3.11a**), with an overall high transmittance in the NIR range and a moderate transparency in the VIS region in its most oxidized state, corresponding to the previously described *warm* mode. In addition to the latter, the intermediate mode is reached upon application of a -1.0 V bias, with an optical modulation of 35-40% and 18-22% in the NIR and VIS range, respectively. This results in an efficiency of 33-35 cm^2C^{-1} (VIS) and 38-40 cm^2C^{-1} (NIR) in the devices. Upon application of a more reducing potential of -3.0 V, the devices appear very dark, with the overall transmittance dropping below 10% in most of the measurement interval. The contrasts between the bleached and dark states are determined to range from 34-36% in VIS to 67-70% in NIR, corresponding to CEs of 10-13 cm^2C^{-1} in the former range and 15-19 cm^2C^{-1} in the latter (**Table 5.6**).

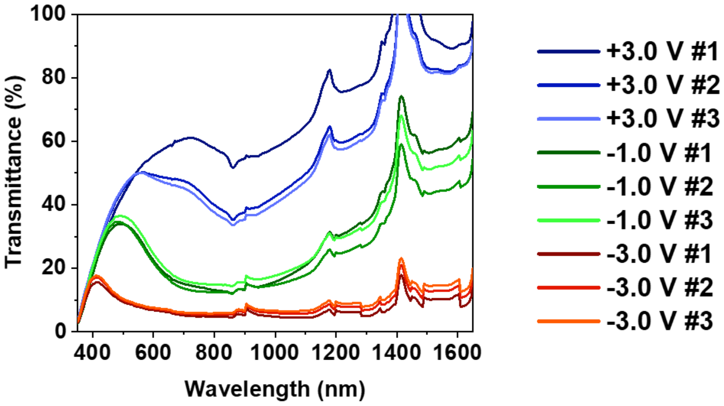

Figure 5.9: Transmittance spectra of the MoWOx/CeMo6 liquid setups as a function of the applied potential, and repeated over three electrochemical cycles.

Table 5.6: Summary of the electrochromic performances of the MoWOx/CeMo6 liquid setups.

+3.0 V		-1.0 V							-3.0 V						
T (%)		T (%)		ΔT (%)		$Q_{in.}$ (mC cm^{-2})	CE (cm^2 C^{-1})		T (%)		ΔT (%)		$Q_{in.}$ (mC cm^{-2})	CE (cm^2 C^{-1})	
VIS	*NIR*	VIS	*NIR*	VIS	*NIR*		VIS	*NIR*	VIS	*NIR*	VIS	*NIR*		VIS	*NIR*
44.2	*76.7*	22.1	*34.2*	22.1	*42.5*	-8.9	33.8	*39.4*	8.5	*6.9*	35.7	*69.7*	-67.7	10.6	*15.5*

In regards to their kinetics, presented in **Figure 5.10**, the MoWOx films display similar coloration and bleaching times to those of the films in the 3-electrode setup from **Chapter 3**. Here again, the coloration and bleaching times are longer in the intermediate -1.0 V state (up to 420 seconds, see **Table 5.7**), especially during the bleaching step. This could be due to the peculiar morphology of the MoWOx particles, with the nanorods covering their surface resulting in longer mean free path of the cations in the electrolyte solution; as discussed earlier (**Chapter 3**). Once the potential increases to reach the dark state, the coloration kinetics improve sharply (< 20 seconds), as the driving force of the applied bias allows the insertion of a large number of cations into the lattice of the active film. Meanwhile, the bleaching times of these samples are similar to those of the intermediate mode, probably arising from the surface morphology of the urchins coupled to the possible trapping of charges inside of irreversible active sites.

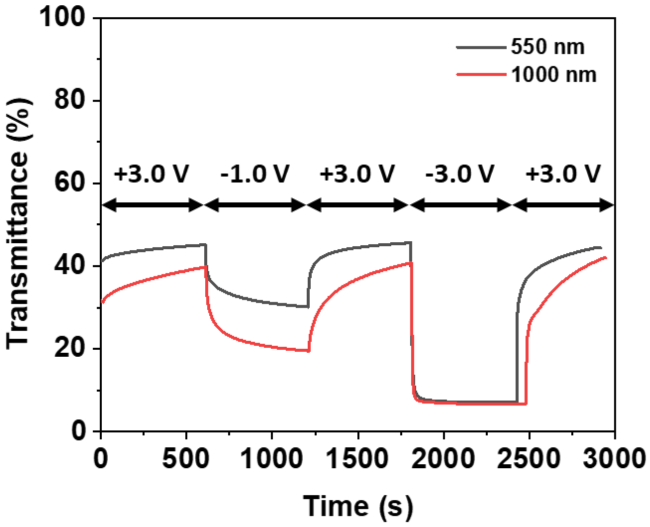

Figure 5.10: Transmittance spectra of the MoWOx/CeMo6 liquid setups as a function of the applied potential and time under tension, measured at two wavelength representing the VIS range (550 nm) and NIR region (1000 nm).

Table 5.7: Summary of the results calculated from the kinetics measurements of the MoWOx/CeMo6 liquid setups .

Intermediate (-1.0 V)				Dark (-3.0 V)			
t_c (s)		t_b (s)		t_c (s)		t_b (s)	
550 nm	1000 nm	550 nm	1000 nm	550 nm	1000 nm	550 nm	1000 nm
294	134	225	417	19	12	228	279

In comparison to their $WO_{3-\delta}$ 1h counterparts, the MoWOx devices exhibit less selective intermediate optical states, with a 20% decrease in VIS transmittance; higher efficiencies in the NIR range are also observed for the $WO_{3-\delta}$ based configurations vs. MoWOx ones. However, in the dark state, the novel MoWOx electrochromic formulations exhibits higher efficiencies in the VIS range, and comparable ones in the NIR range, due to the deep coloration that can be reached by the MoWOx materials upon reduction at the appropriate bias.

In fact, these optical behaviors can be linked to the KM spectra of the powders: in the case of $WO_{3-\delta}$, the absorption peak appears at 1400 nm, resulting in a limited effect on the VIS range, leading to no modulation in the intermediate state, but also a weak coloration in the dark state. On the other hand, the MoWOx KM signature is characterized by a large absorption around 800-900 nm, resulting in a very intense dimming of the NIR wavelengths, especially those in the 750-1250 nm range of interest. Unfortunately, the position of this peak, close to the VIS-NIR transition, compromises the selectivity of the intermediate state, with a small but significant modulation of VIS light. Meanwhile, for the same reason, the modulation of the VIS transmittance at -3.0 V is greater than that of $WO_{3-\delta}$, leading to an increased efficiency in this part of the spectrum for the MoWOx formulation.

Similarly to the $WO_{3-\delta}$ case discussed above, crucially, the use of CeMo as counter electrode for the assembly of devices allows the conservation of the -1.0 V – NIR-preferential – intermediate state (**Table 5.8**). However, in the case of the MoWOx devices, it seems like the reversibility of the electrochemical processes taking place upon cycling, although displaying convincing results, is not as good as those observed in the case of $WO_{3-\delta}$. These results are in good accordance with the previous discussions in **Chapter 3** that concluded on the greater reversibility of the parent oxide. However, this small lack of reversibility does not hinder the expression of the three working modes, even after the complete coloration of the devices, which was shown to be detrimental in the SEC measurements on single films using the 3-electrode setup in a liquid electrolyte.

Table 5.8: SEC characterization of the $WO_{3-\delta}$/CeMo6 liquid devices across multiple electrochemical cycles.

Cycle #	**+3.0 V**		**-1.0 V**				**-3.0 V**			
	T (%)		T (%)		ΔT (%)		T (%)		ΔT (%)	
	VIS	*NIR*	VIS	*NIR*	VIS	*NIR*	VIS	*NIR*	VIS	*NIR*
1	44.2	*76.7*	22.1	*34.2*	22.1	*42.5*	8.5	*6.9*	35.7	*69.7*
2	40.2	*62.1*	22.0	*27.7*	18.2	*34.4*	9.3	*8.7*	30.9	*53.4*
3	39.7	*60.2*	24.1	*32.8*	15.6	*27.4*	9.6	*9.9*	30.1	*50.3*

Another important parameter is the compliance of these devices to commercial requirements, even though further testing will be needed to assess the long-term durability of the devices. As stated earlier, an electrochromic device should switch between 60+% and less than 10% transmittance levels in the bright and dark state, respectively[2]. On the first hand, $WO_{3-\delta}$ easily fulfills the first requirement across all NIR range and most of VIS, but the colored state does not reach a sufficiently dark optical signature. On the other hand, the colored state of the MoWOx devices clearly exhibits a 10% or less transmittance in the majority of the measurement interval and a high transmittance in a large part of the NIR region. However, its bleached state is not transparent enough, especially in the blue part of the VIS and around the absorption peak of the KM spectra (850-900 nm). Therefore, both formulations are in relatively good accordance with the discussed requirements, with the parent oxide devices needing a more intense colored state while the mixed formulation requires a more transparent bright state.

With their dual-band features now retained when assembled as liquid devices, both MoWOx 21 1h and $WO_{3-\delta}$ 1h are confirmed as promising candidates for application as active material in dual band smart windows. While each formulation suffers from some limitations (intensity of VIS modulation in $WO_{3-\delta}$ and lack of selectivity in MoWOx 21 1h), future developments and improvements of these formulations should allow for a better tradeoff between those performances, possibly leading to the production of highly efficient and selective materials suited for commercial applications.

5.5. Application of plasmonic electrochromic materials in solid devices

With the proof-of-concept liquid device produce above, and even displaying improved properties and functionalities in comparison to the standalone film, a solid device can be assembled from both $WO_{3-\delta}$ 1h and MoWOx 21 1h films coupled with CeMo6 counter electrodes and bound together using the gel polymer electrolyte described in the **Materials and Methods** section.

Two solid devices are prepared following the protocol reported in earlier in **Materials and Methods** and electrochemically cycled between +3.0 and -3.0 V, the spectra acquired as a function of the applied potential are presented in **Figure 5. 11** below. Similarly to the previous cases, the general shape of the bleached state is maintained while most of the transmittance intensity is conserved, demonstrating the good transparency of the electrolyte within the boundaries of the wavelength range used in this work. Both devices display the expected three working states associated to their dual band behavior, and can be reached even after the complete coloration of the active material, as observed in the liquid setups and contrary to the standalone films investigated in **Chapter 3**. However, as the solid electrolyte layer is prone to degradation upon electrochemical cycling, the transmittance of the bleached and intermediate states decreases abruptly after the first electrochemical cycle. Indeed, the exposition of the electrolyte to the potential window used here seems to result in damages that could be interpreted as the formation of crystals in the polymer gel (as discussed earlier in this chapter). This is the case in all solid devices, but does not always appear right after the first electrochemical cycle, as in the case of the $WO_{3-\delta}$/CeMo6 device. However, this is probably due to small variations in the assembly protocol, which is still being developed at the GREEnMat. In the current state of the GREEnMat expertise, the gel polymer electrolyte is an acceptable formulation for the production of proof-of-concept demonstrators, but requires intensive and extended work before becoming a totally viable option for the potential future development and scale-up of the devices, and even more towards commercial applications.

From a coloration efficiency point of view, all samples present low values in the VIS at -1.0 V (<4 cm^2/C), and high CE in the NIR at the same bias, ranging from 40 to 130 cm^2/C (**Table 5. 9**). This indicates the good selectivity of the active formulations towards NIR wavelengths: by definition, a small contrast will lead to low CE (this is the case in the VIS range), while a large contrast, coupled to the small density of inserted charges expected from plasmonic phenomena will result in high electrochromic efficiencies. When the potential is changed to -3.0 V, the CE increases in the VIS due to the contrast appearing in this region in the dark mode, while the efficiency of the NIR decreases. This is caused by the large density of charges being inserted into the crystal lattice, as the bias has become strong enough to force the insertion of cations into the material (as opposed to the capacitive charge/discharge of the intermediate state). Therefore, both inserted charges and contrast increase drastically in the VIS, leading to enhanced efficiencies, while the contrast in the NIR only improves by a small margin in comparison to the intermediate state: the combination of more charges for a small increase in the contrast results in lower CE values in this particular range of the spectrum at -3.0 V.

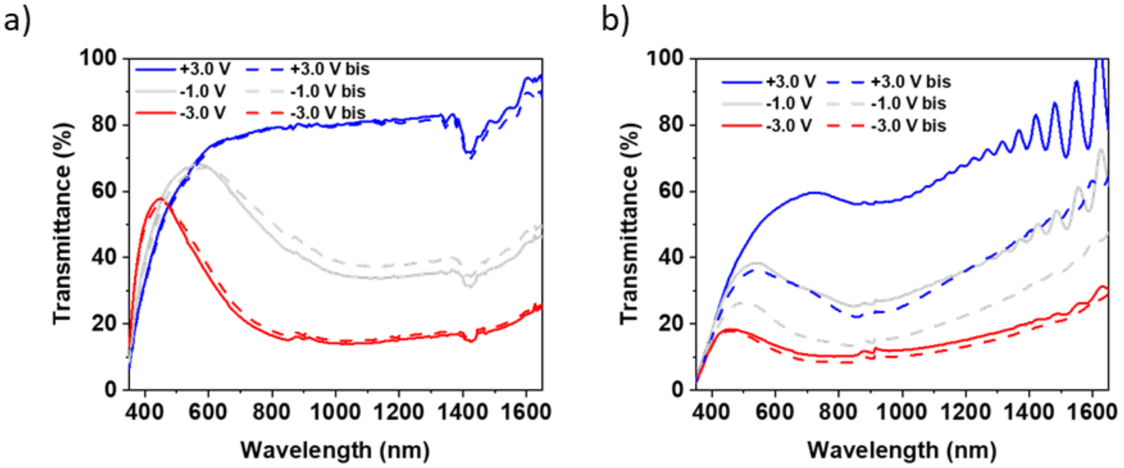

Figure 5. 11: Transmittance spectra of the two investigated dual band solid devices: MoWOx/CeMo6 (a) and $WO_{3-\delta}$/CeMo6 (b) as a function of the applied potential, repeated over two electrochemical cycles.

Table 5. 9: Summary of the electrochromic performances of the two investigated dual band solid devices.

Active Material	+3.0 V		-1.0 V							-3.0 V						
	T (%)		T (%)		ΔT (%)		$Q_{in.}$ (mC cm^{-2})	CE (cm^2 C^{-1})		T (%)		ΔT (%)		$Q_{in.}$ (mC cm^{-2})	CE (cm^2 C^{-1})	
	VIS	*NIR*	VIS	*NIR*	VIS	*NIR*		VIS	*NIR*	VIS	*NIR*	VIS	*NIR*		VIS	*NIR*
MoWOx	43.3	*68.7*	29.9	*34.0*	13.5	*29.7*	5.3	3.6	*46.5*	13.6	*16.9*	29.7	*51.8*	45.5	7.5	*8.0*
$WO_{3-\delta}$	60.0	*81.4*	56.1	*37.7*	3.9	*43.7*	2.6	2.4	*128.6*	38.4	*16.6*	21.7	*64.8*	12.2	13.5	*29.2*

As for the liquid setups investigated above, the kinetics of the devices are investigated in the +3.0 / -3.0 V range, for the four selected assembly (**Figure 5. 12**). The obtained results show quite long coloration times in all four devices, with duration of up to 400 seconds (**Table 5. 10**), even in the intermediate state (supposed to be capacitive). This drop in the kinetic performances of the films, especially $WO_{3-\delta}$, are in good accordance with the expected decrease in ion conductivity and mobility from the electrolyte as the formulation of the latter evolves from the liquid phase to a solid. This change in the ion conductive layer can result in a slower diffusion of the cations through the device, limiting the kinetics of the electrochromic processes at play. Here, the diffusion limiting step impacts $WO_{3-\delta}$ a lot more than MoWOx, as the complicated surface morphology of the latter was already thought to act as a barrier to the efficient diffusion of the Li^+ throughout the active films to reach the available active sites. Nevertheless, the simple nanospherical shape of the $WO_{3-\delta}$ particles, as well as the large surface area of the film produced from this formulation, allows the fast extraction of the cations out of the material lattice.

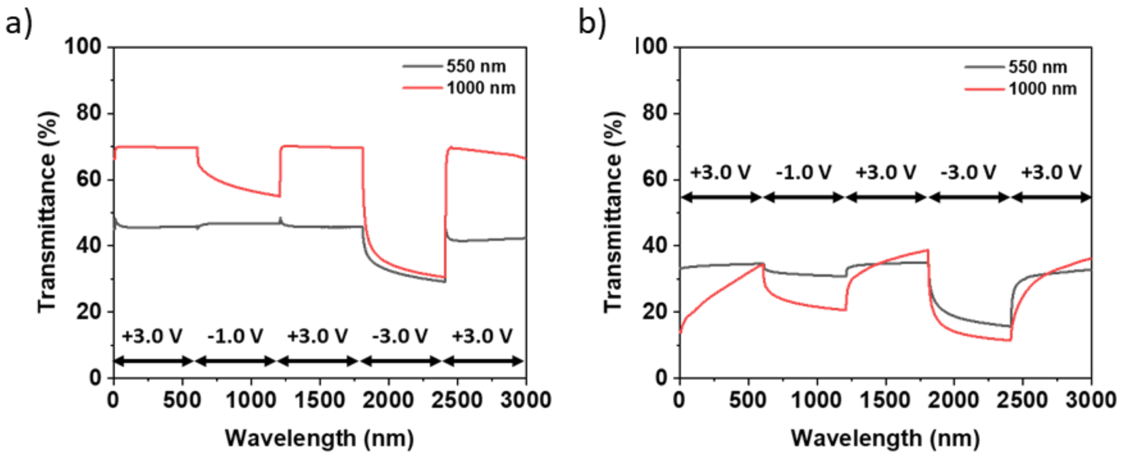

Figure 5. 12: Transmittance spectra of the two investigated dual band solid devices: MoWOx/CeMo6 (a) and $WO_{3-\delta}$/CeMo6 (b) as a function of the applied potential and time under tension, measured at two wavelength representing the VIS range (550 nm) and NIR region (1000 nm).

Table 5. 10: Summary of the results calculated from the kinetics measurements of the two dual band solid devices.

	Intermediate (-1.0 V)				Dark (-3.0 V)			
	t_c (s)		t_b (s)		t_c (s)		t_b (s)	
	550 nm	1000 nm	550 nm	1000 nm	550 nm	1000 nm	550 nm	1000 nm
MoWOx	368	324	248	406	280	190	192	394
$WO_{3-\delta}$	2	410	2	6	354	204	4	8

Given all the results acquired in the scope of this study, the difficulty to transition from liquid setups to solid devices is highlighted. While the three working modes are maintained in the first cycle, with optical signatures similar to those of the standalone active films, or in the liquid setups, a significant loss in performance is observed from the second cycle and onwards. Indeed, as the electrolyte gel is degraded from electrochemical cycling, the layer becomes less transparent (and more diffusive), limiting the contrast between states. Moreover, using a solid media implies a decrease in ionic mobility through the layer, and less available cations in the system (in comparison to the liquid setups in which the electrolyte is present in large excess), resulting in less effective kinetics in the investigated materials. However, even though the properties of the gel polymer electrolyte could be considered as non-satisfactory from these first tests, they already conceptualize the production of fully assembled solid devices, exploiting the dual band plasmonic formulations studied in this thesis as active layers. The obtained results show good electrochromic results in the first coloration / bleaching cycle of these devices, and prove the interesting properties of the two selected plasmonic formulations, placing those as promising candidates for the future development of highly efficient smart windows towards increased energy savings in buildings.

5.6. Conclusions and perspectives

With the previous chapters investigating the development of efficient dual band active materials and passive counter electrodes as individual components of electrochromic systems, their assembly into a complete solid assembly represents the last step towards the production of proof-of-concept dual band devices, notably implementing MoWOx as the active species. In this section, the coupling of MoWOx 2/1 1h and $WO_{3-\delta}$ films with Mo-doped CeO_2 counter electrodes has been studied, first as liquid setups and then as solid devices.

First of all, the assembly and measurement protocol, either in liquid or solid form, has been designed using a reference WO_3 formulation, developed at GREEnMat in the scope of their electrochromic expertise. This conventional electrochromic material has been assembled into devices with all the (Mo)CeO_2 formulations, exploring different Ce/Mo ratios once applied in a complete system. Overall, all formulations are globally exhibiting high contrasts, fast coloration and bleaching kinetics, as well as high coloration efficiencies, demonstrating the good optoelectronic properties of the electrodes. These experiments prove the viability of the developed (Mo)CeO_2 films for the efficient assembly of samples into complete devices. Given the lower transmittance of the MoWOx in the VIS range, CeMo4 and CeMo6 have been chosen as the best tradeoffs between a high transmittance and a large capacity.

Two combinations have been investigated from there, with MoWOx and $WO_{3-\delta}$ each coupled with CeMo6 as the selected counter electrode formulations. Noteworthy, trials have been carried out using CeMo4 as well but displayed similar results to those of the CeMo6 based devices, therefore, only one formulation was chosen to be discussed in this manuscript. Outstandingly, these devices have been shown to exhibit superior properties to those of the standalone films, in particular regarding the maintaining of the intermediate state after the complete coloration into the dark state. Using a more appropriate counter electrode (with a comparable size to that of the working electrode), the active formulations are capable to keep three working states over multiple cycles of coloration / bleaching, in both liquid setups and solid devices. The coloration efficiency of the investigated formulation also improves upon assembly with the (Mo)CeO_2 films, demonstrating their promising performances as passive counter electrodes.

The results of the present chapter highlight the potential use of the MoWOx material within assembled electrochromic devices, which is fully new and original for the state-of-the-art, proving its ability to display a dual band functionality and maintaining it throughout electrochemical cycling in a complete electrochromic cell. The produced MoWOx films are able to switch between the three states in a reversible manner thanks to the action of (Mo)CeO_2 as a counter electrode, avoiding potential damage to the working electrode due to high current densities. This first proof-of-concept demonstrates the applicability of the investigated formulations for smart windows applications, exhibiting high functionality.

Future works might concentrate on the development of more suitable formulations and/or deposition protocols of gel electrolytes, notably in order to avoid the degradation of the latter during the coloration / bleaching cycles. Indeed, most of the loss in contrast observed in the solid devices arose from the crystals forming in the electrolyte layer, becoming hazy and less transparent, as the active material shows no residual coloration upon cycling. Improvement of this limiting factor should result in even greater performances of the devices, approaching those measured in the liquid setups, and moving forward the development of MoWOx-based full scale electrochromic devices, toward the possibility of a future applied use of such a highly functional material.

5.7. References

1. Vondrák, J. *et al*. *Electrochim. Acta* **1999**, 44, 3067, doi.org/10.1016/s0013-4686(99)00022-5.
2. Denayer, J. *et al*. *Sol. Energy Mater. Sol. Cells* **2014**, 130, 623, doi.org/10.1016/j.solmat.2014.07.038.
3. Ficker, T. *J. Phys. D. Appl. Phys.* **1999**, 32, 219, doi.org/10.1088/0022-3727/32/3/007.
4. Runnerstrom, E. L. *et al*. *Chem. Commun.* **2014**, 50, 10555, doi.org/10.1039/c4cc03109a.
5. Tandon, B. *et al*. *J. Phys. Chem. C* **2022**, 126, 9228, doi.org/10.1021/acs.jpcc.2c02155.
6. Dahlman, C. J. *et al*. *J. Am. Chem. Soc.* **2015**, 137, 9160, doi.org/10.1021/jacs.5b04933.

Chapter 6 – Conclusions and outlooks of the PhD thesis work

Chapter 6 – Conclusions and outlooks of the PhD thesis work

6.1. Conclusions

Throughout this doctoral thesis, the design and synthesis of electrochromic metal oxides as electrode materials has been studied for dual band smart windows applications. To this end, several synthesis pathways, deposition methods and characterization techniques were implemented in order to study the morphological, structural, optical and electronic properties of the investigated formulations, as well as the impact of those latter on the optical and electrochemical performances of the materials.

This research work first looked into the synthesis of innovative active materials which could display peculiar optical modes, in particular: $Mo_{1-y}W_yO_{3-\delta}$, also referred to as “MoWOx”. This compound has been synthesized using a simple one step solvothermal route adapted from previous works of the literature[1,2]. The combination of oxygen deficiency[1–9] and Mo/W mixing[10–18] was expected to enhance the electrochromic performances and functionalities of this formulation, especially allowing the support of the plasmonic features required to express dual band functionalities. While MoWOx materials have been applied in several fields such as (photo)catalysis[1,2,6,7,19], NIR shielding[5], and SERS[9], their electrochromic behavior, and in particular their dual band ability, had never been reported, to the best of our knowledge. In this context, MoWOx powders have been formulated in a Mo/W ratio = 2/1, for durations of 1h and 12h; in addition, pure $WO_{3-\delta}$ formulations have also been synthesized in the same conditions to serve as internal reference, as their dual band electrochromism has already been reported in the literature[20–22]. Characterization of the powders show urchin-like morphology in both MoWOx 1h and 12h, while $WO_{3-\delta}$ appears as aggregated nanospheres and $WO_{3-\delta}$ exhibits hexagonal platelets particles. Optical characterization of the powders, using the Kubelka-Munk formulism in diluted conditions, demonstrated the expected improvement of the absorption of the mixed formulations in comparison to the parent oxides, in good accordance with the electronic properties, determined by XPS and EPR. The combined formation of reduced species and oxygen vacancies during the solvothermal synthesis, enhanced by the Mo/W substitution, resulted in a large polaronic absorption, as well as an increase in free charge carriers, allowing the expression of plasmonic signatures in the metal oxides exhibiting nanostructures (surface nanorods in both MoWOx and nanospheres in $WO_{3-\delta}$).

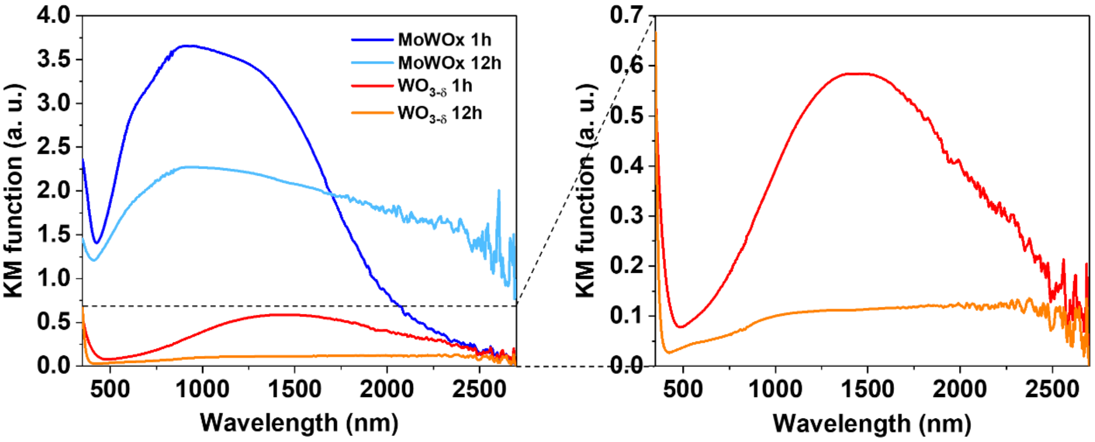

Figure 6.1: KM function obtained from diffuse reflectance data of the MoWOx 1h, MoWOx 12h, $WO_{3-\delta}$ 1h, and $WO_{3-\delta}$ 12h powders (all being diluted in LiF).

These results show the potential for MoWOx formulations to be applied as dual band electrochromic materials, exhibiting large polaronic and plasmonic contributions arising from the concomitant formation of reduced species and oxygen vacancies in the material. Moreover, this work fills a gap in the literature, highlighting the possibility to characterize the absorption of solid samples (powders) using the Kubelka-Munk theory[23,24], provided that some conditions are fulfilled[23]: briefly, diluting the sample in a highly diffusing media (white powder such as LiF, $BaSO_4$, MgO, NaCl) allows the measured spectra to only depend on the absorption coefficient of the sample, which is proportional to its absorption. This proves very useful in the case of a material which is too unstable as a suspension to be measured using Beer-Lambert.

From the four investigated powders (MoWOx and $WO_{3-\delta}$, 1h and 12h), active films were produced by spin coating deposition inks onto FTO-coated glass substrates. These films were then cycled in a lithiated electrolyte ($LiClO_4$ in propylene carbonate), demonstrating the peculiar dual band activity of both MoWOx formulations as well as $WO_{3-\delta}$ 1h, with those three materials displaying an additional intermediate state in comparison to conventional electrochromic compounds such as WO_3 or NiO. This third working state allows the preferential modulation of NIR wavelengths, improving the spectral selectivity of smart windows and leading to significant potential energy savings. Then, in order to highlight the capacitive charge/discharge mechanisms expected in the presence of plasmonic properties, the films were cycled in a $TBAClO_4$ in propylene carbonate electrolyte. Given the large ionic radius of the TBA^+ cations, its insertion into the crystal lattice of the electrochromic material is prohibited, and it can only form a positive layer at the surface of the particles. The transmittance spectra of the three dual band formulations obtained in this setup could only switch from the bright state (VIS-transparent, NIR-transparent) to the intermediate state (VIS-transparent, NIR-darkened), indicating the plasmonic/capacitive nature of the modulation taking place at slightly reducing potentials. Finally, short term stability assessment of the same three films showed the loss of the intermediate state upon completion of an electrochemical cycle, going down to the dark state at -1.0 V and back to the bright state at +1.0 V. From this second cycle, the materials only switched between two optical states, with the bright and intermediate states merging together. Noteworthy, both MoWOx formulations deviate from the classical dual band behavior, starting from an initial state already displaying a partial modulation of the VIS range, corresponding to a so-called "warm" state (VIS-darkened, NIR-transparent), arising from the great polaronic absorption of the materials, and the scattering of light due to the large dimensions of the urchins. To the best of our knowledge, such a warm state has never been reported in Mo or W-based electrochromic materials.

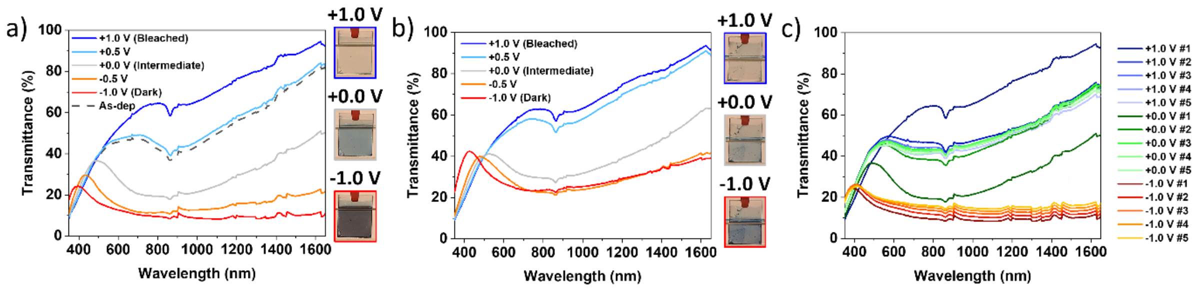

Figure 6.2: SEC transmittance spectra of MoWOx 1h as a function of the applied potential in $LiClO_4$-PC (a), in $TBAClO_4$-PC (b), and for five complete electrochemical cycles in $LiClO_4$-PC.

In order to further push the development of these active materials towards complete electrochromic systems, the formulation of adapted counter electrode materials was required. In this context, the production of CeO_2-based electrodes, using PEG-assisted USP deposition was investigated. As a mean to improve the optoelectronic properties of the cerium oxide, Mo-doping was proposed on the basis of previous literature, involving the use of metallic species with smaller ionic radii than Ce^{4+} (1.03 Å), with Mo^{6+} fulfilling this condition (0.75 Å)[25]. However, this approach has never been reported for the enhancement of the optical and/or electronic performances of CeO_2 films as passive counter electrodes. Nevertheless, Mo had been proposed as a potential doping species by Verma *et al.* back in 2005[26], and was successfully applied as a dopant for SnO_2 by Orel *et al.*[27] and Krašovec *et al.*[28], another widely used passive counter electrode material.

The results obtained in the scope of this research thesis indicated optimum performances for films deposited at 300°C, for 5 sprayed layers, and in the presence of a m_{PEG}/m_{Ce} ratio of 5/1. The undoped films presented excellent properties, with a transmittance of 97% (when the contribution of the FTO-glass substrate is removed from the spectra), and a large capacity of 20.1 mC/cm^2, rivaling or even outperforming most of the previous literature, even when comparing it with the optimal doped species reported in these works. Upon doping, a 95%+ transmittance was retained up to 6%at. Mo, then decreases to 82% at 8%at. and 73% at 10%at. Meanwhile, the capacity consistently increased as a function of the doping rate, increasing from 22.7 to 29.2 mC/cm^2, largely surpassing the existing literature. These results highlighted, for the first time, the efficient formulation of Mo-doped CeO_2 passive counter electrodes, exhibiting large transmittance and capacity, as to not limit the expression of the electrochromic performances of the active material in a complete device setup.

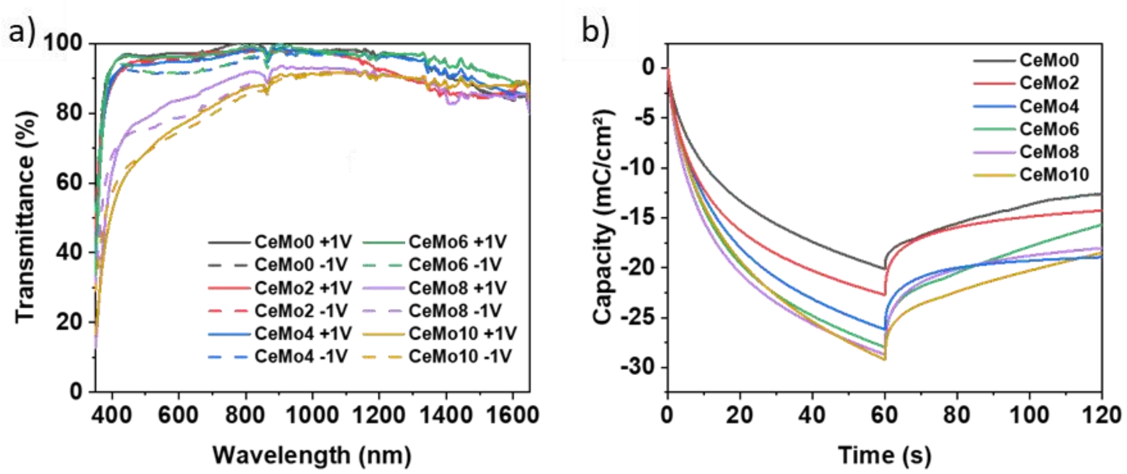

Figure 6.3: SEC transmittance spectra (a), and chronoamperometry curves (b) of (Mo)CeO_2 formulations (0-10%at. Mo).

With efficient formulations now developed for both the working and counter electrodes, the final step of this research work consisted in the production of complete systems involving the two electrodes, placed face to face and separated by the electrolyte layer. In a first step, liquid setups were developed using the same $LiClO_4$ in propylene carbonate formulation used in the previous sections, followed by the manufacture of solid state device, implying the use of a gel polymer electrolyte binding the two electrodes as a single solid unit. Both systems were designed by coupling the (Mo)CeO_2 (0-10%at.) with a conventional WO_3 SMARTSPRAY working electrode as a first trial[29]. As liquid systems, the (Mo)CeO_2 /WO_3 samples displayed contrasts between 65% and 72%, with a bleached transmittance around 80% to 90% and a colored state ranging from 15% to 20% (excepted for CeMo10, with 55% of contrast between 54.2% and 9.1%). Their coloration efficiency reached values between 10 cm^2/C and 15 cm^2/C and a 95%+ reversibility of their coloration. When assembled into solid devices, the same samples exhibited 60% to 73% of contrast (50% for CeMo10) and improved efficiencies of 17 – 23 cm^2/C while their reversibility dropped between 40% and 70% in the solid devices (with the large variability in the results probably arising from the assembly protocol still being optimized). The loss in reversibility arose from the polymer gel degrading upon electrochemical cycling, and resulting in the opacification of the devices, with the lack of residual coloration indicating the solid electrolyte as the weakest link.

In this context, CeMo6 was chosen as the optimal counter electrode formulation, maintaining a high transmittance while optimizing the available capacity, and was coupled with MoWOx 1h and $WO_{3-\delta}$ 1h dual band electrochromic layers. In both liquid and solid state device, the transmittance appeared to be similar to the standalone MoWOx 1h and $WO_{3-\delta}$ 1h, with the occurrence of the three working states at +3.0 V, -1.0 V and -3.0 V (respectively corresponding to +1.0 V, +0.0 V and -1.0 V in the three electrode setup). In addition, the stability of the different optical states upon electrochemical cycling appeared to have greatly improved, with the intermediate state now maintained throughout a few coloration/bleaching cycles, unlike in the three electrode setups.

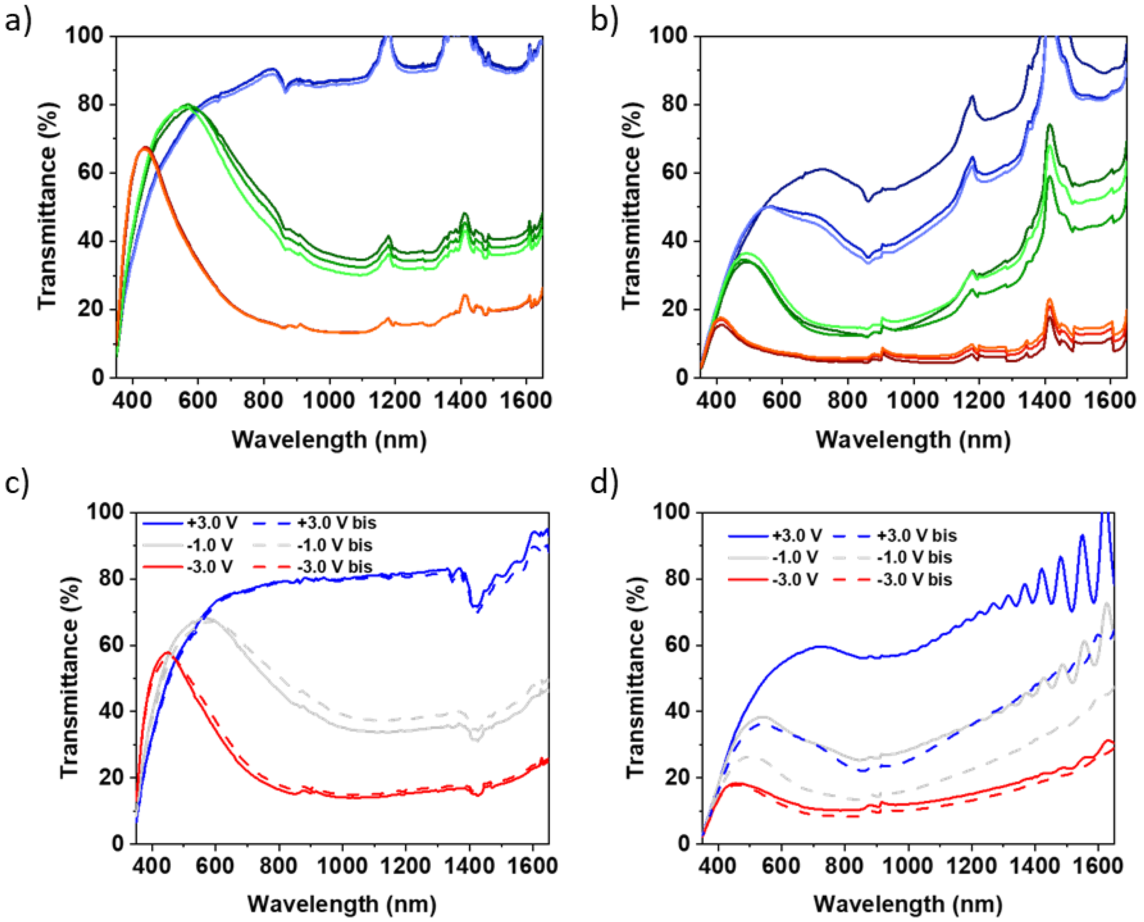

Figure 6.4: SEC transmittance spectra of liquid setups combining CeMo6 and $WO_{3-\delta}$ 1h (a) and MoWOx 1h (b), and solid devices involving CeMo6 and $WO_{3-\delta}$ 1h (c) and MoWOx 1h (d).

The results presented throughout this doctoral research thesis highlighted the peculiar dual band electrochromic behavior of the investigated MoWOx formulations, and the occurrence of a warm state in the latter, arising from the presence of numerous reduced species and oxygen vacancies in the structure, formed during the solvothermal synthesis. These MoWOx materials could be combined with highly efficient (Mo)CeO_2 passive counter electrodes to produce liquid and solid devices exhibiting three optical state as to improve the energy efficiency and spectral selectivity of smart windows. This first proof-of-concept of the dual band electrochromic behavior of MoWOx, as well as the successful assembly of complete devices is highly promising for future research involving the MoWOx formulations, and looking into the further improvement and optimization of their optoelectronic properties.

6.2. Perspectives

While demonstrator dual band devices could be successfully produced, future work is required to further deepen our understanding of the mechanisms at play in the active formulations, and optimize their performances. First of all, other synthetic parameters or routes could be exploited: notably, using thermal degradation under inert atmosphere (Schlenk line), in the presence of surfactants will permit to reach a high control on the morphology and size of the synthesized particles. The refined design of materials with specific morphologies could allow a better tuning of their optoelectronic properties and result in an enhanced efficiency of the layers. Monodisperse nanostructures should allow the support of strong plasmonic features, tuned by modifying their shape, size and composition. In parallel, first principle calculations and modelling could help with the prediction of highly efficient systems through a feedback loop based on the agreement between experimental and theoretical data. In the case of the µm-sized MoWOx urchins, modelling would require extremely important computational power and thus has not been in-depth studied at the present time, but in the case of simpler morphologies such as spheres, cubes, rods etc. the combination of both experimental and theoretical inputs could result in an improved elaboration and production of highly efficient and selective dual band materials.

To transition from powders to active films, the materials need to be formulated into stable inks. Preliminary trials proved this to be difficult in the case of the MoWOx particles, even in the presence of surfactants or after stirring and ultrasonication. While spin coating is easily feasible even if heavy sedimentation occurs in the suspension (the latter can be kept under stirring for the duration of the deposition process, avoiding the sedimentation of the solids in the suspension), other methods require stable inks in a timeframe of at least a few minutes to a few hours. In particular, ultrasonic spray coating, for which GREEnMat has a great expertise, requires stable suspensions in order to avoid clogging as the latter travels into the tubing to the spraying nozzle. If performed correctly, this deposition method allows the production of highly homogeneous and reproducible films (as seen in **Chapter 4**), with the additional benefit of the possible upscaling of the process, adjustable from lab scale to industrial, large scale, deposition. By adjusting the synthetic parameters and suspension conditions, stable electrochromic inks could be obtained, suitable to be deposited via USP.

Different type of substrates could also be investigated, to better harvest the current performances of the films and/or to open the possibility for a wider array of applications. It is well known that the smart glazing industry standards are based on the use of transparent conductive oxides, such as fluorine-doped tin oxide (FTO) or tin-doped indium oxide (ITO), exhibiting excellent electronic conductivity and high transmittance levels in the visible range[30–32]. However, these materials can be problematic for the development of NIR-selective electrochromic coatings, as TCOs present large absorption signals in this part of the solar spectrum (**Figure 6.5**)[33,34]. In this context, alternatives are currently under investigation, in particular, silver nanowires[33–39] which display a constant transmittance across the VIS and NIR ranges, but is still facing issues, especially regarding their durability towards electrochemical cycling[34–36]. In addition, different kinds of substrates could be investigated: for example, coating the films on top of flexible conductive plastics such as poly(ethylene terephthalate) opens up the range of possible applications for the final devices, with the possibility to produced dual band displays and labels such as in the on-going M-ERA.NET funded "PECLABEL" project being conducted notably at GREEnMat[40].

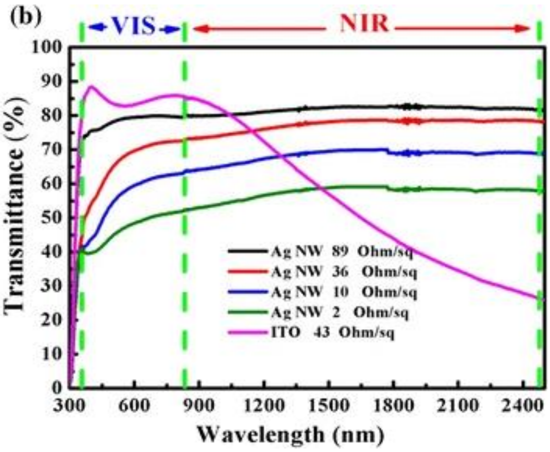

Figure 6.5: Optical spectra of an ITO thin film in comparison to several silver nanowires formulations[33].

By tuning the synthesis and deposition parameters, it is expected that the performances of the films could be improved, especially regarding their stability/reversibility and their spectral selectivity. In the latter case, the formulation of monodisperse powders with a well-defined morphology (possibly supported by theoretical approaches) could lead to a narrower plasmonic signature in the dual band materials, resulting in less overlap between the polaronic and plasmonic contributions, and thus enhancing the NIR selectivity of the materials in the appropriate range of 750-1250 nm. In addition, a more homogeneous distribution of (nano)particles should improve the morphology of the films and therefore their optical properties. Moreover, the smaller size of such particles should greatly increase the available surface area and active sites of the sample, resulting in a better coloration, enhanced kinetics and improved reversibility due to the shorter cationic mean free path.

Finally, as observed in the assembled liquid setups and solid devices, the use of an appropriate counter electrode already solves part of the reversibility issues faced in the case of standalone films. However, the gel polymer electrolyte layer is a limiting factor for the mid/long-term performances of the devices, as it degrades rapidly upon electrochemical cycling. Careful formulation of an adapted electrolyte layer could solve these issues. Notably, its bias window should be large enough for the devices to be operated. In addition, its ionic conductivity should be as high as possible, this way, similar performances can be obtained for slightly less oxidizing/reducing potentials. The long term electrical and thermal stability of the electrolyte should also be assessed during the screening process, as it will impact the long term cycling ability of the devices. Besides, if the intended application does not require the device to be flexible, solid electrolyte formulations could be considered, in particular ceramics such as lithium aluminum based materials, less prone to electrochemical damage than their gel polymer counterparts[30]. In this case, one could imagine the sequential ultrasonic spray coating of the active MoWOx layer, followed by the solid electrolyte, and finally the CeO_2-based counter electrode, with a conductive layer added on top of the stack and connected to the bottom glass substrate, forming an all-solid complete device.

More generally, the formulation of MoWOx active materials displaying a peculiar *warm* mode and their efficient assembly into complete smart windows devices should further improve the energy efficiency of said windows, due to a greater ability to modulate the VIS and NIR ranges independently and better adapt to weather conditions and the users preference. Besides, other formulations might be fit as future candidate for the support of a *warm* state, as observed in MoWOx. For example, careful material design could lead to enough VIS absorption in already reported dual band compounds to access the peculiar *warm* state. Notably, in addition to WO_{3-x} upon which the MoWOx formulations are based, other materials and their doped / mixed versions could be investigated in this perspective, such as TiO_2 [41] and $Nb_{12}O_{29}$ [42]. In particular, V doped TiO_2 reported by Barawi *et al.*[43] is able to selectively modulate the VIS region, but does not exhibit any of the other optical states. Further work on these materials and other similar formulations could lead to the design of highly efficient materials able to reversibly switch between all four modes.

In addition, the interesting optical and electronic properties of MoWOx (and possibly other formulations, as proposed above) could be taken advantage of for others applications, such as catalysis, sensors, batteries of photovoltaic devices. To take it a step further, multiple applications could even be combined in a single system, for example: combining electrochromic and photovoltaic materials could result in a self-powered dual band smart window[44-46], another possibility lies in the possibility of harnessing the energy released during the spontaneous discharge of the electrochromic device to be redirected towards a different system, with the device acting as an electrochromic battery[47,48]. The development of such multifunctional, highly efficient devices could results in even larger energy savings in in buildings in the future.

6.3. References

1. Yin, H. *et al. J. Phys. Chem. C* **2017**, 121, 23531, doi.org/10.1021/acs.jpcc.7b08403.
2. Yin, H. *et al. J. Mater. Chem. A* **2018**, 6, 10932, doi.org/10.1039/c8ta03125h.
3. Zhong, X. *et al. Adv. Funct. Mater.* **2016**, 26, 5778, doi.org/10.1002/adfm.201601732.
4. Zhao, Y. *et al. Int. J. Hydrogen Energy* **2017**, 42, 14534, doi.org/10.1016/j.ijhydene.2017.04.115.
5. Wang, Q. *et al. Appl. Surf. Sci.* **2017**, 399, 41, doi.org/10.1016/j.apsusc.2016.12.022.
6. Yang, M. *et al. ACS Sustain. Chem. Eng.* **2020**, 8, 2957, doi.org/10.1021/acssuschemeng.9b07526.
7. Zhang, N. *et al. J. Am. Chem. Soc.* **2018**, 140, 9434, doi.org/10.1021/jacs.8b02076..
8. Spetter, D. *et al. ACS Sustain. Chem. Eng* **2018**, 6, 12641, doi.org/10.1021/acssuschemeng.8b01370.
9. Li, P. *et al. ACS Appl. Mater. Interfaces* **2020**, 12, 19153, doi.org/10.1021/acsami.0c00220.
10. Li, H. *et al. J. Mater. Chem. C* **2015**, 4, 33, doi.org/10.1039/c5tc02802g.
11. Zhou, D. *et al. J. Colloid Interface Sci.* **2016**, 465, 112, doi.org/10.1016/j.jcis.2015.11.068.
12. Li, H. *et al.* Solution-Processed Porous Tungsten Molybdenum Oxide Electrodes for Energy Storage Smart Windows. *Adv. Mater. Technol.* **2**, 1700047–1700053 (2017).
13. Li, H. *et al. Nano Energy* **2018**, 47, 130, doi.org/10.1016/j.nanoen.2018.02.043.
14. Li, H. *et al. Appl. Mater. Interfaces* **2018**, 10, 10520, doi.org/10.1021/acsami.7b18310.
15. Xie, S. *et al. Appl. Surf. Sci.* **2018**, 459, 774, doi.org/10.1016/j.apsusc.2018.08.045.
16. Wang, B. *et al. Materials* **2018**, 11, 1627, doi.org/10.3390/ma11091627.
17. Kumar, A. *et al. J. Sol-Gel Sci. Technol.* **2019**, 90, 281, doi.org/10.3390/ma11091627.
18. Li, W. *et al. Sol. Energy Mater. Sol. Cells* **2022**, 235, 111488, doi.org/10.1016/j.solmat.2021.111488.
19. Xiong, J. *et al. Sep. Purif. Technol.* **2022**, 294, 121167, doi.org/10.1016/j.seppur.2022.121167.
20. Zhang, S. *et al. Energy Environ. Sci.* **2018**, 11, 2884, doi.org/10.1039/c8ee01718b.
21. Zhang, S. *et al. Mater. Horizons* **2018**, 5, 291, doi.org/10.1039/c7mh01128h.
22. Zhang, S. *et al. Appl. Mater. Interfaces* **2019**, 11, 48062, doi.org/10.1021/acsami.9b17678.
23. Kortüm, G. *Reflectance Spectroscopy: Principles, Methods, Applications*. (published by Springer Science, **1970**).
24. Bourdin, M. *et al. J. Alloys Compd.* **2020**, 823, 153690, doi.org/10.1016/j.jallcom.2020.153690.
25. Zimou, J. *et al. Mater. Sci. Semicond. Process.* **2021**, 135, 1369, doi.org/10.1016/j.mssp.2021.106049.
26. Verma, A. *et al. Indian J. Chem. - Sect. A Inorganic, Phys. Theor. Anal. Chem.* **2005**, 44, 1756, https://nopr.niscpr.res.in/handle/123456789/20191.

27. Orel, B. *et al. J. Mater. Chem.* **1995**, 5, 617, doi.org/10.1039/jm9950500617.

28. Krašovec, U. O. *et al*. *ChemInform* **1998**, 29, 3398, doi.org/10.1149/1.1838025.

29. Denayer, J. *et al*. *Sol. Energy Mater. Sol. Cells* **2014**, 130, 623, doi.org/10.1016/j.solmat.2014.07.038.

30. Kraft, A. *ChemTexts* **2019**, 5, 1, doi.org/10.1007/s40828-018-0076-x.

31. Runnerstrom, E. L. *et al*. *Chem. Commun.* **2014**, 50, 10555, doi.org/10.1039/c4cc03109a.

32. Wang, Y. *et al*. *Annu. Rev. Chem. Biomol. Eng* **2016**, 7, 283, doi.org/10.1146/annurev-chembioeng-080615-034647.

33. Zhou, K. L. *et al*. *J. Mater. Sci.* **2017**, 52, 12783, doi.org/10.1007/s10853-017-1391-0.

34. Bellet, D. *et al*. *Mater.* **2017***,* 10, 570, doi.org/10.3390/ma10060570.

35. Nguyen, V. H. *et al*. *Small* **2022**, 18, doi.org/10.1002/smll.202106006.

36. Khan, A. *et al. ACS Appl. Mater. Interfaces* **2018**, 10, 19208, doi.org/10.1021/acsami.8b03079.

37. Langley, D. P. *et al*. *Nanoscale* **2014**, 6, 13535, doi.org/10.1039/c4nr04151h.

38. Khan, A. *et al*. *ACS Appl. Mater. Interfaces* **2024**, 16, 10439, doi.org/10.1021/acsami.3c14419.

39. Ambreen, A. Développement de couches minces à base de réseaux de nanofils métalliques et d'oxydes fonctionnels pour des fenêtres intelligentes écoénergétiques. (University Grenoble Alpes, **2021**).

40. https://www.peclabel.eu/cms/c_19127792/en/peclabel?id=c_19127792, accessed on 10/09/2024.

41. Barawi, M. *et al*. *ACS Nano* **2017**, 11, 3576, doi.org/10.1021/acsnano.6b06664.

42. Lu, H.-C. *et al*. *ACS Nano* **2020**, 14, 10068, doi.org/10.1021/acsnano.0c03283.

43. Barawi, M. *et al*. *J. Mater. Chem. A* **2018**, 6, 10201, doi.org/10.1039/c8ta02636j.

44. Cho, J. *et al. Adv. Funct. Mater.* **2020**, 30, 1909601, doi.org/10.1002/adfm.201909601.

45. Cánovas-Saura, A. *et al. Electron. Mater.* **2021**, 2, 174, doi.org/10.3390/electronicmat2020014.

46. Huang, J. *et al. Adv. Energy Mater.* **2022**, 12, 2201042, doi.org/10.1002/aenm.202201042.

47. Wang, J. *et al*. *Nat. Commun.* **2014**, 5, 1, doi.org/10.1038/ncomms5921.

48. Zhou, D. *et al*. *J. Colloid Interface Sci.* **2016**, 465, 112, doi.org/10.1016/j.jcis.2015.11.068.

Annexes

Annexes

A.1. Characterization methods

a. TEM

Transmission electronic microscopy (TEM) is an imagery technique that allows the observation of particles at high magnification for determination of their morphology and size. The acquisition of the micrographs is based on the transmission of an electron beam through a thin sample. As the thickness and density of the material increase, fewer electrons reach the detector below. This creates a contrast between the regions of high and low coverage densities, creating a monochromic picture of the sample. In the scope of plasmonic materials, this technique comes in as very useful to investigate the presence of nanostructures in the particles of interest, as they are necessary to support LSPR features.

For the preparation of the samples, a drop of a low boiling point solvent (ethanol for example) containing the compound of interest is placed on a copper grid and evaporated. Thanks to this process, solid particles can be deposited as a monolayer if the concentration is low enough, enabling the observation of individual particles. Sometimes, one side of the grid is covered with a carbon film to allow the deposition of small particles that would otherwise pass through the mesh because of their small size.

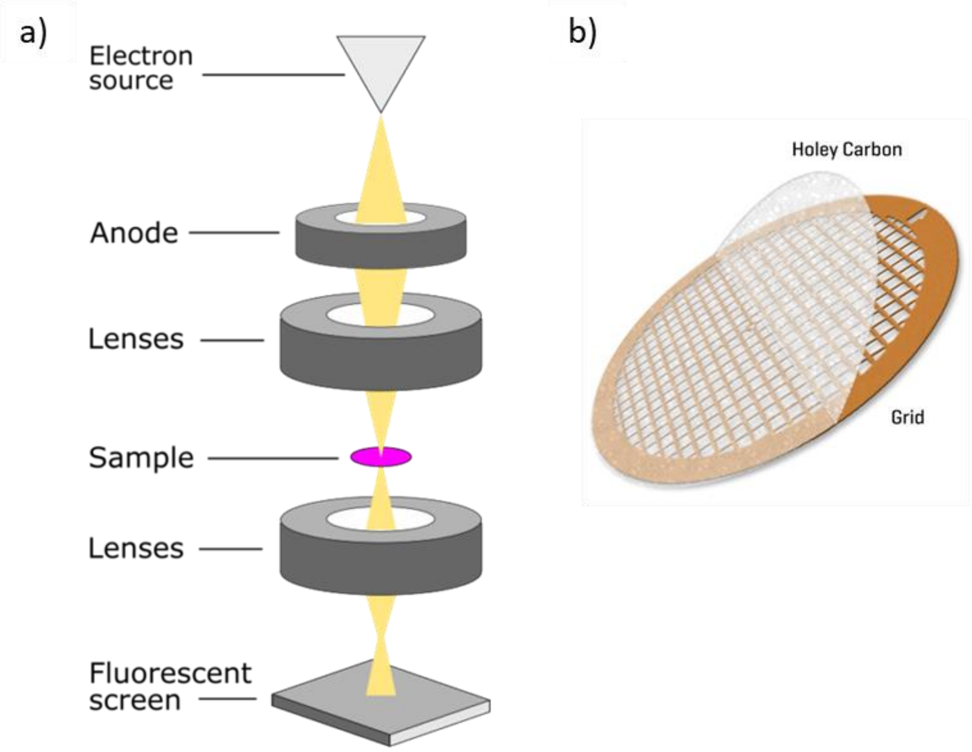

Figure A.1: Schematic representation of the TEM equipment (a)[1] and the copper grid (b)[2].

b. SEM and EDX

Scanning electron microscopy (SEM) is related to the TEM imagery technique to the extent that both allow the characterization and measurement of the morphological properties of a material such as size and shape. However, the principles by which the micrographs are acquired differ significantly.

In SEM, an electronic beam is focused on the sample. If the sample is not intrinsically conductive, the surface can be covered with a layer of a highly conductive material such as Au, Ag, C or Pt. The interaction between the electron beam and the conductive material leads to the emission of secondary electron of lower energy. The detection of these secondary electrons defines a representation of the surface and the topography of the sample.

In addition, the nature of the materials can be studied using the same instrument. Indeed, the interaction between the electron beam and matter can give place to many different signals all bearing information about the sample. Energy dispersive X-ray (EDX) measurement allows the characterization of the material at an elemental level. If the incident electron beam interacts with electrons in the inner electronic shells and transfers its energy, the electron can either "jump" to a higher energy level or can be ejected from the atom. In both case, the displacement of the electron leaves a hole in the low energy shells. An electron from an outer shell will therefore fill this hole. The difference in energy between the two levels can be emitted in the form of X-rays. Each element presents a characteristic EDX signature composed of different rays acting as a "fingerprint" that can be easily spotted in the EDX spectrum of the material. This technique therefore allows the semi-quantification of the species present in a sample. Given the significant effect of their composition on the properties of MoWOx formulations, EDX allows to routinely investigate the composition of different MoWOx composition or check the repeatability of the solvothermal process across multiple batches.

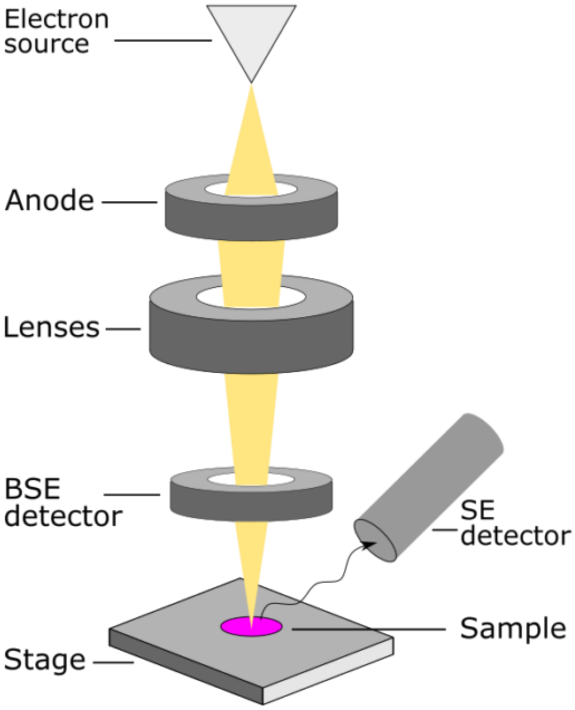

Figure A.2: Schematic representation of the SEM equipment[1].

c. XRD

Information about the crystallinity and the different phases in a given material can be recovered from the characterization of a sample by X-ray diffraction.

When X-rays interact with crystalline substances, they are diffracted by the atoms of the lattice, inducing interferences between the beams. These interference can be constructive if they satisfy Bragg's law, defined as **Equation A.1**:

$$2d\sin\theta = n\lambda \qquad (A.1)$$

With d the reticular distance, θ the scattering angle, λ the wavelength of the incident X-ray beam and n a positive integer.

Depending on the angle of the incident beam and the distance between the atoms forming the lattice of the material, both destructive and constructive interference can take place (as shown in **Figure A.3**). In the case of a constructive interference, the signal will lead to a set of characteristic diffraction rays that can be identified in the diffractogram of the sample. With high quality XRD equipment readily available at GREEnMat, this technique is often used to identify materials and their crystalline phases, on which physico-chemical and optoelectronic properties can depend. Such information is thus essential for the design of efficient formulations.

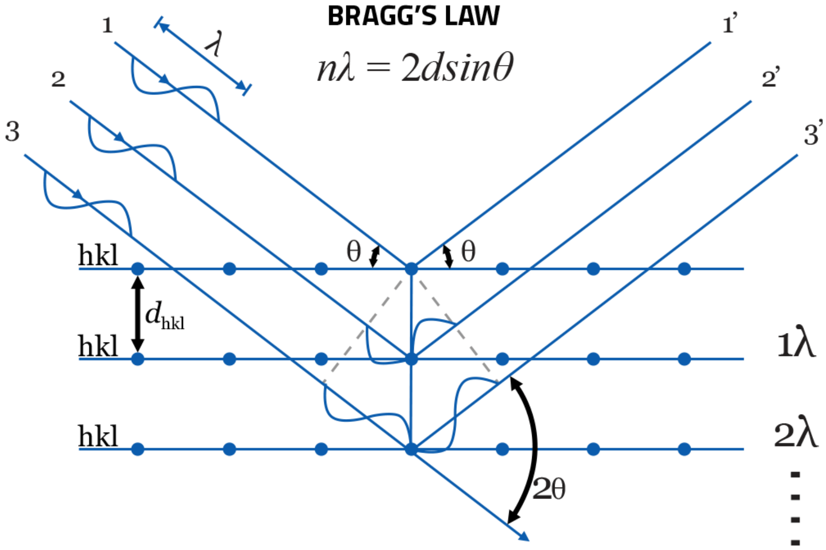

Figure A.3: Representation of the interference phenomenon arising from the diffraction of X-rays in crystals[3].

d. UV-Vis-NIR spectrophotometry

In spectrophotometry, an incident radiation is sent on a sample (suspension, thin film…). Interactions between the optically active species and the incident light wave can give rise to absorbance, emission or scattering from the electronic transition taking place in the active molecules. The measurement of the resulting spectrum highlights the wavelength at which these phenomena take place.

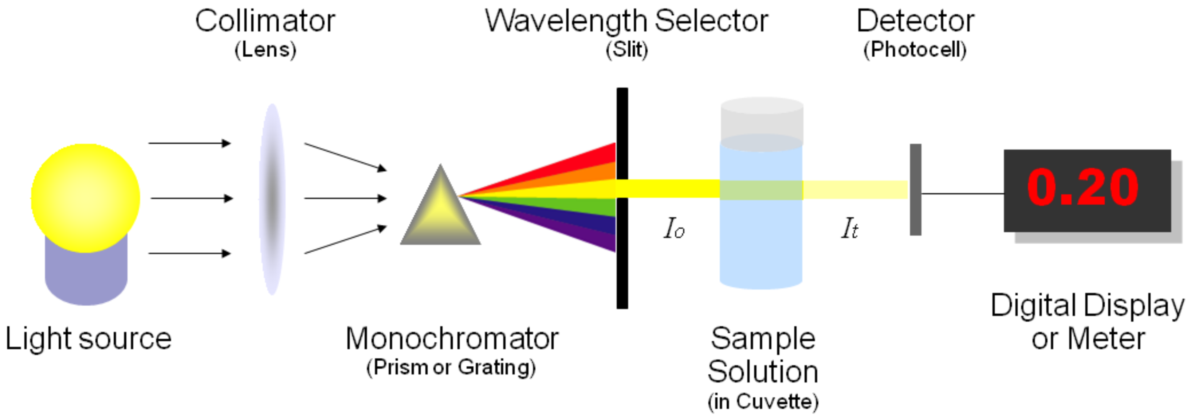

Figure A.4: Schematic representation of the measurement using a spectrophotometer equipment[4].

For diffuse reflectance measurements of powders, the sample needs to be placed in an integrating sphere (**Figure A.5**). If the incident radiation is reflected more than once by the powder and in all directions, it is said to be diffuse reflected light (in comparison with specular reflected light which is only reflected once and at an angle equal to that of the angle formed between the incident beam and the normal to the plan of the reflective material) (**Figure A.5**).

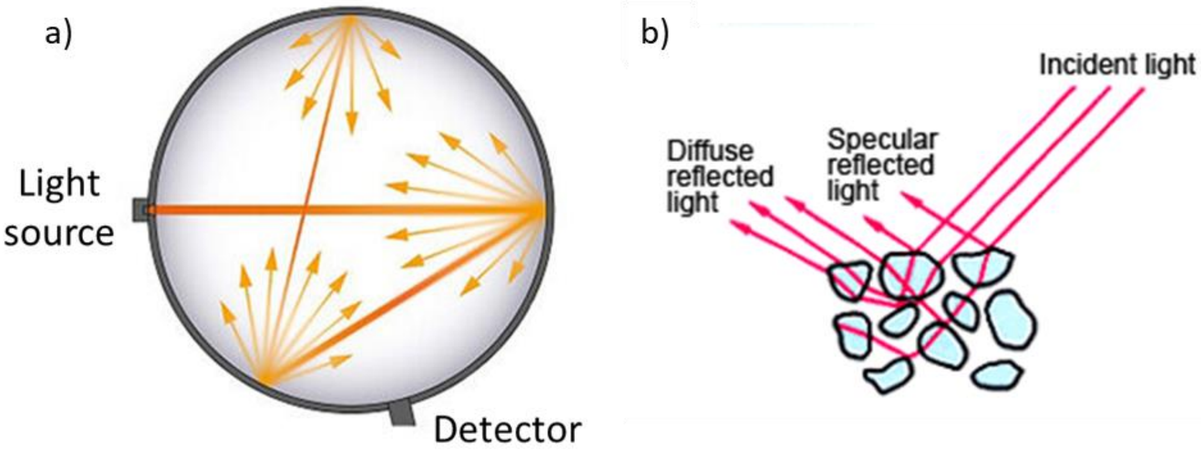

Figure A.5: Representation of the specular and diffuse reflectance in a powder (a)[5] and schematic representation of a integrating sphere set-up (b)[6].

In the framework of electrochromics, the optical properties of the investigated formulations should be thoroughly studied as to assess promising candidates as powder formulations. Diffuse reflectance, coupled with the Kubelka-Munk formulism, allows the characterization of the absorption properties of solid materials, as used to compare the optical signature of the four compounds of interest, namely MoWOx 1h and 12h, and the corresponding $WO_{3-\delta}$ parent oxides.

e. XPS

X-ray photoelectron spectroscopy (XPS) is a semi-quantitative surface analysis technique allowing the characterization of the composition and electronic properties (valence state) of solid samples. Briefly, a monochromatic X-ray beam irradiates a sample: if the energy of the X-ray photon is sufficient, electrons can be emitted from the core of the elements present in the sample through the photoelectric effect. Since the energy of the photons is known (1.4867 keV for Al K_α) and the kinetic energy of the emitted electrons is measured, the binding energy of the latter can be determined using **Equation A.2** below:

$$E_{binding} = E_{photon} - (E_{kinetic} + \Phi) \qquad (A.2)$$

With $E_{binding}$ the binding energy of the core electron, $E_{kinetic}$ the kinetic energy of the same electron after emission, E_{photon} the energy of the monochromatic X-ray beam and Φ is the work function of the material, defined as the difference in energy between the Fermi level and the vacuum level (corresponding to the energy required for the electron to escape the atom).

Using XPS, the surface composition of the studied materials could be quantified, as well as the oxidation levels of the different species composing the formulation (either Mo, W and O in MoWOx or only W and O in $WO_{3-\delta}$. These characterizations could be linked to the optical behavior of the four compounds of interest while the large number of reduced species observed in these materials further supported their deduced ability to support plasmonic phenomena.

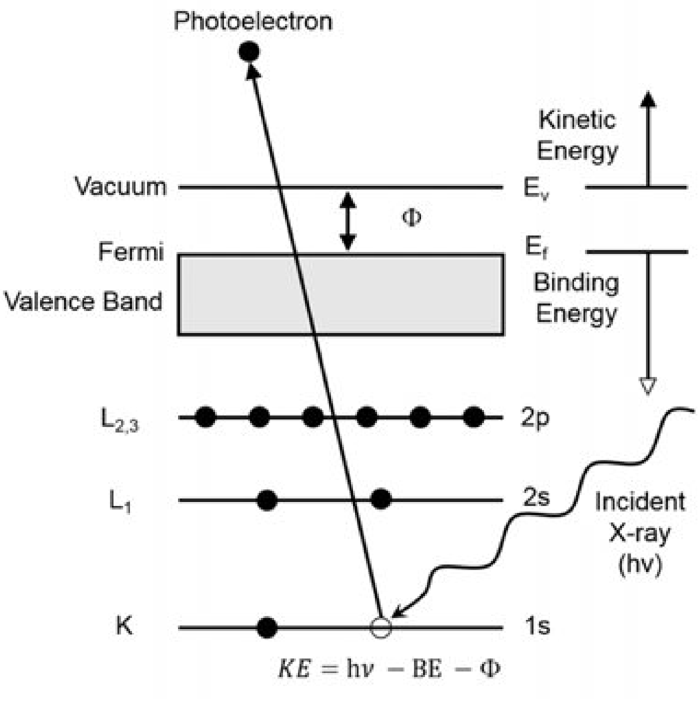

Figure A.6: Schematic representation of XPS highlighting the binding and kinetic energy of the emitted core electron[7].

f. EPR

Electron paramagnetic resonance (EPR) is a spectroscopic analysis technique probing the presence of paramagnetic species, *i. e.* unpaired electrons such as free electrons delocalized in the conduction band, electrons trapped in defects or reduced species. An magnetic field is applied to the sample, resulting in the splitting of the energy levels of the positive and negative spins. In practice, a microwave source of constant frequency is used while the magnetic field increases progressively: the positive and negative spins becomes more separated, up to the point where the difference in their energy levels corresponds to the energy of the microwave photons, the spin of the electrons can thus switch and a net absorption is observed. The absorption of the photon can be described such as in **Equation A.3** below:

$$h\nu = g\mu_B H_0 \qquad (A.3)$$

With $h\nu$ the energy of the absorbed photon, g the Landé g-factor, μ_B the Bohr magneton and H_0 the intensity of the external magnetic field. The g-factor depends on the surrounding environment of the paramagnetic species, leading to spin-orbit coupling and the modification of the absorption properties and the multiplication of the signals into hyperfine patterns.

In comparison to XPS, the probing depth of EPR allows the characterization of the bulk, once again highlighting the presence of reduced species in the investigated formulations. These measurements could once again be linked with the optical behavior of the four materials as powders, with the intensity of the optical signature proportional to that of the EPR spectra.

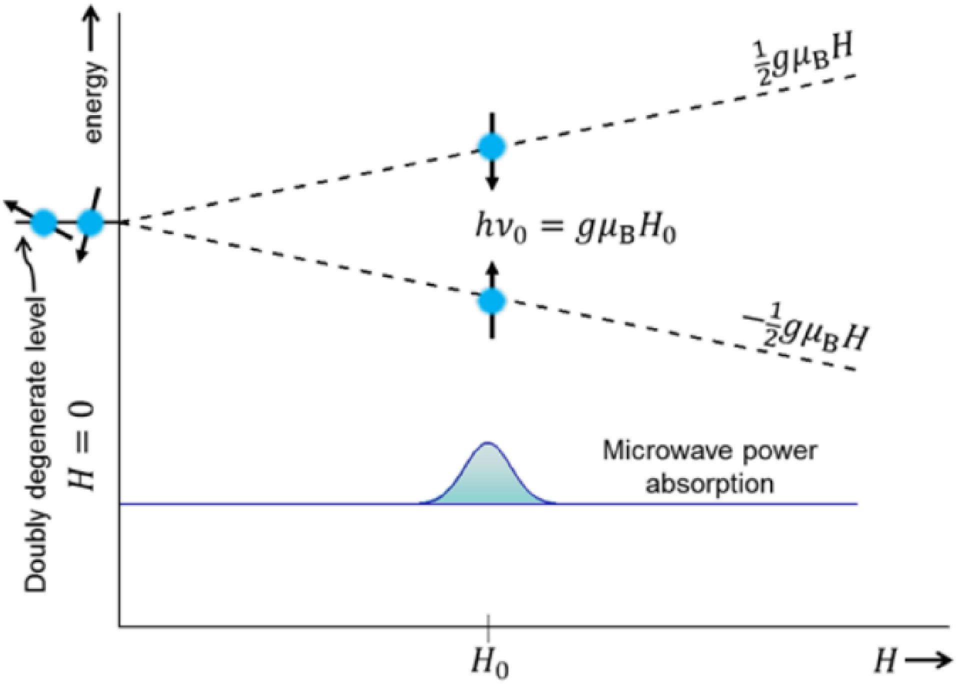

Figure A.7: Schematic representation of the electronic spin states spiltting as a function of the magnetic field, and the absorption at the resonance conditions[8]*.*

g. Zeta potential

The zeta potential describes the charge appearing at the interface between the surface of a particle and a liquid. The charges at the surface of the particles interact with the ions in the liquid, modifying their distribution in the media. This phenomenon causes the formation of a double charge layer at the interface. The first charge layer is well organized and consists in ions tightly bound to the surface of the particles thanks to the attraction between opposite charges. The second layer, farther from the interface, is also called the diffuse layer. In this region, ions are not bound anymore and the potential decreases as a function of the distance to the interface. This effect is due to the increasing role of the random thermal agitation of the ions as the potential gradually decreases. Since the zeta potential can be linked to the charge at the surface of the particles, and therefore to the electrostatic repulsion between the latter, this measurement can be used as an indicator of the colloidal stability of the particles in suspension.

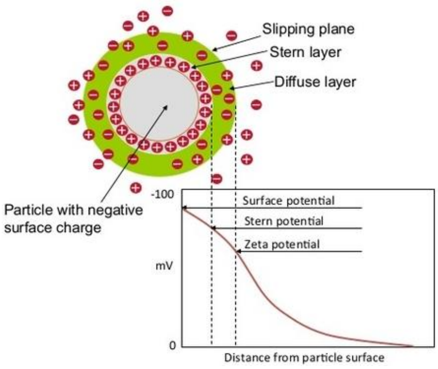

Figure A.8: Representation of the double-layered organization of the charges in the vicinity of a particle in suspension[5]*.*

The zeta potential can be measured using an electroacoustic phenomenon known as the colloid vibration current. When an ultrasound wave propagates through a liquid media, the particles and ions in this media are displaced at different rates, thus disturbing the double layer structure around the particles. The fluid flow caused by the wave drags the ions of the double layer towards one of the poles of the particle. This displacement of charges induces an excess of charges at one of the poles and a corresponding excess of opposite charges at the other pole. This charge gradient in the vicinity of the particle induces a dipole moment in the latter, generating an electric field in the liquid. By measuring the electric current arising from the induced electric field, and knowing the size of the particles, their density and the weight content of the suspension, it is possible to determine the zeta potential per particle of the suspended material. In this work, it has been used to monitor the ageing of MoWOx particles in suspension in ethanol, kept under stirring for up to a week.

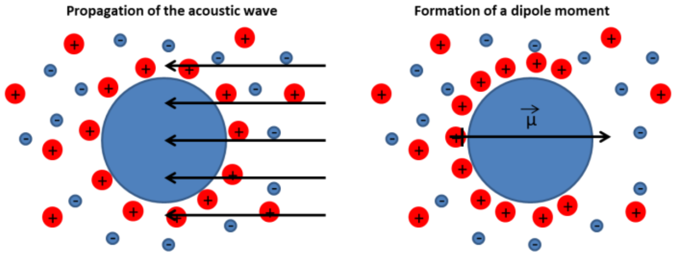

Figure A.9: Electroacoustic measurement of the surface potential of a particle in suspension.

h. Electrochemical techniques: CV & CA

Cyclic Voltammetry (CV) measurements imply the application of a triangular application: a potential ramp is applied at a constant rate, followed by the inverted scan going back to the starting potential.

In a fully reversible system, the CV curves exhibit a “duck” shape, with the oxidation peak and the reduction peak present in similar intensities on the forward and backward scans respectively in the example below. This characteristic shape shows that all the oxidized/reduced species are reduced/oxidized back to their original state during the inverted scan (with the condition that the scanning rate should be faster than the reaction rate for the chemical transformation of the species in the potential interval). CV has been used to investigate the electrochemical behavior of the studied formulations, as well as defining the window of potential in which the materials and electrolyte are stable (as the degradation of the latter would appear in the CV, especially around extreme values).

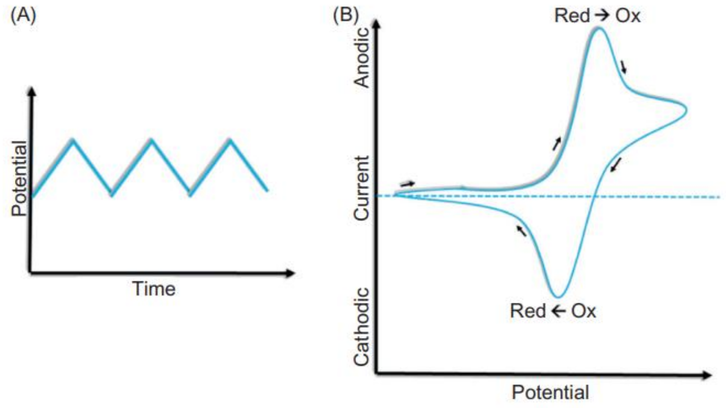

Figure A.10: Triangular variation of the potential as a function of time (a) and the resulting typical CV curve of a reversible sample (b)[9].

Chronoamperometry measurements (CA) imply the application of a stepped potential at the working electrode. The resulting current, arising from the faradaic phenomenon taking place at the electrode after the application of the potential step, is monitored as a function of time. The relationship between the electrical signal and time can be established after a single or multiple potential steps. This technique has been used to color and bleach the samples to study the evolution of their coloration, and also allows the retrieval of Q_{in} (being the density of inserted charges), needed to compute the coloration efficiency of the formulations and be able to compare them.

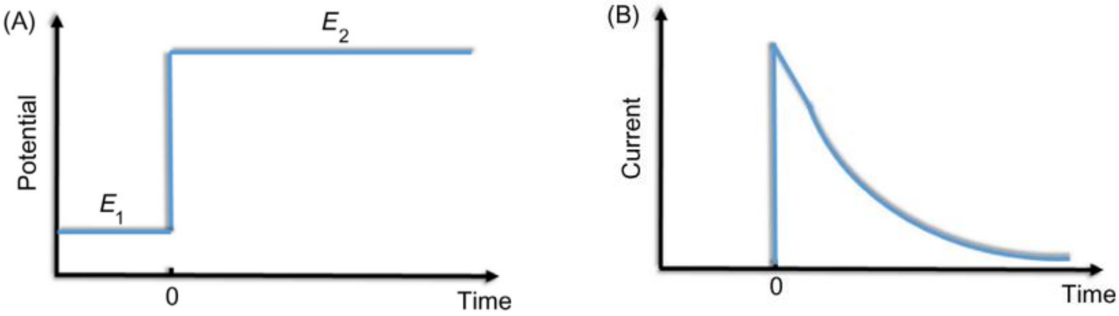

Figure A.11: Representation of the stepped bias (a) and the resulting current response (b)[9].

i. SEC and kinetics

Spectrophotometry and electrochemistry can be coupled to study the optical properties of an electrochromic material *in-situ*. The material is plunged in an electrolyte with a counter electrode (and a reference electrode), or formulated as a solid device, and placed in the analysis chamber of the spectrophotometer. A constant potential is applied for a given duration (as in CA) and a transmittance spectra of the sample is consecutively acquired over a range of wavelengths. Then, a different bias is applied and the process is repeated, allowing the comparison of the transmittance as a function of the applied potential in a wide range of wavelengths, for example: VIS and NIR ranges are simultaneously characterized, demonstrating any selective behavior towards those spectral regions. On the other hand, it is possible to keep the wavelength constant and vary the applied potential over time, resulting in kinetics spectra highlighting the speed of the coloration and bleaching processes.

SEC and kinetics are the most useful characterization technique to assess the electrochromic properties of formulations, allowing the measurement of many important properties such as their contrast, coloration/bleaching time, coloration efficiency, resulting in the complete electrochromic characterization of the investigated formulations for a limited amount of experiments.

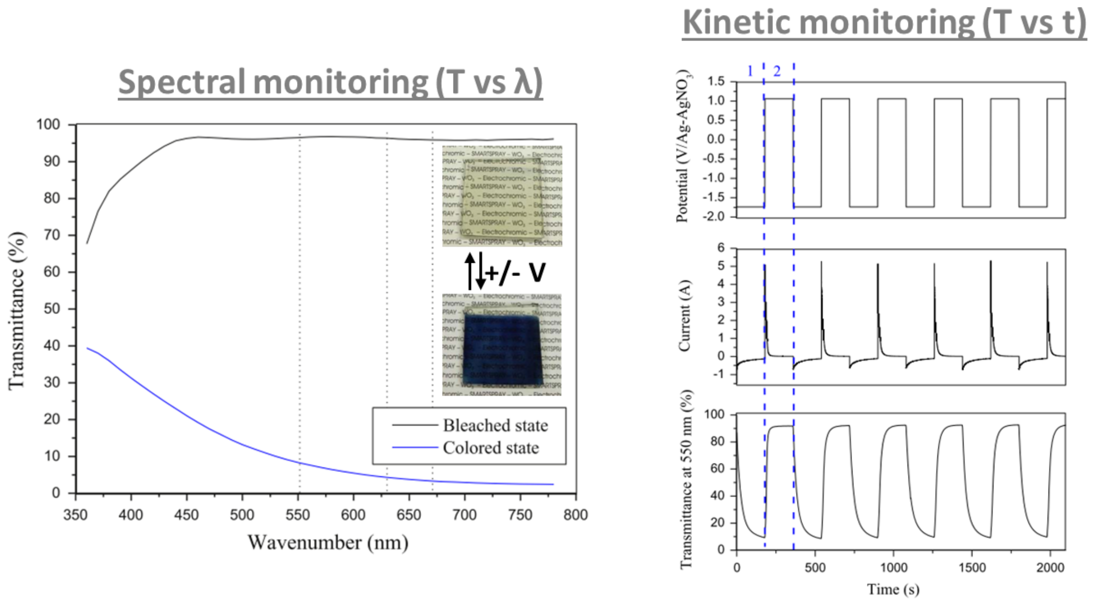

Figure A.12: SEC transmittance spectra at a given bias as a function of the wavelength (a), and kinetics spectra at a given wavelength (550 nm here) as a function of time and the applied bias[10].

j. Raman

Raman spectroscopy allow the determination of vibrational states in materials upon absorption of photons in the visible, near infrared or near ultraviolet range, produced from a laser source. The photons are absorbed and electrons are promoted from their vibrational state to a temporary, virtual state. In most cases, the electron will return to its initial vibrational state (known as the Rayleigh scattering), but a fraction will start from the ground state and return to an excited state or vice versa, after emitting a photon: these phenomena are known as Stokes and anti-Stokes scattering, respectively. In the case of Rayleigh scattering, both absorbed and emitted photons possess the same energy and nothing is observed, however, in the case of (anti-)Stokes scattering, the energy of the emitted photon is (higher) lower than that of the absorbed electron, resulting in a signal describing the vibrational structure of the investigated material. Raman spectroscopy allows the identification of modified structures in materials, indicating the presence of species and defects such as oxygen vacancies, influencing the other properties of the material, especially from an optical and electrochemical point of view.

Typically, the results are expressed as wavenumbers in cm^{-1}, and the Raman shift can be computed from the wavelength of the signal in **Equation A.4** below:

$$\Delta\tilde{\nu} = \left(\frac{1}{\lambda_0} - \frac{1}{\lambda_1}\right) \qquad (A.4)$$

Where $\Delta\tilde{\nu}$ is the Raman shift in cm^{-1}, λ_0 is the excitation wavelength of the laser and λ_1 is the wavelength of the emitted photons.

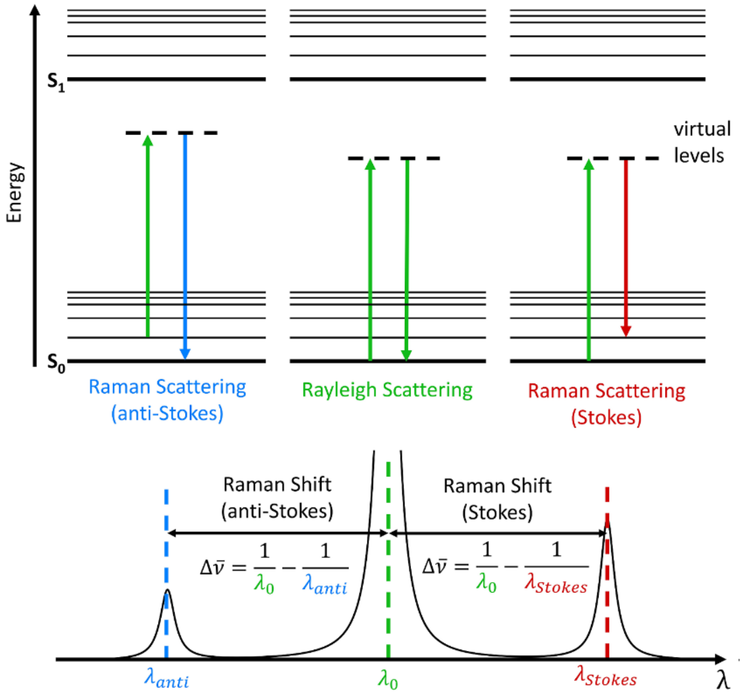

Figure A.13: Schematic representation of the excitation and relaxation process in Raman spectroscopy, and the three different type of scattering (Rayleigh, Stokes and anti-Stokes)[11].

A.2. References

1. https://anapath.ch/electron-microscopy-2/, accessed on 09/10/2024.
2. http://www.emresolutions.com/product-info/support-films-holey-lacey, accessed on 09/10/2024.
3. https://www.veqter.co.uk/residual-stress-measurement/x-ray-diffraction, accessed on 09/10/2024.
4. https://encrypted-tbn0.gstatic.com/images?q=tbn:ANd9GcQ4A5rGi0TSaGT13PYsHejGv7VFd7NXclhfdA&s, accessed on 09/10/2024.
5. http://link.springer.com/10.1007/978-0-387-30160-0_6266, accessed on 09/10/2024.
6. https://onlinelibrary.wiley.com/doi/10.1002/9783527809080.cataz05336, accessed on 09/10/2024.
7. https://www.researchgate.net/publication/333004216_Transition_Metal-Based_Electrocatalysts_for_Alkaline_Water_Splitting_and_CO2_Reduction/figures?lo=1, accessed on 09/10/2024.
8. https://www.pi1.uni-stuttgart.de/research/methods_overview/electron-spin-resonance/, accessed on 09/10/2024.
9. https://www.sciencedirect.com/science/article/abs/pii/B9780128136911000063, accessed on 09/10/2024.
10. Denayer, J. *et al*. *Sol. Energy Mater. Sol. Cells* **2014**, 130, 623, doi.org/10.1016/j.solmat.2014.07.038.
11. https://www.rigaslabs.gr/product-category/molecular-spectroscopy/raman-spectrometers-microscopes/, accessed on 09/10/2024.